

# **Integration of LiDAR and Photogrammetric Data for Enhanced Aerial Triangulation and Camera Calibration**



Abdulhamed Salhen Gneeniss

School of Civil Engineering and Geosciences

Newcastle University

Thesis Submitted for the Degree of

Doctor of Philosophy

November, 2013

# Abstract

---

The integration of complementary airborne light detection and ranging (LiDAR) and photogrammetric data continues to receive attention from the relevant research communities. Such an approach requires the optimized registration of the two data types within a common coordinate reference frame and thus enables the cross-calibration of one information source against another. This research assumes airborne LiDAR as a reference dataset against which in-flight camera system calibration and validation can be performed. The novel methodology involves the production of dense photogrammetric point clouds derived using the simultaneous adjustment of GNSS/IMU data and a dense set of photogrammetric tie points. Quality of the generated photogrammetric dataset is further improved through introducing the self-calibration additional parameters in the combined adjustment. A robust least squares surface matching algorithm is then used to minimise the Euclidean distances between the two datasets. After successful matching, well distributed LiDAR-derived control points (LCPs) are automatically identified and extracted. Adjustment of the photogrammetric data is then repeated using extracted LCPs in a self-calibrating bundle adjustment. The research methodology was tested using two datasets acquired using different photogrammetric digital sensor systems, a Microsoft UltraCamX large format camera and an Applanix DSS322 medium format camera. Systematic sensitivity testing included the influence of the number and weighting of LCPs required to achieve optimised adjustment. For the UltraCamX block it was found that when the number of control points exceeded 80, the accuracy of the adjustment stabilized at c. 2 cm in all axes, regardless of point weighting. Results were also compared with those from reference calibration using surveyed ground control points in the test area, with good agreement found between the two. Similar results were obtained for the DSS322 block, with block accuracy stabilizing at 100 LCPs. Moreover, for the DSS322 camera, introducing self-calibration greatly improved the accuracy of aerial triangulation.

# Acknowledgements

---

In the name of Allah the most gracious the most merciful.

First, praise is due to Allah for both his guidance and support to complete this challenging work.

Second, I would like to thank my supervisors Prof. Jon Mills and Dr. Pauline Miller for their support throughout my research and especially during the hard times when the unrest in my home country Libya has led to major changes in my research objectives and restart my practical work almost from the scratch. I am highly indebted to them for their support and encouragement throughout my study.

I also would like to acknowledge Dr. Michael Cramer and Dr. Manfred Wiggenhag from the Deutsche Gesellschaft für Photogrammetrie, Fernerkundung und Geoinformation (DGPF) for providing the LiDAR data and aerial imagery. I would also like to thank Dr. Karsten Jacobsen from Leibniz Universität Hannover for providing access to the BLUH bundle adjustment software. I would also like to thank Dr. Matthias Kunz for his help and support in performing the surface matching part of my research.

Most importantly, I would like to thank my family, Mother, father and siblings for their support and prayers. Also my special thanks go to my wife and children as they deserve my unending gratitude for their help, support, patience and understanding throughout my study when it has taken most of my time.

My gratitude also extends to Eng. Naji Attumi and Eng Alkuni for their help during the field work performed in Libya in 2010 before the change of my research objectives.

Finally, I would also like to thank the Libyan government for giving me the chance to pursue my postgraduate study. My appreciation is extended to the head and members of the Libyan cultural affairs, London, especially my academic supervisor Faisel Antat for his efforts to make the administrative correspondences as easy as possible.

# Table of Contents

---

<b>Abstract.....</b>	<b>ii</b>
<b>Acknowledgements.....</b>	<b>i</b>
<b>Table of Contents .....</b>	<b>iv</b>
<b>List of Figures.....</b>	<b>xi</b>
<b>List of Tables .....</b>	<b>iv</b>
<b>List of Abbreviations and Notation .....</b>	<b>xviii</b>
<b>1 Introduction.....</b>	<b>1</b>
1.1 Background.....	1
1.2 Calibration of Digital Aerial Cameras .....	3
1.3 Registration of LiDAR and Photogrammetric Data .....	5
1.4 LiDAR Data as Source of Photogrammetric Control .....	7
1.5 Research Motivation .....	8
1.6 Aim and Objectives .....	9
1.7 Thesis Outline .....	9
<b>2 Aerial Camera Systems and Calibration .....</b>	<b>11</b>
2.1 Introduction.....	11
2.2 Large Format Aerial Digital Cameras .....	12
2.2.1 Background .....	12
2.2.2 Large Format Single-head Frame Cameras.....	12
2.2.3 Multi-head Digital Frame Cameras – Simultaneous Imaging.....	13
2.2.4 Multi-head Digital Frame Cameras - Syntopic Imaging.....	15



2.2.5	Large Format Line Scanner Cameras.....	18
2.3	<i>Medium Format Digital Aerial Cameras.....</i>	19
2.3.1	Introduction.....	19
2.3.2	UltraCam L(P) Medium Format Camera .....	20
2.3.3	RMK D Medium Format Camera .....	21
2.3.4	Leica RCD 30 Medium Format Camera .....	21
2.3.5	Applanix DSS322 Medium Format Camera.....	22
2.4	<i>Camera System Calibration.....</i>	24
2.4.1	Purpose of Camera Calibration .....	24
2.4.2	Photogrammetric Camera Model .....	25
2.4.3	Laboratory Camera Calibration.....	26
2.4.4	Simultaneous Camera Calibration .....	29
2.4.5	Test Field Camera Calibration .....	30
2.4.6	Boresight Calibration .....	32
2.5	<i>GNSS/IMU Orientation for Digital Photogrammetry.....</i>	33
2.5.1	Direct Geo-referencing.....	35
2.5.2	Integrated Sensor Orientation (ISO) .....	36
2.6	<i>Summary.....</i>	36
<b>3</b>	<b>Integration of LiDAR and Photogrammetry .....</b>	<b>38</b>
3.1	<i>Introduction.....</i>	38
3.2	<i>Principles and Design of LiDAR System.....</i>	39
3.2.1	Laser Scanner Design and Data Capture.....	42
3.2.1.1	Laser Pulse Generation .....	42
3.2.1.2	Laser Echo Reception .....	43
3.2.2	LiDAR Data Processing.....	45
3.2.3	Accuracy of LiDAR Data.....	46

3.2.4	Improvement of LiDAR Data Accuracy .....	47
3.2.5	Generation of Digital Terrain and Surface Models from LiDAR Data .....	48
3.3	<i>Complementary Characteristics of LiDAR and Photogrammetry</i> .....	49
3.3.1	Advantages and Limitations of LiDAR Systems .....	49
3.3.2	Advantages and Limitations of Photogrammetric Methods .....	50
3.4	<i>LiDAR and Photogrammetry Registration Methods</i> .....	50
3.4.1	Overview .....	51
3.4.2	Types of Registration Methods .....	52
3.4.2.1	Feature-based Registration .....	52
3.4.2.2	Surface-based Registration .....	54
3.4.2.3	Intensity and Frequency-based Registration .....	55
3.4.2.4	Summary of Registration Methods .....	56
3.5	<i>Deriving Reference Control Points from LiDAR Data</i> .....	57
3.5.1	Introduction .....	57
3.5.2	Reference LiDAR-derived Point Features .....	58
3.5.2.1	Centroids of Rectangular Building Roofs .....	58
3.5.2.2	LiDAR Intensity Image .....	59
3.5.2.3	LiDAR Shaded Relief Image .....	60
3.5.2.4	LiDAR Reference Targets .....	60
3.5.3	Linear Features .....	61
3.5.4	Planar Patches .....	61
3.6	<i>Summary</i> .....	62
<b>4</b>	<b>Methodology</b> .....	<b>64</b>
4.1	<i>Introduction</i> .....	64
4.2	<i>Methodology Workflow</i> .....	65
4.3	<i>Matlab Algorithm</i> .....	66

4.3.1	Pre-match Functions.....	66
4.3.2	Post-match Functions .....	67
4.4	<i>Point Measurement criteria</i> .....	69
4.4.1	Image Import and Pre-processing .....	69
4.4.2	Block Setup .....	69
4.4.3	Automatic Dense Point Measurement.....	69
4.5	<i>Reference LiDAR Data Processing</i> .....	71
4.6	<i>Generation of Photogrammetric Tie Point's Mask</i> .....	71
4.7	<i>Integrated Sensor Orientation (ISO)</i> .....	73
4.7.1	Bundle Block Adjustment Using BLUH Software .....	73
4.7.2	Blunder Detection .....	76
4.7.2.1	Blunder Detection Using Data Snooping .....	79
4.7.2.2	Blunder Detection Using Robust Estimators .....	80
4.7.2.3	Self-calibration Using BLUH 12AP .....	80
4.8	<i>Registration of Dense Tie Points to Reference LiDAR Surface</i> .....	83
4.8.1	Three-Dimensional Conformal Transformation .....	84
4.8.2	Surface Matching Theory.....	86
4.8.3	Robust Estimation .....	89
4.9	<i>LiDAR Control Point Selection Strategy</i> .....	90
4.9.1	Distance Test.....	91
4.9.2	Planarity Test .....	92
4.9.3	Slope Test.....	93
4.9.4	Reliability Test .....	94
4.9.5	Configuration Test: .....	95
4.10	<i>Aerial Triangulation and Camera Calibration</i> .....	96
4.11	<i>Assessment of Error Propagation in the Research Methodology</i> .....	97

4.11.1	Accuracy of the Photogrammetric Point Cloud Computations.....	97
4.11.2	Accuracy of the Registration Process .....	98
4.11.3	Accuracy of Aerial Triangulation and Camera Calibration using LiDAR Derived Control Points.....	100
4.12	Summary.....	100
<b>5</b>	<b>Calibration of Large Format Camera.....</b>	<b>102</b>
5.1	Introduction.....	102
5.2	Test Area .....	103
5.3	Photogrammetric Data .....	104
5.3.1	Aerial Imagery .....	104
5.3.2	Reference GNSS Surveyed Ground Control Data .....	104
5.4	Reference LiDAR Data.....	105
5.4.1	LiDAR Data Processing.....	106
5.4.2	Accuracy Assessment of LiDAR data: .....	107
5.4.2.1	Absolute Vertical Accuracy .....	107
5.4.2.2	Relative Vertical Accuracy .....	108
5.4.3	Generation of Reference DTM from LiDAR Data .....	108
5.5	Photogrammetric Point Measurement and Processing .....	109
5.5.1	Block Setup and Tie Point Measurement.....	109
5.5.2	Tie Point Object Coordinates Computation .....	110
5.5.3	Pre-Matching Photogrammetric Point Cloud Processing .....	113
5.6	Photogrammetric Point Cloud Registration .....	113
5.7	Control Point Selection Strategy.....	117
5.8	Results of Aerial Triangulation using LCPs .....	120
5.9	Effects of LiDAR Planimetric Accuracy on the Triangulation Results .....	124
5.10	Camera Calibration and Validation Results.....	128

5.11	<i>Summary.....</i>	<i>130</i>
<b>6</b>	<b>Calibration of Medium Format Camera.....</b>	<b>132</b>
6.1	<i>Introduction.....</i>	<i>132</i>
6.2	<i>Test Area .....</i>	<i>132</i>
6.3	<i>Photogrammetric Data .....</i>	<i>133</i>
6.4	<i>Reference LiDAR Data.....</i>	<i>134</i>
6.4.1	<i>LiDAR Data Processing.....</i>	<i>135</i>
6.4.2	<i>Assessment of the Accuracy of the LiDAR Data.....</i>	<i>135</i>
6.4.3	<i>Generation of Reference DTM from LiDAR Data .....</i>	<i>135</i>
6.5	<i>Photogrammetric Tie Point Measurement and Processing .....</i>	<i>136</i>
6.5.1	<i>Block Setup and Tie Point Measurement.....</i>	<i>136</i>
6.5.2	<i>Computation of Tie Point Object Coordinates.....</i>	<i>137</i>
6.5.3	<i>Pre-Matching Photogrammetric Point Cloud Processing .....</i>	<i>138</i>
6.6	<i>Photogrammetric point Cloud Registration.....</i>	<i>139</i>
6.7	<i>LiDAR-derived Control Point Selection.....</i>	<i>143</i>
6.8	<i>Results of Aerial Triangulation Using LCPs .....</i>	<i>145</i>
6.9	<i>Results of Camera Calibration Using LCPs.....</i>	<i>150</i>
6.10	<i>Summary.....</i>	<i>152</i>
<b>7</b>	<b>Conclusions and Recommendations .....</b>	<b>154</b>
7.1	<i>Revisiting the Research Aims and Objectives .....</i>	<i>154</i>
7.2	<i>Dense Photogrammetric Point Cloud Generation.....</i>	<i>156</i>
7.3	<i>Registration Approach .....</i>	<i>157</i>
7.4	<i>Extraction of LiDAR-derived Control Points.....</i>	<i>158</i>
7.5	<i>Aerial Triangulation Using LCPs .....</i>	<i>159</i>
7.6	<i>Camera Calibration Results.....</i>	<i>160</i>
7.7	<i>Research Limitations.....</i>	<i>161</i>

7.8 <i>Recommendations for Future Work</i> .....	161
<b>References</b> .....	<b>163</b>
<b>Appendix A</b> .....	<b>177</b>
<b>Appendix B</b> .....	<b>180</b>
<b>Appendix C</b> .....	<b>188</b>
<b>Appendix D</b> .....	<b>201</b>

# List of Figures

---

Figure 1-1-1 Photogrammetry workflow using analogue and digital cameras. ....	3
Figure 1-1-2 Left, separate registration to a common reference frame, right, relative transformation to the reference dataset. ....	6
Figure 2-1 Left, concept of the multi-head DMC camera, right, real and final image footprint, adapted from (Dörstel, 2000). ....	14
Figure 2-2 Arrangement of DiMAC two vertical images (Petrie, 2006). ....	14
Figure 2-3 Multi-head UltraCamD model, adapted from (Gruber <i>et al.</i> , 2008). ....	15
Figure 2-4 UltraCam syntopic imaging (Leberl and Gruber, 2003). ....	16
Figure 2-5 UltraCam virtual image stitching using 9 sub-images (Gruber <i>et al.</i> , 2012). ....	16
Figure 2-6 Ultracam frame sizes for different models (Gruber <i>et al.</i> , 2012). ....	17
Figure 2-7 Principal and geometric characteristics of the ADS40 three-line digital sensor, adapted from (Sandau <i>et al.</i> , 2000). ....	18
Figure 2-8 Image acquisition for the SH92 sensor head (Leica, 2013a). ....	19
Figure 2-9 UltraCam L sensor head and integrated data capture and processing unit, adapted from (Ladstädter <i>et al.</i> , 2010b). ....	20
Figure 2-10 Left, RMK D camera, right, four MS camera heads and video camera (centre), adapted from (Dörstel, 2009). ....	21
Figure 2-11 Leica RCD30 camera system (Operator control, camera head and camera control) (Wagner, 2011). ....	22
Figure 2-12 The DSS 322 system (Ip and Mostafa, 2006). ....	23

Figure 2-13 The Applanix DSS322 lenses (40mm, 60mm) (Ip and Mostafa, 2006).....	23
Figure 2-14 Bayer pattern approach (one CCD for RGB colours). .....	24
Figure 2-15 DMC Laboratory calibration - Measurement Unit (Hefele, 2006). .....	27
Figure 2-16 UltraCam three dimensional calibration targets (Gruber and Ladstädter, 2008). .....	28
Figure 2-17 Different configurations of calibration block structures (Honkavaara, 2003). .....	31
Figure 2-18 GCP-distributions in rectangular blocks (Honkavaara, 2003). .....	32
Figure 2-19 Positional relationship between Camera, GNSS and IMU (Jacobsen, 2002). .....	33
Figure 2-20 Direct determination of camera positions and attitudes (Skaloud, 1999). ..	34
Figure 3-1 Components of an airborne LiDAR system (Schmid <i>et al.</i> , 2008). .....	40
Figure 3-2 Measurement principle of pulse (left) and continuous waveform (right) laser scanners (Wehr and Lohr, 1999).....	41
Figure 3-3 Scanning mechanisms and resulting scanning patterns (Baltsavias, 2008)...	43
Figure 3-4 Emitted and received pulse for discrete echo scanners and full-waveform scanners (Cramer <i>et al.</i> , 2012). .....	45
Figure 3-5 Processing scheme for airborne laser scanning (Vosselman and Maas, 2010). .....	46
Figure 3-6 Left, LiDAR target, right, its appearance in the LiDAR data (Csanyi and Toth, 2007).....	47
Figure 3-7 Left, building corners extracted from aerial images, right, building corners extracted from LiDAR data (Mishra and Zhang, 2012).....	53



Figure 3-8 Straight lines extracted from LiDAR data and aerial images (Habib <i>et al.</i> , 2011).	53
Figure 3-9 Plane matching method between aerial images and LiDAR point cloud (Armenakis <i>et al.</i> , 2013).	54
Figure 3-10 Manual registration of LiDAR and stereo images (Rönnholm, 2011b).	55
Figure 3-11 Left, control point selection from optical image, right , LiDAR intensity image (Wong and Orchard, 2008).	56
Figure 3-12 Left, centroid coordinates from aerial image, right, centroid coordinates from LiDAR point cloud (Mitishita <i>et al.</i> , 2008).	59
Figure 3-13 Left, control point in colour-infrared image, right, control point in LiDAR intensity image (Yastikli and Toth, 2007).	60
Figure 3-14 Left, image derived planar feature, right, reference LiDAR patches (Shin <i>et al.</i> , 2007).	62
Figure 4-1 Main steps of the research methodology.	66
Figure 4-2 Functions performed with Matlab algorithm.	68
Figure 4-3 Example of automatic point measurement using the 3 x 3 pattern file with the standard 60% overlap and 30% sidelap (BAE Systems, 2007).	70
Figure 4-4 Model keypoint selection from reference LiDAR data.	71
Figure 4-5 Tie point masking using normalised DSM mask image.	72
Figure 4-6 BLUH bundle adjustment configuration and dataflow, adapted from (Jacobsen, 2008).	74
Figure 4-7 Error in x direction for a two-ray point.	77
Figure 4-8 Error in y direction for a two-ray point.	77
Figure 4-9 Error in x direction for a three-ray point.	78

Figure 4-10 Error in y direction for a three-ray point. ....	78
Figure 4-11 Parameter 1 for angular affinity, Parameter 2 for affinity.....	82
Figure 4-12 Parameters 3 - 6 for general deformation. ....	82
Figure 4-13 Parameters 7 and 8 for tangential distortion.....	82
Figure 4-14 Parameter 9 for radial symmetric distortion, Parameters 10 and 11 for radial symmetric higher.....	83
Figure 4-15 Parameter 12 for general distortion parameter. ....	83
Figure 4-16 Planar interpolation of the reference surface.....	86
Figure 4-17 Matching residuals with 2 cm threshold.....	91
Figure 4-18 Best fit plane for 3 x 3 window. ....	92
Figure 4-19 Selection approach of four reference LCPs.....	95
Figure 4-20 Selection approach of nine reference LCPs. ....	96
Figure 5-1 Vaihingen/Enz test field location map. ....	103
Figure 5-2 Selected UltraCamX sub-block. ....	104
Figure 5-3 Example of signalized ground control points and the corresponding point in the aerial image (Cramer, 2010).....	105
Figure 5-4 Classified LiDAR point cloud data. ....	107
Figure 5-5 Reference DTM surface generated from LiDAR point cloud. ....	109
Figure 5-6 Systematic error pattern, (a) without self-calibration, (b) with BLUH 12AP. .....	111
Figure 5-7 Height differences between photogrammetric points computed with and without self-calibration. ....	112

Figure 5-8 Left, thematic mask before application of 2.5m height threshold, right, after application of 2.5 m height threshold and filtering. ....	113
Figure 5-9 Left, selected check targets points, right, registered check targets overlaid on LiDAR DSM. ....	115
Figure 5-10 Surface matching point residuals (No AP). ....	116
Figure 5-11 Surface matching point residuals (BLUH 12 AP). ....	117
Figure 5-12 Histograms of the surface matching residuals with and without self-calibration. ....	117
Figure 5-13 Selected planarity and slope test area. ....	119
Figure 5-14 Samples of the selected LCPs from the UltraCamX dataset. ....	120
Figure 5-15 Easting RMSE calculated using 100 CPs in the UltracamX block. ....	123
Figure 5-16 Northing RMSE calculated using 100 CPs in the UltraCamX block. ....	123
Figure 5-17 Height RMSE calculated using 100 CPs in the UltraCamX block. ....	124
Figure 5-18 Easting RMSE calculated using 100 CPs using different LiDAR DTMs. ....	126
Figure 5-19 Northing RMSE calculated using 100 CPs using different LiDAR DTMs. ....	127
Figure 5-20 Height RMSE calculated using 100 CPs using different LiDAR DTMs. ....	127
Figure 6-1 Location map of the Haltwistle study area. ....	133
Figure 6-2 Selected block from the DSS322 dataset. ....	134
Figure 6-3 Reference LiDAR DTM with added buildings. ....	136
Figure 6-4 Computed mask for tie points. ....	138
Figure 6-5 Removal of tie points located outside the LiDAR DTM coverage. ....	139

Figure 6-6 Left, measured tie point in SocetSet, right, registered tie points overlaid on LiDAR DSM. ....	141
Figure 6-7 Surface matching point residuals (No AP).....	141
Figure 6-8 Surface matching point residuals (BLUH 12 AP).....	142
Figure 6-9 Histograms of the surface matching residuals before and after self-calibration.....	143
Figure 6-10 Example of nine selected LCPs.....	144
Figure 6-11 Example of 50 selected LCPs.....	145
Figure 6-12 Samples of the selected LCPs from the DSS322 dataset. ....	145
Figure 6-13 Easting RMSE at 50 check-points without self-calibration. ....	146
Figure 6-14 Northing RMSE at 50 check-points without self-calibration.....	146
Figure 6-15 Height RMSE at 50 check-points without self-calibration. ....	147
Figure 6-16 Easting RMSE at 50 check-points with 12AP self-calibration. ....	148
Figure 6-17 Northing RMSE at 50 check-points with 12AP self-calibration.....	148
Figure 6-18 Height RMSE at 50 check-points with 12 AP self-calibration. ....	149
Figure 6-19 Poor image quality due to camera vibration.....	150
Figure 6-20 Camera station heights determined before and after focal length refinement. .....	151

## List of Tables

---

Table 4-1 Statistics of 3x3 point residuals of best fit plane for 17 road and planar surface points. ....	93
Table 5-1 Elevation difference statistics between the LiDAR point cloud and the reference control points.....	107
Table 5-2 Transformation parameters and quality statistics determined by surface matching for the UltraCamX block.....	114
Table 5-3 Error at LiDAR-derived control points with 2 cm LCPs weight.....	121
Table 5-4 Error at LiDAR-derived control points with 5 cm LCPs weight.....	121
Table 5-5 Error at LiDAR-derived control points with 10 cm LCPs weight.....	122
Table 5-6 Error at LiDAR-derived control points with 15 cm LCPs weight.....	122
Table 5-7 Transformation parameters of surface matching results using original and shifted LiDAR DTM.....	125
Table 5-8 Refined camera parameters using reference ground control points.....	128
Table 5-9 Refined camera parameters using different sets of LCPs. ....	129
Table 5-10 RMSE calculated at 17 ICPs in the UltraCamX block using four ground control points and different sets of refined camera parameters. ....	130
Table 6-1 Transformation parameters determined by surface matching. ....	140
Table 6-2 Focal length refinement effect on exterior orientation accuracy. ....	151

# List of Abbreviations and Notation

---

ALS	Airborne Laser Scanning
AP	Additional Parameters
APM	Automatic Point Measurement
ASPRS	American Society for Photogrammetry and Remote Sensing
b/H ratio	Base to height ratio
cm	Centimetre
CP	Check Point
CW	Continuous Wave
DG	Direct Georeferencing
DLR	German Aerospace Centre
DSM	Digital Surface Model
DTM	Digital Terrain Model
EOP	Exterior Orientation Parameters
ETRS89	European Terrestrial Reference System 1989
EuroSDR	European Spatial Data Research
GCP	Ground Control Point
GNSS	Global Navigation Satellite System
ICP	Independent Check Point
IMU	Inertial Measurement Unit
IO	Interior Orientation
IPM	Iterative Point Measurement

ISO	Integrated Sensor Orientation
ISPRS	International Society for Photogrammetry and Remote Sensing
LCP	LiDAR-derived Control Point
LiDAR	Light Detection and Ranging
LS3D	Least Squares 3D
MAD	Median Absolute Deviation
mm	Millimetre
$\mu\text{m}$	Micrometre
MST	Multi Sensor Triangulation
OSGB36	Ordnance Survey Great Britain 1936
TIFF	Tagged Image File Format
TIN	Triangulated Irregular Network
TM	Transverse Mercator
$T_x$	Translation of the x axis
$T_y$	Translation of the y axis
$T_z$	Translation of the z axis
UTM	Universal Transverse Mercator
WAOSS	Wide Angle Optoelectronic Stereo Scanner
WAAC	Wide Angle Airborne Camera
WGS84	World Geodetic System 1984
$\omega$	Rotation around the x axis
$\varphi$	Rotation around the y axis
$\kappa$	Rotation around the z axis
$\sigma$	Standard deviation

# CHAPTER

# 1

---

## 1 Introduction

---

### 1.1 Background

Photogrammetry is defined by the American Society for Photogrammetry and Remote Sensing (ASPRS) as “the art, science, and technology of obtaining reliable information about physical objects and the environment through the process of recording, measuring, and interpreting photographic images and patterns of recorded radiant electromagnetic energy and other phenomena” (McGlone *et al.*, 2004). Images analysed for photogrammetric applications include those acquired using both passive imaging systems, such as photography, which rely on external sources of energy for illumination, and active systems, such as radar, which emit their own source of energy (Mikhail *et al.*, 2001). Wolf and Dewitt (2000) defined two distinct areas of photogrammetry: metric and interpretative. Metric photogrammetry deals with the derivation of information such as distances, angles, areas shapes and volumes from imagery. Such measurements are extensively applied in planimetric and topographic mapping applications. Interpretative photogrammetry, however, deals mainly with the analysis of photos through the identification and recognition of appropriate objects, as well as providing quantitative and qualitative information required for environmental studies, natural resource management, planning and many other applications.

Based on the location of the camera station, photogrammetry can also be classified into two types: terrestrial and aerial photogrammetry (Luhmann *et al.*, 2006). In terrestrial photogrammetry, all images are taken on the ground and from fixed terrestrial location. These images usually represent natural or manmade objects used for producing 3D models but not for topographic mapping. In aerial photogrammetry, images are captured from the air, mainly using aeroplanes. Cameras may either be pointed vertically



downwards, producing what are known as vertical images, or are tilted by more than  $3^\circ$  to produce so-called oblique images (Mikhail *et al.*, 2001).

Photogrammetry has evolved through four phases of development, characterised by the techniques and equipment used to produce maps from imagery. These four phases are known as plane table, analogue, analytical and digital photogrammetry (Konecny, 1985). Plane table photogrammetry was used before the introduction of aerial photos, and here the relationship between objects using geometric principles is extracted using photos taken on the ground. In analogue photogrammetry, overlapping photographs are used to reconstruct the three-dimensional geometry using optical or mechanical instruments to produce topographic maps. In the analytical photogrammetry era, the use of computers resulted in new hybrid analogue/digital devices. These enabled the fast computation of orientation parameters via mathematical algorithms. New types of equipment were developed which became relatively smaller, such as those used for analytical aero-triangulation, analytical plotters and orthophoto projectors. Moreover, the output of the process can either be topographic maps or digital maps and digital elevation models. In digital photogrammetry, following significant developments in computing, all photogrammetric work is processed digitally by computers. Analogue aerial photographs are scanned and transformed into digital format (Linder, 2003). The main advantages of digital photogrammetry relate to automation in terms of image matching and tie point extraction. This has made automatic aerial triangulation more accurate and economical (Kremer and Kruck, 2003). It has also enabled new methods of image processing to be used in automatic image matching for elevation data extraction and orthophoto production (Sandau, 2009). Moreover, following the development and introduction of a new generation of large format digital aerial sensors, a fully digital photogrammetric workflow became possible, as shown in Figure 1-1-1.

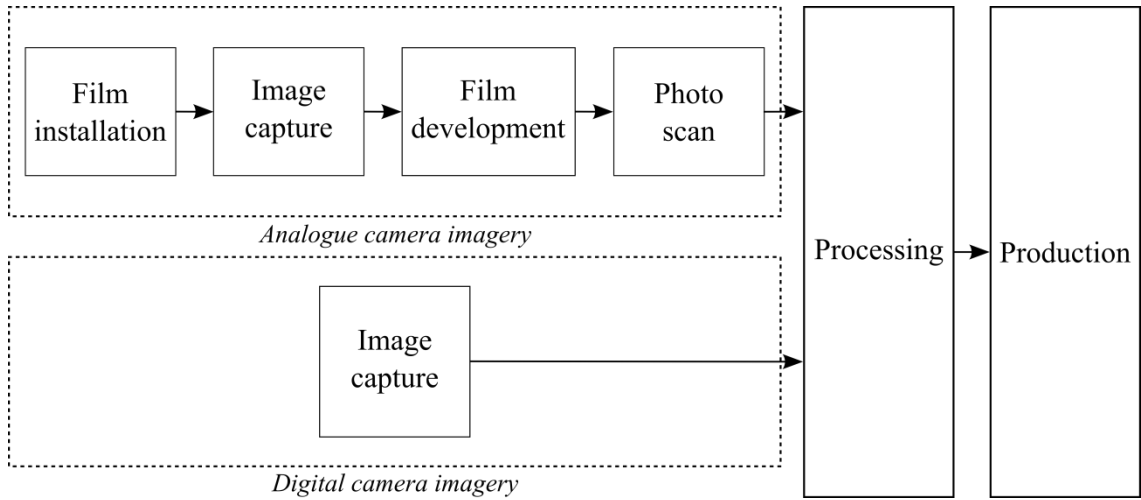


Figure 1-1-1 Photogrammetry workflow using analogue and digital cameras.

## 1.2 Calibration of Digital Aerial Cameras

The calibration process as defined by (Morain and Zanoni, 2004) is the a “process of quantitatively defining the system responses to known, controlled signal inputs”. For aerial camera systems, Honkavaara *et al.* (2008) classified the calibration into geometric calibration, radiometric calibration and spatial resolution calibration. As this research only focuses on the geometric calibration, further details of radiometric and spatial resolution calibration can be found elsewhere (Honkavaara *et al.*, 2006; Markelin *et al.*, 2008).

The camera geometric calibration, performed in this research, as defined by Smith (2007) as “the process of measuring the relationship of a ‘real’ frame camera geometry in comparison to perspective geometry”. As the quality of the final photogrammetric product will be influenced by calibration of the camera system, therefore, the purpose of geometric calibration of the camera is to ensure that the imaging system meets the stringent requirements of topographic mapping and considered as a prerequisite for the achievement of precise photogrammetric measurements using camera imagery (Qtaishat *et al.*, 2008). In geometric camera calibration, the interior orientation (IO) parameters of the camera are estimated. These include the camera’s focal length, principal point coordinates ( $x_0$  and  $y_0$ ) and radial and decentring lens distortion. Geometric camera calibration can be performed either in the laboratory, usually by the manufacturer, or in a test field. In cases of laboratory calibration, the aforementioned parameters are determined under constant and stable temperature, pressure and humidity conditions

which may not simulate real-world operational flight conditions (Yastikli and Jacobsen, 2005; Honkavaara *et al.*, 2008). Therefore, due to changes in environmental conditions, the camera geometry may also change relative to the situation in the laboratory (Kruck, 2006; Jacobsen, 2007a). Meier (1978) found that the focal length in the camera calibration certificate delivered with a Zeiss camera changed due to variations in flying height. Therefore, tests to simultaneously determine camera calibration parameters are usually performed using a permanent test field of control points (Honkavaara *et al.*, 2003). The simultaneous calibration process includes the determination of camera parameters using images acquired over a photogrammetric test field with highly redundant photo coverage, such as 80% overlap and 60% sidelap, to identify and eliminate gross errors, and using a high number of accurately measured reference targets (Mikhail *et al.*, 2001; Honkavaara *et al.*, 2008). The refinement of camera parameters using a test field is useful for project areas which are close to the permanent test field, but may not always be valid for other mapping projects (Yastikli and Toth, 2007). Meanwhile, the availability of data from modern global navigation satellite system and inertial measurement unit (GNSS/IMU) has greatly reduced mapping costs by limiting the number of control points required in aerial triangulation and enabled direct geo-referencing. However, systematic errors in the GNSS/IMU measurements or changes in system parameters between laboratory calibration and actual flights may not be detected without ground control points (Heipke *et al.*, 2002b).

During the last decade, various formats of digital sensors have been introduced as equivalent replacements for existing analogue cameras. Details of these different types of sensor systems are given in Chapter 2. One type of the existing camera systems is the large format digital aerial cameras. These cameras are specifically designed as metric cameras built for mapping purposes, and laboratory calibration by the manufacturer is usually valid and can be used with confidence (Habib *et al.*, 2010). However, despite the advantages of large format digital aerial cameras, they are still not economical to be used for the mapping of smaller areas. Therefore, medium and small format cameras are desirable in such situations (Cramer, 2004b). These smaller areas are usually irregularly shaped or necessitate strip mapping as in the mapping of pipeline or transmission line corridors (Grenzdörffer, 2010a). Moreover, since the introduction of LiDAR<sup>1</sup> systems,

---

<sup>1</sup> The usage of the abbreviation LiDAR in this thesis refers to airborne LiDAR.

medium format cameras have become widely used in conjunction with LiDAR systems. Since the design of medium and small digital format cameras are not tailored purely for photogrammetric purposes, they are generally not as stable as metric mapping cameras. Therefore, the calibration of such camera systems and the stability of the calibration parameters is considered to be crucial (Kim *et al.*, 2006). The stability assessment of such camera systems requires a comprehensive analysis of performance over time (Stensaas and Leeb, 2008). A camera will be considered to be stable if its interior orientation parameters remain the same over a long period of time e.g. (Habib *et al.*, 2006a).

The uncertainty regarding the stability of a camera's parameters necessitates that it should be calibrated in real environmental conditions using a test field with highly accurate signalized control points. The environmental conditions in the test field and mapping areas may still differ, however. Establishing a new test field for every mapping area and the collection of large numbers of ground control points for camera calibration is expensive and largely impractical. Since photogrammetry and LiDAR are the most important recent methods used for 3D topographic data collection (James *et al.*, 2006), different methods have been tested and implemented to integrate these two methods in performing aerial triangulation through the extraction of reference features from LiDAR data (Delara *et al.*, 2004; Habib *et al.*, 2005a; Habib *et al.*, 2006b; Mitishita *et al.*, 2008; Habib *et al.*, 2009; Wildan *et al.*, 2011). Moreover, other tests have been performed where LiDAR data is adopted as the reference and source of control for digital aerial camera calibration (James *et al.*, 2006; Yastikli and Toth, 2007; Mitishita *et al.*, 2012).

### 1.3 Registration of LiDAR and Photogrammetric Data

LiDAR systems were first introduced to the research community in the early 1990s and the first commercial terrestrial laser scanner was unveiled in 1999 (Kolecka, 2011). Aerial LiDAR systems deliver direct dense geometric surface information measurements at high vertical accuracy (Lim *et al.*, 2003). Moreover, continued improvements in the performance and accuracies of LiDAR systems in recent years have enabled the use of LiDAR data as a source of control suitable for photogrammetric applications. This task requires the successful registration of LiDAR and photogrammetric data to a similar reference frame (Habib *et al.*, 2005b). This could be achieved either by separate orientation of the two datasets individually to the common

coordinate system, or considering one of the datasets as reference and obtaining the relative orientation of the two datasets (Figure 1-1-2). According to Rönholm *et al.* (2007), the second method is preferable since it requires the transformation of only one dataset, which ensures greater accuracy. Details of these different types of registration methods are given in Chapter 3.

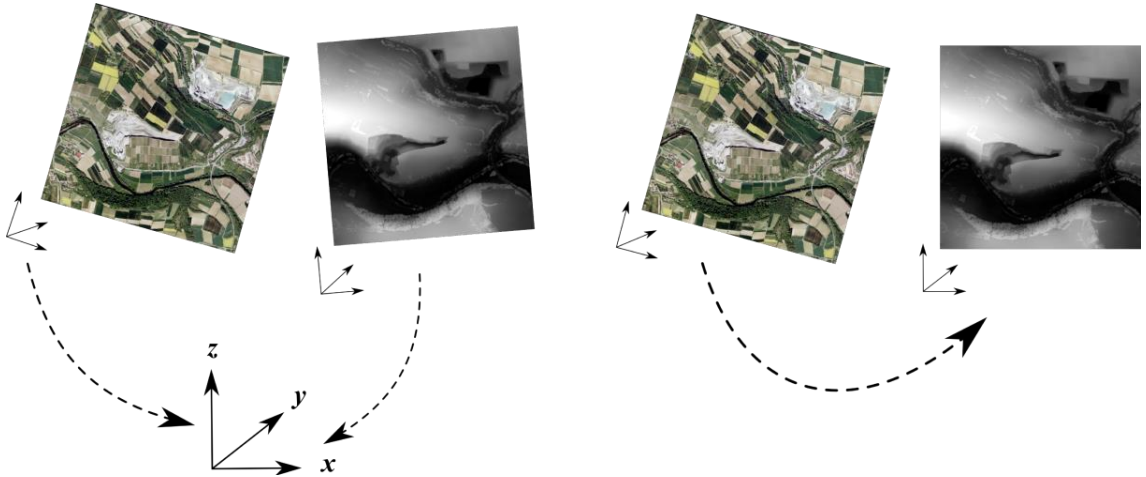


Figure 1-1-2 Left, separate registration to a common reference frame, right, relative transformation to the reference dataset.

The registration methodology includes three essential stages. Firstly, common reference features must be identified and extracted from both datasets. Secondly, a mathematical model that describes the geometric relationship between the two datasets must be established in order to compute the transformation parameters. Thirdly, assessment of the registration procedure is needed to ensure that both datasets are correctly and accurately aligned (Habib *et al.*, 2005b). The common spatial features used in current registration methods are mainly based on the identification and extraction of certain features such as points, lines and planes (Armenakis *et al.*, 2012). Finding robust features interpreted from LiDAR data is usually hindered by the low point density of LiDAR datasets, which makes the accurate identification of tie features difficult (Rönholm *et al.*, 2007). Therefore, feature extraction from LiDAR data is usually performed using the segmentation or classification of groups of LiDAR point clouds. Habib *et al.* (2004b) identified and used straight lines as conjugate features in the registration process. Straight lines were either extracted by intersecting two planes or through direct manual observation. Other methods have used planes as common features (Sampath and Shan, 2006; Brenner *et al.*, 2008). Surface-to-surface registration

is also possible by interpolating both datasets into regular or irregular surfaces, where the LiDAR-derived surface is matched to the photogrammetric surface and registration is accomplished by minimizing either the vertical or Euclidean distances between the two surfaces (Akca, 2007a). The quality of the registration is highly dependent on the registration process, which can be classified as either manual, semi-automatic or automatic (Rönnholm, 2011a). Due to this variety in terms of the requirement of accuracy and level of automation, no single registration process suits all applications and types of data, meaning registration methods are usually case-sensitive (Rönnholm *et al.*, 2007).

## 1.4 LiDAR Data as Source of Photogrammetric Control

Aerial triangulation is a point-based process, which allows the estimation of the exterior orientation parameters (EOP) of camera stations. Since point features are still the main source of photogrammetric control in aerial triangulation (Habib *et al.*, 2006b), a number of different methods have been used to extract reference control points from LiDAR data for subsequent use in aerial triangulation. Mitishita *et al.* (2008) used the centroids of rectangular building roofs as single control points with 3D coordinates in the aerial triangulation process. The coordinates of the roof centroids were measured after calculating the approximate 3D coordinates of the four roof corners from the LiDAR point cloud data. James *et al.* (2006) used high resolution shaded LiDAR digital elevation model (DEM) to manually extract reference control points for use in establishing a photogrammetric model. However, a shaded relief image only provides features where height differences are present such as at wall intersections in buildings and sharp changes in the terrain. Also, it seems impossible to acquire reference points in open featureless pasture areas and hillsides with this approach. Linear features have also been used as reference targets. Habib *et al.* (2005a) directly incorporated linear features as a source of control in photogrammetric bundle adjustment. However, a greater number of linear features are needed to match the accuracy achieved by conventional control point patterns in the photogrammetric block (Mitishita *et al.*, 2008). Moreover, for large photogrammetric blocks, significant numbers and good configurations of these reference targets may not be readily available. Deriving point-based control points from LiDAR data is also hindered by the difficulty in finding corresponding LiDAR point in the photogrammetric dataset (Baltsavias, 1999; Habib *et al.*, 2006b; Mitishita *et al.*, 2008).

Another attempt at camera calibration using LiDAR data was conducted by Yastikli and Toth (2007). In their test, reference control points were manually measured and extracted from the LiDAR point cloud using the LiDAR intensity image to enable the identification of reference features. However, the accuracy of reference control points was adversely affected by errors introduced during manual measurement and the point density of the reference LiDAR point cloud. Moreover, difficulty was found in obtaining reliable reference points in flat and open areas.

Mitishita *et al.* (2012) performed camera calibration using a simultaneous image block adjustment for low cost cameras and LiDAR datasets. This calibration methodology relied on using 3D coordinates of camera position stations as control points as well as signalized vertical control points to compute the camera's interior orientations. Since the LiDAR and image data was acquired simultaneously, this methodology did not apply any registration procedures to the LiDAR data and aerial imagery. Also, the control points used in the test were limited and based only on predefined signalized control points in the test field. The extraction of other reference control points from the LiDAR dataset was not performed. Moreover, simultaneous data acquisition may not always be desirable due to the different technical requirements in flying height or, for example, as LiDAR is an active system, therefore, night LiDAR missions are not suitable for acquiring aerial photography (Rönnholm, 2011a).

## 1.5 Research Motivation

In current registration methods, airborne LiDAR-derived reference control points are still based on feature extraction from the LiDAR data. This is done using either direct method such as measurement from the intensity and range image or indirect methods such as the extraction of features or computing shaded relief images from the LiDAR reference digital terrain model (DTM). For controlling large photogrammetric blocks, these methods do not guarantee that an adequate number of points will be extracted. Also, point distribution, which is a key element in achieving higher block accuracy, depends on the spatial distribution of existing and reliable reference features. Moreover, for a single photogrammetric point, finding the corresponding laser point in the LiDAR dataset is considered to be either very difficult or impossible (Baltsavias, 1999).

Therefore, in order to perform bundle block adjustment and camera calibration for aerial cameras using airborne LiDAR-derived control points, there is a desire to perform registration between the reference LiDAR point cloud data and the entire photogrammetric block without the need of feature extraction. The key element in performing registration using large datasets is automation (Rönnholm, 2011a). Also, to enable a large number of reference points to be derived which will maintain good point distribution, there is a need to register the photogrammetric point features to the corresponding reference LiDAR surface.

## 1.6 Aim and Objectives

This research aims to investigate the use of airborne LiDAR surface for photogrammetric control through which aerial triangulation and camera system calibration can be performed using large and medium format aerial imagery. This aim leads to the following objectives:

1. To investigate the latest sensor technological developments in the field of airborne photogrammetry.
2. To understand the characteristics of airborne LiDAR data and to assess existing methods to integrate with photogrammetric data.
3. To build a knowledge gained from objectives 1 and 2 to develop a methodology which enables extraction of camera self-calibration parameters.
4. To validate the derived self-calibration parameters against the same parameters obtained using the conventional ground control points.
5. To demonstrate the flexibility of the developed research methodology using different types of airborne imagery used for topographic mapping.

## 1.7 Thesis Outline

The thesis is organized into seven chapters in order to describe the achievement of the research objectives. The contents of each chapter is summarised as follows:

Chapter 1 is the introduction which sets the research motivations and also aim and objectives.



Chapter 2 is a background chapter explaining the design concepts of different large format and medium format digital aerial camera systems. It also includes brief discussions of direct geo-referencing (DG) and integrated sensor orientation (ISO). Finally, different methods of camera calibration are briefly explained.

Chapter 3 provides an overview of the design and working concepts of airborne laser scanners. This includes methods of LiDAR data post-processing techniques for strip adjustment, accuracy assessment and also the production of digital surface and terrain models. Methods for registering LiDAR and photogrammetric data are also presented and compared. Finally, an overview is given of available methods where LiDAR data has been used instead of typical ground control points (GCPs) as a source of control to perform aerial triangulation and camera calibration.

Chapter 4 gives detailed descriptions of the research methodology, procedures and workflow and the point selection criteria. This includes automatic dense photogrammetric point measurement, the automatic registration procedure for photogrammetric data and the reference LiDAR surface, the automatic extraction of LCPs, and finally the aerial triangulation approach using the extracted LCPs for camera calibration.

Chapter 5 provides a detailed description of the validation of the methodology using empirical datasets, and presents an experimental validation using aerial imagery from a Microsoft UltraCamX large format camera and 3D LiDAR data captured by a Leica ALS50 laser scanner. Tests are performed with photogrammetric data and the results obtained are presented and discussed in detail.

Chapter 6 presents the methodology validation results using other aerial imagery from the Applanix DSS322 medium format camera system and 3D LiDAR data captured using an Optech ALTM2050 laser scanner.

Chapter 7 draws the conclusions of the research. The research objectives are revisited and recommendations and proposals for future work are given.

---

## 2 Aerial Camera Systems and Calibration

---

### 2.1 Introduction

The last decade has witnessed the start of new era of digital aerial cameras. Since the beginning of the new millennium, different digital camera models have been developed and introduced as replacement to existing analogue cameras. These new camera models have reduced mapping costs by eliminating scanning and chemical processing of the mapping films. They have also provided a simplified and time effective photogrammetric workflow (Petrie and Walker, 2007). In addition to this, these qualities have encouraged the design of smaller and cheaper cameras for smaller photogrammetric projects. Therefore, due to the readily apparent advantages of digital cameras over conventional film cameras in terms of geometry and image quality, the complete replacement of analogue cameras has finally been achieved (Jacobsen, 2011b).

Based on the working principle, the digital aerial cameras can be classified into two groups, frame cameras and line scan cameras. They can also be classified based on the image size into large, medium and small format cameras (Jacobsen, 2011b). Beside this development in the cameras design, new studies on the geometry and systematic distortions caused by the new design principles of the digital aerial cameras have been performed. Also, the heterogeneity of these different mapping cameras necessitates performing an independent calibration procedure and adapting it to meet the requirements of the new aerial systems (Cramer, 2009). Moreover, the use of GNSS/IMU with the new camera system has become a norm and even mandatory for designs of some sensors. Therefore, to achieve the optimum accuracy precise system calibration parameters and the relationship between GNSS/IMU and the camera must be accurately determined.

This chapter will provide an overview of the main types of the new large and medium format digital aerial cameras. It will also introduce the use of GNSS/IMU data for direct geo-referencing and camera calibration methods.

## **2.2 Large Format Aerial Digital Cameras**

### **2.2.1 Background**

Large format aerial digital cameras have been available since the early 2000's and are now in widespread commercial operation. Popular large format photogrammetric camera models include the UltraCam models (D, X, Xp, L, Eagle) produced by Microsoft Vexcel imaging; the ADS models (40, 80, 100) by Leica and the DMC models (I, II<sub>140</sub>, II<sub>230</sub>, II<sub>250</sub>) by Intergraph. Adoption of this new technology has demanded a large amount of technical knowledge and skills, new production procedures and quality control. The most important part of this learning process is that the capabilities of these new systems need to be understood through specific trials and experience (Smith *et al.*, 2005). Moreover, with the growing use of new digital airborne systems in daily operational data acquisition and processing, the need for the development of guidelines and procedures for quality assurance and quality control has become obvious (Cramer, 2006). In the early models of large format cameras, the lack of large commercial charged coupled device (CCD) arrays suited to build large format digital aerial survey cameras resulted in the development of new design principles. These principles were based on either frame based sensor (using single-head or multi-head cameras) or line based systems (using linear CCD arrays). Moreover, the recording concepts of multi-head models were either based on synchronous or syntopic image capture as will be described in Sections 2.2.3 and 2.2.4 (Cramer, 2007a). The following sections describe the differences between the single, multi-head and line scanning design principles.

### **2.2.2 Large Format Single-head Frame Cameras**

Single-head large format digital aerial cameras previously had limited use. This was mainly due to the difficulties in manufacturing affordable large format CCD arrays that met the requirements of aerial mapping applications. The main use of these cameras was predominantly in the field of reconnaissance (Petrie and Walker, 2007). Two examples of such cameras are the Recom/Optical CA-260/50 and the Ultra High Resolution

Reconnaissance Camera by BAE systems that was developed for the US Navy (Petrie and Walker, 2007).

In more recent years, due to the development in the CCD array technology, a new generation of larger sized CCD arrays has enabled the production of new models of single-head large format digital aerial camera systems dedicated for mapping purposes. These models include the DMC II<sub>140</sub>, DMC II<sub>230</sub> and DMC II<sub>250</sub> by Intergraph. These camera models were introduced after the DMC II multi-head camera model as will be discussed in Section 2.2.3. The DMC II<sub>140</sub> camera design concept utilizes a single panchromatic CCD with 7.2 micrometre ( $\mu\text{m}$ ) of 12096 x 11200 pixels and four low resolution multispectral cameras each of 6096 x 6846 pixels. This design provides a higher geometric accuracy in which the stitching process of multiple images is no longer required as with previous models (Jacobsen, 2011a). In addition to the DMC II<sub>140</sub>, two other models were released by Intergraph based on the same concept which provided larger image size. The DMCII<sub>230</sub> uses a 5.6  $\mu\text{m}$  resolution CCD which provides an image size of 15552 x 14144 pixels. The latest model is the DMCII<sub>250</sub> which uses 5.6  $\mu\text{m}$  CCD to provide an image size of 16768 x 14016 (Z/I-Imaging, 2013a).

### 2.2.3 Multi-head Digital Frame Cameras – Simultaneous Imaging

The synchronous multi-head camera approach has been used by some large format camera manufacturers such as Intergraph and DiMAC in order to provide a larger image foot print on the ground over a single-head frame camera. This was achieved by simultaneous capture of sub-images using a group of medium format cameras. The difference between the two design concepts is that the DMC used four convergent camera heads whereas the DiMAC is based on two nadir camera heads. The Intergraph DMC camera concept was first revealed at the international society for photogrammetry and remote sensing (ISPRS) congress Amsterdam in 2000 (Dörstel, 2000), and the first commercial camera model was introduced in 2003 (Dorstel, 2007). The virtual large format image of 13824 x 7680 pixels is produced using four convergent high resolution (12 $\mu\text{m}$ ) panchromatic sub-cameras to allow three dimensional stitching by bundle adjustment (Jacobsen, 2010). Another four lower resolution nadir looking cameras capture images of format size 3042 x 2048 pixels in four bands (red, green, blue and near infrared). Figure 2-1 shows the design concept of the DMC camera.

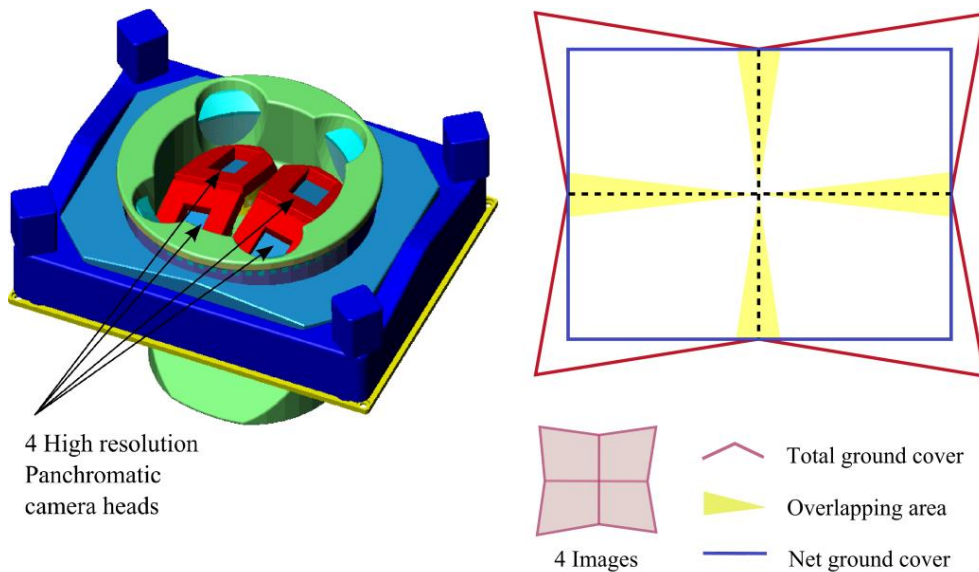


Figure 2-1 Left, concept of the multi-head DMC camera, right, real and final image footprint, adapted from (Dörstel, 2000).

The DiMAC is another type of multi-head large format camera. This camera was introduced by DiMAC Systems at the ASPRS conference in May 2006 (Petrie, 2006). The camera design is based on utilizing two vertical pointing cameras each with 39 Megapixels. The two cameras are arranged in a side-by-side configuration to capture images that cover the areas to the left and right of the flight line with a small overlap area. The final large format virtual image of 10500 x 7200 pixels is produced by merging the two individual images. Figure 2-2 shows the individual image configuration of the DiMAC camera system.

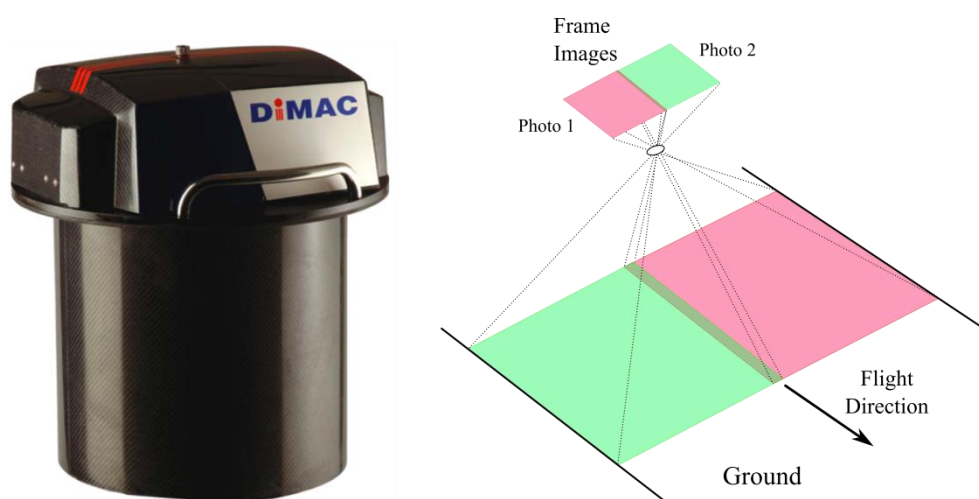


Figure 2-2 Arrangement of DiMAC two vertical images (Petrie, 2006).

### 2.2.4 Multi-head Digital Frame Cameras - Syntopic Imaging

Syntopic imaging involves the creation of a virtual large format digital frame image using a group of medium format cameras. The sub-images are captured sequentially within a narrow period of time from the same exposure station location. This approach was developed and first introduced by Microsoft Vexcel imaging in 2003 (Leberl and Gruber, 2003). The UltraCamD camera model was the first commercial camera model introduced based on this approach. Figure 2-3 shows the configuration of the UltraCamD with its eight medium format camera cones.



Figure 2-3 Multi-head UltraCamD model, adapted from (Gruber *et al.*, 2008).

The eight independent camera cones, includes four high-resolution panchromatic optical cones which all have the same field of view to create the large format panchromatic image of 11500 x 7500 pixels. Another four lower-resolution multispectral camera cones capture images in red, green, blue and near infrared bands with individual image sizes of 4000 x 2700 pixels. The large format image formation as described in Leberl and Gruber (2003) and Kröpfl *et al.* (2004) starts by mounting the four panchromatic cones in a line pointing in the flight direction to allow image capture using the syntopic imaging principle (Figure 2-4).

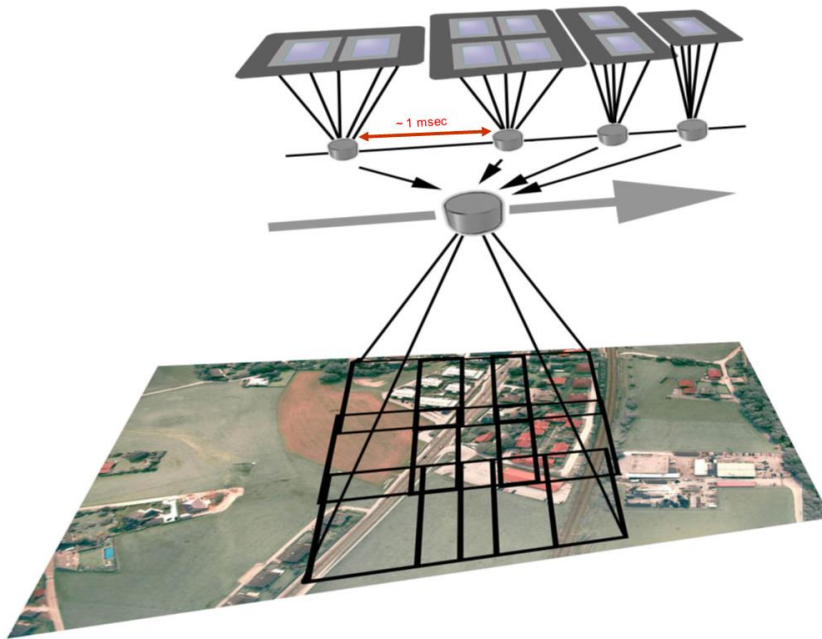


Figure 2-4 UltraCam syntopic imaging (Leberl and Gruber, 2003).

The panchromatic image is formed using nine CCD sensors, where four CCD arrays are placed in the corners of the “master” cone. The other cones, termed “slaves”, comprise two cones (C2 and C3) with two CCD arrays and one cone (C4) with one CCD array. The final virtual image is then formed by stitching the nine sub-images captured from the nine different CCD arrays using the overlap area between the sub-images (Figure 2-5). In the latest camera models, the stitching process has been improved by the introduction of a new stitching technique known as monolithic stitching. This stitching process includes a simultaneous adjustment of all image tiles using their overlaps, and also the green color-channel to determine the 2D Helmert transformation parameters for each individual sub-image (Ladstädter *et al.*, 2010a).

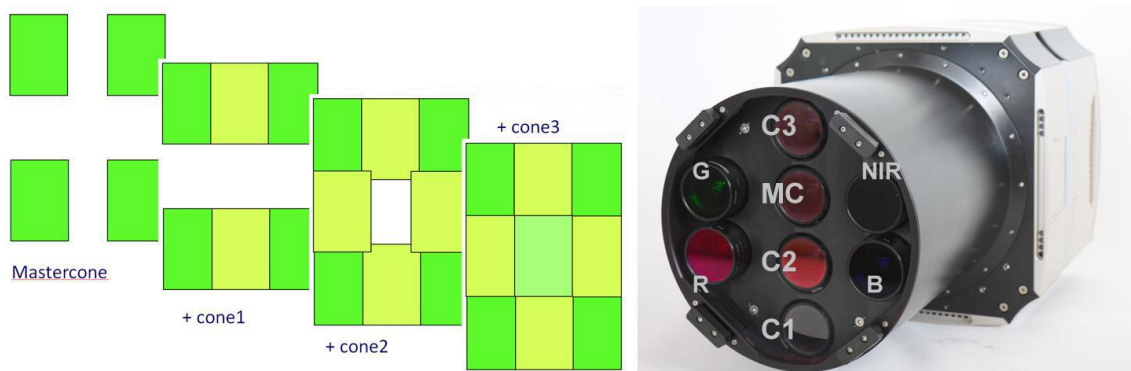


Figure 2-5 UltraCam virtual image stitching using 9 sub-images (Gruber *et al.*, 2012).



After the stitching process, the final colour image is produced by merging the panchromatic image with the multispectral images to produce high resolution colour images. This process is called pan-sharpening (Sandau, 2009). Due to developments in the field of CCD array technology and the increase in their format sizes, new models have been introduced, notably the UltraCamX and UltraCamXp (Gruber *et al.*, 2008; Leberl *et al.*, 2012). The image footprint was increased and image resolution improved from 9  $\mu\text{m}$  in the UltraCamD model to 7.2  $\mu\text{m}$  for the UltraCamX and 6  $\mu\text{m}$  UltraCamXp models.

Further improvement was made in terms of image size by introducing the UltraCam Eagle model in 2011 (Gruber *et al.*, 2012). The new camera utilizes similar design principles as previous models which utilize four cones for the panchromatic image acquisition and four for multispectral. However, new types of CCD detectors were used to build the large 260 Megapixel frame format. The size of the resultant panchromatic image is 20010 x 13080 pixels with 5.2  $\mu\text{m}$  resolution. This model includes two interchangeable lens cones with different focal lengths which can be changed on site. These different lenses allow more flexible data acquisition over different areas. Figure 2-6 shows the image foot print for different models of production UltraCam frame cameras and the improvement in the image size. This improvement has increased the productivity and efficiency of the aerial data acquisition where larger mapping areas could now be covered with fewer images.

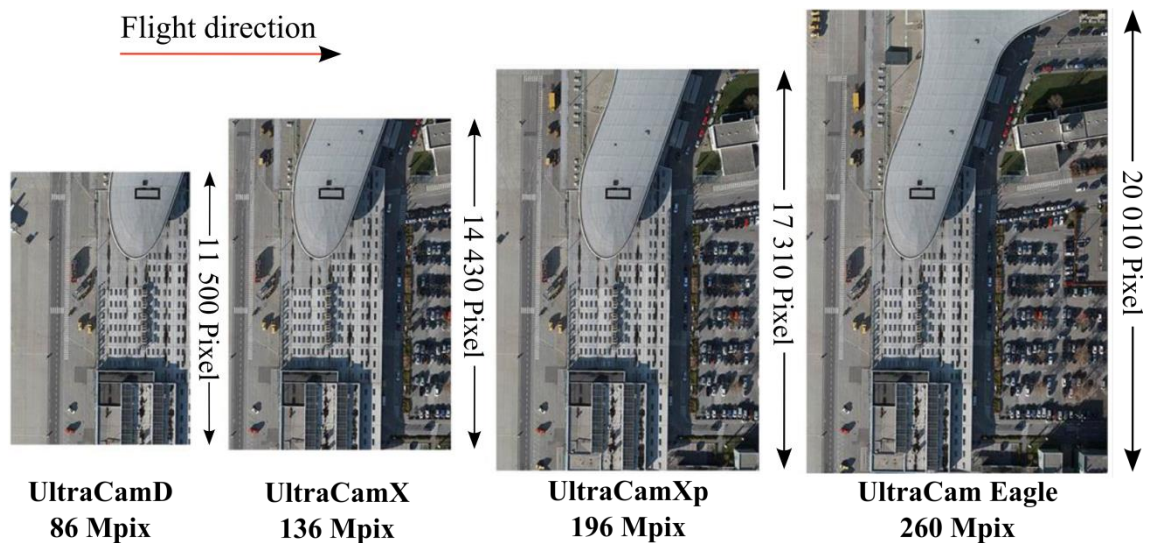


Figure 2-6 Ultracam frame sizes for different models (Gruber *et al.*, 2012).



### 2.2.5 Large Format Line Scanner Cameras

The three-line scanner concept is based on using multiple parallel linear sensors. These sensors are positioned next to one another using a single lens system. These individual linear sensors provide forward, nadir and backward views (Figure 2-7). Leica digital pushbroom line scanners are based on the design of WAOSS/WAAC line scanning system by DLR which was designed for the 1996 Mars mission (Cramer, 2004a). The image is formed by merging the individual three-line images which requires integration of a GNSS/IMU system into the scanner imaging system to integrate the multiple lines into one image carpet. The first pushbroom scanner produced by Leica Geosystems was the ADS40 model. The official release of this model occurred during the ISPRS conference in Amsterdam 2000 (Cramer, 2004a). The ADS40 model was equipped with eight 12,000 pixel parallel sensor lines. Three of the sensors were panchromatic and arranged to capture images in forward, nadir and backward directions. The other five sensor lines were for the multispectral bands (pan, red, green, blue and near-infrared). The spatial resolution of the panchromatic image is doubled using two line with 12,000 pixels CCD adjacent to each other staggered by half a pixel (Sandau *et al.*, 2000).

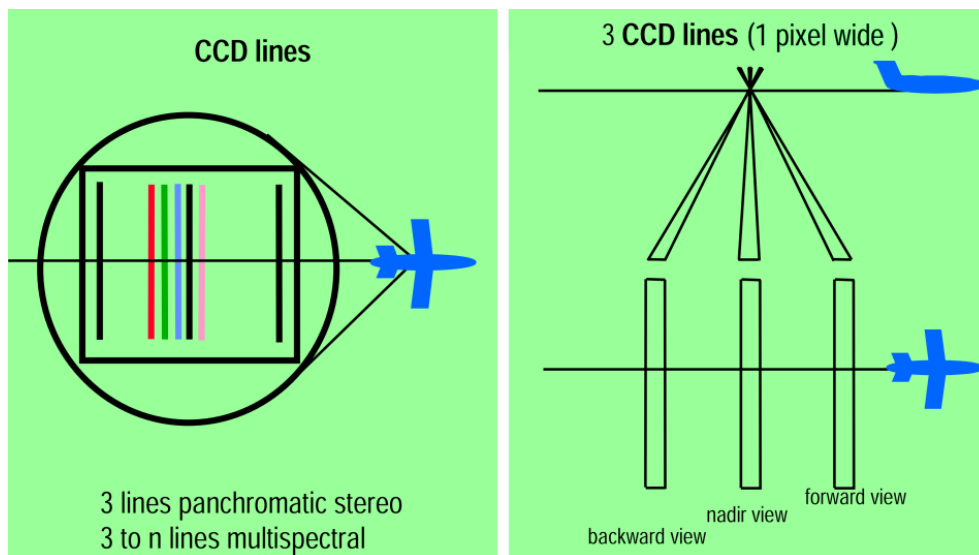


Figure 2-7 Principal and geometric characteristics of the ADS40 three-line digital sensor, adapted from (Sandau *et al.*, 2000).

A new model, named ADS80, was formally announced at the 2008 ISPRS Congress in Beijing (Hobi and Ginzler, 2012). The ADS80 was equipped with two sensor heads configurations (SH91 and SH92). The SH91 sensor head delivered equal-resolution

panchromatic, color and color-infrared imagery. It captured nadir, backward and forward panchromatic imagery and nadir colour-infrared imagery which allowed stereo viewing in both panchromatic and color. The SH92 sensor head, in addition to delivering equal-resolution in all image types, also captured color-infrared imagery in nadir and backward directions (Figure 2-8). This allowed full stereo viewing in panchromatic and color-infrared as well (Leica, 2013a).

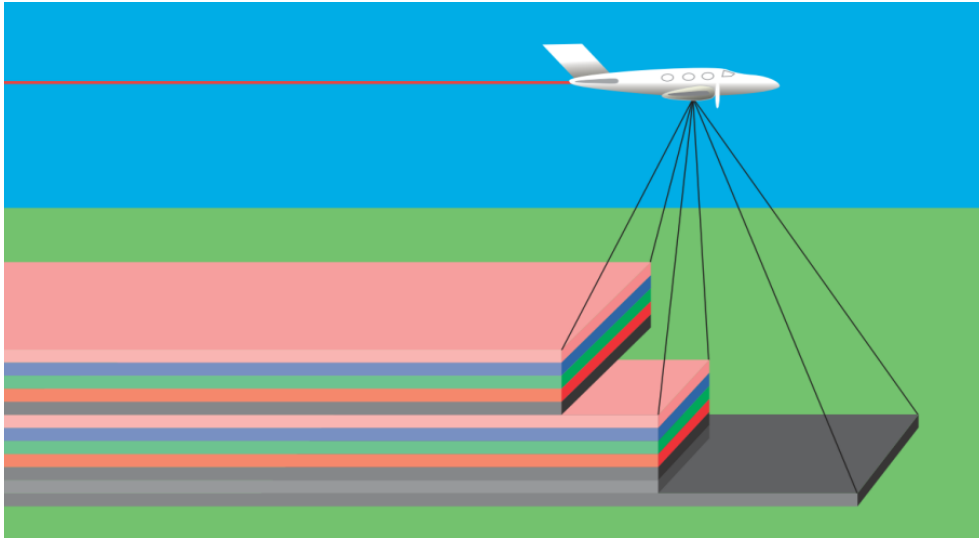


Figure 2-8 Image acquisition for the SH92 sensor head (Leica, 2013a).

The latest model of Leica line scanners, the ADS100 model, was announced on March 2013 (Leica, 2013b). This new model provides an image width of 20000 pixels in color-infrared in forward, nadir and backward viewing directions. This allows full stereo viewing in panchromatic and color-infrared, using all viewing angle data.

## 2.3 Medium Format Digital Aerial Cameras

### 2.3.1 Introduction

Acquisition of digital aerial data for mapping purposes is mainly performed using large format digital aerial cameras. Despite the advantages of these cameras, they are unsuitable for mapping smaller areas. Therefore, the need for smaller and more flexible cameras that suit mapping smaller areas was desirable (Cramer, 2004b). The main advantages of medium format cameras over large format camera models are the lower costs to perform aerial survey and also smaller and cheaper aircraft that could be used in the aerial survey. Moreover, due to the smaller image size, it provides easier and faster

data processing for mapping small areas. In addition to that, medium format cameras have become widely used in conjunction with laser scanners for large scale mapping, 3D city modelling and also disaster monitoring and management (Grenzdörffer, 2008). Due to the demand for smaller, cheaper and high performance cameras suitable for smaller projects, different camera models have been introduced into the market. The main types of medium format digital aerial cameras are introduced briefly in the following sections.

### 2.3.2 UltraCam L(P) Medium Format Camera

The UltraCam L medium format camera was produced by Microsoft Vexcel imaging and first announced in July 2008 as a lower priced camera model suitable for small projects (Ladstädter *et al.*, 2010b). The camera design was based on the multi-head concept using four camera heads. Two heads were dedicated to capture high resolution panchromatic images of 64 Megapixels, one for the RGB image and one for the near Infrared image of 19 Megapixels. The image stitching approach adopted for other UltraCam camera models was also adopted in this camera model. The compact design of this model allowed the integration of the computing unit and data storage components into the sensor head unit, as shown in Figure 2-9 (Ladstädter *et al.*, 2010b).

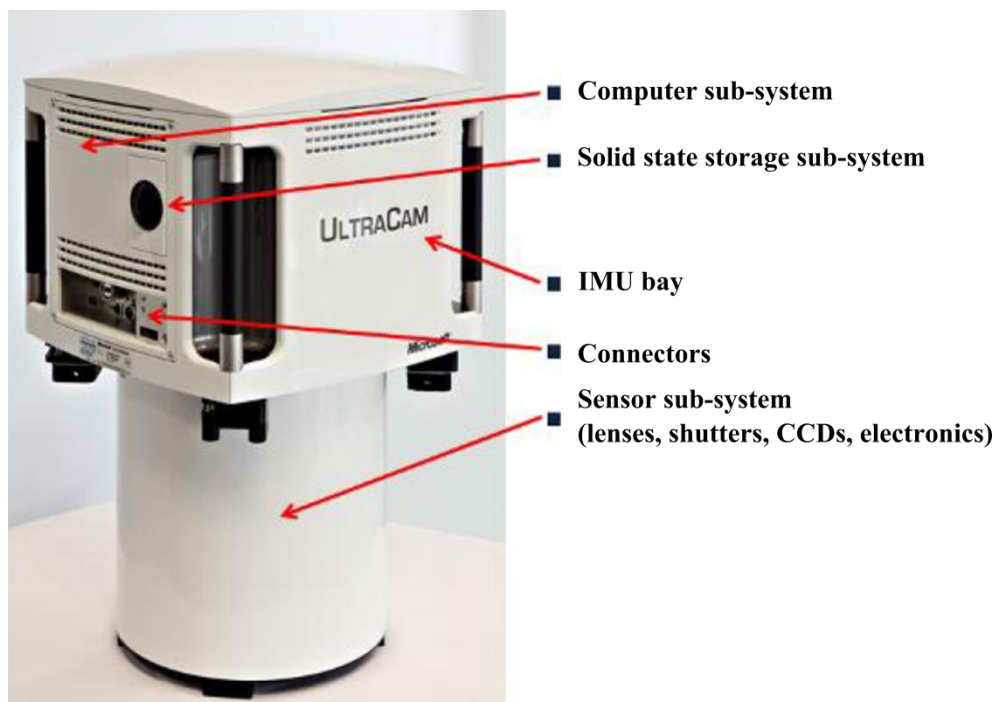


Figure 2-9 UltraCam L sensor head and integrated data capture and processing unit, adapted from (Ladstädter *et al.*, 2010b).

A new updated version of this camera model, named the UltraCam Lp, was introduced in late 2009 which provided an increased footprint of the panchromatic image to 92 Megapixels.

### 2.3.3 RMK D Medium Format Camera

The RMK D digital medium format camera produced by Z/I imaging was introduced in July 2008 (Dörstel, 2009). This camera model was designed to meet the specifications of metric cameras for geometry and also radiometry with a 45 mm focal length and 7.2 $\mu$ m CCD resolution. The camera design includes using four independent camera heads, for RGB and NIR (Figure 2-10). Images are captured simultaneously at 1:1 color resolution offering a 6096 pixels along track and 6500 cross track (Z/I-Imaging, 2013b).



Figure 2-10 Left, RMK D camera, right, four MS camera heads and video camera (centre), adapted from (Dörstel, 2009).

### 2.3.4 Leica RCD 30 Medium Format Camera

The RCD 30 medium format camera by Leica Geosystems was first announced in July 2011 (Figure 2-11). This camera uses a unique beam splitter design to produce co-registered four band imagery in RGB and NIR using a single camera head. The camera design also allows the use of two different interchangeable camera heads. This was considered as a big advantage of medium format cameras where different lenses allows

mission to be flown at different altitudes to either maintain the desired resolution or maintain a predefined strip width during joint flights with others sensors, e.g. laser scanners. Also with interchangeable lenses stereo/DEM capabilities may be changes as well as occlusions in narrow streets etc. during orthophoto production. (Grenzdörffer, 2010a)

Moreover, the camera system allows integration with the Leica ALS70 laser scanning system, using a shared GNSS/IMU and operator control system which simplifies data acquisition and integration between the two systems (Wagner, 2011).



Figure 2-11 Leica RCD30 camera system (Operator control, camera head and camera control) (Wagner, 2011).

### 2.3.5 Applanix DSS322 Medium Format Camera

The DSS322 camera system was developed by Applanix in 2004 (Ip and Mostafa, 2006). It was primarily designed to meet specific data delivery needs such as rapid response, disaster survey and recovery operations. This rapid response was met by integrating the new direct geo-referencing component, the POS Track Flight Management System (FMS) and Yaw stabilized Azimuth mount, into the DSS 322 system. This allowed production of an orthomosaic without the need for GCPs (Ip and Mostafa, 2006). The Applanix DSS array provides a medium format sized 5,436 across and 4,092 along the flight line with 9  $\mu\text{m}$  resolution



Figure 2-12 The DSS 322 system (Ip and Mostafa, 2006).

The ground sampling distance size depends on the platform and the type of lenses (40mm and 60mm), as shown in Figure 2-13, which ranges from 3.3cm to 1.0m. These two interchangeable lenses allow more flexible data capture over areas with high building and also over normal terrain without flying at high altitudes.



Figure 2-13 The Applanix DSS322 lenses (40mm, 60mm) (Ip and Mostafa, 2006).

The images of the DSS322 camera are captured in three multi spectral channels R, G and B, where colours are separated using the Bayer matrix approach. In this approach, the full colour information (RGB) is captured by one CCD using the pixel sized color filters. The pixels of these colours are interleaved in the CCD as described in

Figure 2-14. The final image of each individual colour is derived using colour interpolation from the neighbouring pixels (Cramer *et al.*, 2012)

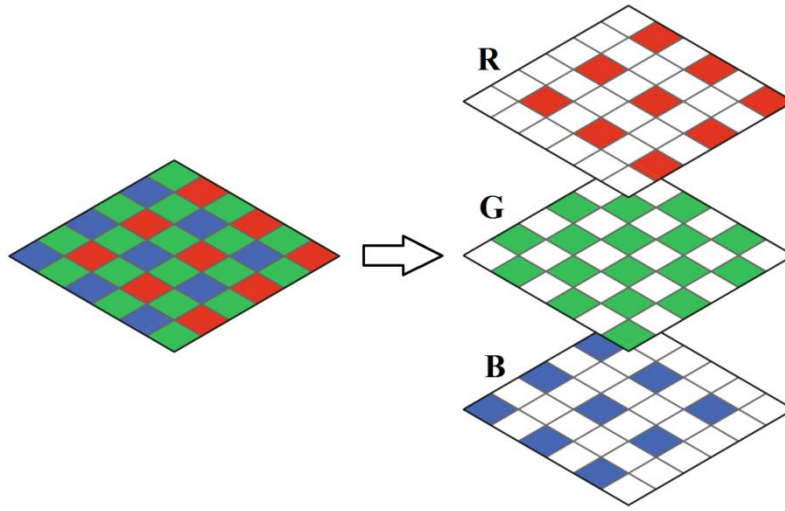


Figure 2-14 Bayer pattern approach (one CCD for RGB colours).

## 2.4 Camera System Calibration

Camera calibration “the process of measuring the relationship of real frame camera geometry in comparison to perspective geometry”, (Smith (2007) has always been an essential task for all aerial mapping cameras. Before any imagery can be used for high precision measurement purposes in photogrammetry there is a need to determine the geometric model of the sensing system described by the parameters of interior orientation, such as principal distance, image coordinates of principal point and radial and tangential distortion (Luhmann *et al.*, 2006).

### 2.4.1 Purpose of Camera Calibration

The geometric camera calibration is mainly performed to establish an explicit relationship between points on an image plane and the object space. This accurate relationship will make the system satisfy the requirements of topographic mapping, as the quality of the photogrammetric product produced will be influenced by system calibration and post-processing methods. Moreover, in order to extract reliable and accurate 3D information from the aerial images, the camera should be accurately calibrated (Remondino and Fraser, 2006). Despite significant efforts in laboratory calibration, the camera’s geometry may change due to different environmental



conditions between laboratory and real flight conditions which (Jacobsen, 2007a). Therefore, a simultaneous calibration has to be performed to refine the camera parameters. In addition, camera self-calibration using additional parameters is performed to compensate for distortions in the aerial images. These distortions, which are known as systematic image errors, are removed to improve the accuracy of aerial triangulation results.

Moreover, by integrating digital cameras with GNSS/IMU positioning and orientation capability which allowed direct geo-referencing of aerial image, the calibration process must ideally include computing the misalignment matrix between the camera and GNSS/IMU units to achieve good accuracy (Cramer, 2007a).

### 2.4.2 Photogrammetric Camera Model

The geometric quality of the digital cameras is mainly related to the camera metric properties, which stands for the accuracy and stability of the camera interior orientation parameters (Grenzdörffer, 2010b). The camera photogrammetric model based on perspective projection, which departures from the collinearity, is further extended by additional parameters to model systematic errors in the image space and any deviations from the perspective geometry (Dörstel *et al.*, 2003). A typical set of these AP are those proposed by Brown (1976) which describes deformations such as errors in the principal distance, offset in the principal point coordinates and other distortions as illustrated in Eq. 2-1 and Eq.2-2.

$$\Delta_x = \Delta_{x_i} + \Delta_{x_r} + \Delta_{x_d} + \Delta_{x_u} + \Delta_{x_f} \quad 2-1$$

$$\Delta_y = \Delta_{y_i} + \Delta_{y_r} + \Delta_{y_d} + \Delta_{y_u} + \Delta_{y_f} \quad 2-2$$

Where  $\Delta_{x_i}$  and  $\Delta_{y_i}$  denotes changes in the camera interior orientation,  $r$  denotes radial distortion,  $d$  the decentric distortion,  $u$  the out of plane unflattens and  $f$  the in plane distortion (Dörstel *et al.*, 2003).

For the camera interior orientation parameters, the initial values must be known before the calibration process. The self-calibration will then determine changes in the camera focal length nominal value ( $\Delta_c$ ) and offsets in the principal point coordinates ( $\Delta_{x_p}, \Delta_{y_p}$ ) as illustrated in Eq. 2-3 and Eq. 2-4.



$$\Delta_{x_i} = \Delta_{x_p} - \frac{\bar{x}}{\bar{z}} \Delta_c \quad 3-2$$

$$\Delta_{y_i} = \Delta_{y_p} - \frac{\bar{y}}{\bar{z}} \Delta_c \quad 2-4$$

Where the image coordinates ( $\bar{x}$ ,  $\bar{y}$  and  $\bar{z}$ ) are obtained as follows:

$$\bar{x} = x - x_p \quad 5-2$$

$$\bar{y} = y - y_p \quad 2-6$$

$$\bar{z} = -c \quad 2-7$$

In addition to the camera interior orientation, the radial distortion which represented by a polynomial is also determined as follows:

$$\Delta_{x_r} = K_1 r^3 + K_2 r^5 + K_3 r^7 \quad 2-8$$

$$\Delta_{y_r} = K_1 r^3 + K_2 r^5 + K_3 r^7 \quad 2-9$$

Where  $K_i$  denotes for the radial distortion coefficients and  $r$  is the radial distance:

$$r^2 = \bar{x}^2 + \bar{y}^2 \quad 2-10$$

According to Dörstel *et al.* (2003) that for high quality lens systems, the parameters of the decentric distortion and out of plane unflattens are small and usually insignificant. Further details of camera calibration parameters can be found elsewhere (McGlone *et al.*, 2004).

### 2.4.3 Laboratory Camera Calibration

For metric cameras, laboratory calibration is used only to determine the interior orientation parameters of the camera. This task is normally performed by a camera manufacturer using optical alignment measuring devices such as goniometers or collimators (Luhmann *et al.*, 2006).

In the case of the recent digital aerial camera systems where multi-heads are used in the camera design, the calibration is performed in two steps. Firstly, after camera assembly, each camera head is individually calibrated. Secondly, to produce the final image, the relative orientation of each camera's head is determined using camera images captured during the real acceptance test (Hefele, 2006). For the DMC large format aerial camera, Hefele (2006) described the laboratory calibration method using a newly developed calibration stand (Figure 2-15).

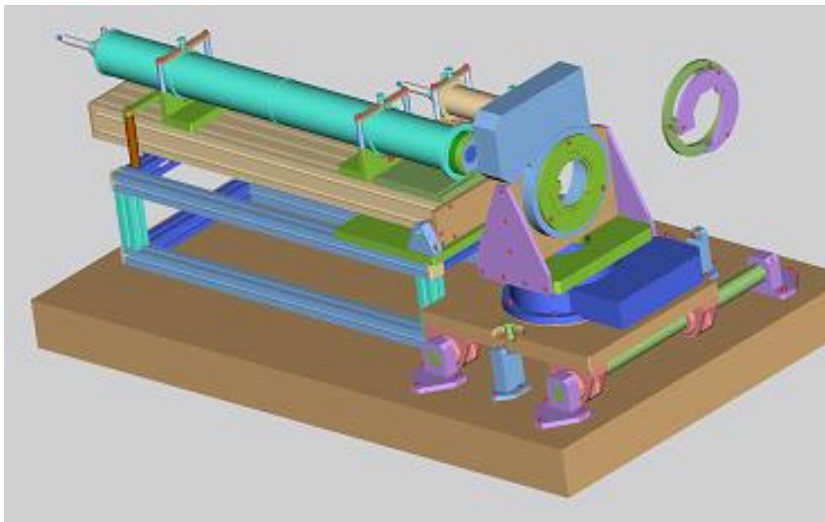


Figure 2-15 DMC Laboratory calibration - Measurement Unit (Hefele, 2006).

This stand uses two highly accurate rotation tables to measure a number of circular targets used to determine the camera calibration parameters. The result of the calibration process is then validated using another calibration method known as test field calibration (Section 2.4.5). For the UltraCam multi-cone camera models, the laboratory calibration is performed using a specially designed calibration chamber. This chamber consists of 367 highly accurate circular three dimensional calibration targets (Gruber and Ladstädter, 2008) (Figure 2-16).

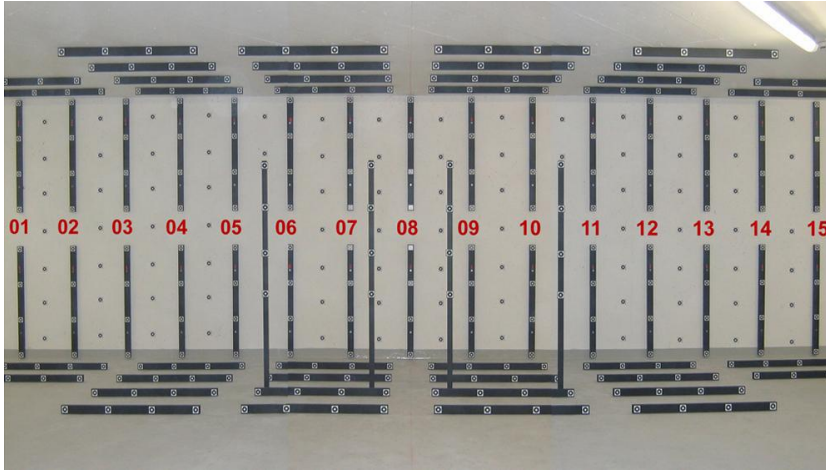


Figure 2-16 UltraCam three dimensional calibration targets (Gruber and Ladstädter, 2008).

The first calibration step starts by measuring highly redundant observations using the circular three dimensional calibration targets in the calibration chamber. Secondly, an automated image processing techniques is used to provide images coordinates of well-defined three dimensional targets. Thirdly, unknown cameras parameters (e.g. focal distance, principal point coordinates and lens distortion parameters) are estimated simultaneously (section 2.4.4) using an automatic adjustment process. Finally, the remaining distortion parameters are then computed and added to the calibration process using a bundle block adjustment process (Gruber and Ladstätter, 2006; Gruber and Ladstädter, 2008).

Laboratory calibration for line scanning imaging systems may not be feasible due to the difference in the design concept. The ADS40 pushbroom geometry, for example, is completely different from frame based imaging systems. Also, there is no standard international guidelines for calibrating such systems (Tempelmann *et al.*, 2003). Moreover, besides the optical system components of the lens system (such as CCD lines and beam splitter), the use of the IMU system (which is a crucial component in the ADS40 design) made it impossible to apply laboratory calibration for the whole system. The only alternative was to calibrate the system under practical working conditions using a test field calibration (Tempelmann *et al.*, 2003). Test field calibration methods are discussed in Section 2.4.5.

#### 2.4.4 Simultaneous Camera Calibration

Since the development of the bundle adjustment by Brown in 1965, published in 1966 in (Brown, 1966), the simultaneous determination of lens calibration parameters along with exterior orientation elements became practically possible using three-dimensional coordinates of reference targets (Clarke and Fryer, 1998). The process of simultaneous calibration is also known as self-calibration, where additional parameters are introduced to compute camera parameters. Such an approach also enabled determination of geometric discrepancies between real image geometry and the mathematical model of perspective images. These discrepancies are usually called “systematic errors” (Jacobsen, 1998b). Tests conducted by Alamús *et al.* (2006) showed that these systematic errors introduce height errors to the image points, and these errors increase at the edge of the image block.

According to Brown (1989), the camera self-calibration process needs to meet certain conditions: Firstly, a minimum of three images captured by the same camera are required. Secondly, the camera must have stable interior orientation elements during the period of image capture. Thirdly, strong photogrammetric block geometry is needed using highly convergent images. Fourthly, the roll angle must be different in at least one image. Fifthly, points used in the adjustment must have good spatial distribution.

To model image distortions or systematic errors, different sets of additional parameters are introduced. These parameters are implemented in a bundle adjustment in two approaches. Firstly, using simple orthogonal polynomial parameter set. These parameters are based on pure mathematical justification such as the Ebner 12 additional parameters or Grün 44 additional parameters (Ebner, 1976; Grün, 1978). Secondly, using a physical significant parameters set such as Brown 1971 parameters set (Brown, 1971). These parameters are implemented to model physically justified effects such as camera focal length, principal point offset, tangential lens distortion and radial symmetry (Cramer, 2002; Jacobsen *et al.*, 2010). Other bundle adjustment programs such as BLUH (Jacobsen, 2007b) use mainly physically justified 12 additional parameters. However, due to the special design principles of recently introduced digital aerial cameras, the use of a standard set of additional parameters such as BLUH 12 or Ebner 12 is not sufficient to model the systematic errors in image space. Therefore, a special set of additional parameters were added to the BLUH bundle adjustment

software in order to compensate for deformations caused by the stitching process of the virtual image in the large format cameras UltraCam and DMC (Cramer, 2007b).

### 2.4.5 Test Field Camera Calibration

The development of the bundle adjustment and simultaneous calibration using additional parameters enabled a new calibration approach known as test field calibration. The merit of this calibration approach is that camera calibration is performed in environments similar to a real-world operational environment. However, a sufficient number of highly accurate control points and high level of observation redundancy are needed to perform such a calibration (Honkavaara, 2003).

For digital aerial cameras, a similar standard set of additional parameters as designed for film cameras can be used in addition to the special additional parameters added for the new breed of digital aerial cameras. For a line sensor, as the standard set of additional parameters do not fully describe and model the residual distortions, modelling these distortions line by line is advisable (Sandau, 2009).

According to Honkavaara (2003), calibration block structure plays an important role in determining various camera calibration parameters. This necessitates certain requirements to avoid correlation between the parameters and improve the accuracy. Firstly, a large block size is needed in order to achieve good accuracy. Secondly, multiple flight lines must be flown in opposite directions to enable the separation between the correlated parameters such as direction dependent shifts ( $f$ ,  $x_0$ ,  $y_0$  and  $(dx, dy, dz)_{lever}$ ) boresight parameters ( $d_\omega$ ,  $d_\varphi$ ,  $d_\kappa$ ). Thirdly, multiple parallel flight lines are needed to determine the datum parameters. Fourthly, two different flying heights are needed to separate focal length correction and height shifts such as  $d_z$  of the lever arm and  $d_z$  datum. Finally, each flight line must contain at least 10 images.

The efficiency and the accuracy of the test field calibration are significantly affected by the structure of the calibration block. Therefore, different calibration block structures have been proposed by Honkavaara (2003) to perform test field calibration as shown in Figure 2-17. The calibration tests showed that without the opposite direction strips, the accuracy of the interior orientation parameters and boresight parameters will be low. Also, results showed that, the most accurate results have been obtained using the comprehensive block structure. However, due to the added cost to the comprehensive

block structure which sometimes is not applicable, the results from the L and 4 parallel strips block with 80% overlap and 60% sidelap provided also reliable results with lower cost. The worst results were obtained using the I block structure and 4 parallel strips with 60% overlap and 30% sidelap. Therefore, these configurations are considered as not recommended for camera calibration purposes due to the correlation between the calibration parameters.

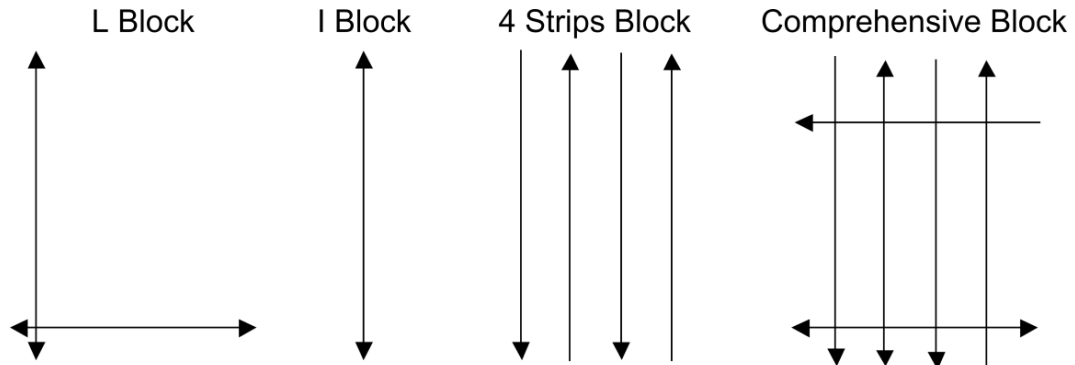


Figure 2-17 Different configurations of calibration block structures (Honkavaara, 2003).

In addition to the block structure, the number of GCPs has also significant effect on the determination of some of the calibration parameters. Figure 2-18 shows the GCPs configurations used by Honkavaara (2003). The results showed that the principal point coordinates are not significantly affected by the number of used GCPs. These parameters are mainly affected by the amount of image overlap and use of opposite strips. On the other hand, the precision of the focal length correction is significantly affected the number of used GCPs, where the accuracy deteriorates when smaller number of GCPs is used in the block adjustment. For example, the focal length precision was 1.5  $\mu\text{m}$  when 12 GCPs are used and 2  $\mu\text{m}$  with 4 GCPs at the block corners and 4  $\mu\text{m}$  with only one GCP at the middle of the block. Further details of bundle adjustment and simultaneous camera calibration can be found elsewhere (McGlone *et al.*, 2004).

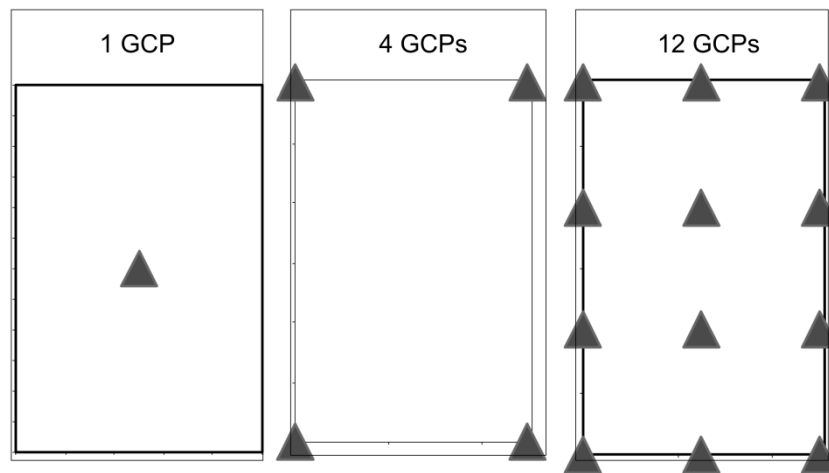


Figure 2-18 GCP-distributions in rectangular blocks (Honkavaara, 2003).

Besides the validation of the camera parameters (interior orientation) during the test field calibration, the use of GNSS/IMU data in the calibration process made it mandatory to include it within the overall system calibration (Cramer, 2006).

#### 2.4.6 Boresight Calibration

GNSS coordinates refer to the position of the GNSS antenna, and the IMU attitudes refer to the orientation of the IMU body (Figure 2-19). Therefore, the coordinates and orientations of the camera perspective centre are determined by computing the translation and rotational offsets between camera perspective centre and GNSS antenna and IMU body. The GNSS antenna translation, also known as lever arm offsets, is usually determined using conventional surveying methods and normally made after camera installation (Cramer *et al.*, 1999).

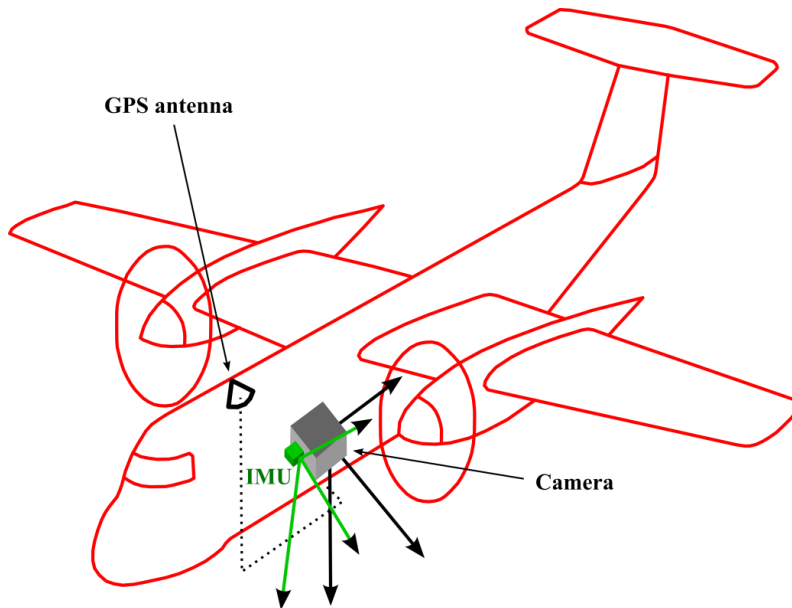


Figure 2-19 Positional relationship between Camera, GNSS and IMU (Jacobsen, 2002).

The boresight misalignment angles, which is the rotational offset between the camera and IMU body, however, is usually determined using one of two common approaches. In the first approach, which is known as the 2-step approach, the boresight estimation is performed by comparing the orientations obtained using reference aerial triangulation with GNSS/IMU orientation. In the second approach, known as the 1-step approach, the boresight angles are estimated as additional unknowns during a bundle adjustment (Skaloud and Schaer, 2003). The accuracy of the determined misalignment angles is greatly dependent on the quality of the GNSS/IMU data processing. Also, unstable mounting between the camera and IMU body and the presence of any remaining systematic errors in the GNSS/IMU data might significantly influence the boresight estimation results (Cramer, 2003).

## 2.5 GNSS/IMU Orientation for Digital Photogrammetry

The use of GNSS/IMU data for direct measurement of camera stations during flight has greatly reduced mapping costs by limiting the number of GCPs needed for aerial triangulation. It has also become an essential pre-requisite for geometric quality assessment of imagery from terrestrial, airborne and satellites sensors (Cramer, 1999). Moreover, it has become crucial part in the design of the new push-broom line scanner aerial imaging systems. For example, the ADS40 is equipped with a GNSS/IMU system to record the absolute and relative positions and attitudes of the sensor continuously to



enable the production of the final image carpet (Section 2.2.5). Moreover, for the recently developed digital aerial frame cameras, the importance of the GNSS/IMU data is evident from the possibility of achieving near real time mapping, where orthoimages could immediately be available after data capture (Wegmann, 2002). The main advantages of integrating GNSS positions and IMU attitudes as described by Skalous (1999) are that it improves the position and velocity accuracy, attitude data is determined with high degree of precision, the navigational data can be estimated during loss of GPS signal and detection and correction of GPS cycle slip. Figure 2-20 depicts the concept of direct determination of camera positions and attitudes using a GNSS/IMU system.

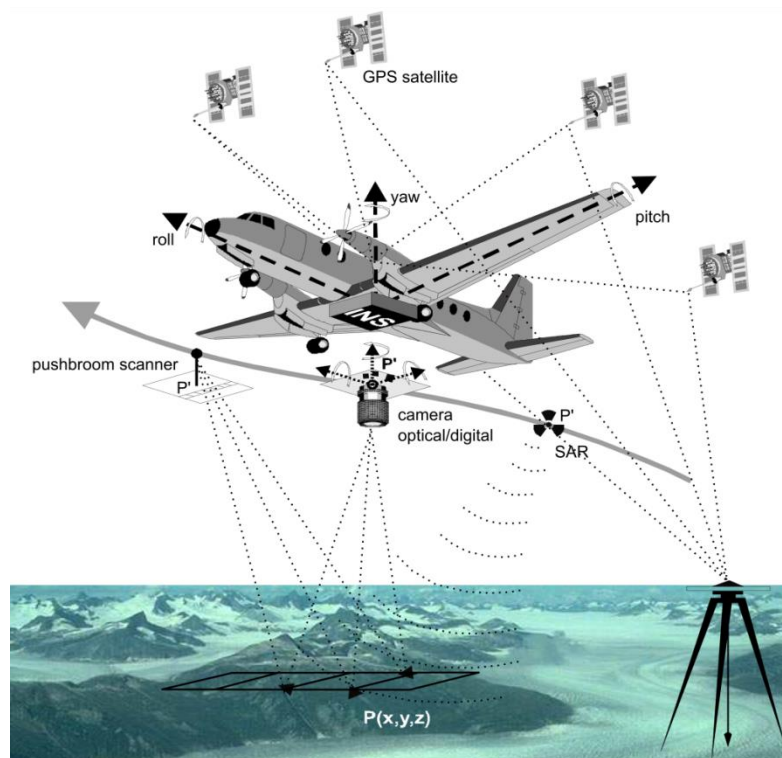


Figure 2-20 Direct determination of camera positions and attitudes (Skalous, 1999).

Integration of GNSS and IMU data is usually performed via a method known as the Kalman filtering (Wegmann, 2002). This method performs a combined adjustment of IMU attitudes together with GNSS positions for determining GNSS cycle slips caused during the turnaround from one flight line to another and it also removes drifts from the IMU data (Jacobsen, 2000).

### 2.5.1 Direct Geo-referencing

Traditionally, geo-referencing of aerial imagery is achieved indirectly by identifying the corresponding image coordinates for well-known ground control points. This is followed by transformation between object and image space using an appropriate mathematical model to compute the exterior orientation parameters. These parameters directly relate the object ground coordinates with image coordinates (Cramer, 1999). However, relying only on ground control points for image geo-referencing is expensive and time consuming. Therefore, direct geo-referencing using GNSS/IMU data provides the ability to directly relate aerial and space images to the correct geographic location, through immediate and accurate measurement of camera coordinates and orientations without the need for any control points (Ip *et al.*, 2008).

Direct geo-referencing has many advantages. For example, it enables a faster acquisition of image exterior orientation. Quicker and more economic automatic aerial triangulation can be performed. In the case of direct geo-referencing, flight path restrictions and limitations can be removed, which make direct geo-referencing independent of block or strip configurations. Moreover, it is useful for a number of applications such as mapping steep slopes, forests and large water bodies, where image matching can be very difficult or tie points could not easily be found. Finally, for small format cameras to be used economically instead of standard large format aerial imagery, direct geo-referencing is considered as a prerequisite (Cramer, 1999; Jacobsen, 2004).

On the other hand, direct geo-referencing has also some disadvantages. Firstly, the accuracy of object point coordinates (obtained by direct extrapolation from the projection centres to the ground) is mainly dependent on a precise sensor calibration and known misalignment parameters between the IMU and the aerial camera (Jacobsen, 2002; Yastikli and Jacobsen, 2005). For example, for aerial images acquired at 1530m above ground, changes in the focal length of 153mm by 47  $\mu\text{m}$  will cause an error in the flying height by 0.47cm (Jacobsen, 2004). Secondly, a direct geo-referencing solution suffers from missing reliability due to the lack of redundancy and errors can also be introduced by large y-parallaxes when tie points are not included in the solution (Jacobsen, 2004). This can be improved using a combined adjustment known as Integrated Sensor Orientation (ISO) where tie points are introduced into the solution. This combined adjustment minimises the RMS of y-parallaxes and improves the point

quality without the need for any GCPs in the bundle block adjustment (Heipke *et al.*, 2002a).

### 2.5.2 Integrated Sensor Orientation (ISO)

ISO is an extended form of direct geo-referencing, where image tie points and GNSS/IMU data are simultaneously processed for the determination of exterior orientation elements. This technique could also be used to perform a simultaneous adjustment using all available inputs, such as image coordinates of tie points, GNSS/IMU data and other control information in image and object space to determine accurate exterior orientation elements. This simultaneous adjustment provides better point accuracy and high reliability, even without using GCPs (Heipke *et al.*, 2002b; Kremer and Kruck, 2003). The ISO approach is feasible for many applications where introducing tie points in the solution minimises the RMS of y-parallaxes and improves the point quality without the need for GCPs in the bundle block adjustment. Moreover, adopting large amounts of image overlap provides strong block geometry, improving point height accuracy by increasing the number of rays per observed point on the ground (Ladstädter and Gruber, 2008). The main concern in ISO is that systematic errors in the GNSS/IMU measurements, or changes in the system calibration parameters between calibration and actual flight, may not be detected without the presence of GCPs (Heipke *et al.*, 2002b). Also, similar to the direct geo-referencing approach, changes in the camera focal length and errors in the flying height will cause errors in the object coordinates of image tie points.

## 2.6 Summary

This chapter has presented a review of the development of different digital aerial cameras, methods of camera calibration and methods of direct geo-referencing. These camera models have helped establish a new fully digital photogrammetric work flow. The virtual images created from this new era of large format camera models are based either on a multi-head design using syntopic or synchronous principles or on the multi-line scanner concept. After introducing the new single frame large format digital aerial camera models such as DMC II<sub>140</sub>, DMC II<sub>230</sub> and DMC II<sub>250</sub>, a complete replacement of the old analogue aerial camera systems is finally achieved and the era of analogue film cameras can be considered at an end.

The use of large format digital camera models is now in a wide spread of commercial operations. This was driven by the better image quality and high product accuracy. In addition to this, these qualities have encouraged the use of medium format cameras for smaller photogrammetric projects where the use of digital large format cameras is not economical. Moreover, the geometry and systematic distortions caused by the new design principles of the digital aerial cameras have been studied throughout the last ten years. These studies resulted in developing new calibration procedures and adding new sets of additional parameters which best suits each camera type. These special parameters have been empirically tested and prove to compensate for systematic errors and improve the quality of the final mapping product.

The use of GNSS/IMU data has greatly reduced mapping costs by limiting the number of required control points. However, the optimum accuracy requires precise system calibration parameters and the relationship between camera and GNSS/IMU should be accurately determined. Camera calibration parameters provided by a camera manufacturer may change under real world flight conditions relative to the situation in the laboratory. Therefore, test field calibration is usually performed with a permanent test field using a large number of control points. Environmental conditions between the test field and mapping areas may still differ, however. Establishing a new test field for every mapping area is expensive and largely impractical. Therefore, the possibility of extracting reference control targets from other 3D data such as LiDAR data has become an interesting research topic.

Chapter three will provide an overview of existing methods where LiDAR data has been used as source of control to perform aerial triangulation instead of using typical GCPs.

# CHAPTER

# 3

---

## 3 Integration of LiDAR and Photogrammetry

---

### 3.1 Introduction

Chapter Two introduced the major types of commercial digital airborne cameras and also explained the design concepts of different large format and medium format digital aerial camera systems. In addition to airborne image acquisition, new technology has emerged which gives accurate and direct three dimensional object space coordinates using laser scanners. This technology has come to be known as “LiDAR”, an acronym derived from “light detection and ranging”. LiDAR is classified as an active system since it emits its own source of energy in order to compute the distance between the LiDAR sensor and the object of interest. This LiDAR capability will provide direct and highly accurate 3D elevation information which is also spatially dense (Postolov et al., 1999). The use of LiDAR for measuring distance goes back to the 1960s, but the use of this technology on a large scale to suit mapping applications was hindered by the lack of proper supporting technology in the fields of both computing and positioning devices (Petrie and Toth, 2009). Subsequently, after rapid developments in computer technology and the introduction of direct geo-referencing using GNSS data, the first laser scanner was introduced to the research community in the early 1990s (Kolecka, 2011). In addition to the 3D coordinates of the object, LiDAR systems also record the intensity of the reflected laser pulse. These intensity values can be visualized in a form of 2D image, which has similar characteristics to an ortho image. The intensity values of the returns echoes are a function of various different factors and also depend on the physical characteristics of the object (Liu *et al.*, 2007).

Despite the accurate height measurements provided by LiDAR systems, this technology still cannot be used independently for accurate mapping purposes due to lower

planimetric accuracy and the lack of sufficient semantic information. Therefore, the integration of complementary airborne LiDAR and photogrammetric data continues to attract the attention of researchers. An integrated approach offers many potential benefits, such as improved capability for automated information extraction that may result in enhanced accuracy and reliability, as well as reduced costs in a variety of downstream products and applications. Such an approach requires the optimized registration of the two data types within a common coordinate reference frame, which would thus enable the cross-calibration of one information source against another.

Chapter Three provides brief information about the design and working principles of LiDAR systems, including the pre- and post-processing of LiDAR data to generate the reference 3D data. Moreover, the chapter describes the complementary characteristics of LiDAR and photogrammetry and also the different methods of integration used by researchers, in addition to methods in which LiDAR generated 3D surfaces have been used for controlling photogrammetric images and blocks.

## 3.2 Principles and Design of LiDAR System

The basic principle of a LiDAR system is that it computes the time delay between the emitted and reflected focussed laser pulse in order to compute the distance between the LiDAR sensor and the object of interest. The distance is then computed by multiplying the time delay of the reflected pulse by the speed of light (Liu *et al.*, 2007). Depending on the type of measurement method used, laser scanners can be categorised into two types: time-of-flight and triangulation. The former is based on the time delay in measuring the distance and is mostly used in long-range scanners, whereas triangulation is based on the cosine law between the directions of illumination and observation direction. This method is used in the close-range measurement methods (Blais, 2004). Since the airborne scanners used in this research are long-range, based on the time-of-flight, this chapter only focuses on the design details and working principles of these types of scanners. Details and information related to the other types of scanning methods can be found elsewhere (Vosselman and Maas, 2010).

The major components of modern airborne laser scanning systems, as illustrated in Figure 3-1, are as follows. Firstly, the main part of the system is the laser scanning unit, which includes the scanning tools and optical components. Secondly, the GNSS unit

provides the 3D coordinates of the laser scanner at the time of data capture. The GNSS antenna is usually mounted on top of the aircraft to give a better satellite view. Thirdly, the IMU unit which is attached to the scanner provides the orientation angles of pitch, roll and yaw of the aircraft at the time of data capture. Fourthly, the data recorder unit is responsible for controlling the time synchronization of the other system components. Also, it stores all system data, such as the scanner ranging data, IMU and GPS data. Fifthly, the flight management system is a standard component in airborne sensor systems and is mainly used to support the pilot during the project flying mission. Finally, another common component is a laptop which allows the operator to manage control commands using the system software (Vosselman and Maas, 2010).

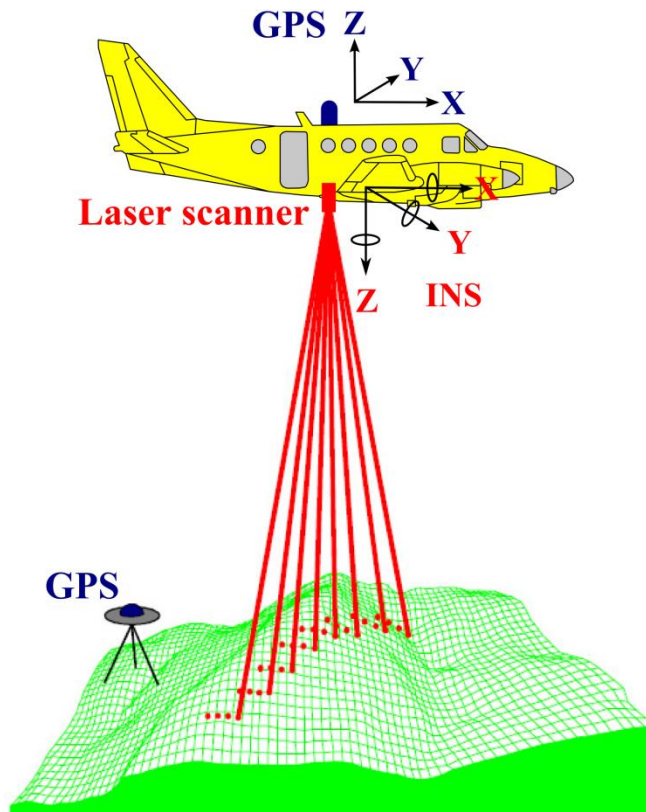


Figure 3-1 Components of an airborne LiDAR system (Schmid *et al.*, 2008).

Based on the type of the laser beam used, LiDAR systems are classified into two groups: discrete pulse and continuous waveform laser scanners as shown in Figure 3-2. In the pulse laser scanners, the distance from the target is measured based on computing the travelling time between the generated and received short laser pulses. The range distance between the target and the sensor is measured using Eq. 3-1.

$$R = \frac{1}{2} c \cdot t_L \quad 3-1$$

Where

$R$  is the distance between the target and scanning unit.

$c$  is the speed of light.

$t_L$  is the traveling time.

With continuous waveform laser scanners, the complete waveform of the reflected laser signal is recorded and the traveling time is computed by measuring the phase difference between the transmitted and reflected signals using Eq. 3-2 (Wehr and Lohr, 1999).

$$t_L = \frac{\phi}{2\pi} \frac{1}{f} \quad 3-2$$

Where

$\phi$  is the phase difference.

$f$  frequency of the laser signal.

Then the range distance is measured using Eq. 3-3.

$$R = \frac{1}{4\pi} \frac{c}{f} \phi \quad 3-3$$

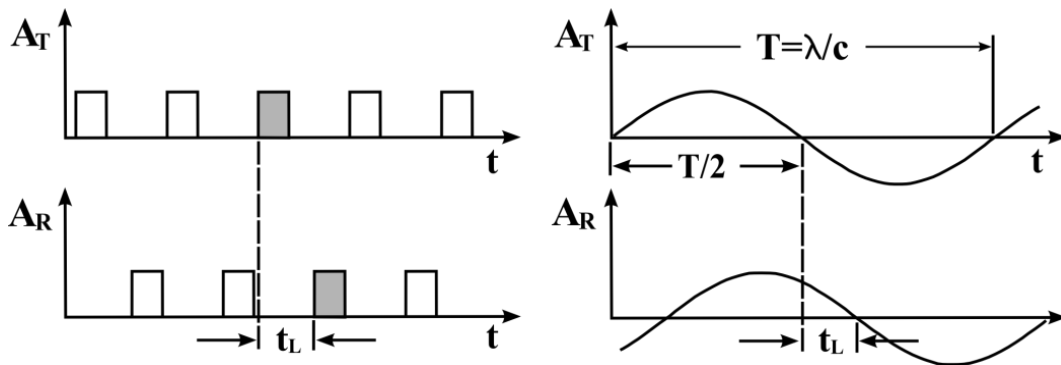


Figure 3-2 Measurement principle of pulse (left) and continuous waveform (right) laser scanners (Wehr and Lohr, 1999).

According to Cramer *et al.* (2012), pulsed lasers are the most commonly used scanners for the following reasons. Firstly, precise time-lapse computations are now possible due to advances in the development of more accurate quartz-stabilised oscillators. Secondly,



pulse intervals can now reach levels of below a nanosecond using existing laser generators and shutters which allowed collection of denser and accurate 3D data.

### 3.2.1 Laser Scanner Design and Data Capture

The scanning unit in the laser scanner consists of two main parts: a pulse generator and a pulse signal receiver. This section briefly describes types of generated laser pulses and also the methods used to receive the reflected laser echoes.

#### 3.2.1.1 Laser Pulse Generation

The laser generator is a device that provides very highly coherent light beam (Wehr and Lohr, 1999). For airborne LiDAR systems, this coherence, both in space and time, is achieved by using a single solid state laser source known as neodymium doped yttrium aluminium garnet laser (Nd:YAG) (Koechner, 2006). The Nd:YAG laser generators, which provide laser pulses in the range of 0.8 to 1.6  $\mu\text{m}$  wavelength, are the most commonly used type in airborne laser scanners. The generated laser pulses have a signal duration usually between 10 to 15 ns (Liu *et al.*, 2007). The laser pulses are repeated at a constant high density rate in order to enable more data to be acquired that will represent the terrain in more detail. This characteristic is known as the pulse repetition frequency (PRF), which differs from one system to another. In the current systems the PRF reaches up to 300kHz (Vosselman and Maas, 2010). Since the technology is still developing, the main focus of sensor manufacturers is to increase the PRF so as to compete with rival manufacturers (Liu, 2008).

In order for the transmitted laser pulses to cover larger areas, different scanning mechanisms are used to move the laser pulses over the terrain surface. Therefore, different scanning methods have been developed and used for airborne laser scanning (Baltsavias, 2008; Vosselman and Maas, 2010). These include an oscillating mirror, rotating polygon mirror, nutating mirror (Palmer scan) and fibre switch mirror, as shown in Figure 3-3.

- **Oscillating mirror:** In this technique, the mirror is swivelled to direct the laser pulse to the ground in a zigzag pattern across the swath. In this mechanism, point density is variable across the scan line due to mirror acceleration.

- **Rotating polygon mirror:** With this mirror, the laser pulses are scanned in one direction. This forms multiple parallel scan lines which give a raster pattern. However, these types of scanning mirrors provide smaller scanning angles compared to the other scanning methods.

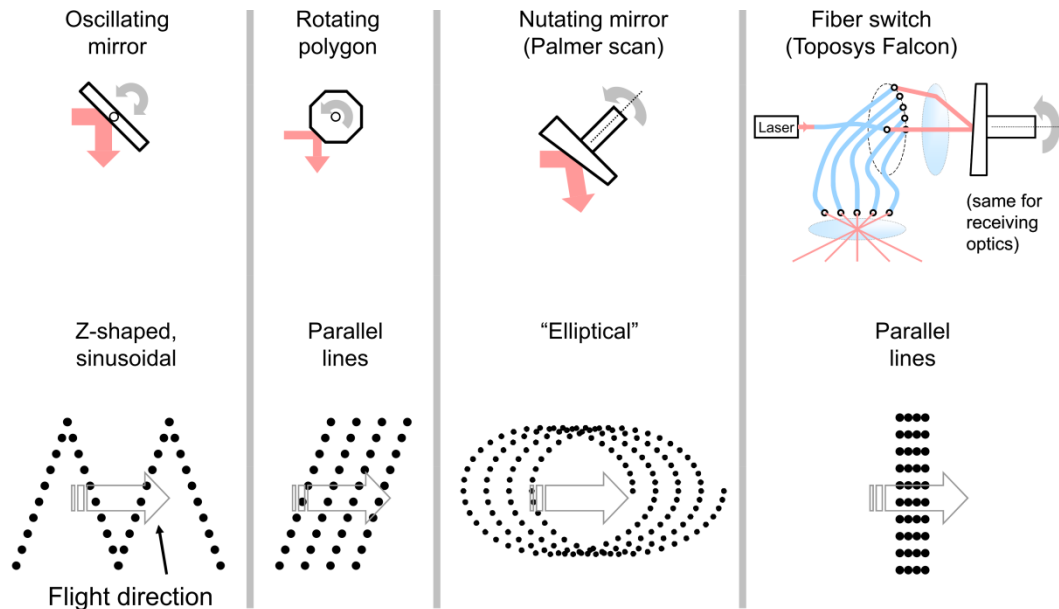


Figure 3-3 Scanning mechanisms and resulting scanning patterns (Baltsavias, 2008).

- **Nutating mirror:** This type of mirror is mainly used in terrestrial laser scanners. The mirror is rotated around inclined axes with an angle not equal to  $90^\circ$ . The laser pulses are then deflected towards the target, forming an elliptical pattern. This type of mirror will provide along-track overlap.
- **Fibre switch scanner:** In this type of scanner, the laser pulse is fed into a group of glass fibres arranged in a linear array to produce multiple simultaneous pulses. These pulses are then projected to the ground forming a parallel line scan pattern.

### 3.2.1.2 Laser Echo Reception

The other main part of the laser scanner is the receiving unit, which collects the reflected laser echoes from the objects scanned. In pulsed laser systems, the most commonly used types of laser collectors are p-n photodiode, avalanche photodiodes (Koskinen *et al.*, 1992) and photo-multipliers (Vosselman and Maas, 2010). The shape and number of returning laser echoes is affected by the nature of the object illuminated.

Therefore, LiDAR systems are designed to detect multiple return echoes. Some systems record the first and last, while others are designed to record up to five return echoes (Wagner *et al.*, 2004). Multiple returns occur when the laser pulses are not completely blocked by the target, as shown in Figure 3-4. This frequently happens when mapping forest areas, where gaps between tree branches may cause the laser pulse to be partially reflected by the top, middle or lower branches and the ground (Reutebuch *et al.*, 2005).

In pulsed airborne laser scanners, the return echoes are digitised in discrete pulses and other returns below a predefined threshold are discarded as shown in Figure 3-4. In 2004, new LiDAR systems were developed, known as full-waveform LiDAR, which record the complete waveform of the reflected laser pulse (Mallet and Bretar, 2009). In this approach, there is no need for pulse separation between the multiple return echoes, and the full-waveform returns will be digitized with an interval usually of 1ns. Also, the analysis of the multiple returns is usually performed by the user in the post-processing stage (Cramer *et al.*, 2012). The full-waveform is very useful in mapping forest areas where the full-waveform returns will be rich with information from different levels of the forest canopy.

In addition to the 3D data derived from the reflected laser pulses, modern LiDAR systems also record the intensity of the reflected laser echoes. These intensity values can be visualized in a form of 2D image, which has similar characteristics to an ortho image. The intensity values of the returned echoes are a function of various different factors and also depend on the physical characteristics of the object (Liu *et al.*, 2007). Cramer *et al.* (2012) described the most influential factors here as follows: firstly, the wavelength of the laser pulse and the reflectance of the target object; secondly, the incidence angle of the laser pulses; and thirdly, the effect of the atmospheric illumination that surrounds the object, which will have an effect on the intensity of the return echoes.

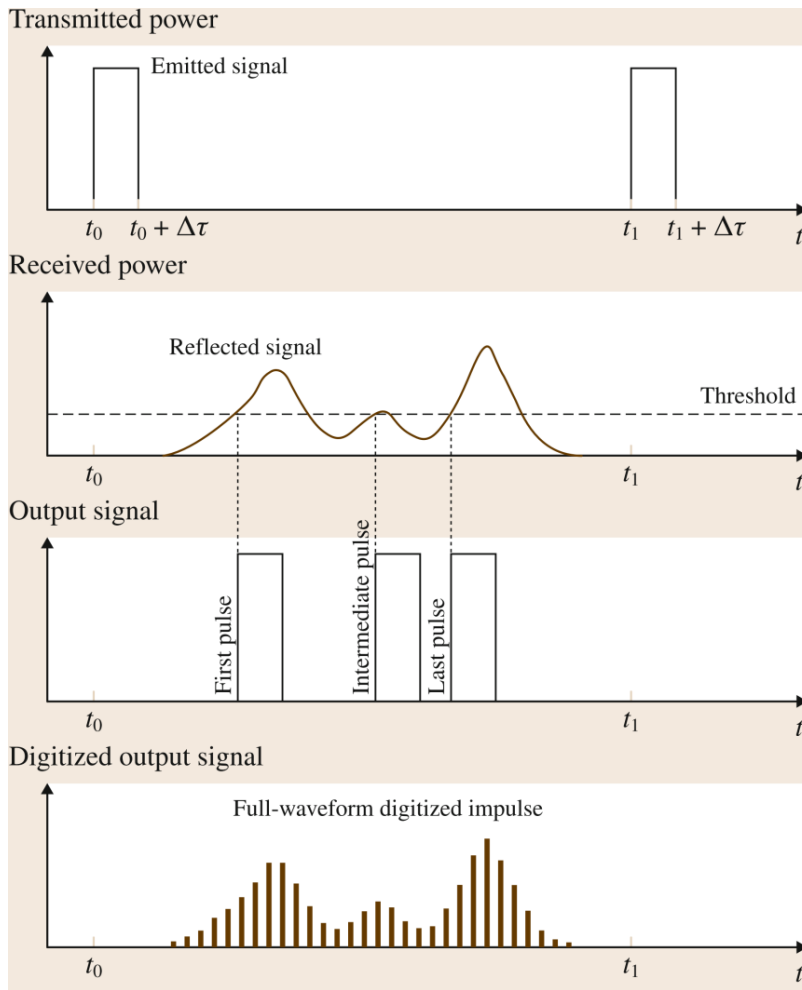


Figure 3-4 Emitted and received pulse for discrete echo scanners and full-waveform scanners (Cramer *et al.*, 2012).

### 3.2.2 LiDAR Data Processing

The processing of the collected LiDAR data usually goes through two main processing steps: pre-processing, usually performed by the contractor; and post-processing. Vosselman and Maas (2010) described the pre-processing step as illustrated in Figure 3-5. At this stage, three types of data are included: GNSS ground station data; navigational data from the GNSS and IMU; and the ranging data including the time tags and other information data such as number of echoes and intensity. Before processing the LiDAR data, GNSS/IMU data are first processed in order to obtain higher levels of accuracy using the information from the reference ground GNSS station. The ranging data are simultaneously processed with the GNSS/IMU data, including the calibration and mounting data, using the time tags to compute the X, Y and Z coordinates of each LiDAR point in WGS84 coordinates. Finally, the data are stored in a standard LiDAR

data format, usually in LAS format which contains point coordinates and also the intensity data (Vosselman and Maas, 2010).

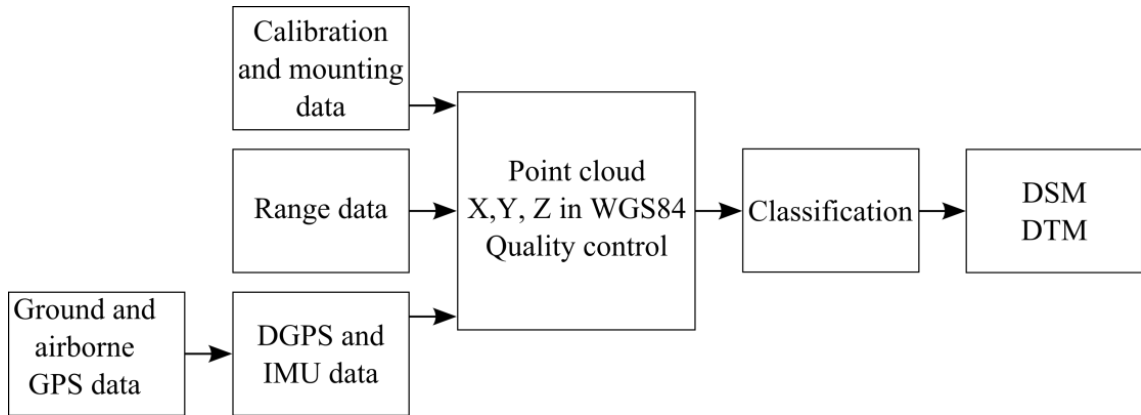


Figure 3-5 Processing scheme for airborne laser scanning (Vosselman and Maas, 2010).

In the post-processing stage, the LiDAR data are normally checked for any remaining systematic errors which would lead to positional offsets between the LiDAR strips. The main source of error is the remaining positional and misalignment errors between the scanner and the body of the GNSS/IMU (Morin and El-Sheimy, 2002). These errors are usually eliminated by performing a strip adjustment using the overlapping areas between LiDAR strips (Rönnholm, 2011a). Finally the post-processing of LiDAR data includes the filtering or classification of the LiDAR point cloud for feature extraction or the production of reference surface models in the form of TIN, DSM and DTM.

### 3.2.3 Accuracy of LiDAR Data

The final absolute accuracy of LiDAR data is affected by various error components (Schenk, 2001). These sources of error are summarized by Vosselman and Maas (2010) as follows, firstly, errors in the GNSS/IMU data; and secondly, the physical properties of the target in terms of shape and slope will also affect absolute accuracy.

In real data acquisition, at a flying height up to 2000m, normal vertical accuracy is in the range from 0.05m to 0.2m, and planimetric accuracy varies from 0.2m to 1m (Vosselman and Maas, 2010). Other information on the different sources of errors is described in detail elsewhere (Vosselman and Maas, 2010).

### 3.2.4 Improvement of LiDAR Data Accuracy

The accuracy of LiDAR data are degraded mainly due to the unmodelled systematic errors introduced thorough various LiDAR system components. Therefore, in order for LiDAR data to be used for high accuracy applications, these errors must be eliminated. One of the methods used to correct systematic errors between LiDAR strips is the strip adjustment method (Vosselman and Maas, 2010). This method is used to minimize the relative horizontal and vertical offsets between overlapping LiDAR strips. Existing methods of strips adjustment are mainly based on two main approaches. The first approach uses common lidar tie points from the overlapping areas between lidar strips and minimizes the offsets between these points and usually requires surface gradient to achieve good results (Filin and Vosselman, 2004). However, these methods are greatly affected by the low point density of the LiDAR data. The second methods are based on extracting linear features using either direct or indirect methods of feature extraction. These features will then be used to estimate the offsets between the lidar strips. Vosselman (2008) used automatically extracted ridge lines of building roofs in the overlap areas between LiDAR strips. This method allowed removing both height and planimetric mismatch between strips. Also this method has demonstrated that relative accuracy in from 2-3 cm can be achieved if dense point cloud data is available.

The main concern of these methods that it still do not reflect the absolute of the LiDAR data. Therefore, Csanyi and Toth (2007) have proposed the use of lidar-specific ground targets ,as shown in Figure 3-6, to improve the absolute planimetric and vertical accuracy.

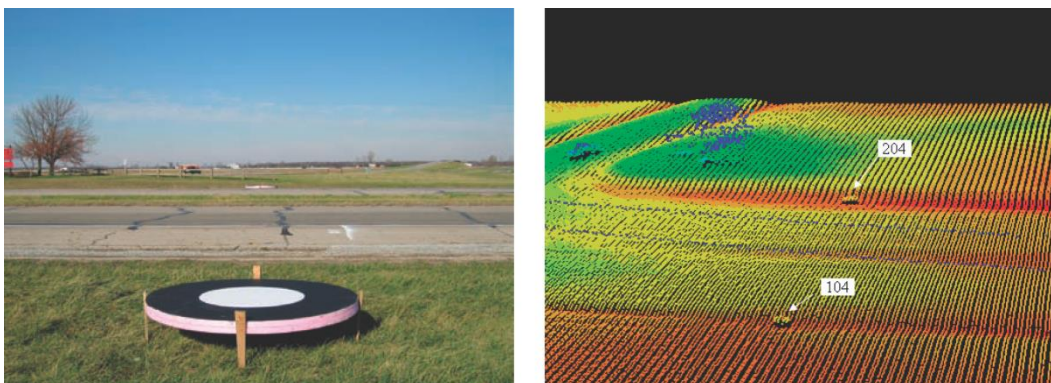


Figure 3-6 Left, LiDAR target, right, its appearance in the LiDAR data (Csanyi and Toth, 2007).

These control targets 3D coordinates are measured in the LiDAR data using target identification algorithm and matched to the GNSS surveyed coordinates. The results showed that the estimated absolute accuracy of LiDAR data was 2-3 cm in height and 5-10 cm in horizontal.

### 3.2.5 Generation of Digital Terrain and Surface Models from LiDAR Data

Digital elevation models are commonly produced either from field survey data, topographic maps, aerial images or satellite images (Liu *et al.*, 2007). However, in comparison with the dense and direct 3D measurement achieved by LiDAR systems, producing a detailed DTM using sparse field survey data appear to be neither reliable nor cost-effective.

The ground surface elevations can be represented in two types of models. Digital surface models (DSM) include the heights of the ground, buildings, trees, etc., whereas digital elevation (or terrain) models (DEM) includes only the bare earth surface without including buildings, trees and other above-ground features. In order to generate the DEM, the LiDAR point cloud data need to be classified into ground and non-ground points. The process of removing non-ground points from the LiDAR data is usually called filtering (Vosselman, 2000). Shan and Sampath (2005) categorized the filtering techniques used into two main approaches: labelling and adjustment. In the labelling approach, certain operators, for example a morphological operator, are used to identify LiDAR points which represent the ground surface. These results are then refined using an auto-regression process in the final step to remove forest coverage from the DEM. In the adjustment approach, an adjustment process based on a mathematical function of two dimensional polynomials is applied in the filtering process. The ground points are treated as a continuous surface and the non-ground points are detected based on distance from the ground surface.

To generate the final DEM surface, the discrete LiDAR points are interpolated to fill the gaps between LiDAR points so as to form a continuous DEM surface. According to Aguilar *et al.* (2005), the absolute accuracy of the surface model produced depends on three factors: the morphology filter, the density of the 3D points, and the methods of interpolation used. Types of interpolation methods and their effect on the accuracy of the generated DEM can be found elsewhere (Aguilar *et al.*, 2005). However, the

accuracy of the final DEM surface can be improved by increasing point density in order to eliminate interpolation errors (Hu *et al.*, 2009; Aguilar *et al.*, 2010). Practical tests performed by Al-Durgham *et al.* (2010) showed that an absolute accuracy from 2cm to 6cm is achievable.

### 3.3 Complementary Characteristics of LiDAR and Photogrammetry

LiDAR and photogrammetry are considered as the main sources of 3D data for many mapping applications. The main focus of any mapping project is to improve efficiency and reliability and also to reduce the cost of these projects (Mitishita *et al.*, 2011). LiDAR systems can provide direct 3D surface data at high levels of accuracy. However, they still cannot completely substitute for traditional data sources such as aerial and hyper-spectral images (Baltsavias, 1999; Liu *et al.*, 2007). Therefore, the advantages and limitations of each type of data are briefly described in the following sections.

#### 3.3.1 Advantages and Limitations of LiDAR Systems

Since LiDAR is an active data acquisition system, it has some advantages compared to photogrammetric methods. These advantages can be summarised as follows (Baltsavias, 1999; Shin *et al.*, 2007; Vosselman and Maas, 2010):

- LiDAR systems can operate in the day and at night, since they do not rely on other sources of illumination.
- LiDAR can provide direct dense 3D point cloud measurements, and can achieve up to 30 measurements/m<sup>2</sup>.
- LiDAR provides better elevation accuracy, which usually ranges from 5cm to 20cm.
- LiDAR is considered to be a very fast means for generating digital surface and elevation models.
- LiDAR systems involve high levels of automation during data capture and post-processing.
- LiDAR can penetrate sparse tree cover and canopy which is not very dense. This is very useful for forest applications in mapping the understory vegetation using multiple returns data.



- The use of LiDAR for mapping large blocks usually involves a minimal amount of ground surveying.
- In addition to 3D data, LiDAR can provide intensity information about the return pulses.

Despite the aforementioned advantages of LiDAR data acquisition techniques, they also entail some limitations which can be summarized as follows:

- The planimetric accuracy of LiDAR data is still lower than that provided by photogrammetric and surveying methods.
- LiDAR data suffer from a lack of semantic information.
- Geometric features such as building corners, edges, ridges and break lines are obtained indirectly after performing segmentation or classification processes.
- There is lack of inherent redundancy in LiDAR data.

### 3.3.2 Advantages and Limitations of Photogrammetric Methods

To overcome the limitations of LiDAR data, a new trend in research is to use photogrammetric methods alongside LiDAR data. However, photogrammetric methods also have advantages and drawbacks. The advantages can be summarized as follows (Baltsavias, 1999; Shin *et al.*, 2007; Vosselman and Maas, 2010):

- Photogrammetric data are rich in semantic information compared to LiDAR.
- Better planimetric accuracy is provided than with LiDAR data.
- There is also a high level of redundancy.
- Geometric features are directly and easily extracted from the aerial images.

However, despite these advantages, the limitations of photogrammetry can be summarized as following:

- Data can only be collected during daylight.
- Lower point height accuracy is provided than with LiDAR data.
- 3D data are indirectly obtained after image matching and triangulation.
- The matching procedures are sometimes complex and unreliable.

## 3.4 LiDAR and Photogrammetry Registration Methods

### 3.4.1 Overview

To overcome the limitations and drawbacks of data derived using each individual system, the trend has been to integrate these two data sets in order to obtain more accurate and reliable surface information (Baltsavias, 1999). The term ‘integration’ as defined by Rönnholm *et al.* (2007) means the fusion of two separate entities, resulting in the creation of a new entity. In order to successfully combine different datasets and to obtain reliable and accurate information, the registration process must be accurately performed since it plays a key role in the integration process (Rönnholm, 2011a).

The usual methodology for the integration and registration of LiDAR and photogrammetric data includes defining common reference features, establishing a mathematical relationship with the corresponding model, and undertaking similarity assessment which includes the transformation model (Habib *et al.*, 2005b). However, various factors can hinder the registration process for LiDAR and photogrammetric data. These factors can be described as follows (Wong and Orchard, 2008; Mishra and Zhang, 2012). Firstly, the selection of accurate and reliable reference conjugate control points from the two datasets may be problematic. Due to the different characteristics of the two datasets, easy and accessible targets in the aerial images could be difficult to observe in the LiDAR data. Secondly, the registration process can be improved using LiDAR intensity data. However, due to the differences between LiDAR intensity and optical imagery, it is sometimes difficult to find the optimum similarity between the two datasets. Thirdly, some registration methods use structural characteristics to determine the level of similarity between the two datasets. However, in the extraction of reliable structural targets such as edges and shapes which may look easy to identify from the aerial images, it is still difficult to perform the process using LiDAR data. Finally, the registration of raw images with LiDAR data will be contaminated by uncorrected errors in the aerial images, such as scale differences caused by relief displacement. Therefore, due to differences in the quality and density of the LiDAR data produced, a registration method must be selected based on the quality of information that could be obtained from the datasets involved (Rönnholm, 2011a).

### 3.4.2 Types of Registration Methods

Current registration methods are mainly based on the identification and extraction of common spatial features, such as points, lines and planar patches. According to Rönnholm (2011a), the extraction of common targets is usually performed employing three simple approaches as follows. Firstly, extraction may be based on common 3D features from the LiDAR and photogrammetric data. Secondly, 3D features from the LiDAR data are selected which match the 2D features from the photogrammetric data. Thirdly, all common features can be selected from the 2D LiDAR synthetic images and the 2D photogrammetric images. This is followed by determination of the parameters of the transformation required to align the two datasets, which is usually based on a 3D conformal transformation (Armenakis *et al.*, 2013).

From the three basic registration methods mentioned by Rönnholm (2011a), and also the methods used for registration as described by Mishra and Zhang (2012), the main registration methods currently used for photogrammetric and LiDAR data registration can be classified based on the type of features used in the registration process as follows.

#### 3.4.2.1 Feature-based Registration

Reference targets from the LiDAR surface, which are usually extracted using classification and segmentation techniques, are used as conjugate features in the registration process (Wang and Tseng, 2011). In this approach, the reliability of the registration process depends on the accuracy of the feature extraction process either from the aerial images or LiDAR data (Mishra and Zhang, 2012). These features can take the form of points, lines and planes.

**Point Features:** Due to the lack of sufficient semantic information in the LiDAR data, point features are usually extracted after defining existing geometric shapes such as buildings. The extracted point features could be building corners, as in Figure 3-7 (Mishra and Zhang, 2012), roof corners, or man-made or natural features manually extracted from the LiDAR intensity image (Habib *et al.*, 2005a).

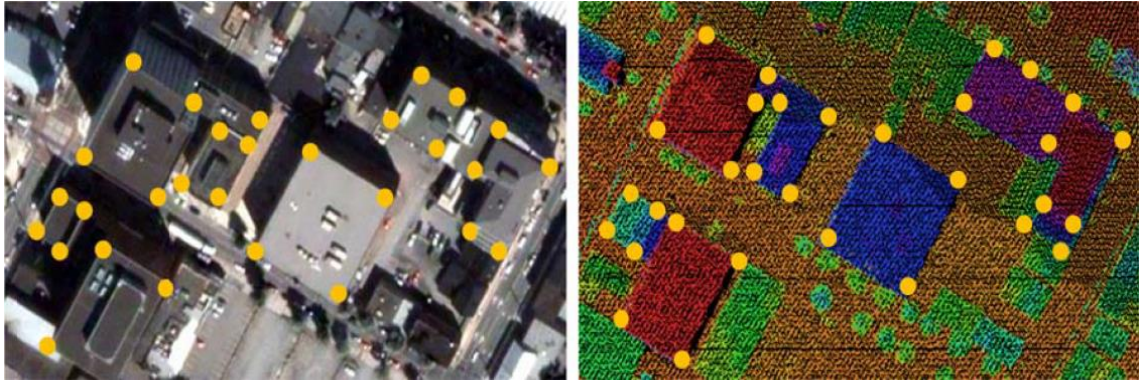


Figure 3-7 Left, building corners extracted from aerial images, right, building corners extracted from LiDAR data (Mishra and Zhang, 2012).

**Line Features:** Line features can be easily identified and extracted from aerial images. Using LiDAR data, however, straight lines are extracted either by intersecting two planes or through direct manual observation, as conjugate features in the registration process (Shin *et al.*, 2007). This method has been used by Habib *et al.* (2005c; 2011) where straight lines were used in the registration process, as shown in Figure 3-8.

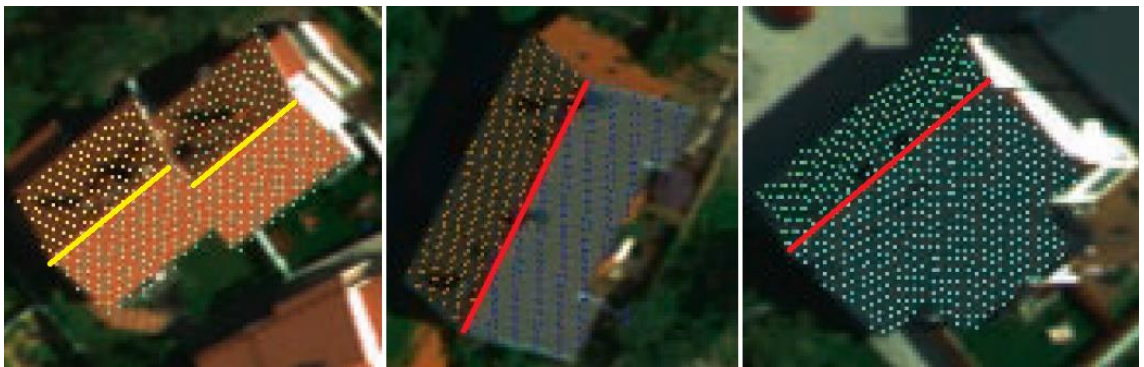


Figure 3-8 Straight lines extracted from LiDAR data and aerial images (Habib *et al.*, 2011).

**Planar Features:** Other methods of registration have used planes as common features, especially in urban environments where flat planes could be extracted using either an automatic or semi-automatic approach. Armenakis *et al.* (2013) used planes as the co-registration features between aerial images and LiDAR data. The planes are automatically extracted using a region-growing algorithm using the triangulated irregular network (see Figure 3-9). After plane extraction, the automatic identification of corresponding planes from the two datasets was performed. The final step was to

apply the registration process by obtaining the transformation parameters between the two datasets.



Figure 3-9 Plane matching method between aerial images and LiDAR point cloud (Armenakis *et al.*, 2013)

#### 3.4.2.2 Surface-based Registration

Surface-to-surface registration is also possible if both datasets can be interpolated into regular or irregular surfaces, with registration accomplished by minimizing either the vertical or Euclidean distances between the two datasets (Akca, 2007b). The photogrammetric DTM and DSM are generated using image matching techniques and the LiDAR surface is generated after the classification of the LiDAR point cloud as described in section 3.2.5.

This method can be performed automatically or manually. Automatic registration is usually achieved using either the least squares surface matching method (Ressl, 2011) or the ICP method (Böhm, 2011). In the manual method, the interactive orientation of the stereo images relative to the reference LiDAR surface is performed at different areas in the image block, where at least six areas are selected, as seen in Figure 3-10. The final step is to use the least squares method to determine the 3D rigid transformation parameters (Rönnholm, 2011b).



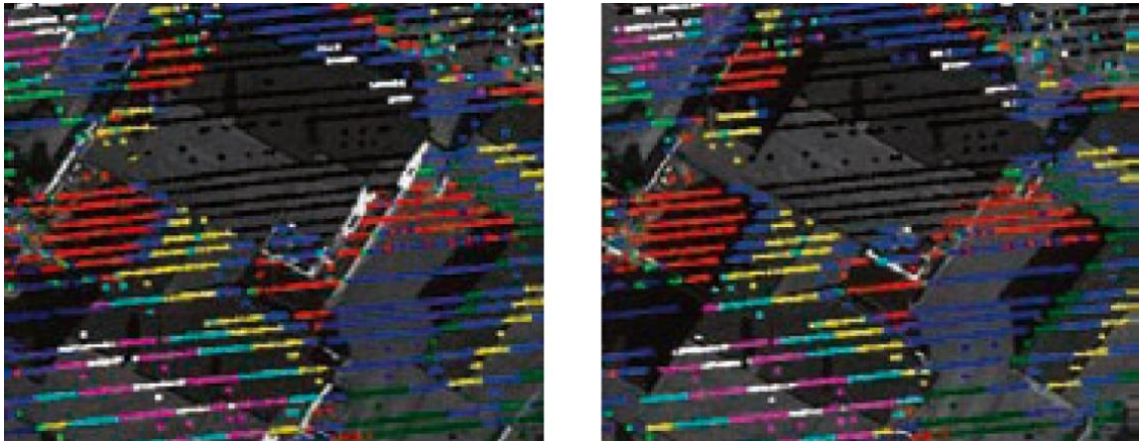


Figure 3-10 Manual registration of LiDAR and stereo images (Rönnholm, 2011b).

### 3.4.2.3 Intensity and Frequency-based Registration

The registration of aerial images and LiDAR data could also be achieved using correlational methods. These methods could either be intensity-based methods using cross-correlation techniques (Kekre *et al.*, 2011; Mooney, 2011), or frequency based methods using the fast Fourier transform (FFT) technique (Wong and Orchard, 2008; Mishra and Zhang, 2012). One example of the intensity based method was demonstrated by Mooney (2011). This method is based on generating 2D grey scale images from the LiDAR and photogrammetric DSMs. Then, cross-correlation is performed to identify the corresponding points from different areas in the DSMs. Finally, the 2D rigid transformation parameters are computed based on image coordinates of the selected corresponding points. Meanwhile, Wong and Orchard (2008) used the FFT method in frequency based registration. The method is based on the detection of control points and regions of interest using feature detectors from the two datasets (Figure 3-11), followed by finding the correspondence between the reference targets using structural linear features. Finally, the 2D translation and rotation parameters are computed.



Figure 3-11 Left, control point selection from optical image, right , LiDAR intensity image (Wong and Orchard, 2008).

#### 3.4.2.4 Summary of Registration Methods

The focus of the aforementioned description of registration methods was only on approaches used to register the aerial imagery with the reference LiDAR data. Other possible methods of registration used for medical, computer vision and close range photogrammetry are not directly relevant to this research. However, the quality of registration is strongly dependent on the process adopted (Rönnholm, 2011a). Moreover, a specific registration method might be suitable in one area, but could be unsuitable for other areas. Therefore, the advantages and drawbacks of different registration methods are summarized as follows (Mishra and Zhang, 2012).

*Feature-based Registration:* The advantages of these methods include that features can easily be identified and extracted either manually or automatically from LiDAR and photogrammetric data, and they are suitable for use in built-up areas. However, these methods may not be suitable for open areas where no buildings or linear features are available. Furthermore, methods of feature extraction are computationally expensive and manual selection and measurements may lack reliability.

*Surface-based Registration:* Most of these methods are based on the automatic registration of the LiDAR and photogrammetric surfaces. An exception is the manual method used by Rönnholm (2011b). According to Rönnholm (2011a) automation still plays an important role in achieving reliable registration results. Another advantage is that no feature extraction is needed, since the registration method is based on height variations in the two datasets. Moreover, these methods use all input data in the registration process. This provides high redundancy which allows the detection and elimination of outliers and the application of accurate statistical analysis, finally leading to more reliable registration results. The disadvantage is that these methods require height variations in the two datasets since they cannot be performed in flat areas.

*Intensity and Frequency-based Registration:* These methods are easy to implement and involve rapid computation. The disadvantages are that they provide low registration accuracy and the transformation parameters are limited to 2D rigid transformation which involves two shift parameters, one rotation angle and scaling.

## **3.5 Deriving Reference Control Points from LiDAR Data**

### **3.5.1 Introduction**

Due to their complementary characteristics, the integration of photogrammetry with LiDAR can potentially reduce overall costs and improve accuracy in many mapping applications (Liu *et al.*, 2007). LiDAR provides direct and highly accurate 3D elevation information which is both accurate and spatially dense (Postolov *et al.*, 1999). Moreover, continuing improvements in the accuracy of LiDAR systems have enabled the use of such data as a source of photogrammetric control (Habib *et al.*, 2005b). The usual methodology for using LiDAR as reference for photogrammetric control includes defining the reference features such as points, lines and plane features. These reference features must be accurately identified and extracted from the reference LiDAR and also the photogrammetric data (Shin *et al.*, 2007).

Aerial triangulation is a point-based process which allows the estimation of the exterior orientation parameters (EOPs) of camera stations. Since point features are still the main source of photogrammetric control in aerial triangulation (Habib *et al.*, 2006b), a number of different methods have been used to extract reference control points from LiDAR data for subsequent use in aerial triangulation. These methods include using



LiDAR point cloud data, LiDAR intensity images and shaded relief images from the LiDAR derived DSM. However, since a bundle adjustment is classically a point-based observation process, introducing other types of features such as straight lines and planes for photogrammetric control requires the adjustment of the mathematical model to accommodate these control features into bundle adjustment, as used by Jaw (1999) and Shin *et al.* (2007).

The following sections describe the different existing methods where LiDAR data are used as a source of control for image geo-referencing and camera calibration.

### 3.5.2 Reference LiDAR-derived Point Features

There are various methods used for extracting point-based features from LiDAR data. These differ due to the characteristics of the reference LiDAR data, which could be in the form of a raw LiDAR point cloud, LiDAR intensity image, LiDAR-derived DSM or LiDAR-derived shaded relief image. These methods can be summarised as follows.

#### 3.5.2.1 Centroids of Rectangular Building Roofs

Kwak *et al.* (2006) and Mitishita *et al.* (2008) used the centroids of rectangular building roofs as single control points with 3D coordinates in the aerial triangulation process. The approach used by Mitishita *et al.* (2008) was based on the manual measurement of building corners from the LiDAR intensity image followed by interpolation of the LiDAR point cloud into a regular grid. Then, only points located on the roofs of building are selected by examining the height differences between neighbouring points. The 3D coordinates of the centroid point is determined by calculating the mean values of X and Y coordinates and the point's elevation. In the image space, however, the coordinates of the image building centroid are computed using the formula for 2D straight line intersection using the 2D coordinates of the building corners extracted from the aerial image, as shown in Figure 3-12.

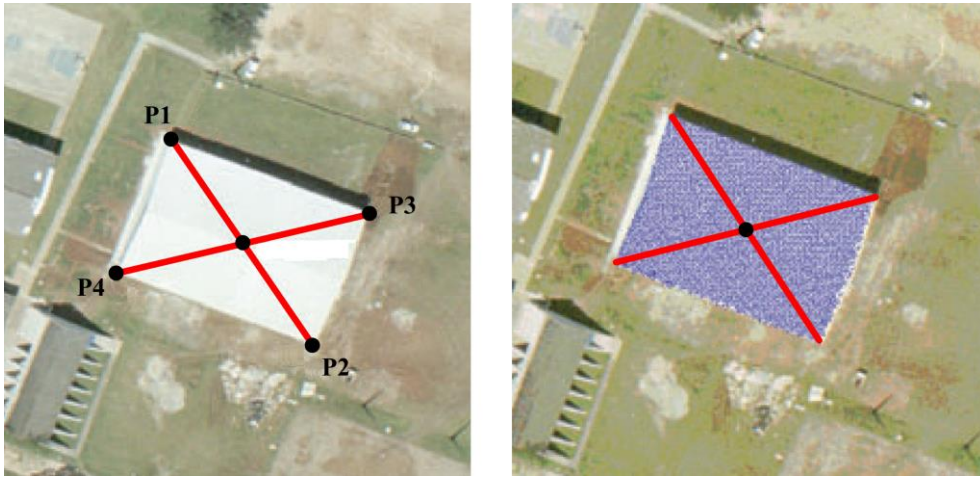


Figure 3-12 Left, centroid coordinates from aerial image, right, centroid coordinates from LiDAR point cloud (Mitishita *et al.*, 2008).

The same approach was used by Kwak *et al.* (2006). The only difference is in the point selection strategy used. The new selection strategy is based on the automatic detection of building edges and corners from the aerial images using the Canny edge detector (Canny, 1986). The image coordinates of the centroid point are computed using the straight line equation. For the LiDAR data, the building corners are detected using the local maxima filtering method. A detailed description of the building border detection method can be found elsewhere (Kwak *et al.*, 2006).

In real world applications, these methods seem to be applicable only in urban areas. Moreover, it is difficult to define the point of the centroid for complex and irregular roof structures.

### 3.5.2.2 LiDAR Intensity Image

Other methods of extracting point-based LiDAR-derived control points, as described by Habib *et al.* (2004a), Habib *et al.* (2004b), Liu *et al.* (2007) and Yastikli and Toth (2007), use the LiDAR intensity image. In this approach, reference control points are manually measured and extracted from LiDAR intensity images using identifiable and reliable ground objects, as shown in Figure 3-13.

However, the accuracy of reference control points may be adversely affected by errors introduced during manual measurement and the point density of the reference LiDAR point cloud. Moreover, difficulties were found in obtaining reliable reference points in flat and open areas.

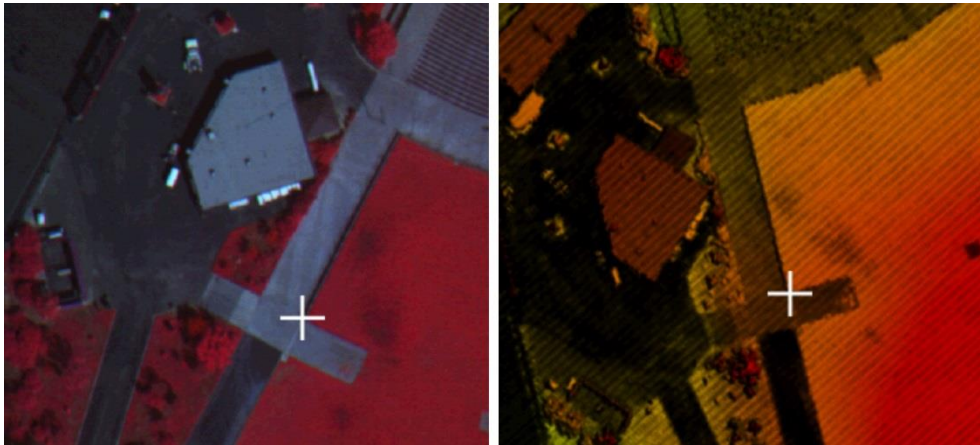


Figure 3-13 Left, control point in colour-infrared image, right, control point in LiDAR intensity image (Yastikli and Toth, 2007).

### 3.5.2.3 LiDAR Shaded Relief Image

Another method for identifying point-based reference targets was used by James *et al.* (2006). This approach uses a high resolution shaded LiDAR digital elevation model (DEM) to manually extract reference control points for use in establishing a photogrammetric model. However, a shaded relief image only provides features where height differences are present, such as at wall intersections in buildings and sharp changes in the terrain. Also, it seems impossible to acquire reference points in open featureless pasture areas and hillsides.

### 3.5.2.4 LiDAR Reference Targets

In some cases where LiDAR data are simultaneously captured alongside aerial images, the LiDAR reference targets used in LiDAR data processing and adjustment have also been used by some authors as vertical control points to control the photogrammetric blocks as they can be identified in both datasets. For example, Mitishita *et al.* (2012) performed camera calibration using a simultaneous image block adjustment for low-cost cameras and LiDAR datasets. This calibration methodology relied on using 3D coordinates of camera position stations as control points as well as signaled vertical control points to compute the camera's interior orientations.

However, since the LiDAR and image data were acquired simultaneously, this methodology did not apply any registration procedures between the LiDAR data and aerial imagery. Moreover, simultaneous data acquisition may not always be desirable

due to the different technical requirements associated with flying height or, for example, when night-time LiDAR missions are not suitable for image acquisition. Also, the specifications of LiDAR reference targets may not be suitable for all photogrammetric applications (Rönnholm, 2011a).

### 3.5.3 Linear Features

As with the LiDAR registration process described in section 3.4.2.1, linear features can be easily identified and extracted from aerial images whereas from LiDAR data they are extracted either by intersecting two planes or through direct manual observation as conjugate features in the registration process (Shin *et al.*, 2007). Habib *et al.* (2005b) directly incorporated linear features as a source of control in photogrammetric bundle adjustment. Details of the mathematical representation used in this method can be found elsewhere (Habib *et al.*, 2002; Shin *et al.*, 2007).

However, in this approach, large numbers of linear features with good spatial distribution are needed to achieve levels of accuracy similar to those achieved when using conventional control point patterns in the photogrammetric block (Mitishita *et al.*, 2008). Moreover, for large photogrammetric blocks, significant numbers of well-distributed linear reference targets may not be readily available.

### 3.5.4 Planar Patches

Jaw (1999), Jaw and Wu (2006) and Shin *et al.* (2007), for example, extended the photogrammetric model by establishing a new relationship among planar surfaces. These methods are based on minimizing the normal distance between the plane, which is defined by group of points measured from aerial imagery, and the LiDAR points, as shown in Figure 3-14.

Jaw (1999) and Jaw and Wu (2006) performed aerial triangulation by including reference planar patches as reference targets in addition to the ground control points. Meanwhile Shin *et al.* (2007) established the relationship between the photogrammetric plane measured in the image space with reference LiDAR points covered by the plane area. However, these methods use only height information from the LiDAR data and not the full X, Y and Z coordinates.

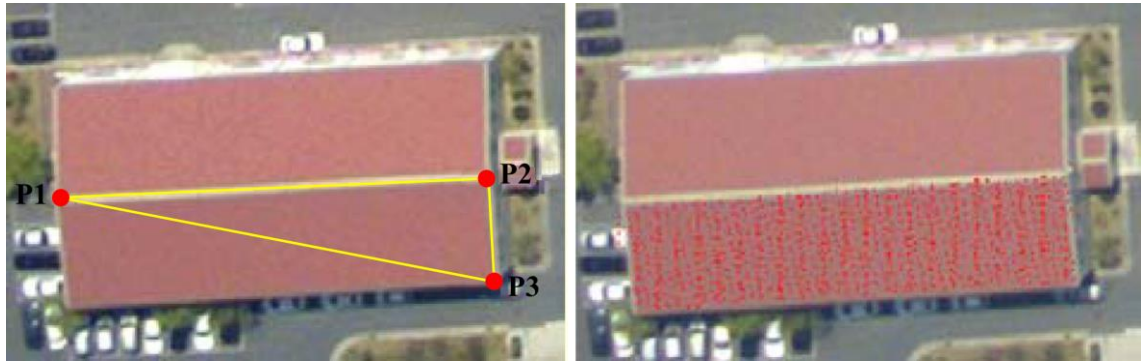


Figure 3-14 Left, image derived planar feature, right, reference LiDAR patches (Shin *et al.*, 2007).

### 3.6 Summary

This chapter has presented background information on airborne LiDAR technology, including the system components, working principles and types of laser scanning systems for data acquisition. This chapter has also briefly described the stages of LiDAR data processing, which include a pre-processing stage conducted by the system operator and post-processing stage accomplished by the end user. Part of the post-processing relating to the generation of the DEM from LiDAR data has also been discussed. Factors that affect the accuracy of the DEM generated were also addressed.

In addition, the complementary characteristics of LiDAR and photogrammetric data have been described, including the relative advantages and disadvantages of each data type. Moreover, a number of registration methods have been presented and discussed. These methods are classified based on the type of reference data used in the registration process. They include feature-based methods which include the use of points, lines or planes as registration targets. Conversely, surface-based methods register the two datasets based on variations in the height of surfaces. The final type of registration method is based on intensity and frequency information in the two datasets. The registration process uses 2D image correlation to recover misalignments between the two datasets. The strengths and weaknesses of each of these methods have been presented.

Methods of using LiDAR as a source of control for aerial image georeferencing and calibration have been addressed giving relevant examples. The control features have been classified into point-based, line-based and planar patch-based control features.

Based on the shortcomings of the control point extraction methods described, a new methodology is developed in this study to overcome these weaknesses. The methodology developed is based around an automatic least-squares surface matching algorithm. Chapter four introduces a detailed description of the research methodology developed to overcome some of the weaknesses present in existing methods. The new methodology is based on the registration of the dense photogrammetric point cloud surface with a LiDAR reference DTM, followed by the automatic extraction of point-based control points ready to be used for aerial triangulation and camera calibration.

---

## 4 Methodology

---

### 4.1 Introduction

The research methodology is based on the automatic registration of a dense photogrammetric point cloud derived through ISO and a reference LiDAR DTM. Chapter Three provided background information concerning the different registration methods used to integrate and register the photogrammetric data to the reference LiDAR dataset as well as methods for reference control point extraction from the LiDAR dataset. In current registration methods, LiDAR-derived reference control points are still based on feature extraction from the LiDAR data using either direct methods, such as measurement using the intensity image, or indirect methods such as the extraction of the features of buildings or computing shaded relief images from the LiDAR reference DTM. For controlling large photogrammetric blocks, these methods do not guarantee that large numbers of points can be extracted, nor that proper point distribution (which is a key element in achieving strong block accuracy) can be achieved. However, point distribution depends on the spatial distribution of existing and reliable reference features in the landscape.

The novel research methodology developed here consists of three main stages: firstly, computing the coordinates of the photogrammetric point cloud using ISO. Secondly, the photogrammetric points cloud are registered to the reference LiDAR DTM using the least-squares surface matching method which minimises the Euclidean distance between the two datasets. Finally, automatic extraction of LiDAR derived control points from the registered photogrammetric point cloud data followed by aerial triangulation and camera calibration using the derived reference points. The main advantages of this methodology are as follows: firstly, no dedicated calibration test field, or even ground

control, is necessary; secondly, all photogrammetric tie points are measured automatically to provide better point measurement accuracy; thirdly, any residual shifts, rotations or scale errors in the photogrammetric point clouds, caused for example by changes in camera parameters or errors in the GNSS/IMU data, will be (at least partly) recovered by the surface matching registration procedure; and finally, all extracted features are in point form, meaning data can be directly introduced into a bundle adjustment using any existing triangulation software - in this case, Leibniz Universität Hannover's BLUH software (Jacobsen, 2008). This chapter provides a detailed description of the different stages of the developed research methodology.

## 4.2 Methodology Workflow

The general workflow of the research methodology is illustrated in Figure 4-1. The main steps comprise: (a) a combined adjustment of the GNSS/IMU data together with image coordinates but without any GCPs (known as an integrated sensor orientation (ISO) process (Jacobsen, 2004)), to determine the initial coordinates of the photogrammetric point cloud; (b) the registration of the photogrammetric point cloud to the reference LiDAR surface using the least-squares surface matching method. The workflow can terminate (or end) at this stage if no refinement of camera calibration parameters is needed. The outcome will then only be the determination of object space coordinates from the photogrammetric data; (c) the automatic extraction of reference LiDAR control points (LCPs); (d) the refinement of camera calibration parameters using the derived LCPs in a full aerial triangulation. The whole procedure is performed in a semi-automated manner using an algorithm developed to bridge between BLUH and the surface matching algorithm.



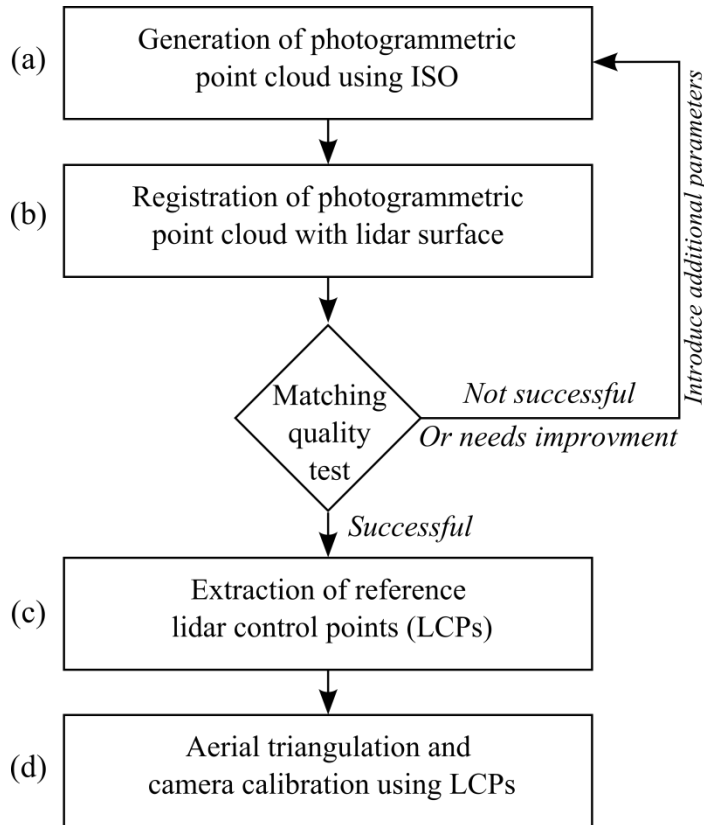


Figure 4-1 Main steps of the research methodology.

### 4.3 Matlab Algorithm

In addition to the general workflow diagram described in Section 4.2, details of the other functions performed using the algorithm developed in Matlab (version R2012a) are illustrated in Figure 4-2. The algorithm performs pre-match and post-match tasks, and the functions applied in each task can be summarised as follows:

#### 4.3.1 Pre-match Functions

As will be discussed in Section 4.4, the dense tie points are measured in SocetSet using the automatic point measurement module (APM). These measured points are then exported into an ASCII point file ready to be used by the BLUH bundle adjustment software. BLUH modules run in a DOS commands window, and therefore bundle adjustment is performed independently of the Matlab algorithm. However, to allow a smooth transition in the workflow, the Matlab algorithm is written so that it directly reads the output files generated by the BLUH software. These files include the BLUH list file for the point redundancy check, a point coordinate file for the matching process, and a detected blunders file for the selection criteria test.

The first task of the algorithm is to prepare the generated dense photogrammetric point cloud for the surface matching software. Since the matching will be performed using a LiDAR reference DTM file, the photogrammetric point clouds will be pre-processed in order to eliminate high points located over buildings or trees, as will described in Section 4.6. The algorithm reads the mask file and eliminates undesired points. The remaining points are then saved in an X, Y and Z ASCII file format ready to be read by the matching software.

### 4.3.2 Post-match Functions

After successful matching and registration between the photogrammetric point cloud and the reference LiDAR DTM, the Matlab algorithm is also written to automatically read the output files of the matching software. These files include the transformed photogrammetric points and corresponding residuals for each of the photogrammetric points. The transformed photogrammetric points are sorted and indexed using the point IDs since the matching software only uses the X, Y and Z coordinates.

In the point selection task, as will be described in Section 4.8, the algorithm reads the different data types required to apply the selection criteria for LCPs. Firstly, it reads data from the surface matching software, which includes the indexed and transformed point coordinates and the point residuals from the point residual file. Secondly, it reads the list of detected blunder points from the BLUH output files. Thirdly, it reads the DSM file to be used for the planarity test. Finally, it reads the input thresholds for the planarity and slope tests as defined by the user.

After reading the input data and the threshold values, the algorithm performs the selection criteria tests in the flowing order: (a) point residuals test; (b) reference surface planarity test; (c) reference surface slope test; (d) point redundancy check; (e) detected blunder list check. Finally, using the selected 'good' reference LCPs, the algorithm will perform the optimum point configuration procedure as described in Section 4.9.5. Each group of selected points is saved as a control point file in an ASCII format which is directly accepted by the BLUH software.

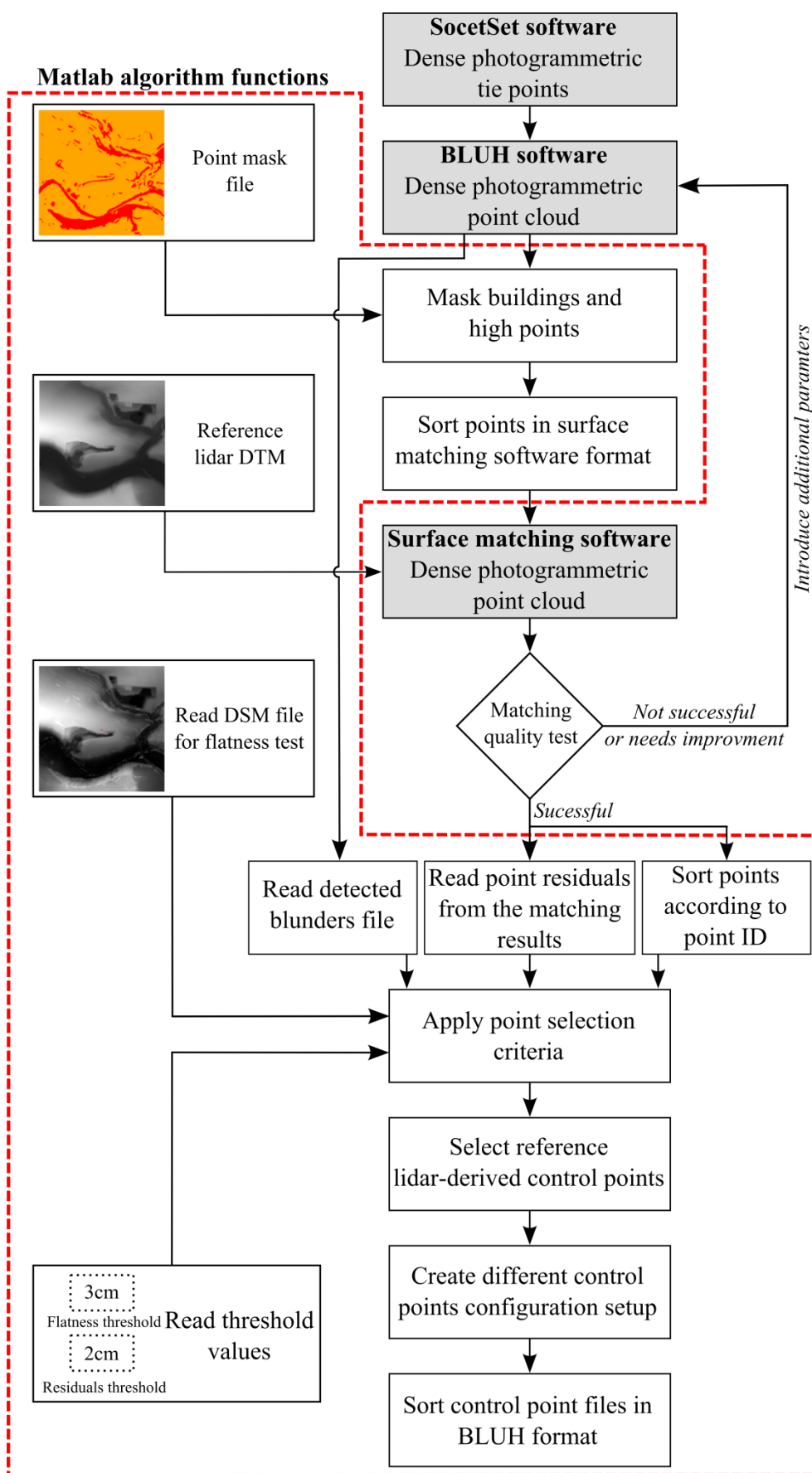


Figure 4-2 Functions performed with Matlab algorithm.

## **4.4 Point Measurement criteria**

The methodology begins with automatic dense tie point measurement of the photogrammetric block. This step was performed using BAE Systems SocetSet v5.4.1. Automatic image measurement provides higher measurement precision than manual observation, which helps improve height recovery which is typically degraded by the smaller B/H ratio characteristic of digital cameras (Alamús and Kornus, 2008). It also increases point density in order to provide a strong surface description for subsequently achieving optimised surface matching results.

### **4.4.1 Image Import and Pre-processing**

The first step in SocetSet before importing the aerial imagery is to create a project folder which contains all relevant information of the imagery utilized, including the coordinate system and datum to be used in the data processing. The aerial images are defined as frame digital camera images which are usually provided in TIF format. Camera interior orientation parameters were defined through the SocetSet camera file, which contains the information provided in the latest camera calibration report. During the import of the aerial imagery, the GNSS/IMU data for camera perspective centre coordinates were defined and provided in an ASCII file. These data of the image's station coordinates will be used in the block setup and definition.

### **4.4.2 Block Setup**

Before performing any point measurement, the image block needs to be defined. This includes specifying the number of image strips in the photogrammetric block, assigning images to be used in each individual strip and finally the image overlap for aerial data. Since the GNSS/IMU data were included in the image import, the software will automatically define the distance between the images. Block setup is configured using the multi-sensor triangulation model (MST) in SocetSet where the block strips are defined in top to bottom order.

### **4.4.3 Automatic Dense Point Measurement**

After block definition, the image coordinates of tie points in the overlapping images were measured using the automatic point measurement (APM) module. In SocetSet,

APM starts by selecting the strategy file for automatic point matching from the internal SocetSet database. This strategy file will guide the matching algorithm to perform fully automatic point measurement, since manual and semi-automatic point measurement methods are also available. The measurement process was accelerated by using the estimates of the exterior orientation parameters of the camera stations as defined during the import process (see section 4.4.1) to measure the tie point coordinates in different images. Also, in order to decide upon the number and configuration of the desired points, another file known as the point pattern file must be selected from the internal SocetSet database. This file defines for the APM the pattern of the desired tie point distribution in the overlapping image areas, and is used to control the locations of tie points.

The available pattern files in the existing SocetSet database provide a minimum of 3 X 3 point patterns (Figure 4-3) up to a maximum 141 point pattern. As these pattern files will not provide the dense tie points needed for the matching process, new pattern files were created. The new files provide a point pattern of 50 X 60 points per image, which will give a maximum of 30,000 point observations in the full overlapping block area, depending on the availability of reliable tie features.

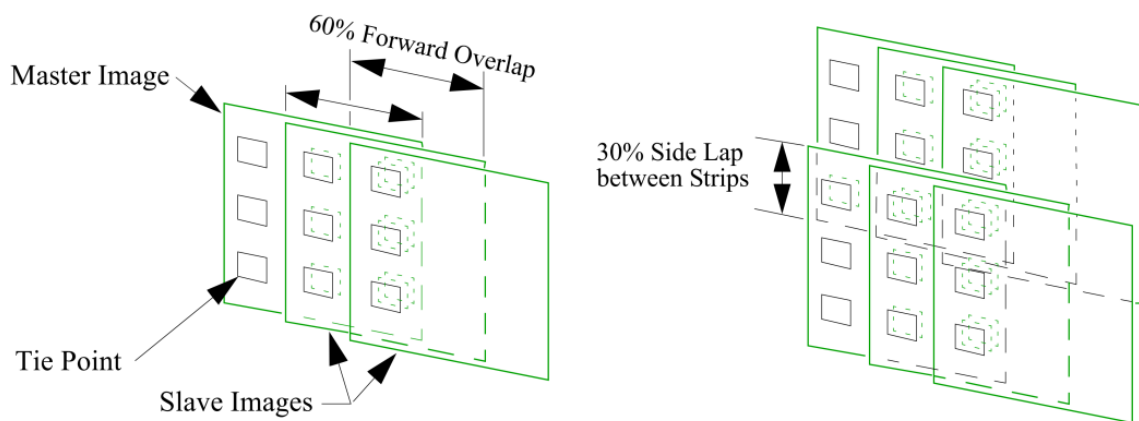


Figure 4-3 Example of automatic point measurement using the 3 x 3 pattern file with the standard 60% overlap and 30% sidelap (BAE Systems, 2007).

The image coordinates of all reference ground control points are then manually determined using the interactive point measurement (IPM) module. These points are introduced to be used as check points and also for performing reference calibration tests. These reference tests were used to validate the research methodology and results.

## 4.5 Reference LiDAR Data Processing

The LiDAR data used in this research consists of multiple strips. The data pre-processing, including the strip adjustment, was conducted by the data provider. In this research, post-processing was performed through the filtering and classification of the LiDAR data to produce the reference DTM file needed for surface matching registration. However, before using this data for methodology validation, it was necessary to investigate the relative and absolute accuracy of the LiDAR datasets using all available reference control points.

LiDAR data was processed using TerraScan software (Terrasolid, v013.008) in which point cloud data was filtered to remove non-ground points, such as buildings and vegetation. The filtering process in TerraScan software is performed using the progressive TIN densification filter developed by Axelsson (2000). As this produces many millions of points, which would be prohibitive and overly-redundant in terms of inclusion in the surface matching algorithm, the ground class was thinned and cleaned. A keypoints class, which represent the minimum number of points required to create the reference surface within the given accuracy, was extracted from the ground class and used to produce the reference DTM. To maintain the accuracy of the reference LiDAR data, the height tolerance used for extracting the model keypoints was set at  $\pm 5\text{cm}$ . Figure 4-4 shows an example of the keypoints extracted from the ground class. The extracted model keypoints are then used to create a thinned reference DTM model. Selection of the DTM surface rather than DSM was mainly driven by the hardware limitations, where the DSM requires more memory size to perform the Delaunay triangulation.

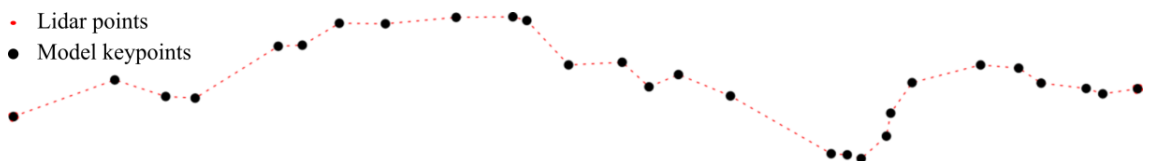


Figure 4-4 Model keypoint selection from reference LiDAR data.

## 4.6 Generation of Photogrammetric Tie Point's Mask

The photogrammetric point cloud was extracted in SocetSet using the automatic point matching method, thereby delivering a random distribution of dense tie points across the

aerial images. As a consequence, tie point features are located over different types of land cover. These include buildings, grass areas, roads, trees and other types of vegetation. In order to ensure that the photogrammetric points represent only the ground surface, tie points were filtered to remove all points located over buildings and woodland. Leaving these points in the matching process would cause the matching alignment to deteriorate by introducing anomalous regions with associated large residuals. Other features such as vineyards could not be eliminated since they represent large areas across the test site. Accordingly, it was necessary to deliver an approach which retained these features, so as to avoid any discontinuity in the photogrammetric surface description. Therefore, a thematic image mask was applied for areas exceeding 2.5 m above ground level. This was obtained by using a normalised digital surface model (nDSM) (Eq. 4-1), generated using the LiDAR-derived DTM and digital surface model (DSM), and was used to only omit points located over buildings and woodland..

$$nDSM = DSM - DTM \quad 4-1$$

$$\begin{cases} \text{for } nDSM > 2.5 & \text{Mask} = 1 \\ \text{for } nDSM < 2.5 & \text{Mask} = 0 \end{cases} \quad 4-2$$

Figure 4-5 shows typical features represented by the DSM and those represented by the DTM. It also shows areas included in the thematic image mask and as well as the photogrammetric tie points before and after the masking procedure.

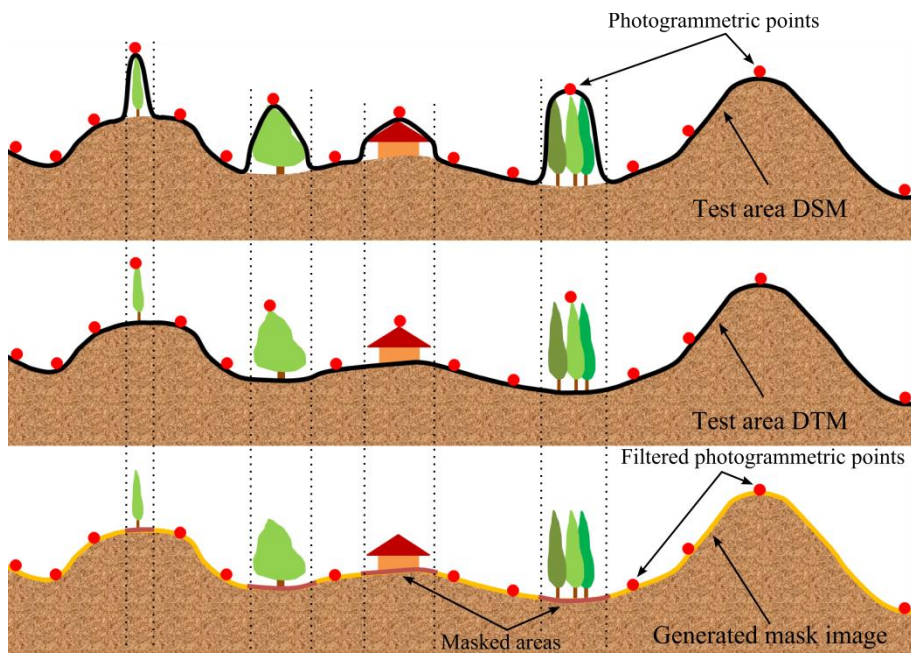


Figure 4-5 Tie point masking using normalised DSM mask image.

## 4.7 Integrated Sensor Orientation (ISO)

The ISO process includes simultaneous adjustment using GNSS/IMU data and the coordinates of the image tie points to obtain the 3D object coordinates of the dense photogrammetric point clouds. Introducing tie point coordinates into the solution minimises the RMSE of y-parallaxes and improves point quality without the need for GCPs in bundle block adjustment (Heipke *et al.*, 2002a). Moreover, adopting large image overlap provides strong block geometry and improves point height accuracy by increasing the number of rays per point observed on the ground (Ladstädter and Gruber, 2008). Increasing the number of rays also aids the removal of the effects of any remaining errors in the orientation parameters (Cramer and Stallmann, 2001). However, the main concern in ISO is that systematic errors in the GNSS/IMU measurements, or changes in the system calibration parameters between calibration and actual flight, may not be detected without the presence of GCPs (Heipke *et al.*, 2002a). The effects of these changes on the object coordinates will be recovered using the surface matching registration approach used in this research.

In the present study, large image overlap and sidelap is used in order to improve the photogrammetric point quality. This will also provide strong block geometry, so that blunders can be detected and eliminated, and errors in the orientation angles can also be minimized (Cramer and Stallmann, 2001).

The object coordinates of tie points are obtained by performing combined bundle block adjustment using the GNSS/IMU data and the image coordinates of tie points. This process is based on extrapolation from the image projection centres to the ground coordinates of tie points.

### 4.7.1 Bundle Block Adjustment Using BLUH Software

BLUH is a bundle adjustment software suite developed by the University of Hanover. Bundle adjustment is based on the collinearity equations (Eq. 4-3). The observations used in the bundle adjustment are the image tie point coordinates measured using SocetSet, and the GNSS/IMU data which represent the coordinates of the camera stations. In addition, the camera's interior orientation (IO) parameters are utilized and



provided through the camera calibration certificate. Ground control points are only used for validation purposes in the camera calibration test.

BLUH consists of different program modules used to perform different tasks, which finally lead to the computation of the bundle block adjustment. Figure 4-6 shows the sequence and task of each module. This includes the preparation of image point measurements into a format accepted by BLUH, computation of the approximate image orientations, blunder detection and elimination, sorting of the image coordinate input of the control data for bundle block adjustment, and finally computation of the bundle block adjustment.

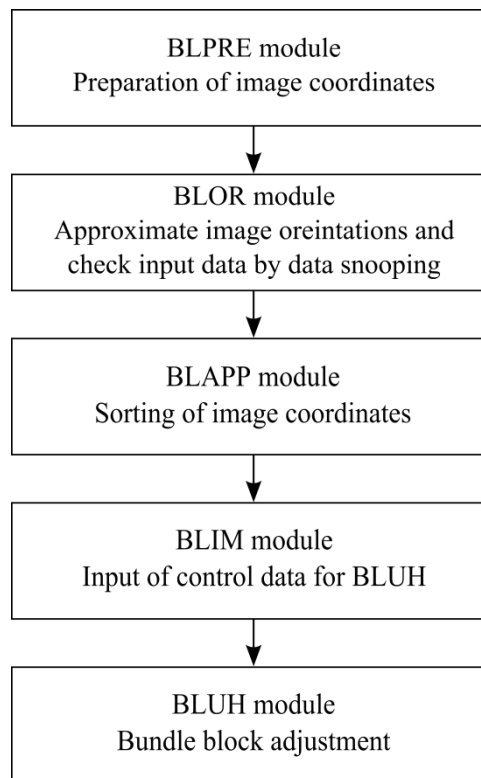


Figure 4-6 BLUH bundle adjustment configuration and dataflow, adapted from (Jacobsen, 2008).

**BLPRE:** Dense tie point image measurement was performed using SocetSet, and the input point measurements were transformed into BLUH standard format using the BLPRE module. Also, information about the camera focal length and coordinates of the principal point were defined in the standard data file.

**BLOR:** Since the collinearity condition requires the approximate image model coordinates to be generated before block adjustment (Mikhail *et al.*, 2001), the BLOR

module is used to compute the approximate image orientations. The computation starts by computing the relative orientations between images, then forming the individual block strips, transforming all strips into one block and finally transforming the block to the GNSS/IMU projection centres as control points were not used at this stage. The final step in BLOR is to perform blunder detection using data snooping. This method of error detection and elimination will be described in section 4.7.2.

**BLAPP:** After arranging the images into a defined block and performing blunder detection using data snooping, the BLAPP module will correct the detected blunders and collect them in the error correction list. Also, it sorts the image coordinates into a sequence which is used subsequently by BLUH.

**BLIM:** After image sorting, the BLIM module will define the input options for BLUH before running the bundle adjustment. These options include the input of the control data files such as ground control points and the GNSS/IMU data file. Also, weighting for the input data such as image measurements, ground control points and GNSS/IMU data are defined during the BLIM dialogue. Moreover, the option of using a robust estimator in bundle adjustment should be enabled during the BLIM dialogue (Section 4.7.2.2). In this methodology, where self-calibration is introduced into the bundle adjustment, the input self-calibration parameters are defined at this stage. These parameters include the standard BLUH 12 set of additional parameters and also other parameters used for the refinement of camera parameters such as focal length and principal point coordinates.

**BLUH:** Bundle block adjustment is performed using the BLUH module. In this program there is no dialogue; however, the computations are based on the input from other programs such as BLIM and BLAPP. The bundle adjustment in BLUH is based on the collinearity equations (Eq. 4-3). The known components in the present approach are the image coordinates of tie points, coordinates of camera stations represented by the GNSS/IMU data, coordinates of the principal point, and camera focal length. The unknown components are the object coordinates of tie points, refined camera parameters, and additional parameters in the case of self-calibration.

$$\begin{cases} X - X_L = (Z - Z_L) \frac{m_{11}(x - x_0) + m_{21}(y - y_0) + m_{31}(-f)}{m_{13}(x - x_0) + m_{23}(y - y_0) + m_{33}(-f)} \\ Y - Y_L = (Z - Z_L) \frac{m_{12}(x - x_0) + m_{22}(y - y_0) + m_{32}(-f)}{m_{13}(x - x_0) + m_{23}(y - y_0) + m_{33}(-f)} \end{cases} \quad 4-3$$

Where:

X, Y and Z are the object space coordinates.

x and y are the point image coordinates.

$X_L$ ,  $Y_L$  and  $Z_L$  are the object space coordinates of the camera station at the time of exposure.

$f$  is the camera focal length.

$x_0$  and  $y_0$  are the coordinates of the principal point

$m$  is the matrix of rotation angles.

#### 4.7.2 Blunder Detection

Gross error detection is mainly dependent on point redundancy and the direction of the error, which could be in x or y components. Points measured in a large number of images will be more error tolerant since errors can be detected and eliminated in either direction, x or y. Conversely, points with small numbers of rays will be less tolerant to gross errors since errors will be difficult to detect, or even if detected there will not be sufficient redundancy to correct the error. Figure 4-7 shows the error of incorrect measurement in two images only. Since the error is in the x direction, in this case it cannot be detected to provide possible solutions as the two rays will intersect.

Figure 4-8 shows as example of gross error in the y direction (across the base direction). In this case the errors are detected because the rays will not intersect when one point is incorrectly measured. These two types of errors show that points with two rays are less reliable than those measured in more than two images. Figure 4-9 shows error in the x direction in a point measured in three images. In this case, the error is detected but it is not possible to identify which measurement is in error, as any of the points might be correct and lead to one possible solution. Figure 4-10 shows error in the y direction when a point is measured in three images. In this case, the error is detected and also

identified since the erroneous point will not intersect with any other point. Therefore, that measurement can be eliminated from the adjustment.

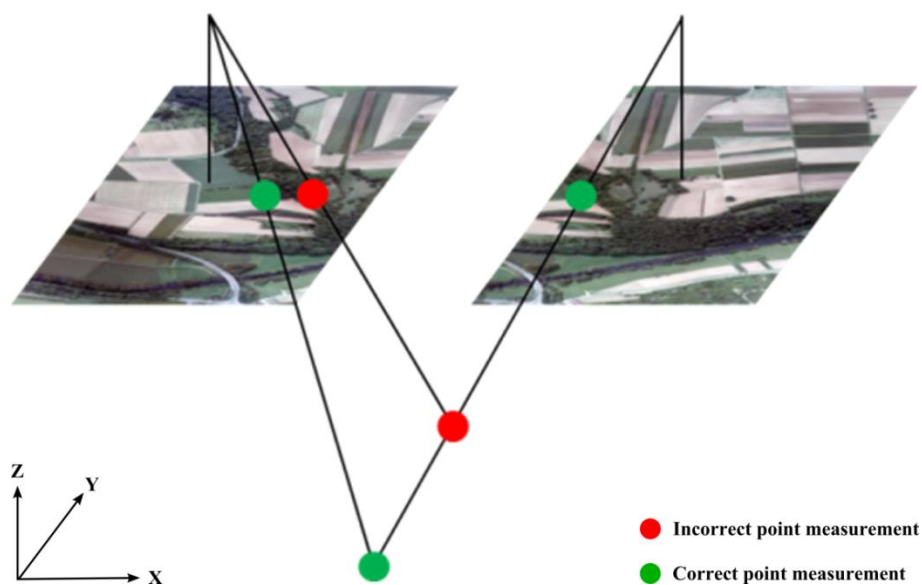


Figure 4-7 Error in x direction for a two-ray point.

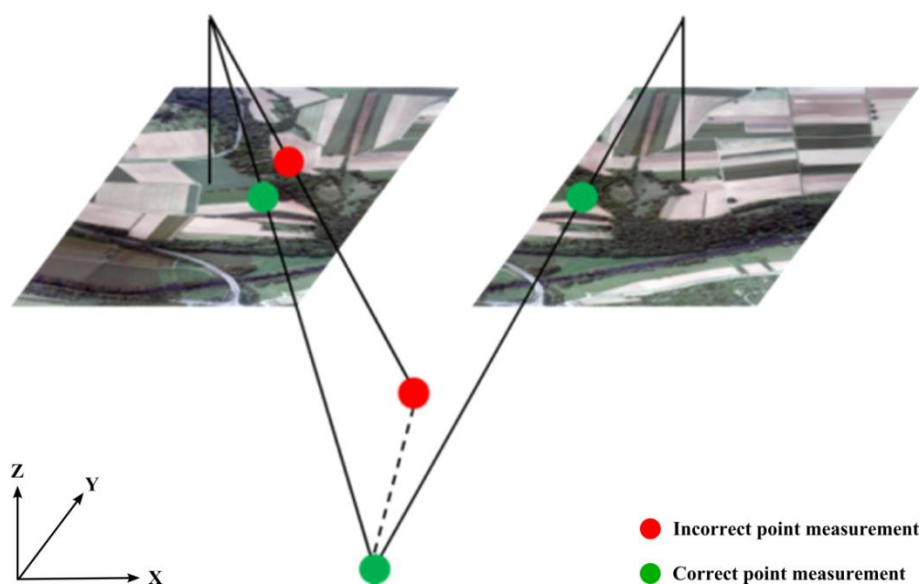


Figure 4-8 Error in y direction for a two-ray point.

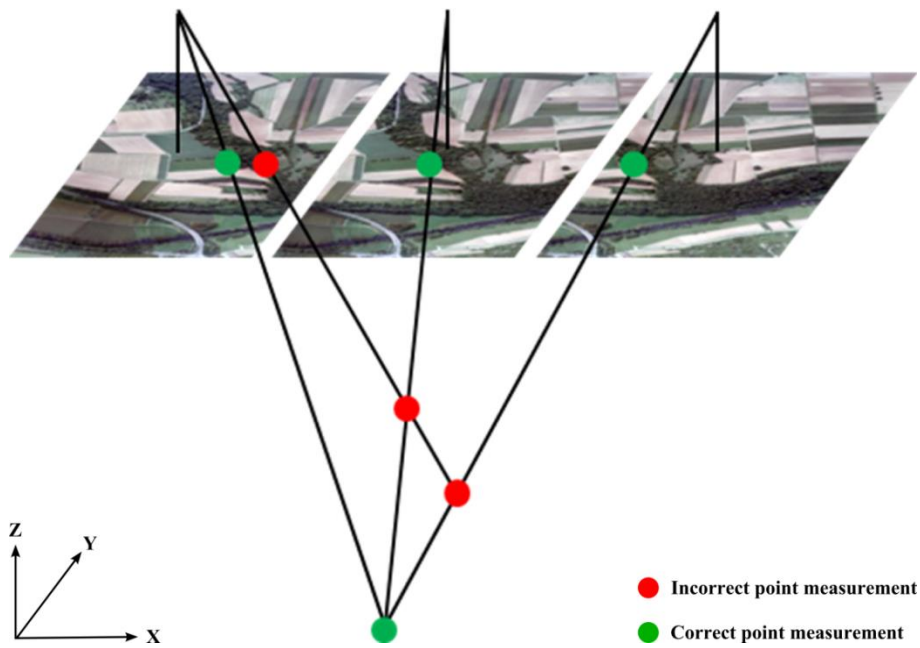


Figure 4-9 Error in x direction for a three-ray point.

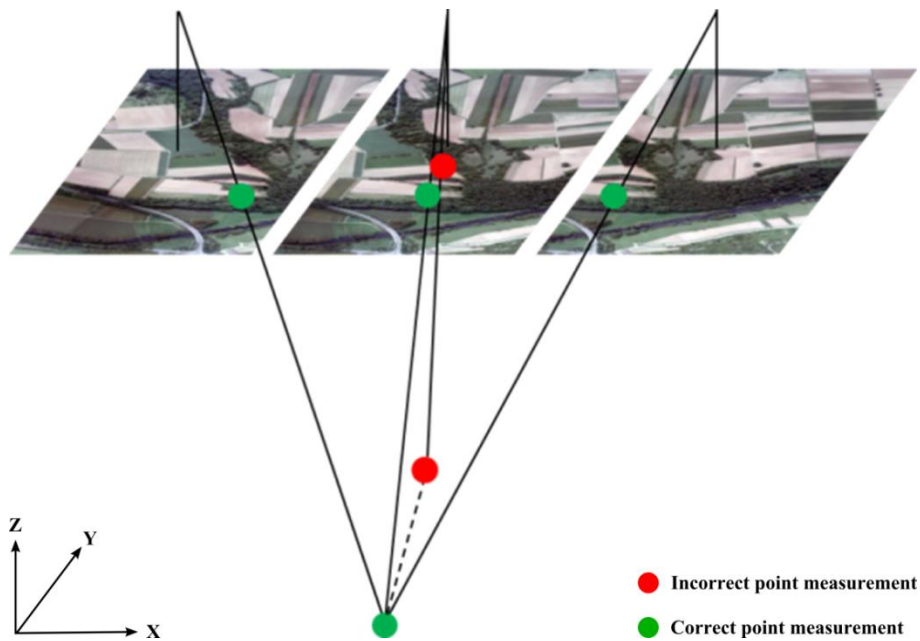


Figure 4-10 Error in y direction for a three-ray point.

In the approach used in this study, there was potential for a large number of blunders, due to the large number of tie points used in the bundle adjustment. Therefore, blunder detection and elimination was performed by BLUH in two steps: firstly, using data snooping during the approximate image orientation calculations using the BLOR

module; and secondly enabling the robust estimators in the first run of bundle block adjustment using the BLUH module.

#### 4.7.2.1 Blunder Detection Using Data Snooping

Data snooping is a process where the elimination of blunders is performed by examining the point residuals after adjustment. The Baarda method (Baarda, 1968) is used to detect blunders in the BLOR module while computing the image orientation.

This method, which implemented in BLUH (Jacobsen, 1998a), works by computing the partial redundancy  $r_i$ , which is defined as the relationship between the original error  $s_i$  and the correction  $v_i$  of an observation (Eq. 4-4), where:

$$v_i = -r_i \cdot s_i \quad 4-4$$

And the partial redundancy which is the redundancy number is computed by (Eq. 4-5):

$$r_i = (Q_{ee}P_{ee})_{ii} \quad 4-5$$

where

$Q_{ee}$  is the cofactor matrix of observations, and  $P_{ee}$  is the weight matrix of observations.

During the computation of relative orientations, the partial redundancy differs between the model centre of the block compared to the model corners. Therefore the normalised correction is computed (Eq. 4-6) with respect to the partial redundancy:

$$w_i = \frac{v_i \cdot \sqrt{P_i}}{\sqrt{r_i} \cdot \sigma} \quad 4-6$$

where

$w_i$	Normalised correction
$v_i$	Correction
$P_i$	Weight of observation $i$
$\sigma$	Standard deviation of unit weight

Finally, the limits of the possible blunder for each observation which can be included are computed by dividing the point correction by the point partial redundancy ( $v_i/r_i$ ).

#### 4.7.2.2 Blunder Detection Using Robust Estimators

BLUH also uses the robust estimators method to eliminate the effect of the remaining blunders after performing the data snooping process. In the robust estimator process, error elimination is performed by reducing the weight of observations which contain blunders to remove their effect on the bundle block adjustment. This process is performed in an iterative approach, where the point weight changes relative to the size of the point residual. The weight of defective observations will change at each iteration until they have no more influence on the adjustment. Also, the weight functions used by BLUH (Jacobsen, 1998a) can be determined using two methods. The first weighting function is known as the Danish method (Eq. 4-7) and the second is the special weighting function (Eq. 4-8).

$$P = e^{-\text{REA} \cdot \left(\frac{r}{\sigma_0}\right)^{\text{REC}}} \quad 4-7$$

where

<b>P</b>	Point weight
<b>r</b>	Maximum of the absolute values of the residuals of the <i>x</i> and <i>y</i> photo coordinates.
<b>σ<sub>0</sub></b>	Standard deviation of unit weight of the preceding iteration
<b>REA and REC</b>	Robust estimator's factors.

$$\begin{aligned} \text{for } V < 2 * \sigma_0 : \quad & P = 1.0 \\ \text{for } V > 2 * \sigma_0 : \quad & P = \frac{\sigma_0 * \sigma_0 * 4}{V * V} \end{aligned} \quad 4-8$$

As the first method requires a more stable block with good connection, the second method was used since it is more flexible and can be used with different block geometries. This is also the default function used in BLUH.

#### 4.7.2.3 Self-calibration Using BLUH 12AP

If the matching was not successful or falls below the expected accuracy, the ISO process is repeated to allow further improvement of the registration results through the

introduction of additional parameters in the bundle adjustment. Systematic image errors are determined by self-calibration with additional parameters in the bundle adjustment. These additional parameters are included in the adjustment as unknowns in order to find the difference between the mathematical model and the real image perspective geometry. This will remove any distortions from the aerial imagery and improve the tie point quality. The additional parameters are a standard BLUH 12 set designed to model physically justified effects such as radial lens distortion. These parameters are also designed to maintain the smallest correlation between the parameters, and are related to the specific existing physical problem, which is always the case when using polynomial expressions (Jacobsen, 1998a). These parameters (from P1 to P12) can be introduced into the bundle adjustment even without control points. The standard set of additional parameters used by BLUH is as follows:

P 1	$x' = x - y \cdot P1$	$y' = y - x \cdot P1$
P 2	$x' = x - x \cdot P2$	$y' = y + y \cdot P2$
P 3	$x' = x - x \cdot \cos 2b \cdot P3$	$y' = y - y \cdot \cos 2b \cdot P3$
P 4	$x' = x - x \cdot \sin 2b \cdot P4$	$y' = y - y \cdot \sin 2b \cdot P4$
P 5	$x' = x - x \cdot \cos b \cdot P5$	$y' = y - x \cdot P5$
P 6	$x' = x - x \cdot \sin b \cdot P6$	$y' = y - y \cdot \sin b \cdot P6$
P 7	$x' = x + y \cdot r \cdot \cos b \cdot P7$	$y' = y - x \cdot r \cdot \cos b \cdot P7$
P 8	$x' = x + y \cdot r \cdot \sin b \cdot P8$	$y' = y - x \cdot r \cdot \sin b \cdot P8$
P 9	$x' = x - x \cdot (r^2 - 16384) \cdot P9$	$y' = y - y \cdot (r^2 - 16384) \cdot P9$
P 10	$x' = x - x \cdot \sin(r \cdot 0.049087) \cdot P10$	$y' = y - y \cdot \sin(r \cdot 0.049087) \cdot P10$
P 11	$x' = x - x \cdot \sin(r \cdot 0.098174) \cdot P11$	$y' = y - y \cdot \sin(r \cdot 0.098174) \cdot P11$
P 12	$x' = x - x \cdot \sin 4b \cdot P12$	$y' = y - y \cdot \sin 4b \cdot P12$

where  $r^2 = x^2 + y^2$   $\arctan b = \frac{y}{x}$



As there is no advanced knowledge about image distortions or systematic errors, the complete set of additional parameters in the BLUH 12 standard set is immediately introduced in the BLIM module. Each of the introduced parameters are used to determine certain type of distortions in the image space as illustrated from Figure 4-11 to Figure 4-15. These parameters are assigned to each image strip individually due to the use of GNSS/MU data in the ISO process. To allow individual processing of each strip, a unique camera number is assigned to each strip in the photogrammetric block by the BLOR module. Different statistical tests will be performed during the bundle adjustment to test the significance of each single additional parameter as well as the total correlation and the correlations between these parameters. Insignificant additional parameters will be removed automatically from the adjustment by BLUH. The following figures show the effect of each of the BLUH 12 additional parameters on the image coordinates (Jacobsen, 2008).

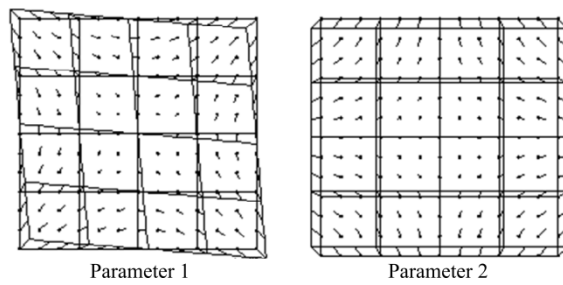


Figure 4-11 Parameter 1 for angular affinity, Parameter 2 for affinity.

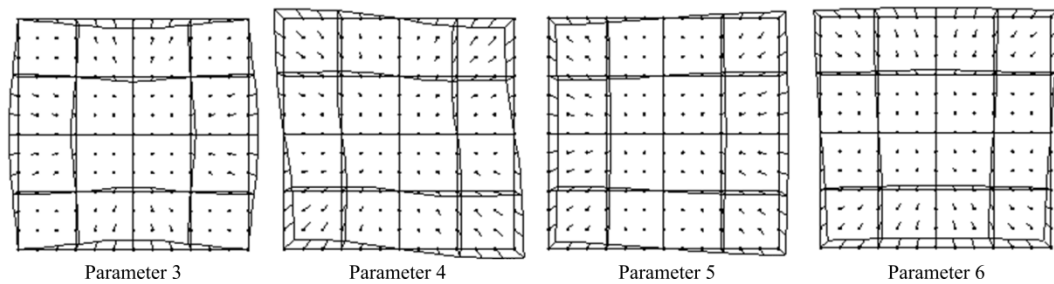


Figure 4-12 Parameters 3 - 6 for general deformation.

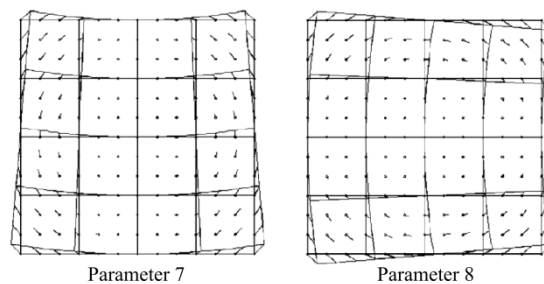


Figure 4-13 Parameters 7 and 8 for tangential distortion.

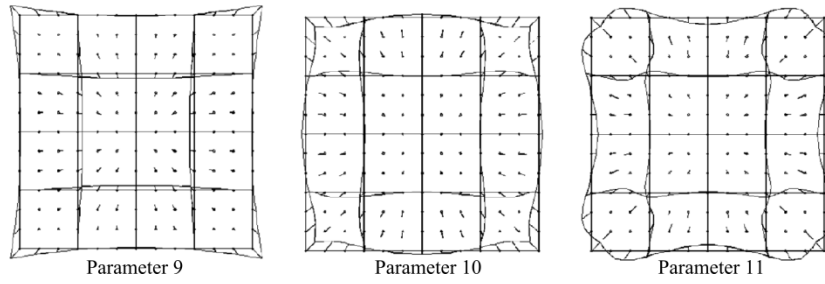


Figure 4-14 Parameter 9 for radial symmetric distortion, Parameters 10 and 11 for radial symmetric higher.

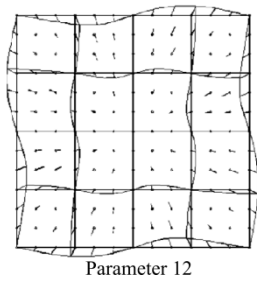


Figure 4-15 Parameter 12 for general distortion parameter.

## 4.8 Registration of Dense Tie Points to Reference LiDAR Surface

Registration of the photogrammetric points to the LiDAR reference DTM was performed using the in-house, robust surface matching software LS3D (Miller *et al.*, 2008). The software was initially developed and implemented by Buckley (2003) for change monitoring, and also to assess coastal change (Mills *et al.*, 2005). It was further improved by introducing the automatic down-weighting of outliers using iteratively re-weighted least squares (Miller *et al.*, 2008). The algorithm was later improved and rewritten in order to handle datasets of larger volume more effectively and was also adapted to minimize the Euclidean distance between the two surfaces in addition to the vertical distances (Kunz *et al.*, 2012).

Least squares surface matching minimizes the vertical or Euclidean distances between two surfaces to achieve the best possible alignment. The 3D conformal transformation solution based on seven transformation parameters is the most commonly used in surveying and photogrammetry (Dewitt, 1996). The benefits of this method are that it provides an automated registration procedure to register the reference LiDAR surface with the dense photogrammetric point clouds, it removes the need for physical control points and it allows the use of highly redundant LCPs. It is also a flexible method that can be used to match a dense reference LiDAR surface with less a dense surface or one

with sparse and well distributed point cloud data (Akca, 2007a). Pilgrim (1996) has pointed out other encouraging features of the least squares matching method, such as that it is well established in areas such as photogrammetric applications. It also provides a high degree of redundancy which enables statistical analysis of the transformation parameters to be performed and, moreover, this approach can be adapted to allow the weighting of input observations to achieve more robust results. Therefore, this weighting will be very useful to eliminate the effects of undetected blunders using the BLUH software.

#### 4.8.1 Three-Dimensional Conformal Transformation

LS3D minimises vertical or Euclidean distances using a point-to-surface approach to obtain the seven parameters of a 3D conformal transformation. These parameters as described by Wolf and Dewitt (2000) include three translations, three rotations and a scale factor ( $T_x, T_y, T_z, \omega, \phi, \kappa, S$ ). This three-dimensional conformal transformation is also known as the similarity transformation and is expressed as follows in Eq. 4-9:

$$\begin{bmatrix} X_l \\ Y_l \\ Z_l \end{bmatrix} = \begin{bmatrix} T_x \\ T_y \\ T_z \end{bmatrix} + SR(\omega, \phi, \kappa) \begin{bmatrix} X_p \\ Y_p \\ Z_p \end{bmatrix} \quad 4-9$$

where

$X_l, Y_l$  and  $Z_l$  are the final transformed coordinates of the registered photogrammetric data;

$T_x, T_y$  and  $T_z$  are the translation vector between the origin of the reference LiDAR DTM and photogrammetric point data;

$X_p, Y_p$  and  $Z_p$  are the coordinates of the unregistered photogrammetric data;

$S$  is the scale factor; and  $R(\omega, \phi, \kappa)$  is the 3D orthogonal rotation matrix.

The rotation matrix  $R$ , which represents the three rotations around the three axes  $x, y$  and  $z$ , is expressed as follows:

$$R = \begin{bmatrix} m_{11} & m_{12} & m_{13} \\ m_{21} & m_{22} & m_{23} \\ m_{31} & m_{32} & m_{33} \end{bmatrix} \quad 4-10$$

Where

$$\begin{aligned} m_{11} &= \cos \varphi \cos \kappa \\ m_{12} &= \sin \omega \sin \varphi \cos \kappa + \cos \omega \sin \kappa \\ m_{13} &= -\cos \omega \sin \varphi \cos \kappa + \sin \omega \sin \kappa \\ m_{21} &= -\cos \varphi \sin \kappa \\ m_{22} &= -\sin \omega \sin \varphi \sin \kappa + \cos \omega \cos \kappa \\ m_{23} &= \cos \omega \sin \varphi \sin \kappa + \sin \omega \cos \kappa \\ m_{31} &= \sin \varphi \\ m_{32} &= -\sin \omega \cos \varphi \\ m_{33} &= \cos \omega \cos \varphi \end{aligned} \quad 4-11$$

In order to perform the least-squares solution, redundant observations for each photogrammetric point are obtained using the following equations:

$$\begin{aligned} X_l &= s(m_{11}X_p + m_{21}Y_p + m_{31}Z_p) + T_x \\ Y_l &= s(m_{12}X_p + m_{22}Y_p + m_{32}Z_p) + T_y \\ Z_l &= s(m_{13}X_p + m_{23}Y_p + m_{33}Z_p) + T_z \end{aligned} \quad 4-12$$

These equations are then linearized using the Taylor's series expansion and solved using least squares which expressed in a matrix form as follows:

$$AX = L + V \quad 4-13$$

where  $A$  is the design matrix,  $X$  is the vector of parameter correction,  $L$  is the vector of differences between start values and current values, and  $V$  is a residual vector.

### 4.8.2 Surface Matching Theory

Surface matching, as applied in the field of Geomatics, is usually based on least-squares adjustment which minimises the sum of squares of the vertical and/or Euclidean distances between two surfaces (Buckley, 2003). The mathematical concepts underlying matching theory are described in detail by Rosenholm and Torlegard (1988); Akca (2007a); Buckley (2003) and Miller (2007). Brief details of the matching approach implemented by Buckley (2003), Miller (2007) and (Matthias, 2013) are given below.

Two conjugate points from the two surfaces are identified:  $P_1$  located at  $(X_1, Y_1, Z_1)$  on surface  $S_1$ , which in the present research is the LiDAR reference surface; and  $P_2$  located at  $(X_2, Y_2, Z_2)$  which is the photogrammetric point cloud data denoted as  $S_2$ . The reference surface representation is carried out using a triangulated irregular network (TIN), which can be described as planar surface elements. The TIN is established by reading the XYZ ASCII file of the reference LiDAR DTM. For each point on the surface to be matched (i.e. photogrammetric tie points), the coordinates of corresponding reference LiDAR surface points are interpolated on the reference surface (Figure 4-16). A planar interpolation approach is used as it will provide more reliable results with less interpolation error than a polynomial approach (Mitchell, 1994).

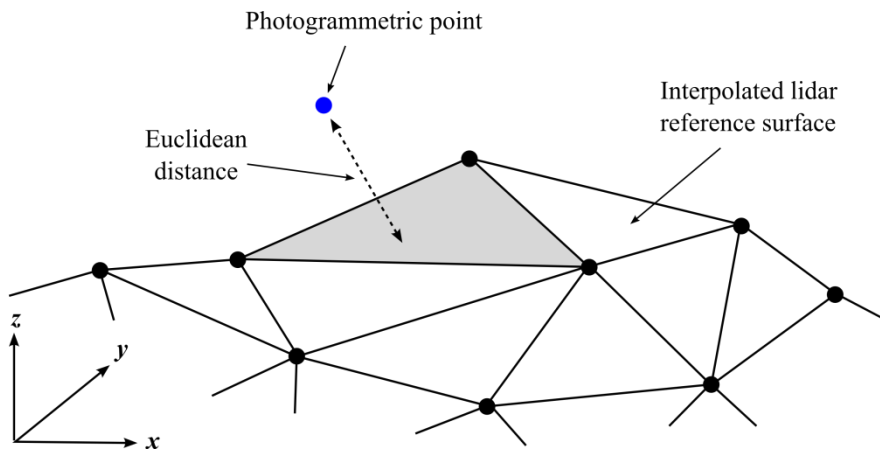


Figure 4-16 Planar interpolation of the reference surface.

The transformation of  $(X_p, Y_p, Z_p)$  into the object space of  $(X_l, Y_l, Z_l)$  is achieved using a set of 7 transformation parameters  $p = \{p_i\}$ , where  $p_i = p_i^0 + \Delta p_i$ , and the distance between the two surfaces should be zero, and the minimization is expressed as follows:

$$\sum_{i=1}^m d_i^2 \rightarrow \min \quad 4-14$$

Where  $d^2$  denotes the squared differences between the photogrammetric point cloud and LiDAR interpolated plane which represent point-to-plane approach. This plane is defined in the Euclidean space as follows:

$$S_1(x, y, z) = Ax + By + Cz + d \quad 4-15$$

The normal vector to the plane is defined as:  $\vec{n} = \begin{pmatrix} A \\ B \\ C \end{pmatrix}$

The three points that form the corresponding triangle are used to derive the plane equation. And the corresponding point on the LiDAR plane is computed using linear interpolation. To achieve the correct alignment between the two dataset, the Euclidean distance between photogrammetric points and corresponding plane must be minimized which satisfies the functional model as follows:

$$S_1(x, y, z) = S_2(x, y, z) + v(x, y, z) \quad 4-16$$

Therefore, the distance between the photogrammetric point and the reference LiDAR surface along the surface normal  $\vec{n}$  of the plane is computed as follows:

$$d = \frac{|\vec{n} \cdot w|}{|\vec{n}|} \quad \text{with } w = \begin{pmatrix} x_{\Delta x} - x \\ y_{\Delta y} - y \\ z_{\Delta z} - z \end{pmatrix} \quad 4-17$$

where  $d$  is a component of  $w$  along  $n$  and can be written as:

$$d = \frac{|Ax_{\Delta x} + By_{\Delta y} + Cz_{\Delta z} + D|}{\sqrt{A^2 + B^2 + C^2}} \quad 4-18$$

Where  $x_{\Delta x}, y_{\Delta y}, z_{\Delta z}$  denotes the functions of the transformation parameters  $p_i \in \{T_x, T_y, T_z, \omega, \phi, \kappa, s\}$ . In order to minimize the Euclidian distance, the equation 4-18 is linearized using Tylor expansion as follows:

$$\frac{\delta d}{\delta p_i} = \frac{\delta d}{\delta x} \frac{\delta x}{\delta p_i} + \frac{\delta d}{\delta y} \frac{\delta y}{\delta p_i} + \frac{\delta d}{\delta z} \frac{\delta z}{\delta p_i} = \nabla x \cdot dx + \nabla y \cdot dy + \nabla z \cdot dz \quad 4-19$$

where  $\nabla$  denotes the surface gradient for the Euclidean case in the three directions of  $x, y, z$ , and are expressed as:

$$\begin{aligned}\nabla x &= \frac{A}{\sqrt{A^2 + B^2 + C^2}} \\ \nabla y &= \frac{B}{\sqrt{A^2 + B^2 + C^2}} \\ \nabla z &= \frac{C}{\sqrt{A^2 + B^2 + C^2}}\end{aligned}\tag{4-20}$$

Differentiation of Equation (3.9) gives:

$$\begin{aligned}dx &= dT_x + a_{10}ds + a_{11}d\omega + a_{12}d\varphi + a_{13}d\kappa \\ dx &= dT_x + a_{20}ds + a_{21}d\omega + a_{22}d\varphi + a_{23}d\kappa \\ dx &= dT_x + a_{30}ds + a_{31}d\omega + a_{32}d\varphi + a_{33}d\kappa\end{aligned}\tag{4-21}$$

where the  $a_{ji}$  are the coefficient terms:

$$\begin{aligned}a_{10} &= m_{11}x_p + m_{21}y_p + m_{31}z_p \\ a_{20} &= m_{12}x_p + m_{22}y_p + m_{32}z_p \\ a_{30} &= m_{13}x_p + m_{23}y_p + m_{33}z_p \\ a_{10} &= 0 \\ a_{12} &= s(-\sin \varphi \cos \kappa x_p + \sin \varphi \sin \kappa y_p + \cos \varphi z_p) \\ a_{13} &= s(m_{21}x_p - m_{11}y_p) \\ a_{21} &= s(-m_{13}x_p - m_{23}y_p - m_{33}z_p) \\ a_{22} &= s(-\sin \omega \cos \varphi \cos \kappa x_p - \sin \omega \cos \varphi \sin \kappa y_p + \sin \omega \sin \varphi z_p) \\ a_{23} &= s(m_{22}x_p - m_{12}y_p) \\ a_{31} &= s(m_{12}x_p + m_{22}y_p + m_{32}z_p) \\ a_{32} &= s(-\cos \omega \cos \varphi \cos \kappa x_p - \cos \omega \cos \varphi \sin \kappa y_p - \cos \omega \sin \varphi z_p) \\ a_{33} &= s(m_{23}x_p - m_{13}y_p)\end{aligned}\tag{4-22}$$

The observation equations can now be formed to solve the equation 4-16 as follows:

$$\begin{aligned}
d + v(x, y, z) = & \nabla x \cdot dT_x + \nabla y \cdot dT_y + \nabla z \cdot dT_z \\
& + (\nabla x \cdot a_{10} + \nabla y \cdot a_{20} + \nabla z \cdot a_{30})ds \\
& + (\nabla x \cdot a_{11} + \nabla y \cdot a_{21} + \nabla z \cdot a_{31})d\omega \\
& + (\nabla x \cdot a_{12} + \nabla y \cdot a_{22} + \nabla z \cdot a_{32})d\phi \\
& + (\nabla x \cdot a_{13} + \nabla y \cdot a_{23} + \nabla z \cdot a_{33})d\kappa
\end{aligned} \tag{4-23}$$

With this equation, one observation is formed for every point in the photogrammetric surface,  $S_2$ . These equations are then solved using least squares as specified in Eq. 4-13. Where the approximated transformation parameters are applied to the photogrammetric data until the convergence between the two datasets is achieved. The iterations will continue until the changes in the corrections of the estimated transformation parameters and also the reference standard deviations are considered as insignificant (Matthias, 2013).

### 4.8.3 Robust Estimation

In the surface matching method, the detection and elimination of outliers is a crucial task if reliable matching results are to be achieved. Before the matching process, outliers must be detected and eliminated, and this can be performed either using data snooping or robust estimators. Data snooping was used by Karras and Petsa (1993) before the least-squares surface matching process for deformation detection in medical applications. However, this kind of basic method may only eliminate one outlier at a time, which may not be suitable for a large number of redundant observations as in the present approach. In this regard, the surface matching software has been enhanced by introducing the automatic down-weighting of outliers to make the solution more robust with respect to outliers (Miller *et al.*, 2008). The robust estimation function is implemented by including the weight matrix in the matching process through the technique of iteratively reweighted least squares (IRLS). This technique enables automated robust estimation, since it will reduce and eliminate the influence of less reliable observations by altering the weights of observations during every adjustment iteration. Wager *et al.* (2005) suggested that the IRLS technique can be used to incorporate the weighting function in the following way. Firstly, the proper weighting scheme must be selected. In LS3D, the weighting scheme is based on the Biweight function as defined in Eq. 4-24:



$$w_b(u) = \begin{cases} (1 - u^2)^2 & |u| \leq 1 \\ 0 & |u| > 1 \end{cases} \quad 4-24$$

where  $w_b$  are the weights computed from the standardised least-squares residuals ( $u$ ).

The initial residuals must be obtained in the first iteration using un-weighted ordinary least-squares regression. From the second iteration, the robust weights are computed based on the standardised residuals and are placed on the diagonal of the weight matrix. The standardised residuals are computed using the following equations:

$$u_i = \frac{r_i}{c \cdot S} \quad 4-25$$

where  $c$  is the M-estimator tuning constant which was fixed to  $c = 4.685$  (Miller, 2007).  $S$  is the robust variance computed from the normalised  $MAD$ , where both quantities are computed using Eq. 4-26 and 4-27. To take account of different leverage of observation, the adjusted least squares residual  $r_i$  is computed as follows (Hoaglin and Welsch, 1978):

$$MAD = \text{med}|r_i - \text{med}(r_i)| \quad 4-26$$

$$S = \frac{MAD}{0.6745} \quad 4-27$$

$$r_i = \frac{v_i}{\sqrt{(1 - h_i)}} \quad 4-28$$

where the  $h$  is the diagonal elements of the Hat matrix,  $H$ .

Subsequent iterations use the least squares estimates with the new weight matrix as mentioned above until the convergence is detected by LS3D. Details of other computational aspects of the robust estimators and methods of matrix decomposition can be found elsewhere (Miller, 2007).

## 4.9 LiDAR Control Point Selection Strategy

Software was developed in Matlab to perform the automatic extraction of reliable LiDAR-derived control points (LCP). These points were then used to perform aerial triangulation and camera calibration. The algorithm also controls all of the steps of the methodology by performing pre-match and post-match tasks. In the pre-match task, the

ground coordinates of the photogrammetric point clouds computed by the BLUH bundle adjustment software are filtered using the thematic image mask detailed in Section 4.6. Points determined to be located over buildings or woodland areas are automatically removed. Finally, points are sorted, indexed and saved into two separate files in X, Y and Z format for the matching algorithm, and ID, X, Y and Z format as the reference point list file. In the post-matching step, the output files of the surface matching software, which contains the transformed and registered points cloud data, are read and re-indexed using the reference point list file. At this stage, if the matching is not successful or accuracy is low, a new surface matching run will commence after improving the photogrammetric point quality by introducing a self-calibrating bundle adjustment in the BLUH software and repeating the pre-match task for the new set of photogrammetric points. On the other hand, if the matching is successful, the algorithm will start the LCP selection procedure. This procedure includes various different tests, as summarised below.

#### 4.9.1 Distance Test

Points located in the “best” matched areas, defined as those with the smallest residuals, are initially selected. Since the accuracy of the provided reference GCPs used in this research is 2 cm (Cramer, 2010), a threshold of  $\pm 2$  cm was set as a maximum residual Euclidian distance (Figure 4-17).

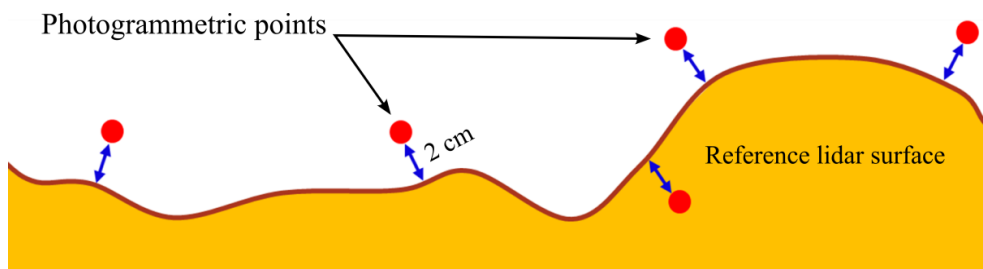


Figure 4-17 Matching residuals with 2 cm threshold.

Information about the matching residuals is obtained from the post-match file, which provides the coordinates of each transformed point, those of the corresponding interpolated LiDAR point, the point residual. The developed Matlab algorithm reads the values of these residuals for each point after reassigning each point ID.

### 4.9.2 Planarity Test

From the points initially selected on the basis of the  $\pm 2$  cm Euclidean distance threshold, to further minimise the potential for erroneous point selection, only points located over planar areas are retained. These criteria, as for the subsequent slope test, are based on classical best practice of selecting height control points in the field, ensuring points are located in well defined, flat areas (Hodgson and Bresnahan, 2004). As surface roughness is better described by the DSM than the DTM, an external DSM file was used for measuring planarity by finding the best-fit plane of a 3 x 3 pixel (0.25 m) window from the DSM surrounding each point (Figure 4-18).

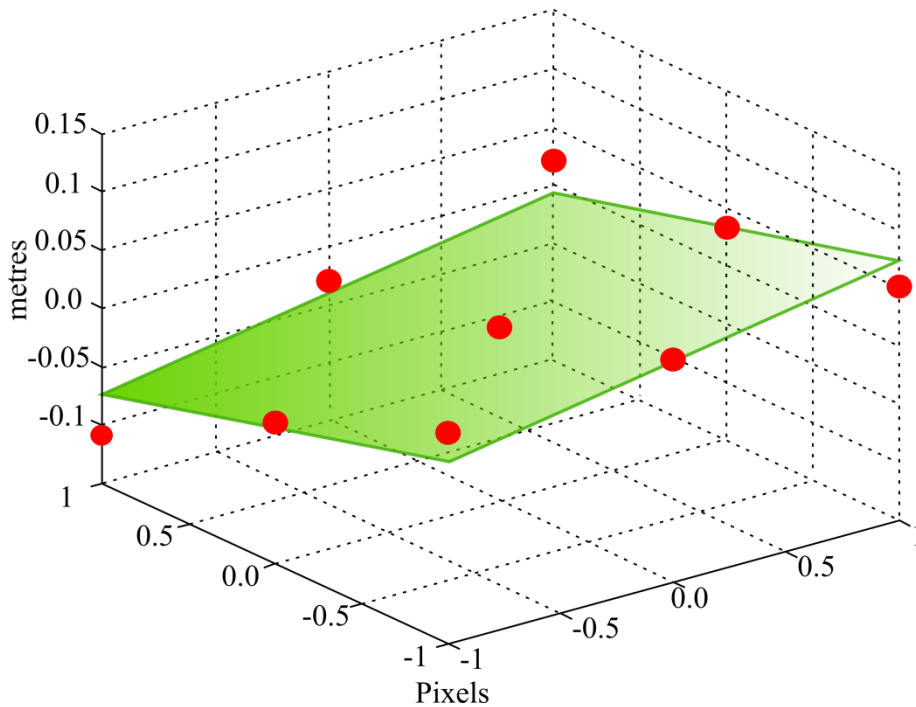


Figure 4-18 Best fit plane for 3 x 3 window.

The best fitting plane for the pixels surrounding each photogrammetric point is determined using the Matlab least squares plane estimation algorithm. The plane equation is formulated as follows:

$$Ax + By + Cz + D = 0 \quad 4-29$$

The best fit is computed by minimizing the sum of squared distances from each grid point to the fitting plane window from the DSM file surrounding each point. The Euclidean distance from each grid point to the best fitting plane is computed as follows:

$$d_i = \frac{|Ax_i + By_i + Cz_i + D|}{\sqrt{A^2 + B^2 + C^2}} \quad 4-30$$

Then, the minimum sum of squares which determines the best-fit condition is defined as:

$$\sum_{i=1}^N d_i^2 = 0 \quad 4-31$$

In order to distinguish between planar and non-planar surfaces, a threshold of  $\pm 3$  cm was set as the maximum distance between every window point and the computed best fit plane. This threshold represents the average maximum distance from the best fit plane for 17 selected points located over asphalt and concrete surfaces believed to be “flat” (Table 4-1). By setting this threshold, photogrammetric points located over local regions which meet this planarity tolerance will be selected and subjected to further testing in order to be considered as reference control points.

<i>Min (m)</i>	<i>Max (m)</i>	<i>Average (m)</i>	<i><math>\sigma</math> (m)</i>
0.005	0.212	0.024	0.028

Table 4-1 Statistics of 3x3 point residuals of best fit plane for 17 road and planar surface points.

### 4.9.3 Slope Test

Since the selected points could be on a planar surface, but that plane could still be steeply inclined and errors in the point elevation might be introduced due to the terrain slope (Maling, 1989), the slope test was introduced to avoid points located on steep surfaces. A slope threshold representing the average slope angles for the same 17 points used in the plane threshold test was determined. An average angle of  $10.3^\circ$  was set as a maximum surface angle. Slope was measured using the method proposed by Horn (1981) for calculating the gradient and aspect for a 3X3 grid of 3D data. This method is based in computing the gradient in the x and y directions before computing the final slope.

$$\tan(slope) = \sqrt{S_x^2 + S_y^2} \quad 4-32$$

$$\tan(aspect) = \frac{S_y}{S_x} \quad 4-33$$

Where:

$S_x$  denotes gradient in the x direction.

$S_y$  denotes gradient in the y direction.

These slopes are determined for the 3X3 windows using the following equations:

$$S_x = \frac{[(Z_{i+1,j+1} + 2Z_{i+1,j} + Z_{i+1,j-1}) - (Z_{i-1,j+1} + 2Z_{i-1,j} + Z_{i-1,j-1})]}{8\Delta X} \quad 4-34$$

$$S_y = \frac{[(Z_{i+1,j+1} + 2Z_{i,j+1} + Z_{i-1,j+1}) - (Z_{i+1,j-1} + 2Z_{i,j-1} + Z_{i-1,j-1})]}{8\Delta Y} \quad 4-35$$

Where:

$\Delta X$  and  $\Delta Y$  are the grid spacing in the X and Y directions, which are 25 cm for the two test sites used for the evaluation process presented in later chapters and  $i$  and  $j$  are the pixel order from 1 to 3 in X and Y directions

By computing the average vertical and horizontal distances, the mean slope angle was computed and set as the threshold for the reference surface.

#### 4.9.4 Reliability Test

As mentioned in Section 4.7.2, the number of rays is important in detecting blunders that may contaminate the photogrammetric points. After applying the aforementioned tests, the possibility of including blunders still exists. Although these errors would have been detected and down-weighted during adjustment, they would not have been removed. Therefore, reliability testing was introduced to remove any points detected as blunders by robust estimators during the bundle adjustment. All retained points must also be observed in at least four images. This condition was set to avoid any undetected blunders, since in “two ray points” errors in the x direction cannot be readily detected, and in “three ray points” errors in the x direction may be detected but cannot be corrected as discussed in Section 4.7.2.

### 4.9.5 Configuration Test:

After all candidate reference LCPs have been identified, point distribution is also considered as this plays a critical role in achieving high accuracy in triangulation (McGlone *et al.*, 2004). Accordingly, the algorithm was extended to ensure good point distribution based on the number of LCPs selected. A number of options were configured to allow selection of an increasing number of LCPS in order to assess the impact of this on the overall accuracy of the triangulation. In the four control point option, the block is divided into four sub-blocks and the nearest LCP to the centre of each sub-block is selected, as illustrated in Figure 4-19.

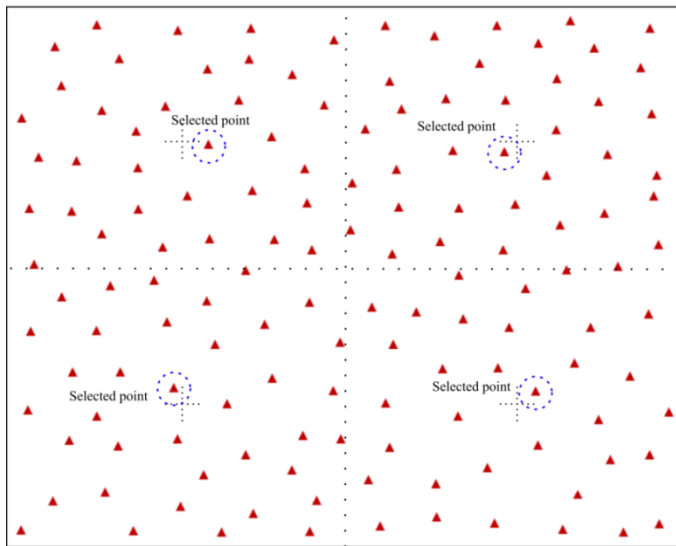


Figure 4-19 Selection approach of four reference LCPs.

The coordinates of the sub-block centres are automatically determined using the extent of block coverage. The UTM coordinates of the block corners were used to divide the block area into four sub-blocks. The centre of each sub-block are determined and saved for automatic LCPs selection. A similar approach is adopted if there are nine control point coordinates. However, in this case, the block area is divided into nine sub-blocks and the nearest good LCP to the centre of the nine sub-block centres will be selected, as illustrated in Figure 4-20.

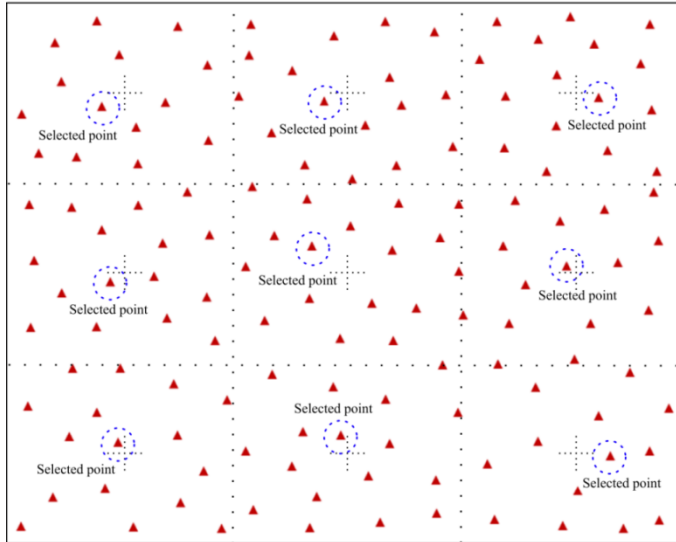


Figure 4-20 Selection approach of nine reference LCPs.

In the same manner, if 15 or 20 LCPs are required, the block will be divided into 15 or 20 sub-blocks and the nearest point to the centre of each sub-block is selected. However, for large numbers of points (from 50 to 300) the LCPs will be randomly selected from the control point lists.

In the case of irregularly structured blocks, coordinates could be pre-defined manually by the user. The algorithm will then read these coordinates and select the closest LCP point to each of the predefined locations. Finally, all selected points are saved in a separate BLUH control point file based on the point number. These control files include the point ID, X coordinates, Y coordinates, Z coordinates and the weight factor or point type. The point type should be 1 if points are to be used as vertical control points, 2 for horizontal control points and 3 for full control points. The file is prepared in a simple ASCII format.

#### 4.10 Aerial Triangulation and Camera Calibration

The final step in the methodology was to validate the developed approach, as well as assess transferability. Consequently, two different photogrammetric image blocks, together with complementary LiDAR, were investigated. These were captured using a Microsoft UltraCamX large format digital camera and an Applanix DSS322 medium format camera respectively. To test the influence of the number of LCPs on block accuracy, different BLUH control point files were created for different numbers of LCPs. In addition to assessing the number of LCPs, tests included the assignment of

different point weights to the input LCPs in the bundle block adjustment in order to check their influence on the block accuracy. Further, the utility of the developed methodology for camera self-calibration was also investigated. The self-calibration at this stage included introducing the BLUH standard 12 AP and parameters 13, 14 and 15. Where parameters 13 correspond to the refined camera focal length and 13,14 are X and Y shifts in the principal point coordinates. Detailed analysis of the validation and results obtained for aerial triangulation using the LCP results are described in Chapters five and six.

## **4.11 Assessment of Error Propagation in the Research Methodology**

The proposed research methodology workflow comprises different steps as described in Section 4.2. During each of these stages, many errors sources might be introduce into the workflow affecting the registration process, degrade quality of the reference targets and finally the precision of the camera calibration. Therefore, during the data processing and registration stages, careful consideration was taken to control the possible sources of errors and also to make sure that propagation of these errors through the workflow is eliminated or at least minimised.

### **4.11.1 Accuracy of the Photogrammetric Point Cloud Computations**

The methodology begins with automatic dense tie point measurement of the photogrammetric blocks. Therefore, the first possible source of errors is the measurement error. The average quality of the image measurement in the manual photogrammetry is 15  $\mu\text{m}$  (Baltsavias, 1999). However, using automatic point measurement techniques, as used in this research, accuracy of 1/10 of a pixel is expected (Alamús and Kornus, 2008). In addition to the high accuracy of the measured tie points, introducing tie points in the solution minimises the RMS of y-parallaxes and improves the point quality without the need for GCPs in the bundle block adjustment (Khoshelham, 2009). Moreover, large amount of image overlap was adopted in this research to provide strong block geometry. This has improved point height accuracy by increasing the number of rays per observed point on the ground (Ladstädter and Gruber, 2008). Increasing the number of rays also aids the removal of the effects of any remaining errors in the orientation parameters (Cramer and Stallmann, 2001). The



remaining random errors are eliminated from the adjustment using data snooping and robust estimators methods as described in Section 4.7.2.

The other source of error is the systematic errors in the image plane. These systematic errors do have an effect on the point height accuracy (Alamús *et al.*, 2006). Therefore, to model these errors, self-calibration with additional parameters was introduced as described in Section 4.7.2.3.

In addition to the point measurement errors, the precision assigned to coordinates of GNSS camera projection centres used in the adjustment was 10 cm in X, Y and Z. Therefore, the accuracy and precision of the ISO process was assessed using sigma naught and elements of the covariance matrix  $Q_{xx}$  (Grün, 1982). Sigma naught value will assess the quality level of image coordinate measurements and elements of the covariance matrix will be used to assess the root mean square error (*RMSE*) error at the GNSS camera coordinates. The sigma naught is computed using the following formula:

$$\hat{\sigma}_0^2 = \frac{\hat{v}^t C_{ll}^{-1} \hat{v}}{R} \quad 4-36$$

Where  $C_{ll}$  denotes the coefficient matrix,  $R$  denotes the adjustment redundancy and  $\hat{v}$  is the vector of residuals or corrections.

However, as the ISO process will be based on the nominal camera parameters, the main concern is that changes in the camera interior orientation will not be detected at this stage as no GCPs were used. For example, any change in the camera focal length will cause systematic offsets in the height components in the object space (Heipke *et al.*, 2002a).

#### 4.11.2 Accuracy of the Registration Process

Two potential error sources are expected in the registration process. Firstly, error in the reference LiDAR DTM introduced through the surface interpolation process. This error is minimised by maintain the original large point density when thinning the overlap areas between the LiDAR strips (see Chapter 3, Section 3.2.5). Where practical tests performed by Al-Durgham *et al.* (2010) showed that an absolute accuracy from 2cm to 6cm is achievable at higher point density. Secondly, errors in the 3D quality of the derived photogrammetric data. These errors can be classified as random or systematic

errors. Random errors are mainly introduced due to measurement errors and were undetected due to low redundancy and also some artefacts. During the surface matching, these random errors are treated individually, where erroneous points will be down-weighted until it has no more influence in the surface matching results as described in Section 4.8.3. Systematic error however, is the significant systematic 3D offset in the photogrammetric data caused by errors in the camera interior orientation or errors in the GNSS/IMU data. These errors are removed using the 7-parameter 3D similarity transformation between the LiDAR and photogrammetric data. In the registration process, the errors were first checked by calculating the mean elevation difference between the reference LiDAR surface and photogrammetric point cloud:

$$\mu = \bar{x} = \frac{1}{n} \sum_{i=1}^n x_i \quad 4-37$$

where  $x_i$  represents the elevation difference after the final iteration.

If the systematic errors are removed and the remaining random errors are normally distributed around the mean, this value should be zero. Moreover, standard deviation of a sample was also used as measure of uncertainty and was computed as follows:

$$\sigma = \sqrt{\frac{1}{n-1} \sum_{i=1}^n (x_i - \bar{x})^2} \quad 4-38$$

The standard deviation of the computed 7 transformation parameters was also estimated through the diagonal element of the estimated covariance matrix of the unknowns.

The registration accuracy was also assessed using the *RMSE*, which is a measure of difference between estimated and reference values as shown in Eq. 4-39, is computed using the remaining point residuals between the reference LiDAR interpolated surface and the transformed photogrammetric data.

$$RMSE = \sqrt{\frac{1}{n} \sum_{i=1}^n (x_{ref} - x_{check})^2} \quad 4-39$$

### 4.11.3 Accuracy of Aerial Triangulation and Camera Calibration using LiDAR Derived Control Points

Despite the careful consideration taken to keep the error sources under control through the implemented research workflow, the possibility of some remaining errors is still exist. Therefore, since the exact accuracy of the lidar-derived reference points are not precisely known, sensitivity tests were performed using values which were assumed to be representative in the aerial triangulation. Thus, input weights of the LCPs ranged from 2 to 15 cm in both horizontal and vertical components were assigned. The effect of different input weights on the accuracy of aerial triangulation and precision of the refined camera parameters.

The internal and external accuracy of the aerial triangulation are assessed using the elements of the covariance matrix. Sigma naught is computed using Eq. 4.36 (Section 4.11.1). Also, the standard deviations of the obtained unknowns  $\hat{x}$  are computed using the value of sigma naught and the elements of the covariance matrix as shown in Eq. 4.37.

$$\hat{\sigma}_{\hat{x}_u} = \hat{\sigma}_0 \sqrt{C_{\hat{x}_u \hat{x}_u}} \quad 4-37$$

Where  $C_{\hat{x}_u \hat{x}_u}$  is the  $u^{th}$  diagonal element of the estimated covariance matrix of the unknowns.

The internal accuracy was also assessed by calculation the *RMSE* of the adjusted ground coordinates of the input control data (LCPs and GNSS data) obtained from the covariance matrix. The external accuracy was assessed by calculating the *RMSE* from the difference between reference CP and the adjusted coordinates of the input LCPs.

## 4.12 Summary

This chapter has presented a detailed description of the research methodology. The overall aim of the research methodology was to evaluate LiDAR data as a source of control in order to perform aerial triangulation and camera calibration. To achieve this aim, the research methodology was designed to include successive steps controlled by software implemented using Matlab in a semi-automated approach. These steps include automatic generation of a dense photogrammetric point cloud to provide the surface description needed for the registration process. The 3D coordinates of the photogrammetric points were computed using the combined adjustment of GNSS/IMU data and tie points. The accuracy and quality of the photogrammetric point cloud data is improved through introducing self-calibration additional parameters in the ISO process.

In the next step, registration between the dense tie points and the reference LiDAR surface was undertaken using a robust 3D least squares surface matching algorithm, which minimizes the Euclidean distance between the reference (LiDAR) and floating surface (photogrammetric point cloud). This procedure was repeated after introducing self-calibration parameters into the bundle adjustment. Following this, reference LiDAR-derived control points were automatically extracted from the transformed and registered dense photogrammetric tie points. Point selection was based on certain criteria. These criteria include requirements that a point must have minimum matching residuals, pass planarity and slope tests, pass a reliability test and finally the selected points must maintain a good point distribution within the photogrammetric block.

Finally, aerial triangulation and camera calibration are performed using the selected LCPs. The testing and validation of the developed approach is described in Chapter 5 and Chapter 6 through empirical tests performed using a large format digital aerial camera (UltraCamX) and a medium format digital aerial camera (Applanix DSS322). These chapters also provide detailed results for the extracted reference LiDAR-derived control points as well as assessment of the resultant aerial triangulation and camera calibration tests.

# CHAPTER

# 5

---

## 5 Calibration of Large Format Camera

---

### 5.1 Introduction

Chapter Four presented a detailed description of the research methodology developed in this study. The methodology implements a novel automatic extraction of reference LiDAR derived control points through automatic registration between a dense network of photogrammetric tie points obtained from ISO and a reference LiDAR DTM. To validate the research methodology, as well as to assess the transferability of the approach, two different photogrammetric image blocks, together with complementary LiDAR data, were investigated. This chapter presents the results of the validation process using data captured by a Microsoft Vexcel Imaging UltraCamX large format digital camera. Reference LiDAR data captured by a Leica ALS50 airborne laser scanner have been used to create the reference DTM for the test area.

After dense photogrammetric point cloud measurement and undertaking the integrated sensor orientation process using the GNSS/IMU data, the object coordinates of the dense photogrammetric point cloud data were computed and improved by introducing the self-calibration parameters in the ISO process. Registration of the photogrammetric point cloud data with the reference LiDAR-derived DTM surface was then performed using an automatic least-squares surface matching procedure. The LiDAR derived reference control points are then extracted using the developed automatic extraction procedure. Finally, aerial triangulation and camera calibration were performed using these points. The results of aerial triangulation and camera calibration for the UltraCamX large format camera are presented in this chapter. Validation of these

calibration results were also performed using the existing GNSS surveyed ground control points.

## 5.2 Test Area

The Microsoft UltraCamX data used in the calibration and evaluation tests were acquired over the Vaihingen/Enz test field located in the south-east of Germany, as shown in Figure 5-1. According to Cramer (2005), this test field was established in 1995 to test the geometric performance of new digital frame cameras and line scanning systems. It has also been used for other investigations related to the use of GNSS/IMU data for direct georeferencing of aerial data acquisition systems. The test field is located in a hilly region which extends 7.5 km in the east-west direction and 4.8km in the north-south direction. This region includes different types of land cover and vegetation such as small areas of forest, vineyards and villages (see Figure 5-1). At time of data capture, 200 signalized reference control targets were distributed over the site. These points provided dense and accurate reference targets which can be used as control points and also as independent checkpoints required for the calibration procedures. These permanent targets are currently maintained by the University of Stuttgart (Cramer, 2010).

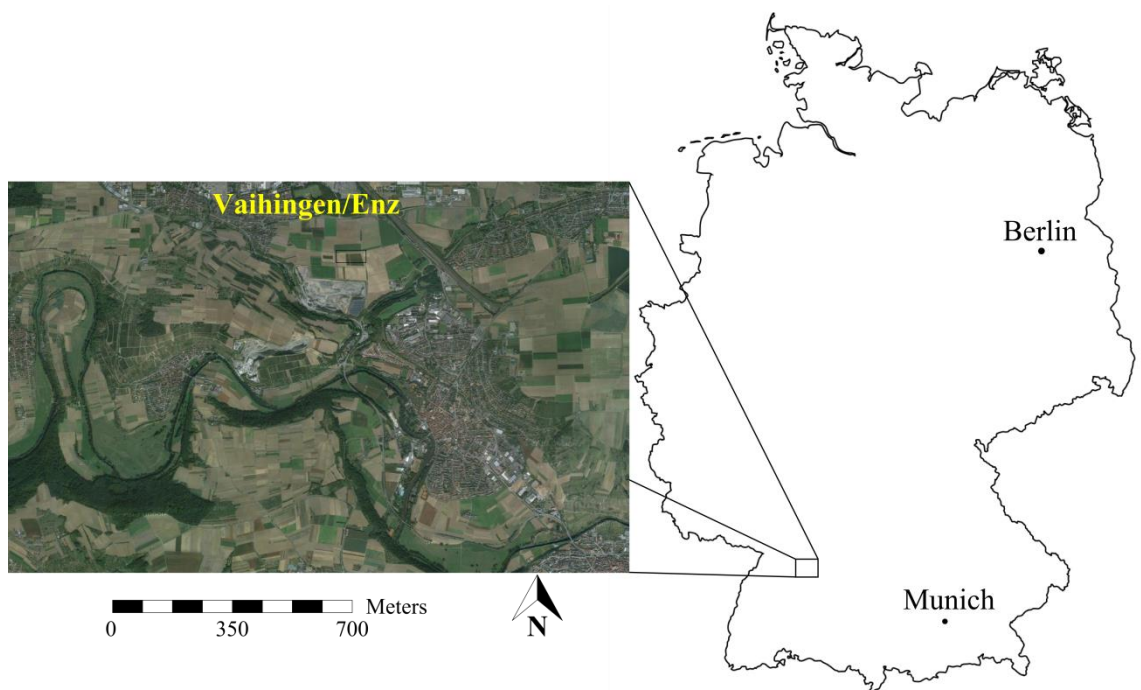


Figure 5-1 Vaihingen/Enz test field location map.

## 5.3 Photogrammetric Data

### 5.3.1 Aerial Imagery

The data used in this test was provided by the Germany Society of Photogrammetry and Geoinformation (DGPF), and was captured in 2008 as part of the DGPF camera evaluation project (Cramer, 2010). The evaluation tests were based on data captured on 11<sup>th</sup> September 2008 using the UltraCamX camera system with 80% forward overlap and 60% sidelap (Cramer, 2010). The selected sub-block used in the evaluation tests consisted of four parallel strips of 40 images acquired at a flying height of 1500 m giving a ground sample distance of 8 cm, as shown in Figure 5-2. Two strips were flown in an east-west direction and two in a west-east direction, giving a total ground coverage of approximately 7 km<sup>2</sup>.

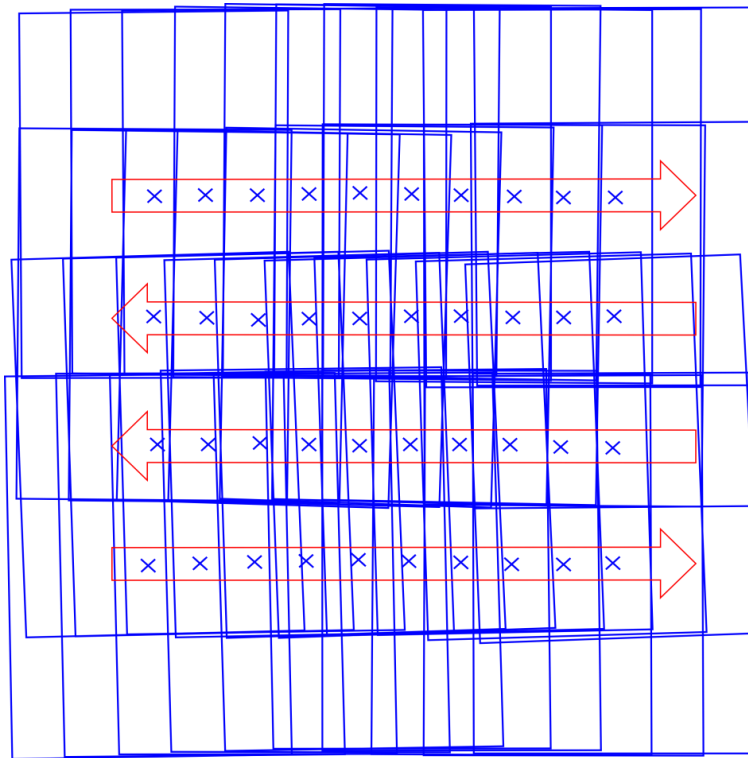


Figure 5-2 Selected UltraCamX sub-block.

### 5.3.2 Reference GNSS Surveyed Ground Control Data

As mentioned in Section 5.2, the Vaihingen/Enz test field consists of 200 signalized permanent control points. These are marked with white paint covering an area of

60 x 60 cm<sup>2</sup> and each also has a 30 x 30 cm<sup>2</sup> black painted square in the middle of a larger white square, as illustrated in Figure 5-3 (Cramer, 2010).

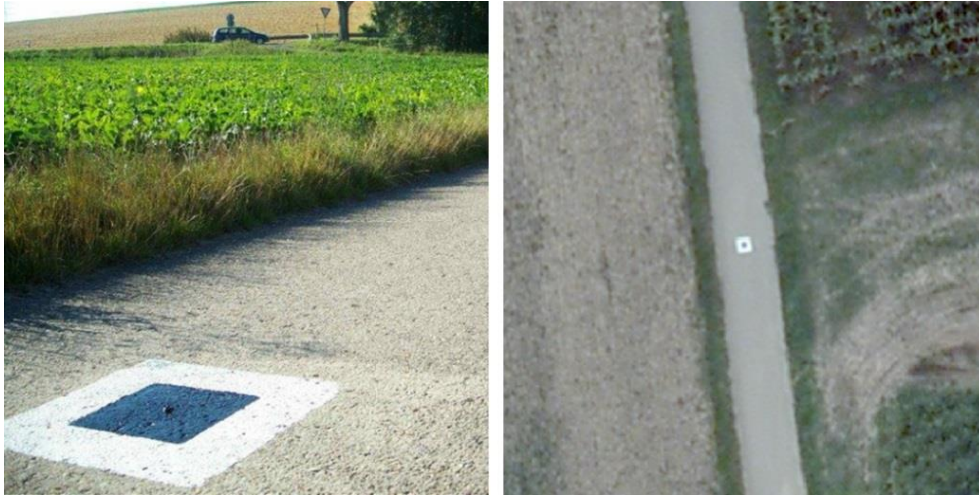


Figure 5-3 Example of signalized ground control points and the corresponding point in the aerial image (Cramer, 2010).

These reference targets are clearly visible and can be easily identified in the UltraCamX imagery used, where the inner block square is represented in approximately four pixels and the outer white square represented by eight pixels, which should provide a good basis for the user to achieve a realistic accuracy through manual measurement (Jacobsen *et al.*, 2010).

The object space coordinates of the reference control points were provided in ETRS89/UTM zone 32 coordinates with ellipsoidal heights. These coordinates were determined using GNSS static survey methods, which provides 1 cm horizontal and 2 cm vertical accuracy (Cramer, 2010). During the DGPF camera evaluation project, the coordinates of 111 points were delivered as reference control points (Cramer, 2010). Since the selected sub-block only covers a small part of the whole test site, only 21 reference control points were available for use in the validation test.

## 5.4 Reference LiDAR Data

The complementary LiDAR dataset was captured on 21<sup>st</sup> August 2008 using a Leica ALS50 laser scanner at a flying height of approximately 500 m. Ten LiDAR data strips were captured with a mean lateral overlap of 30% and a median point density of 6.7 points/m<sup>2</sup>. The data pre-processing, including the strip adjustment, was conducted



by the data provider as part of the data preparation phase of the DGPF camera evaluation project (Haala et al., 2010). Nevertheless, the height accuracy of LiDAR was assessed using the existing reference ground control points. In addition, the relative accuracy between different LiDAR strips was also assessed, as described in Section 5.4.2.

#### 5.4.1 LiDAR Data Processing

LiDAR data was processed using TerraScan software (Terrasolid, Version 013.008), where the point cloud data were separated into classes of ground, buildings and trees as shown in Figure 5-4. This step was performed through the filtering and classification of the LiDAR point cloud data, using TerraScan's in-built algorithms. Since the ground class is needed to classify the other classes such as buildings and trees, the first step was to classify the ground points using the ground classification routine. This routine classifies the ground points in an iterative approach, where LiDAR points are triangulated in order to determine the ground points that are close to the triangle planes based on a predefined threshold, which was set to 15 cm at this stage. Since the test site is hilly and contains a significant range of elevations, the iteration angle used to detect big jumps in the heights of points caused by buildings and other high features. This angle which represents the maximum angle between the LiDAR point and its projection to the nearest triangle plane and vertex, was altered to be  $4^\circ$  for the flat areas and  $10^\circ$  for the other hilly areas (Soininen, 2004).

After identifying the ground points, further data cleaning was conducted to manually remove misclassified points. To obtain an accurate classification of the building class, the vegetation class was classified using the 'detect trees' routine, which automatically detect trees from the LiDAR point cloud based on the pre-defined shapes of trees according to the software database, which can detect spruce and birch tree types. The final vegetation class included some misclassified features such as cars; however, these were ignored since the vegetation class was not used in DTM generation. Finally, the building class was classified after defining the ground class using the building classifier routine. This routine is based on detecting building roofs through tests of planarity of the LiDAR points.



Figure 5-4 Classified LiDAR point cloud data.

## 5.4.2 Accuracy Assessment of LiDAR data:

Before using the LiDAR point cloud data for the validation of the methodology, it was necessary to investigate the relative and absolute accuracy of the LiDAR datasets. Absolute vertical accuracy was assessed using all available reference control points, and relative accuracy was assessed by measuring the height differences between the different LiDAR strips.

### 5.4.2.1 Absolute Vertical Accuracy

The absolute vertical accuracy, which represents the accuracy of LiDAR data relative to the reference ground survey data, was assessed in TerraScan using all 80 available control points. To eliminate the effects of large errors, the threshold was set to  $3\sigma$ ; all points with differences outside the threshold limit were then eliminated from the test. A total of 67 points were then used in the assessment. Table 5-1 shows that the RMS difference between the ground control points and LiDAR data was in the range of 2.5 cm. Detailed results for this test can be found in Appendix A.

<i>Data</i>	<i>RMS (m)</i>	<i><math>\sigma</math> (m)</i>	<i>Mean (m)</i>	<i>Min (m)</i>	<i>Max (m)</i>	<i>No. of Points</i>
LiDAR	0.025	0.025	-0.002	-0.048	0.043	67

Table 5-1 Elevation difference statistics between the LiDAR point cloud and the reference control points.

### 5.4.2.2 Relative Vertical Accuracy

Relative accuracy, which refers to the height consistency between the multiple LiDAR strips, was assessed as the average height difference between the LiDAR strips. This was assessed using the TerraMatch module, and was achieved by measuring the average elevation differences between the different LiDAR strips used in computing the reference DTM. These differences were measured using buildings and ground class LiDAR points located in the overlapping area. The average height difference between the LiDAR strips was 2.5 cm. A similar test for the quality assessment of overlapping LiDAR strips conducted by Haala *et al.* (2010) showed that the standard deviation derived from the median absolute differences,  $\sigma_{MAD}$ , was only 2.9 cm for the LiDAR data acquired over the entire test area. This accuracy is below the LiDAR nominal accuracy ( $\pm 10$ ) and provides a good fitness between the different LiDAR strips.

### 5.4.3 Generation of Reference DTM from LiDAR Data

After the classification of the LiDAR point cloud data and extraction of the ground class, the ground class was cleaned and thinned to reduce the volume and size of the data. Then, as described in Section 5.4.1, the model keypoints were extracted to be used for creating a thinned reference DTM model. In order to maintain the accuracy of the reference LiDAR data, the height tolerance used for extracting the model keypoints was set at  $\pm 5$  cm, and the model will set the above model to +5 and the below model to -5 and the maximum difference in the elevation will be 10 cm. This procedure will keep the accuracy range within 10 cm (Rönnholm, 2011a). Finally, the DTM was computed using the model keypoints using the TerraModeler module. This involved creating a triangulated surface from the input LiDAR point cloud as shown in Figure 5-5. The DTM file was then exported into ASCII XYZ file format in order to be read by the surface matching software.

In addition to the raw point cloud, the DGPF also provided a DSM grid file with 0.25 m spatial resolution, which was used in the research methodology. A subset from the DSM which covers the test site used in this research was created and saved in a separate DSM file to be used for the surface planarity test as described in Section 4.8.2.

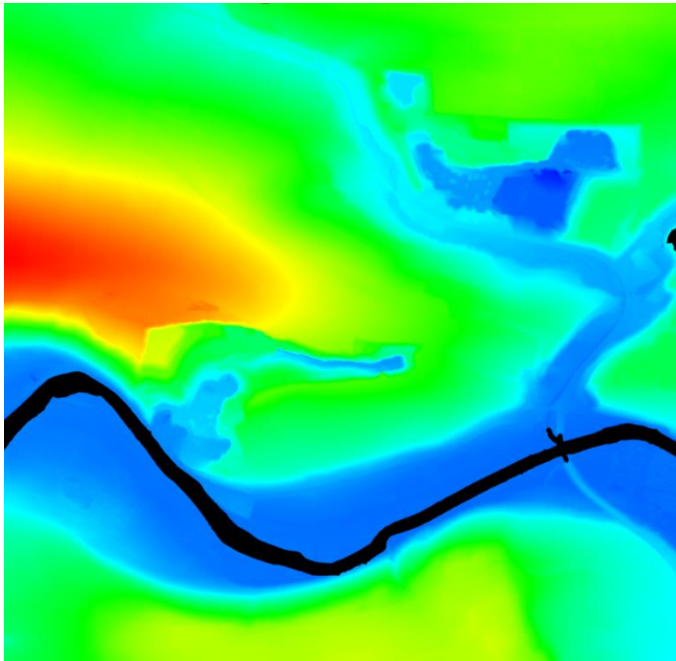


Figure 5-5 Reference DTM surface generated from LiDAR point cloud.

## 5.5 Photogrammetric Point Measurement and Processing

### 5.5.1 Block Setup and Tie Point Measurement

As described in Section 4.4, the UltraCamX data was imported into SocetSet. The GNSS/IMU camera station coordinates and attitudes were used in the image import process to assess in the block definition process, as the coordinates and orientations of each image station will be known and it requires grouping of these images into different strips, as follows. The first ten images of the northern strip were defined as the first strip in an image numbering order from left to right. As the strip numbering order was from top to bottom, the images were imported into four strips, where each strip contains 10 images. Then, the photogrammetric tie points were measured using the Automatic Point Matching (APM) procedure in the Multi-Sensor Triangulation (MST) module of SocetSet with the densified tie point grid (see Section 4.4). In addition to the tie point pattern grid, the GNSS/IMU data used in the import process are also used by the APM to initialize the image matching when determining the image coordinates of the tie points in the overlapping areas of the whole block.

Automatic image measurement provides more precise measurement than manual observation, which helps to improve height recovery which is typically degraded by the smaller B/H ratio characteristic of digital cameras compared to their analogue

counterparts (Alamús and Kornus, 2008). In this research, it is also useful because it increases point density in order to provide a strong surface description for subsequently achieving improved surface matching results. Due to the high percentage of image overlap in the dataset, tie points located near buildings or trees are occluded in some images. This caused the APM to fail to derive the correct image coordinates in some images. These mis-measurements appear as blunders in the later stages of processing.

Finally, each tie point is given a unique ID which is derived from the image and strip number. These points are then exported into a point format accepted by the BLUH bundle adjustment software. In addition to the image tie points, image coordinates for all reference ground control points are also manually measured to be used in the validation tests.

### 5.5.2 Tie Point Object Coordinates Computation

The object coordinates of the dense photogrammetric point cloud are obtained using the ISO process using the BLUH software. The ISO process was performed using the GNSS/IMU data and MST observed tie points (See Section 4.6). The precision assigned to the coordinates of GNSS camera projection centres was 10 cm in X, Y and Z (Honkavaara, 2003; Sandau, 2009). Blunder detection and elimination was performed in BLUH software in two steps as described in Section 4.6.2. The first step using data snooping during the approximation of image orientation and the second using robust estimators in the first run of bundle block adjustment.

In general, to achieve optimum accuracy in the bundle adjustment, self-calibration with AP should be used (Jacobsen, 2008). For evaluation purposes, ISO adjustments were performed both with and without self-calibration being enabled. Therefore, the initial ISO process was performed with robust estimators in order to eliminate the effect of defective observations, and the second iteration was computed with AP incorporated into the bundle adjustment to allow potential improvements in the subsequent registration results. In this case the AP adopted is a standard BLUH 12 set, designed to model physically justified effects. These parameters can be introduced into the bundle adjustment even without control points and are statistically tested and reduced by the BLUH software, with any insignificant parameters being automatically eliminated from the solution (Jacobsen, 2008). The number of tie points totalled 15,707, resulting in

315,232 observations in the photogrammetric adjustment. The maximum number of observations in any one image was 5,943 and the minimum was 1,753 at the edges of the block. After the final iteration, the RMSE of difference at the GNSS coordinates was as follows:  $RMSE_x = \pm 0.019$  (m),  $RMSE_y = \pm 0.022$  (m),  $RMSE_z = \pm 0.008$  (m); and  $\sigma_0$  was  $0.67 \mu\text{m}$ .

The UltraCamX is a large format metric camera system and as expected, it showed relatively small systematic errors in the image space. Figure 5-6 shows the point residuals in the image space before and after introducing the self-calibration parameters in the bundle adjustment. This shows that there is a pattern of systematic errors in in some parts of the image. Also, the BLUH 12 AP set do not significantly compensate for the remaining systematic errors in the image space. Moreover, closer inspection of these systematic patterns at the image corner shows that these errors maybe related to the geometry of the camera 9 panchromatic CCDs. However, these systematic errors were in the range of  $2 \mu\text{m}$  and considered as small errors.

However, the effect of these systematic errors on the height of the photogrammetric point cloud can be further investigated by computing the height difference between point heights obtained with and without self-calibration with AP.

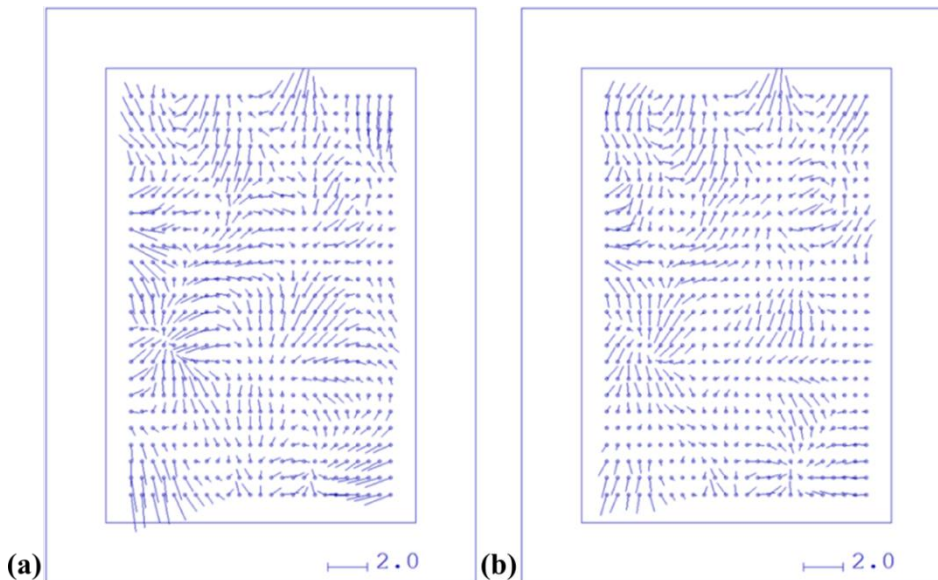


Figure 5-6 Systematic error pattern, (a) without self-calibration, (b) with BLUH 12AP.

According to Alamús *et al.* (2006), self-calibration with additional parameters eliminates distortions and systematic errors from the aerial images and improves the

image point height. Also, point height accuracy is affected by the planimetric point location and also the distance from the edge of the image block.

Although the results reported by Alamús *et al.* (2006) were for a DMC image block, similar effects can be expected on the UltracamX block used in this research. Results showed that self-calibration does have an effect on the point height determination and it is also worst in the block corners. Figure 5-7 shows the height differences between the photogrammetric point cloud heights before and after introducing the self-calibration parameters into the bundle adjustment. Figure 5-7 also shows that height differences were in the range of  $\pm 5$  cm, which includes the central area of the block and the other areas near the edge of the block, whereas these differences reached 15 cm at the extreme edges of the block. These results showed that the photogrammetric block provides good photogrammetric point quality and introducing self-calibration parameters will only have minor improvement in the registration of the photogrammetric data to the reference LiDAR DTM.

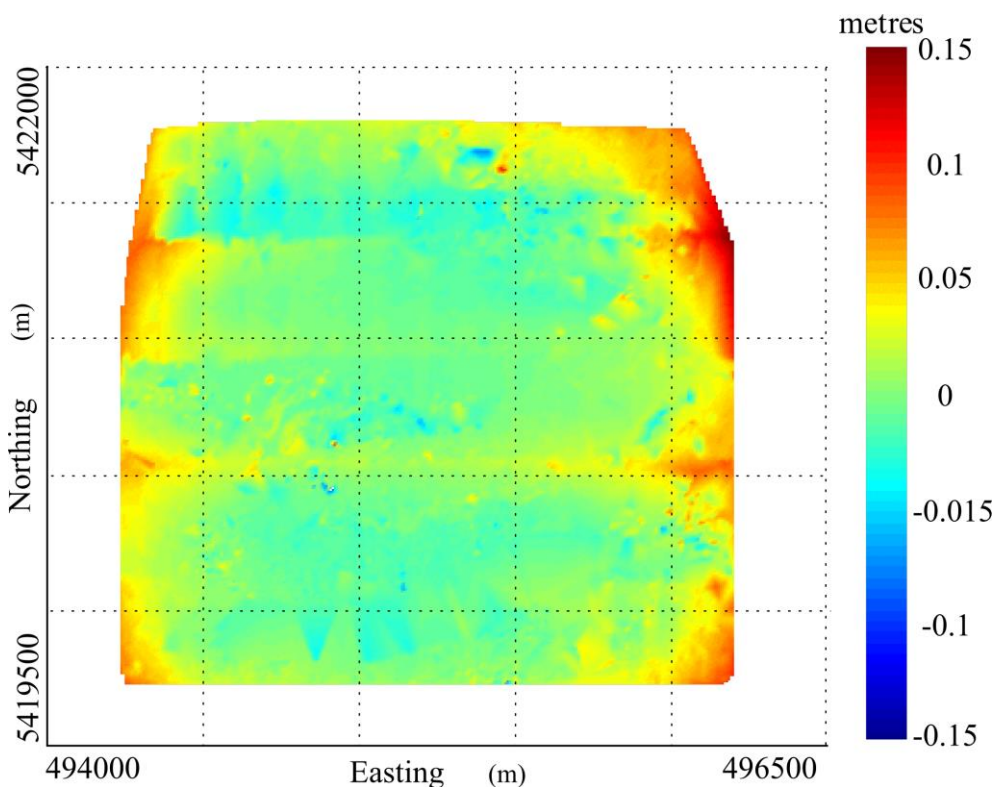


Figure 5-7 Height differences between photogrammetric points computed with and without self-calibration.



### 5.5.3 Pre-Matching Photogrammetric Point Cloud Processing

In order to ensure that the photogrammetric data represented only the ground surface, tie points were filtered to remove all points located over buildings and woodland as detailed in Section 4.5.1. Therefore, a thematic image mask for areas exceeding 2.5 m above ground level (a nominal elevation for vineyard features), obtained using a normalised digital surface model (nDSM) that was generated (as discussed in Section 4.5.1) using the LiDAR derived DTM and digital surface model (DSM), was used to omit all points located over buildings and woodland. Further processing was undertaken to remove the river area, followed by application of a 3 X 3 pixel erosion filter to remove single isolated pixels from the mask and also to remove the single pixel holes from the mask area, as shown in Figure 5-8.

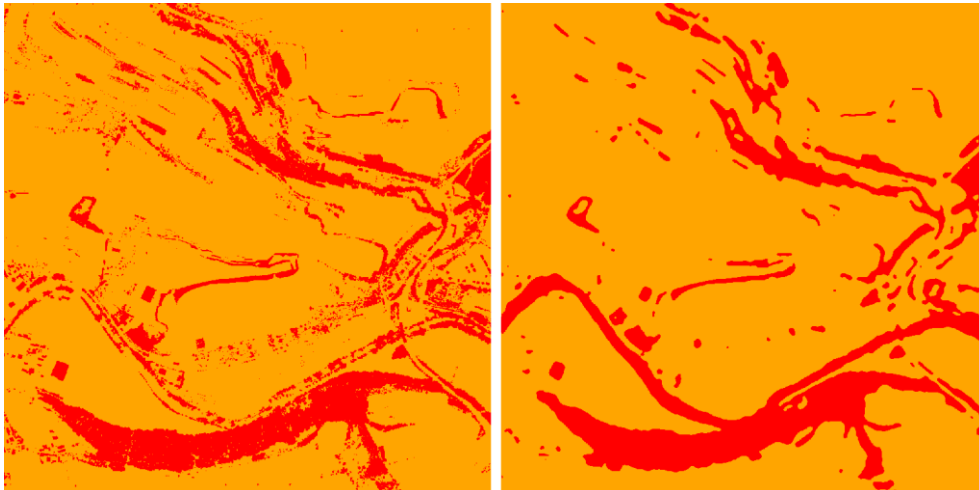


Figure 5-8 Left, thematic mask before application of 2.5m height threshold, right, after application of 2.5 m height threshold and filtering.

### 5.6 Photogrammetric Point Cloud Registration

The registration of the photogrammetric point cloud to the LiDAR reference DTM was performed using the in-house, robust surface matching software LS3D (Miller *et al.*, 2008), as described in Section 4.7. Surface matching was performed with the LiDAR DTM treated as a fixed reference surface, while the photogrammetric point cloud was treated as the floating surface to be transformed. All point coordinates were in the UTM32, ETRS89 reference system. The seven transformation parameters of a 3D conformal transformation were determined and used to align the two datasets. The



precision and accuracy of the transformation were estimated from the residuals. Table 5-2 shows the final transformation parameters, and residual ( $\nu$ ) statistics for the matching results. The matching was successful from the first run due to the small systematic errors in the image space, as discussed above. Therefore, introducing self-calibration parameters into the bundle adjustment had only a limited influence on the surface matching results, as reflected by the small changes in the final residual statistics. As could be seen in

Transformation Parameters	Surface Matching Results			
	ISO, no self- calibration	$\sigma$	ISO, with self- calibration	$\sigma$
$T_x$ (m)	-0.039	0.009	0.008	0.009
$T_y$ (m)	0.175	0.007	0.178	0.007
$T_z$ (m)	-0.196	0.004	-0.153	0.004
$\omega$ ( $^\circ$ )	0.00414	0.0006	0.00448	0.0006
$\phi$ ( $^\circ$ )	-0.00074	0.0001	-0.00103	0.0001
$\kappa$ ( $^\circ$ )	-0.00857	0.0001	-0.00637	0.0001
Scale	1.00021	0.0	1.00020	0.0
Mean $\nu$ (m)	-0.214		-0.216	
RMSE $\nu$ (m)	0.578		0.580	
$\sigma \nu$ (m)	0.100		0.098	

Table 5-2, the change in the transformation parameters was mainly in  $T_z$ , with a change of approximately 4 cm.

Transformation Parameters	Surface Matching Results			
	ISO, no self- calibration	$\sigma$	ISO, with self- calibration	$\sigma$
$T_x$ (m)	-0.039	0.009	0.008	0.009
$T_y$ (m)	0.175	0.007	0.178	0.007
$T_z$ (m)	-0.196	0.004	-0.153	0.004
$\omega$ ( $^\circ$ )	0.00414	0.0006	0.00448	0.0006
$\phi$ ( $^\circ$ )	-0.00074	0.0001	-0.00103	0.0001
$\kappa$ ( $^\circ$ )	-0.00857	0.0001	-0.00637	0.0001
Scale	1.00021	0.0	1.00020	0.0

Mean $v$ (m)	-0.214	-0.216
RMSE $v$ (m)	0.578	0.580
$\sigma v$ (m)	0.100	0.098

Table 5-2 Transformation parameters and quality statistics determined by surface matching for the UltraCamX block.

To check the correctness of alignment between the two surfaces, a number of common point features were selected to assess the registration process. The registration was performed with the LiDAR DTM reference surface, and therefore it was not possible to use any feature-based assessment. A group of points surrounding one of the buildings in the test area was therefore used to assess the registration. Figure 5-9 shows the group of points used to check the alignment between the original tie points in SocetSet and the registered tie points overlaid on the LiDAR DSM.

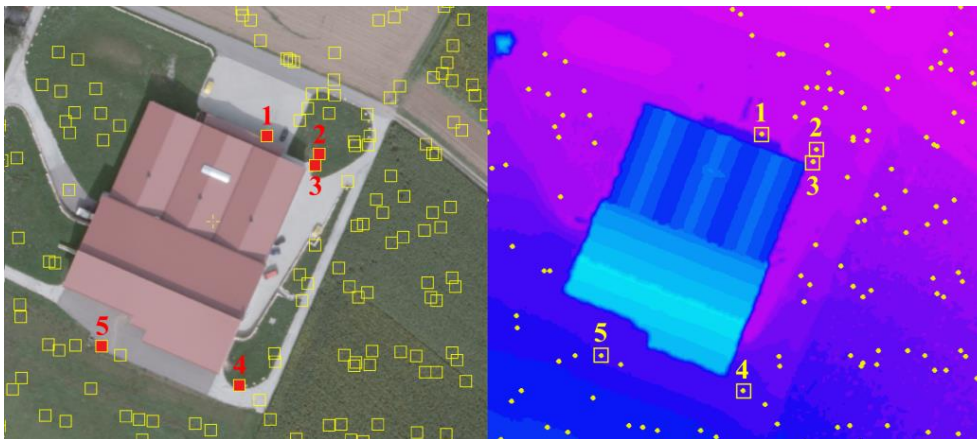


Figure 5-9 Left, selected check targets points, right, registered check targets overlaid on LiDAR DSM.

Further assessment was conducted for the point matching residuals for the block. Figure 5-10 shows the point matching residuals for the tie points after the final matching iteration and without self-calibration. It is clear that the majority of points show a good correspondence with the LiDAR reference surface. Some areas have relatively large residuals, due to undetected errors for points with low redundancy and also artefacts such as vineyards which are not represented in the LiDAR DTM and were not omitted from the photogrammetric data due to their height being below the 2.5 m threshold of the thematic image mask. Moreover, the three-week difference in the dates of capture of the datasets may have contributed to some minor differences due to, for

example, vegetation growth. As described in Section 5.5.2, the UltraCamX camera showed relatively small systematic errors which in the range of 2  $\mu\text{m}$ . These small systematic errors displayed limited influence on the quality of the photogrammetric point cloud data. Therefore, repeating the surface matching with self-calibration led to only small changes in the transformation parameters shown Table 5-2 where the difference in  $T_z$  was 4 cm. Moreover, self-calibration also led to small changes in the point matching residuals, as shown in Figure 5-11. These small changes were mainly in the heights of the photogrammetric point cloud data. These changes in point height, which are reflected in the resulting point residuals, are clearly visible in the analysis of the histograms before and after the self-calibration process. Figure 5-12 shows the two resulting histograms of the point residuals where a small improvement in the matching residuals was achieved. The residuals from the self-calibration surface are more tightly clustered around the mean (which is also very close to zero), with few outliers. The residuals relating to the surface with no self-calibration show a little larger dispersion away from the mean, indicating slightly poorer agreement between the two surfaces.

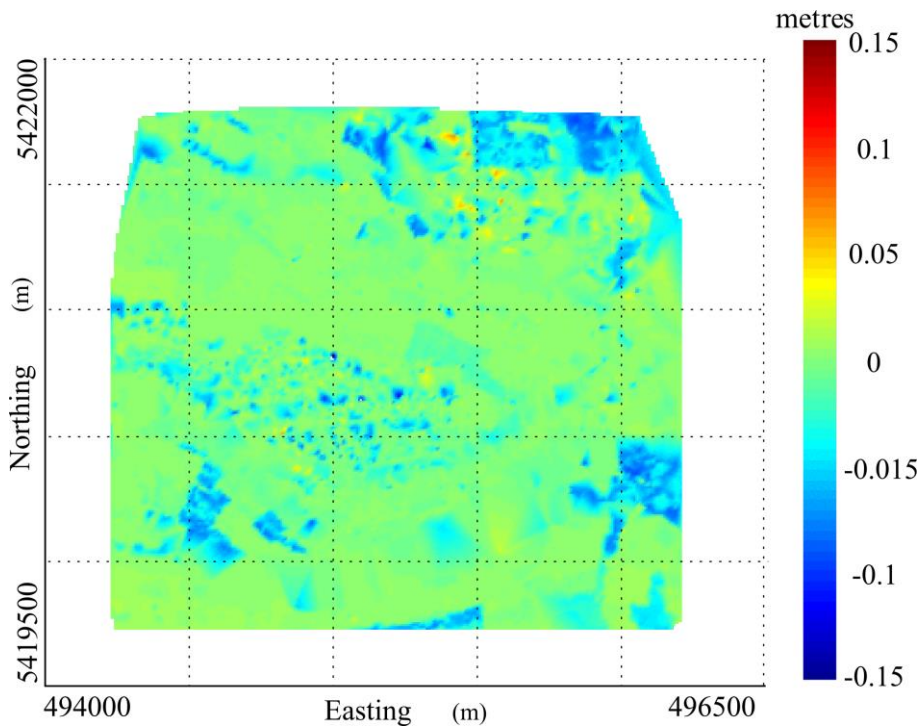


Figure 5-10 Surface matching point residuals (No AP).

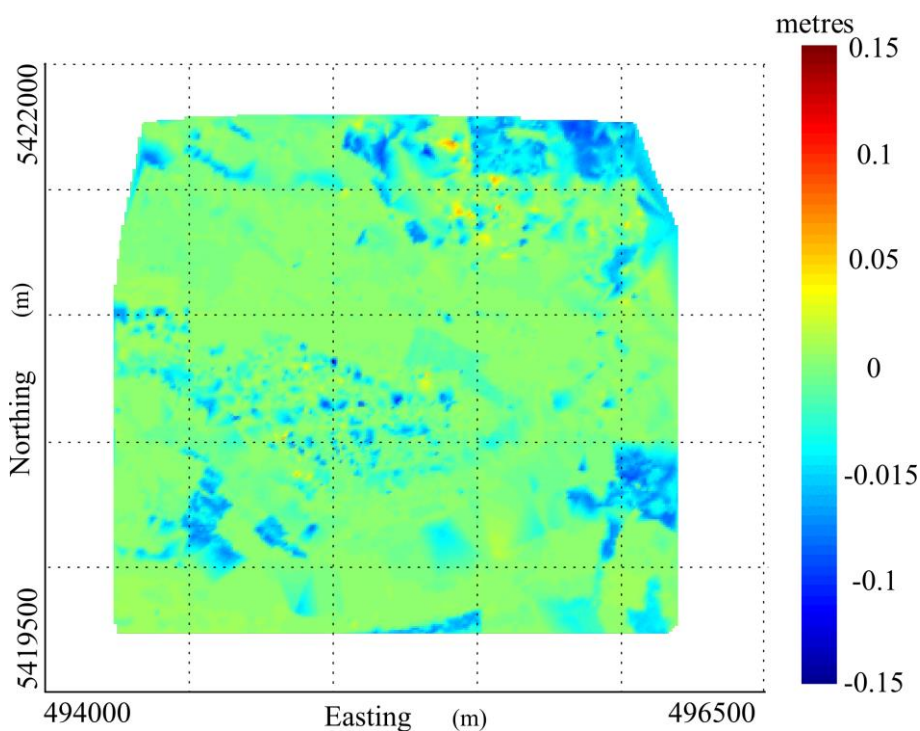


Figure 5-11 Surface matching point residuals (BLUH 12 AP).

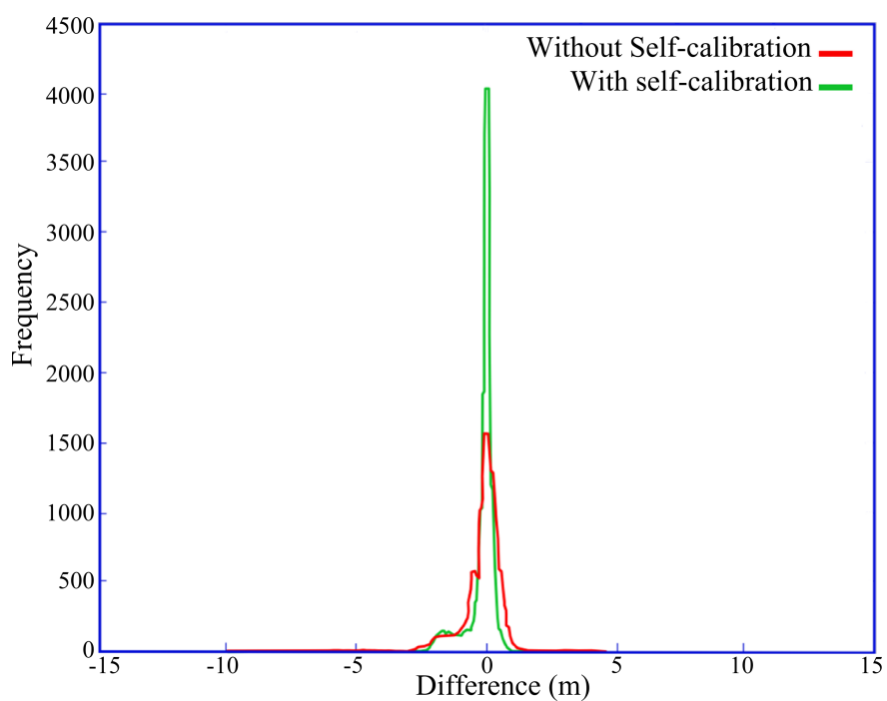


Figure 5-12 Histograms of the surface matching residuals with and without self-calibration.

## 5.7 Control Point Selection Strategy

Despite these minor errors, matching was regarded as successful and LCP extraction was performed based on the methodology described in Section 4.8. The selection methodology was performed using software developed in Matlab for the automatic extraction of reliable LCPs. The selection of LCPs was performed based on the matching conducted after the self-calibrating bundle adjustment, since the results of the analysis described in Section 5.6 showed that this provided a slightly better alignment between the reference LiDAR surface and the photogrammetric point cloud data, as evidenced through the smaller point residuals as shown in Figure 5-12.

The LCPs were selected by first reading the output files from the surface matching software. The output files were re-indexed using the reference point list file for the photogrammetric point cloud data. Then, from the indexed and registered point cloud data, a series of different assessments were conducted to select the most reliable points based on the predefined criteria, as follows. Firstly, all points located in the ‘best’ matched areas, which were defined as those with the smallest residuals of  $\pm 2$  cm, were initially selected. Secondly, from the points initially selected on the basis of the Euclidean distance threshold, only those located over planar areas were retained. As surface roughness is better described by a DSM than a DTM, the planarity test was performed using the area DSM with 25 cm resolution where the flatness test threshold was set to  $\pm 3$  cm. This threshold was selected based on the average of the maximum distances from the best fit plane using the same 3 x 3 window approach for points in 17 manually observed patches located over asphalt and concrete surfaces believed to be ‘flat’ as described in Section 4.8.2. To investigate the performance of the planarity testing procedure in representing true planar surfaces, a small area which includes different surface types such as asphalt, concrete, bare soil, grass areas and buildings was selected to test the effectiveness of the developed planarity testing procedure. The result of this test, as illustrated in Figure 5-13, showed the threshold value used to select all planar surfaces in the test area. As can be seen, the building roofs were also identified as planar surface, these were omitted using the slope test as areas with slope exceeding  $10^\circ$ .

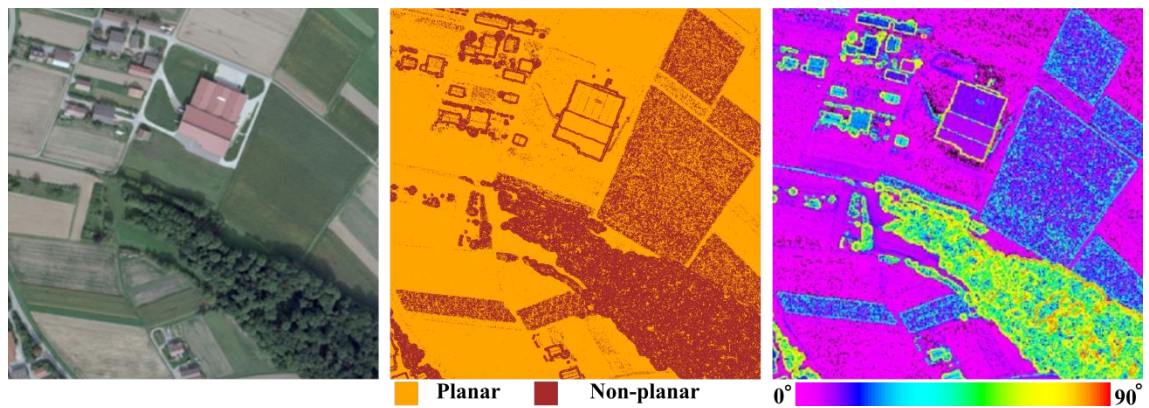


Figure 5-13 Selected planarity and slope test area.

These criteria, as for the subsequent slope test, are based on the classical best practice of selecting height control points in the field, ensuring that points are located in well defined, flat areas (Hodgson and Bresnahan, 2004). Moreover, as errors in point elevation might be introduced due to the slope of the terrain (Maling, 1989), the slope test was introduced to avoid points located on steeply sloping surfaces. The threshold for the maximum slope represents the average slope angles for the same 17 ‘flat’ patches, and was set to  $10.3^\circ$ . A similar test was conducted using the same test area as that used for the planarity test, where the slope map was computed as shown in Figure 5-13.

After applying the aforementioned tests, a reliability test was performed where only points with at least four rays were selected. And, finally, to enable an evaluation of the effect of the number of LCPs on the accuracy of aerial triangulation, different point configurations arranged in different ground control point files were generated, as described in Section 4.8.5.

After applying all selection criteria and conditions to the transformed photogrammetric point cloud, samples of the selected LCPs which were considered to represent the most reliable reference LCPs were selected for further use in aerial triangulation and camera calibration tasks. These points were located on main roads, secondary roads, pasture areas and ploughed land, as shown in Figure 5-14. These areas passed the flatness test and were considered as flat areas using the available DSM with 25 cm spatial resolution. Also, samples of the created LCP control file are shown in Appendix D.





Figure 5-14 Samples of the selected LCPs from the UltraCamX dataset.

## 5.8 Results of Aerial Triangulation using LCPs

After surface registration and the selection of reference LCPs, aerial triangulation was performed using the BLUH bundle adjustment software and the extracted LCPs. Since the quality of the derived LCPs is strongly dependent on the matching results, the tests included an investigation of the influence of the number and weight of the input LCPs on the resulting block accuracy. Aerial triangulation solutions were computed using increasing numbers of well-distributed LCPs (from 9 to 250). Since the exact accuracy of the LiDAR-derived reference points is not precisely known, sensitivity tests were performed using values which were assumed to be representative. These were based on the absolute accuracy of the LiDAR data (2 cm, as previously stated), and 15 cm due to the likely deterioration in the accuracy of points extracted over different types of land cover. Thus, input weights ranging from 2 to 15 cm in both horizontal and vertical components were assigned. To assess the accuracy of aerial triangulation, 100 LCPs were randomly selected from across the block and were omitted from use in adjustment and used instead as check-points (CPs).

After performing the bundle block adjustment using different sets of the derived LCPs, the estimated block precision (internal accuracy) are depicted in Table 5-3 to 5-6. These

results show that, when the input is high (2 cm, see Table 5-3) the precision was in the range of 3 cm in horizontal and 7 cm in the vertical component. As the number of input LCPs increases, the precision increases until it stabilised at approximately 2 cm (c. 0.25 pixel) in the three Cartesian components (easting, northing and height) after using 80 LCPs. Comparing these results with results of Table 5-4 with 5 cm LCPs weight, Table 5-5 with 10 cm LCPs weight and Table 5-6 with 15 cm LCPs weight, it shows that a similar trend was observed in all other triangulation results, the internal accuracy stabilising at approximately 2 cm after using 80 LCPs regardless to the input LCPs weight.

Number of LCPs	$\sigma_0(\mu\text{m})$	RMSE at LiDAR-derived control points		
		$RMSE_x(m)$	$RMSE_y(m)$	$RMSE_z(m)$
9	5.17	0.036	0.032	0.070
15	5.17	0.034	0.038	0.060
20	5.16	0.031	0.036	0.055
40	5.15	0.025	0.022	0.028
80	5.14	0.021	0.023	0.018
100	5.13	0.021	0.022	0.017
150	5.11	0.021	0.023	0.019
200	5.10	0.019	0.023	0.018
250	5.08	0.020	0.022	0.017

Table 5-3 Error at LiDAR-derived control points with 2 cm LCPs weight.

Number of LCPs	$\sigma_0(\mu\text{m})$	RMSE at LiDAR-derived control points		
		$RMSE_x(m)$	$RMSE_y(m)$	$RMSE_z(m)$
9	5.17	0.041	0.031	0.074
15	5.17	0.034	0.034	0.066
20	5.16	0.032	0.033	0.059
40	5.15	0.027	0.022	0.028
80	5.14	0.023	0.023	0.018
100	5.13	0.022	0.023	0.016
150	5.11	0.022	0.024	0.018
200	5.09	0.02	0.024	0.016
250	5.07	0.022	0.023	0.016

Table 5-4 Error at LiDAR-derived control points with 5 cm LCPs weight.

Number of	$\sigma_0(\mu\text{m})$	RMSE at LiDAR-derived control points		
-----------	-------------------------	--------------------------------------	--	--



LCPs		$RMSE_x(m)$	$RMSE_y(m)$	$RMSE_z(m)$
9	5.17	0.068	0.057	0.075
15	5.17	0.044	0.040	0.067
20	5.16	0.039	0.037	0.060
40	5.15	0.029	0.023	0.028
80	5.14	0.024	0.024	0.018
100	5.13	0.024	0.023	0.016
150	5.11	0.023	0.024	0.018
200	5.07	0.021	0.024	0.016
250	5.07	0.023	0.023	0.016

Table 5-5 Error at LiDAR-derived control points with 10 cm LCPs weight.

Number of LCPs	$\sigma_0(\mu m)$	RMSE at LiDAR-derived control points		
		$RMSE_x(m)$	$RMSE_y(m)$	$RMSE_z(m)$
9	5.17	0.104	0.095	0.074
15	5.17	0.063	0.060	0.068
20	5.16	0.054	0.051	0.061
40	5.15	0.033	0.026	0.028
80	5.14	0.025	0.025	0.018
100	5.13	0.025	0.023	0.015
150	5.11	0.024	0.025	0.018
200	5.09	0.021	0.025	0.016
250	5.07	0.023	0.023	0.016

Table 5-6 Error at LiDAR-derived control points with 15 cm LCPs weight.

In the addition to the internal accuracy assessment, the absolute accuracy was also assessed through analysing errors at the check points. As expected, the resulting aerial triangulation accuracy was lowest when a small number of LCPs was used with 10 cm and 15 cm point weightings. Accuracy improved when the input weighting was tightened up or when the number of LCPs was increased. Figures 5-15 to 5-17 show the RMSE values at the CPs for the three Cartesian components (easting, northing and height). It can be seen that all lines converge at approximately 80 LCPs, with the RMSE of the aerial triangulation stabilising at approximately 2 cm (c. 0.25 pixel) in plan components beyond this number, regardless of weighting. The height component also converges at c. 80 LCPs, although in this case some further improvement in RMSE is evident with increasing numbers of LCPs. Due to this stabilization in the horizontal and vertical component after 80 LCPs, the number of total number of LCPs was limited to

250 LCPs. Also, comparison of the precision and absolute accuracy shows that both accuracies are the same after 80 LCPs which indicates that minimum of 80 LCPs should be adopted when using this research methodology.

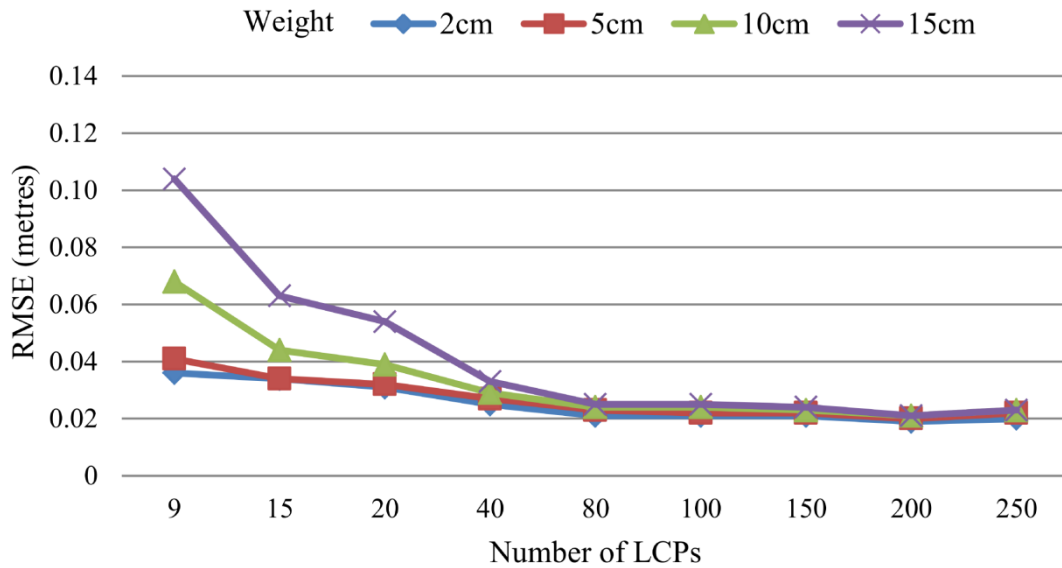


Figure 5-15 Easting RMSE calculated using 100 CPs in the UltracamX block.

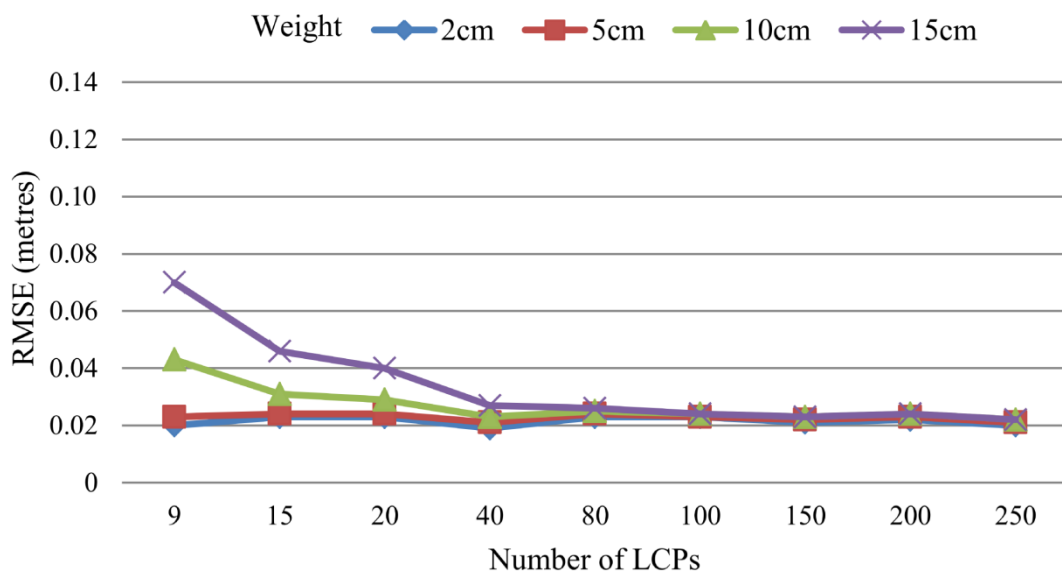


Figure 5-16 Northing RMSE calculated using 100 CPs in the UltraCamX block.

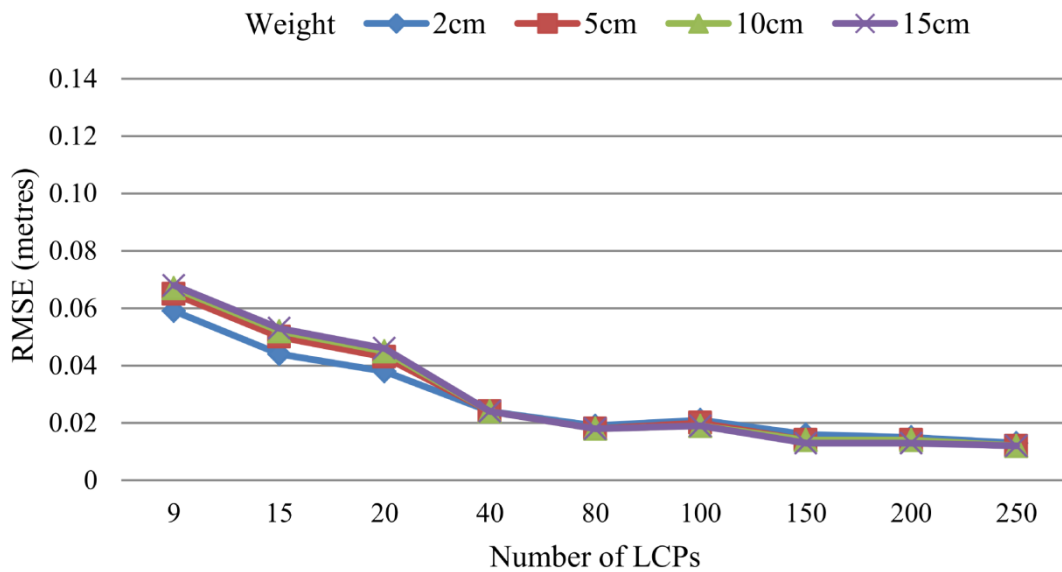


Figure 5-17 Height RMSE calculated using 100 CPs in the UltraCamX block.

## 5.9 Effects of LiDAR Planimetric Accuracy on the Triangulation Results

As accuracy tests performed in Section 5.4.2 only focused on the vertical accuracy of LiDAR point cloud data, the planimetric could not be assessed. Normally, LiDAR point cloud data has lower planimetric accuracy than vertical accuracy. According to Vosselman and Maas (2010) LiDAR data captured at flying heights up to 2000 m has planimetric accuracy ranging from 0.2 m to 1.0 m. Considering the good consistency between the different LiDAR strips described in Section 5.4.2 the LiDAR data was considered as free of any systematic errors. Therefore, further investigation was conducted to check the effect of different levels of LiDAR horizontal absolute accuracy on the results of aerial triangulation through introducing horizontal shifts to the reference LiDAR DTM surface. These shifts were introduced in the X, Y and Z components to the original LiDAR reference DTM surface, where in the first dataset a 1 metre shift was introduced to the X, Y and Z coordinates, and in the second dataset a 2 metre shift was added.

To allow comparison between the different sets of results, the same photogrammetric point cloud data, which was obtained with added self-calibration parameters in the bundle adjustment, was registered to the newly shifted LiDAR DTM surfaces and compared with the reference surface matching results obtained in the previous tests. Table 5-7 shows the transformation parameters of the different surface matching tests.

These results shows that the shifts made to the reference LiDAR DTM appeared as shifts in the X, Y and Z directions for the photogrammetric point cloud.

To allow aerial triangulation, reference LCPs were extracted from each transformed photogrammetric dataset. Also, the derived LCPs were selected in different configurations and saved in separate BLUH control files as full control points.

Transformation Parameters	Matching Results with Self-calibration		
	Original LiDAR data	1 m shifted LiDAR data	2 m shifted LiDAR data
$T_x$ (m)	0.008	0.996	1.987
$T_y$ (m)	0.178	1.170	2.167
$T_z$ (m)	-0.153	0.847	1.847
$\omega$ (°)	0.00448	0.00452	0.00454
$\phi$ (°)	-0.00103	-0.00103	-0.00104
$\kappa$ (°)	-0.00637	-0.00648	-0.00634
Scale	1.00020	1.00020	1.00020
Mean $v$ (m)	-0.216	-0.216	-0.217
RMSE $v$ (m)	0.580	0.580	0.580
$\sigma v$ (m)	0.098	0.098	0.098

Table 5-7 Transformation parameters of surface matching results using original and shifted LiDAR DTM.

Similar to the previous triangulation procedure, as discussed in Section 5.8, aerial triangulation solutions were computed using increasing numbers of reference LCPs. In these tests, the standard deviation of the reference LCP was set to 2cm since the test was mainly designed to check for any influence on aerial triangulation accuracy of the shifts introduced to the reference LiDAR DTM. Also, in these tests, the BLUH 12AP were introduced in the bundle adjustment process. Figures 5-18 to 5-20 show the results for aerial triangulation accuracy assessed using the same set of check-points used in the previous tests. The results show that the three tests achieved a similar accuracy trend in the X, Y and Z components, which indicates that the accuracy of the coordinates of the LCPs is mainly dependent on the correct alignment to the reference DTM surface. The correct alignment was achieved by recovering the introduced shifts using the surface

matching method, followed by the automatic extraction of the reference LCPs using the method developed in this study.

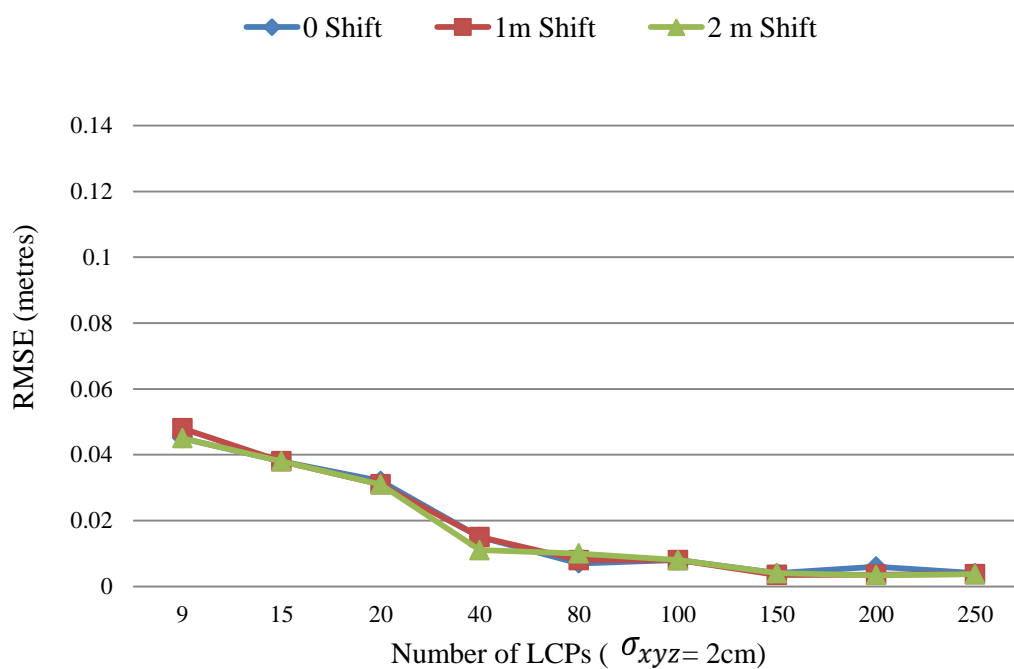


Figure 5-18 Easting RMSE calculated using 100 CPs using different LiDAR DTMs.

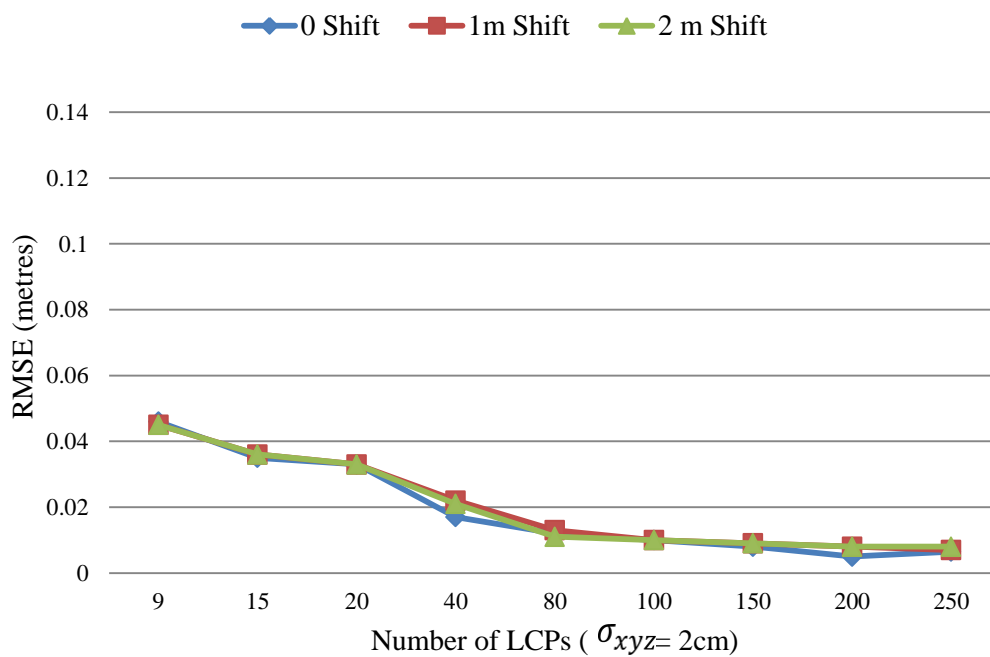


Figure 5-19 Northing RMSE calculated using 100 CPs using different LiDAR DTMs.

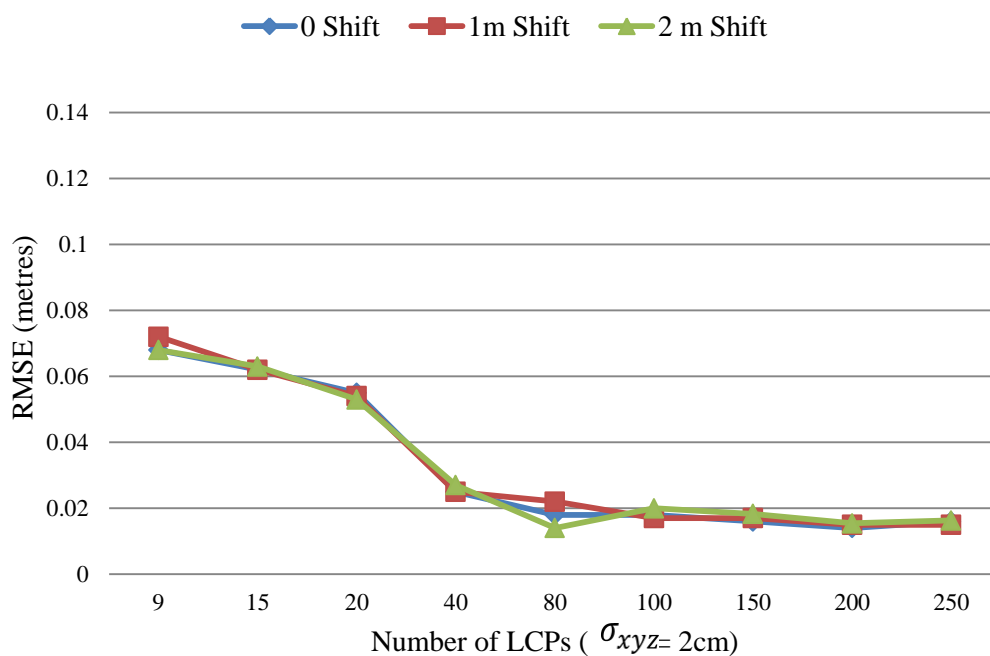


Figure 5-20 Height RMSE calculated using 100 CPs using different LiDAR DTMs.

## 5.10 Camera Calibration and Validation Results

Due to the availability of 21 field-surveyed GCPs in the test area, an independent triangulation with self-calibration was performed to be used as benchmark results. This was used as an independent benchmark to validate the calibration results obtained using differing numbers of derived LCPs. Table 5-8 shows the reference calibration results for the refined camera parameters determined using 4 and 21 reference GCPs along with the GNSS/IMU data. The weight given to the input control points was 2 cm to X, Y and Z and 10 cm for the GNSS data. These tests are denoted as *Ref 1* and *Ref 2*.

<i>Test No.</i>	<i>No. of reference GCPs</i>	<i>f (mm)</i>	<i><math>\sigma</math> (mm)</i>	<i><math>x_0</math> correction (mm)</i>	<i><math>\sigma</math> (mm)</i>	<i><math>y_0</math> correction (mm)</i>	<i><math>\sigma</math> (mm)</i>
<i>Ref 1</i>	4	100.493	0.003	0.016	0.001	-0.004	0.001
<i>Ref 2</i>	21	100.495	0.001	0.015	0.001	-0.004	0.001

Table 5-8 Refined camera parameters using reference ground control points.

Other calibration tests were performed using the methodology derived LCPs. As the triangulation results showed that at 80 LCPs the input weight appeared to have less influence in the adjustment, as shown in Figures 5-15, 5-16 and 5-17, therefore, the input weight for LCPs was set to 15 cm and the input weight for the GNSS data was set to 10 cm and the different sets of LCPs used in the calibration tests include 80, 150 and 250 LCPs. Table 5-9 shows results of these calibration tests which were performed with increasing numbers of LCPs (no GCPs). All the derived parameters were significant using the student test, except for the  $y_0$  correction using 250 LCPs, where the changes were insignificant. The result shows also, the precision of the focal length correction was 1 $\mu$ m which is similar to the precision achieved using 21 GCPs (Table 5-8). For the principal point coordinates correction, results obtained using the 80, 150 and 250 LCPs were in similar precision compared to the reference results (Table 5-8). Comparing the two results in Table 5-8 and 5-9, it can be seen that the results from *Ref 1* test is close to *LDR 1* test and results from *Ref 2* test are close to *LDR 2* test with similar precision. As the number of LCPs increase, the value of calibrated focal length approached the nominal focal length value (100.500 mm).

<i>Test No.</i>	<i>No. of reference LCPs</i>	<i>f (mm)</i>	<i><math>\sigma</math> (mm)</i>	<i><math>x_0</math> correction (mm)</i>	<i><math>\sigma</math> (mm)</i>	<i><math>y_0</math> correction (mm)</i>	<i><math>\sigma</math> (mm)</i>
<i>LDR 1</i>	80	100.493	0.001	0.017	0.001	-0.003	0.001
<i>LDR 2</i>	150	100.495	0.001	0.016	0.001	-0.004	0.001
<i>LDR 3</i>	250	100.497	0.002	0.017	0.002	-	

Table 5-9 Refined camera parameters using different sets of LCPs.

To validate the camera refined parameters, a combined bundle block adjustment was performed (ISO plus GCP) using 4 GCPs to allow using the other 17 points as independent check points. The combined block adjustment was repeated using each set of derived camera parameters obtained in Table 5-8 and Table 5-9. Block accuracy for each adjustment was assessed using the remaining 17 points as independent check-points (ICPs), and Table 5-10 shows the resulting RMSE in the three Cartesian components (easting, northing and height) at the 17 ICPs. The results show that the planimetric RMSE remained stable in all tests. However, primarily due to changes in the refined camera focal length, the height RMSE improved with increasing numbers of LCPs, the best results being obtained with the camera calibration parameters determined using the maximum number of 250 LCPs. This number was selected as the maximum number since the triangulation results described in Section 5.8 showed no more significant improvement in the triangulation accuracy. In this instance, the RMSE in height was almost twice as good as that determined using the field-surveyed GCP solution. Moreover, comparison with the results achieved for the adjustment using the nominal parameters indicates that using the largest number of LCPs (250) in self-calibration actually validates the nominal calibration values. This case with the UltraCamX camera indicates that the calibrated camera focal length provided in latest camera certification report is still valid.

Finally, the introduction of BLUH 12 additional parameters compensated for the remaining systematic errors in the image space. The root mean square error of the effect of additional parameters was 2.5  $\mu\text{m}$  in X and 3.5  $\mu\text{m}$  in Y. The comparison of the residuals represented by root mean square errors at GCPs and GNSS camera coordinates (Table 5-11) computed using the maximum number of GCPs and LCPs, showed accuracies in the range of one pixel and below.



Results of test No.	Refined camera parameters			RMSE at 17 independent check points		
	$f$ (mm)	$x_0$ (mm)	$y_0$ (mm)	RMSE <sub>x</sub>	RMSE <sub>y</sub>	RMSE <sub>z</sub>
<i>Ref 1</i>	100.493	0.160	-0.004	0.107	0.052	0.099
<i>Ref 2</i>	100.494	0.159	-0.004	0.107	0.052	0.085
<i>LDR 1</i>	100.493	0.161	-0.003	0.107	0.052	0.059
<i>LDR 2</i>	100.495	0.160	-0.004	0.107	0.052	0.052
<i>LDR 3</i>	100.497	0.161	0.000	0.109	0.053	0.043
<i>Nominal</i>	100.500	0.144	0.000	0.108	0.052	0.043

Table 5-10 RMSE calculated at 17 ICPs in the UltraCamX block using four ground control points and different sets of refined camera parameters.

No. of Points	$\sigma_0$ ( $\mu\text{m}$ )	Residuals at control points (m)			Residuals at GNSS camera coordinates (m)		
		RMSE <sub>x</sub>	RMSE <sub>y</sub>	RMSE <sub>z</sub>	RMSE <sub>x</sub>	RMSE <sub>y</sub>	RMSE <sub>z</sub>
21 GCP	5.43	0.072	0.062	0.046	0.061	0.040	0.019
250 LCP	13.57	0.096	0.059	0.074	0.077	0.033	0.057

Table 5-11 Errors at ground and Lidar control points and GNSS camera coordinates.

## 5.11 Summary

This chapter has presented the results of the evaluation of the methodology introduced in Chapter 4 using a large format digital aerial camera, the UltraCamX. The aerial data was acquired at a flying height of 1500 m above sea level giving an image resolution of 8 cm. The selected block consists of four parallel strips flown in the west-east and east-west directions with 80 % overlap and 60 % sidelap. The reference LiDAR data was acquired using a Leica ALS50 laser scanner at a flying height of approximately 500 m above ground level, which provided a point density of 6.7 points/m<sup>2</sup>. The registration process between the photogrammetric data and reference LiDAR dataset was performed after the generation of reference LiDAR DTM and a dense photogrammetric point cloud using the ISO process with and without self-calibration. After the successful registration between the two datasets, analysis of the matching results showed that introducing the self-calibration parameters in the ISO process provided more accurate matching results

with smaller residuals. Therefore, these results were used to automatically select the reference LCPs in different numbers and configurations based on predefined criteria. These points were then used to perform aerial triangulation and camera calibration using the same image dataset.

During the triangulation procedure, sensitivity tests were performed by assigning different weight values to the input LCPs ranging from 2cm to 15cm in the X, Y and Z components. Also, the accuracy of aerial triangulation was assessed using 100 LCPs which were randomly selected from across the block. These were omitted from use in the adjustment and used instead as check-points (CPs). The aerial triangulation results showed that the accuracy of the resulting aerial triangulation was lowest when a small number of LCPs was used with different weighting values, and block accuracy was improved when the number of LCPs was increased. Also, the results showed that, where the number of LCPs used exceeded 80 points, similar levels of accuracy were achieved regardless of the weight values of the LCPs. This makes that 80 LCPs is the minimum number should be used to achieve good accuracy using the derived LCPs. In addition, camera calibration was performed and the results were compared with the reference results obtained using the available field-surveyed ground control points. Comparison of the two sets of results indicated that using the largest possible number of LCPs in self-calibration validates the nominal calibration values, with the refined camera focal length remaining virtually unchanged from the nominal value.

The next chapter provides another evaluation test in order to show the transferability of the presented research methodology to other types of aerial cameras. These tests are performed using the Applanix DSS322 medium format digital aerial camera.

# CHAPTER

# 6

---

## 6 Calibration of Medium Format Camera

---

### 6.1 Introduction

Chapter Five demonstrated and validated the results of the novel methodology for automatic extraction of reference LiDAR-derived control points using the UltraCamX large format digital aerial camera. This chapter demonstrates the transferability of the research methodology using a different type of low cost digital aerial camera system. The investigation is driven by the differences in performance and stability between large and medium format digital aerial camera systems. Therefore, the methodology is further tested using the Applanix DSS322 medium format camera system. The design concept of this camera is described in Section 2.3.5. A block of 70 aerial images with GNSS/IMU data was used to generate dense photogrammetric point cloud data. This photogrammetric data is then registered to the reference LiDAR DTM surface. The detailed results and analysis are then presented for the registration between the photogrammetric point cloud and reference LiDAR DTM data. Also, the automatic extraction of LiDAR-derived control points is performed, followed by aerial triangulation and the camera calibration procedure and assessment.

### 6.2 Test Area

The aerial data was acquired over the Haltwistle area located between Newcastle and Carlisle in the north of England on 23<sup>rd</sup> of July 2007. Figure 6-1 shows a map of the location of the selected study area. The study area includes approximately 8 km of highway and a railway corridor, and data was captured for purposes of monitoring slope stability in order to assess landslide hazards (Lim *et al.*, 2007; Miller *et al.*, 2012). A sub-set of this dataset was selected which extends approximately 1.5 km in both the

east-west and north-south direction. The selected test data for this test includes seven strips which were flown mostly in the east-west direction and the north-west direction in some other areas. Also, the test area was located in a hilly area which provides a maximum height difference of 77m between the lowest and highest points across the whole study area. This variation is required in applying the surface matching registration procedure between the photogrammetric point clouds and the reference LiDAR DTM as a lack of sufficient geometric information in the test area may mean that the least-squares surface marching approach fails to find the correct alignment between the two datasets (Akca, 2007a). Moreover, the sub-area includes different land cover types such as small areas of forest, pasture, roads, railway, a river and some scattered buildings.

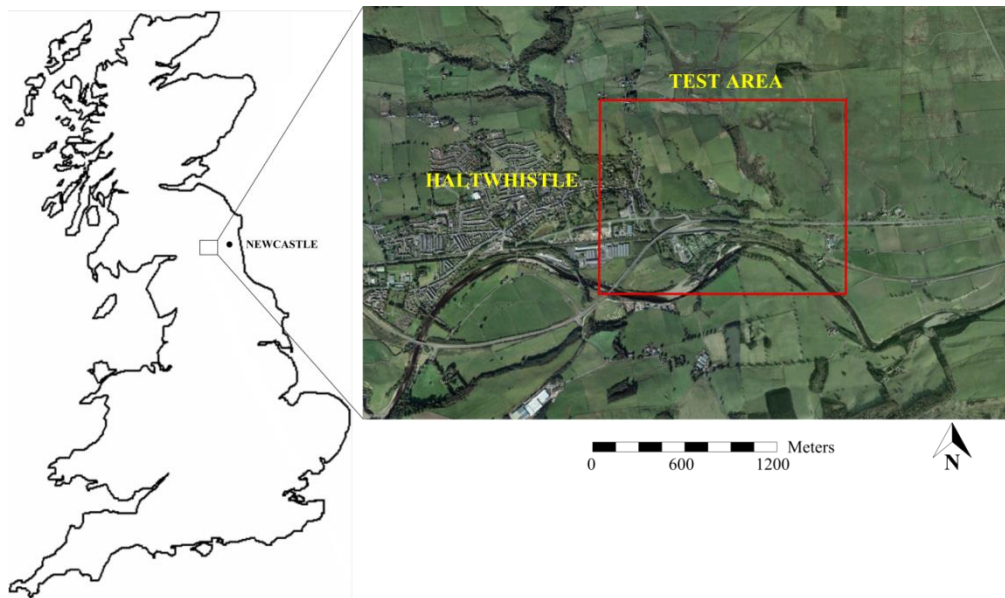


Figure 6-1 Location map of the Haltwhistle study area.

### 6.3 Photogrammetric Data

The aerial imagery was captured using an Applanix DSS322 digital camera system. The Applanix DSS322 array provides a medium format sized 5,436 pixels across and 4,092 pixels along the flight line with 9  $\mu\text{m}$  resolution. The camera was mounted on a helicopter and flown at an altitude of approximately 400 metres above the ground level, which resulted in ground coverage of approximately 193 m x 256 m with 5 cm ground resolution. As the main purpose of the original survey was capture of LiDAR data, the accompanying aerial images and the selected sub-block had an irregular structure and

variable image overlap, unlike what would be expected from a conventional photogrammetric survey. Moreover, the study area included strips which were flown mostly in the east-west direction and the north-west direction in some areas. The total number of selected images was 70, arranged in 7 strips with an irregular structure and image overlap as shown in Figure 6-2.

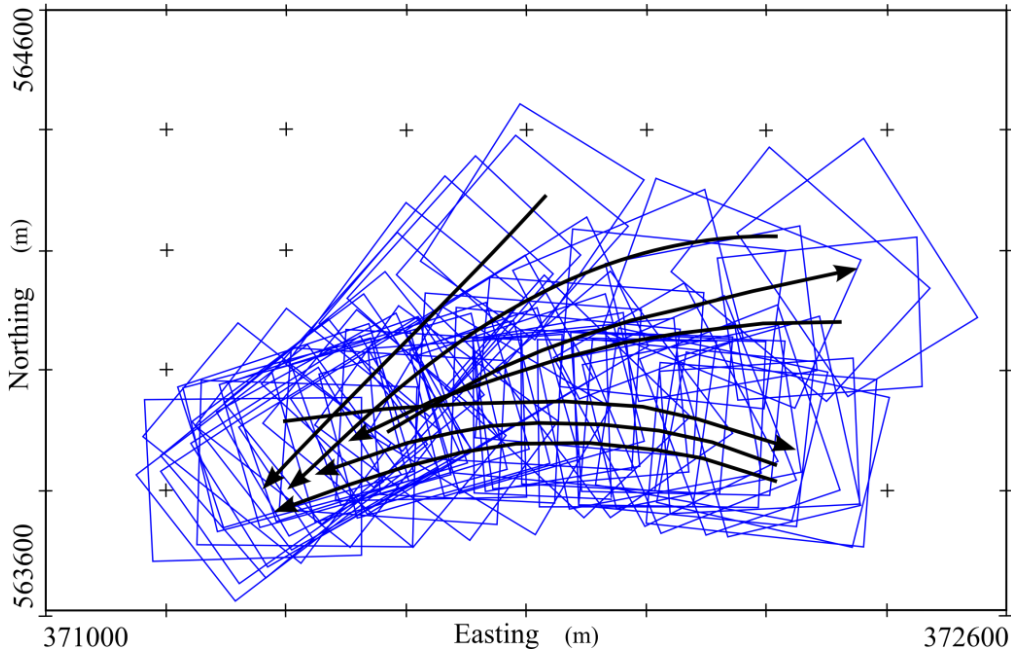


Figure 6-2 Selected block from the DSS322 dataset.

As the data acquisition was planned mainly to acquire the reference LiDAR dataset in order to monitor slope stability and assess landslide hazard, the reference targets utilised were designed to be used for the adjustment and assessment of LiDAR data. These reference targets were in the form of black, circular wooden boards 1 m in diameter, each with a 50 cm white circle placed in the middle (Csanyi and Toth, 2007). Eight reference targets were placed along the railway corridor throughout the test area. The coordinates of these reference targets were surveyed using the differential GNSS method (Lim et al., 2007). To enable direct georeferencing of the LiDAR data, the aircraft was equipped with a GNSS/IMU system in order to provide accurate data on the position and orientation of the sensor. As the selected sub-area does not contain any of these LiDAR reference targets, the GNSS camera coordinates were used as control information for the assessment and validation of the methodology.

## 6.4 Reference LiDAR Data

The LiDAR dataset was captured using a discrete pulse Optech ALTM 2050 laser scanner flown at 400 metres. The data was recorded at a pulse repetition rate of 50 kHz. This resulted in the production of point densities up to 15 points/m<sup>2</sup>. Seven LiDAR data strips were captured and have variable lateral overlap, where in some areas there is 100% overlap between strips. As the LiDAR data was mainly captured for the assessment of the railway embankment slope stability, the multiple passes of the different LiDAR strips produced larger point density in some areas up to 100 points/m<sup>2</sup> (Lim *et al.*, 2007).

#### **6.4.1 LiDAR Data Processing**

LiDAR data was processed using TerraScan software, where a processing approach, as described in Section 5.4.1 in the case of the UltraCamX, was also applied. To briefly recap, LiDAR data were classified into ground, buildings and trees. The data was provided in Transverse Mercator (TM) projection (Airy ellipsoid) and OSGB 1936 datum.

#### **6.4.2 Assessment of the Accuracy of the LiDAR Data**

Before using LiDAR data as reference in the registration of the photogrammetric point cloud, an investigation was conducted regarding the relative and absolute accuracy of the LiDAR datasets. Absolute vertical accuracy has been assessed in previous work by Lim *et al.* (2007) using reference LiDAR targets as check-points. The absolute accuracy was found to be less than 10 cm in the X, Y and Z components. Detailed assessment and analysis of the use of check-points is described in detail by Lim *et al.* (2007).

The relative accuracy between LiDAR strips was also assessed by measuring the average height difference between the LiDAR strips using the TerraMatch module. This process was performed after classifying the LiDAR data, and the comparison was based on LiDAR points classified as ground and buildings located in the overlapping areas. The average height difference between the LiDAR strips was 4.4 cm.

#### **6.4.3 Generation of Reference DTM from LiDAR Data**

For reference DTM generation, Terrascan was used to process the LiDAR data. After eliminating gross errors, and low and isolated points, key points, as described in

Section 4.5, were generated from the ground class. These key points were then thinned to reduce the data size. The height tolerance was set to  $\pm 5$  cm in order to maintain the same absolute accuracy as in the original dataset at 10 cm. The reference LiDAR DTM was finally computed using the thinned key points. However, due to the limited height variation in the east-west direction in the test area, buildings were added to the reference DTM so as to introduce further surface gradients in a variety of directions, which is necessary for surface matching (Akca, 2007a). Figure 6-3 shows the reference LiDAR DTM with added buildings.

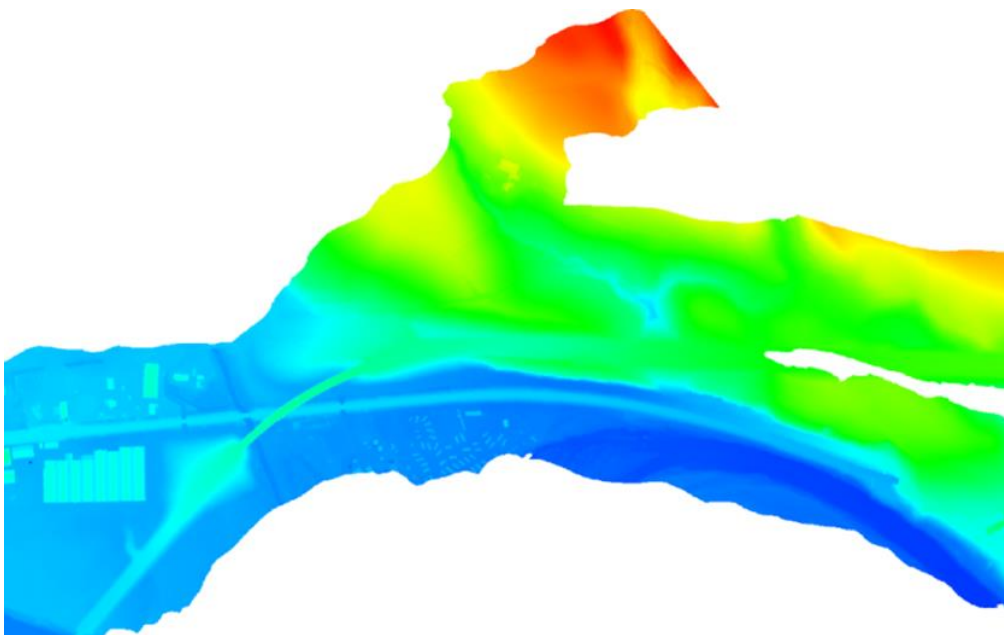


Figure 6-3 Reference LiDAR DTM with added buildings.

## 6.5 Photogrammetric Tie Point Measurement and Processing

### 6.5.1 Block Setup and Tie Point Measurement

As described in Section 5.5, automatic dense tie point measurement was performed using BAE Systems SocetSet 5.4.1. Due to the irregular structure of the image block, as shown in Figure 6-2, the aerial images were imported to SocetSet software along with GNSS camera station coordinates in order to assist in the block definition process. In the block definition process, as required by the SocetSet software, the horizontal strips flown in the east-west and west-east directions were defined before the other diagonal strips. All 70 images were assigned to the 7 strips in a left to right numbering order. MST was again used to obtain a dense network of photogrammetric tie points using a new tie point pattern file which provided a denser point pattern. Due to the smaller image footprint of the DSS322 medium format camera and lower image quality, the

number of measured tie points per image is less than those measured using images from the large format camera. This was mainly due to the fewer features for the matching software in order to achieve good correlation between the images. Therefore, the maximum number of points per image in this block was 824 and the minimum number of points was 172. The total number of tie points was 4,155, resulting in 70,258 observations in the photogrammetric block.

### 6.5.2 Computation of Tie Point Object Coordinates

Combined aerial triangulation with GNSS/IMU data and tie points (ISO) was then performed using the BLUH software in order to obtain the object coordinates of the dense photogrammetric tie points. The GNSS coordinates of camera perspective centres were provided in OSGB36 national grid coordinates. The IMU attitude angles were provided in the form of navigational HRP (heading, roll and pitch) orientations. These orientations are then converted to POK (phi, omega and kappa) photogrammetric orientations using the BLUH IMUPRE program which is part of other BLUH supporting programs dedicated for data conversion and pre-processing. The accuracy assigned to GNSS coordinates was 10 cm in the X, Y and Z axes (Honkavaara, 2003; Sandau, 2009). Due to the large number of tie points used in the bundle adjustment, blunder detection and elimination was performed in two steps: firstly, using data snooping during the approximate image orientation calculations; and secondly, using robust estimators in the first run of the bundle block adjustment, as explained in Section 4.7.2.

In the second run of ISO with GNSS/IMU data, tie point object coordinates were obtained with self-calibration using the BLUH 12 AP added in the bundle adjustment. This step was conducted in order to improve the point quality by removing distortions from the image space. After the final iteration with additional self-calibration parameters, the RMSE of differences at the GNSS coordinates were as follows:  $RMSE_x = \pm 0.728$  m,  $RMSE_y = \pm 0.459$  m,  $RMSE_z = \pm 0.642$  m and  $\sigma_0$  was 51  $\mu$ m. These results show that errors at the GNSS camera stations coordinates are 72 cm in height and 45 cm/64 cm in horizontal. These larger values are mainly due to the uncompensated systematic errors and distortions in the aerial imagery. Also, the BLUH 12 AP do not fully appropriate to model distortions of the medium format camera. Therefore, a new set of additional parameters were introduced into the BLUH software



in the latest versions (Jacobsen, 2013). This new version was unfortunately not available for this research.

### 6.5.3 Pre-Matching Photogrammetric Point Cloud Processing

Before registering the photogrammetric tie points to the reference LiDAR DTM, and in order to ensure that the photogrammetric data only represented the ground surface and added building points, the photogrammetric point cloud data was filtered to remove other points located over woodland areas. As stated in Section 5.5.3, leaving these points in the matching process would cause the matching alignment to deteriorate by introducing anomalous regions with associated large residuals. Therefore, as described in Section 4.6., a similar threshold value was used in the creation of the thematic image mask for areas exceeding 2.5 m above ground level, and this was obtained using a normalised digital surface model (nDSM). **Error! Reference source not found.** shows the derived mask image, illustrating included and omitted areas from the surface matching.



Figure 6-4 Computed mask for tie points.

Due to the irregular structure of the LiDAR data, the photogrammetric point cloud data were further filtered to remove points located outside the area covered by DTM. Therefore, the extent of the reference DTM was defined by a vector polygon and only

points located inside this polygon were selected to be used in the registration process, as shown in Figure 6-5.

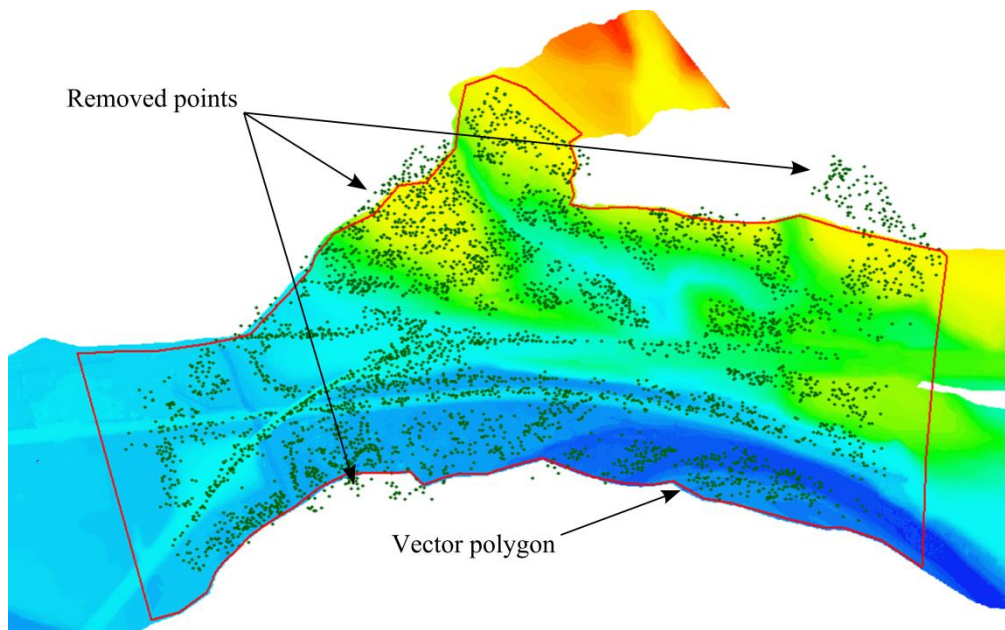


Figure 6-5 Removal of tie points located outside the LiDAR DTM coverage.

## 6.6 Photogrammetric point Cloud Registration

The registration of the photogrammetric points to the LiDAR reference DTM was performed using the same in-house, robust surface matching software LS3D as described in Section 5.6. The ISO process for the DSS322 medium format camera block provided the coordinates of the dense photogrammetric point cloud. These points were treated as the floating surface to be registered with the LiDAR reference DTM. The first matching run was performed using the photogrammetric point cloud obtained without self-calibration. This matching was not successful due to the low quality of the photogrammetric point cloud data caused by large distortions in the aerial imagery. After improving the point quality by introducing the BLUH 12 self-calibration parameters in the bundle block adjustment, the matching was repeated using the improved photogrammetric point cloud, which led to the correct alignment between the two datasets.

Transformation	Surface Matching Results
----------------	--------------------------

Parameters	ISO, no self-calibration	$\sigma$	ISO, with self-calibration	$\sigma$
T <sub>x</sub> (m)	- 2.511	0.421	0.382	0.074
T <sub>y</sub> (m)	18.332	0.391	0.284	0.053
T <sub>z</sub> (m)	- 1.226	0.082	- 7.144	0.025
$\omega$ (°)	2.43325	0.061	0.06973	0.008
$\varphi$ (°)	-0.30478	0.028	0.01002	0.004
$\kappa$ (°)	0.73172	0.016	0.07830	0.002
Scale	-	-	1.00099	0.000
Mean $\nu$ (m)	-0.935		-0.177	
RMSE $\nu$ (m)	6.123		1.313	
$\sigma \nu$ (m)	4.123		0.556	

Table 6-1 shows the matching results before and after self-calibration.

Transformation Parameters	Surface Matching Results			
	ISO, no self-calibration	$\sigma$	ISO, with self-calibration	$\sigma$
T <sub>x</sub> (m)	- 2.511	0.421	0.382	0.074
T <sub>y</sub> (m)	18.332	0.391	0.284	0.053
T <sub>z</sub> (m)	- 1.226	0.082	- 7.144	0.025
$\omega$ (°)	2.43325	0.061	0.06973	0.008
$\varphi$ (°)	-0.30478	0.028	0.01002	0.004
$\kappa$ (°)	0.73172	0.016	0.07830	0.002
Scale	-	-	1.00099	0.000
Mean $\nu$ (m)	-0.935		-0.177	
RMSE $\nu$ (m)	6.123		1.313	
$\sigma \nu$ (m)	4.123		0.556	

Table 6-1 Transformation parameters determined by surface matching.

In order to make sure that the two datasets were correctly aligned, a number of photogrammetric points were selected. These points are located at the roof corners of one of the buildings included in the registration process. Figure 6-6 shows the

corresponding points used to check the correct alignment between the original tie points located on building roof corners measured in SocetSet software and the registered tie points overlaid on the LiDAR DSM.

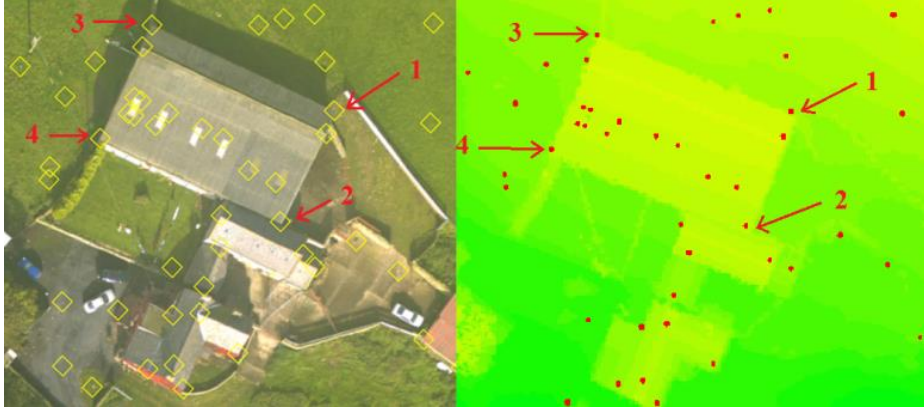


Figure 6-6 Left, measured tie point in SocetSet, right, registered tie points overlaid on LiDAR DSM.

The point matching residuals of the block area were further assessed before and after the introduction of the self-calibration parameters in the bundle block adjustment. Figure 6-7 shows the point matching residuals after the final iteration for the photogrammetric points calculated without self-calibration. Since this surface matching attempt was not successful, the misalignment between the two datasets caused the large point residuals as shown in Figure 6-7.

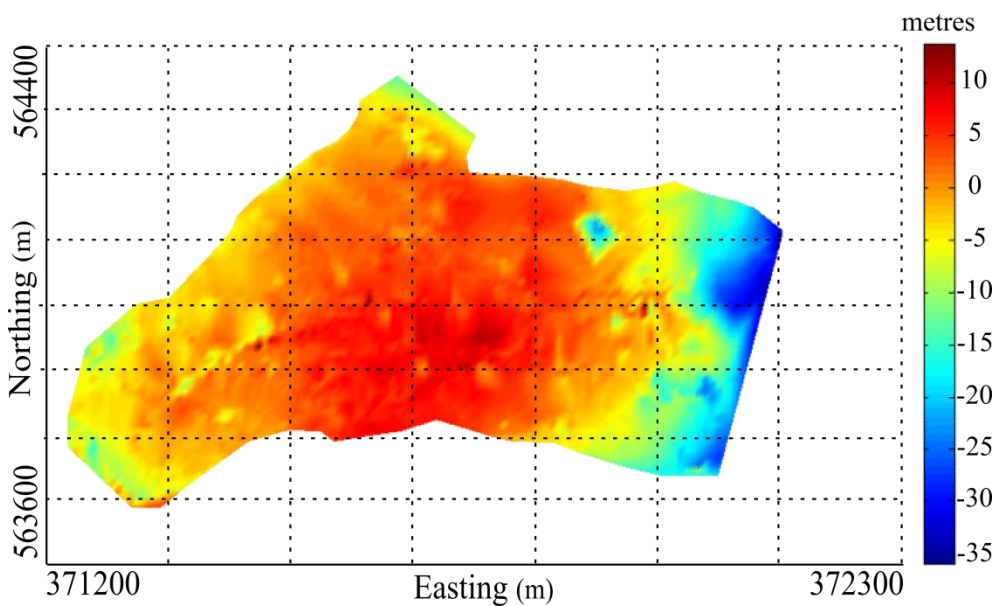


Figure 6-7 Surface matching point residuals (No AP).

However, the point residuals have been largely reduced after the correct alignment was achieved with self-calibration in the bundle adjustment. Figure 6-8 shows that the majority of points show a good correspondence with the LiDAR reference surface. Some areas have relatively large residuals, due to some undetected and remaining errors. Further analysis of the point residuals was conducted using the residual histograms for the two matching results. Figure 6-9 shows the two resulting histograms of the point residuals, where a large improvement in the matching residuals was achieved in the second run. The larger peak is formed around the mean value of the successful matching, which indicates that higher similarity was achieved between the two surfaces after the minimization of the point residuals with self-calibration in the bundle block adjustment. Therefore, this result was used as the reference for the extraction and selection of LiDAR-derived control points to be used for aerial triangulation followed by the refinement of camera parameters.

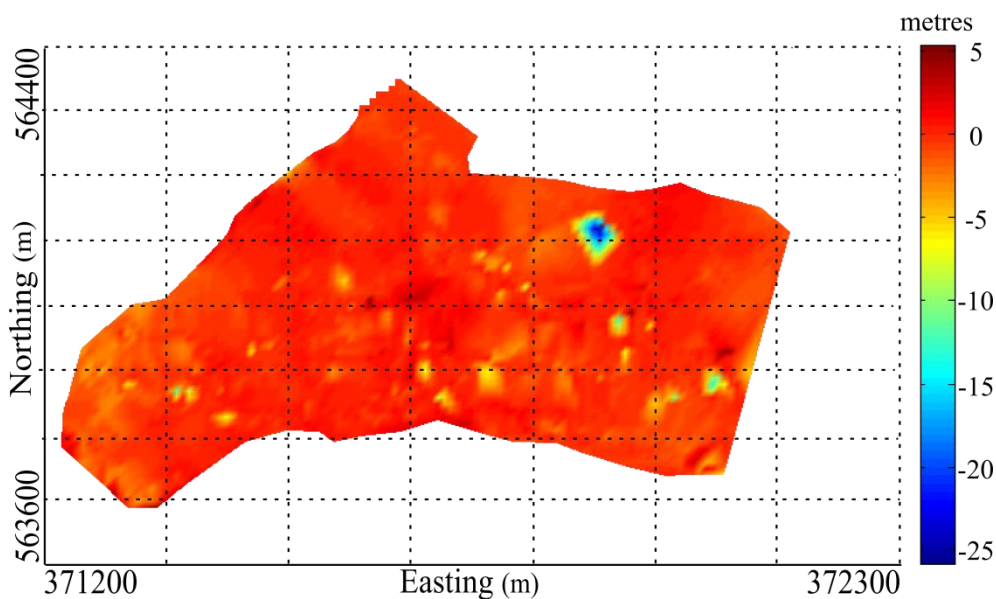


Figure 6-8 Surface matching point residuals (BLUH 12 AP).

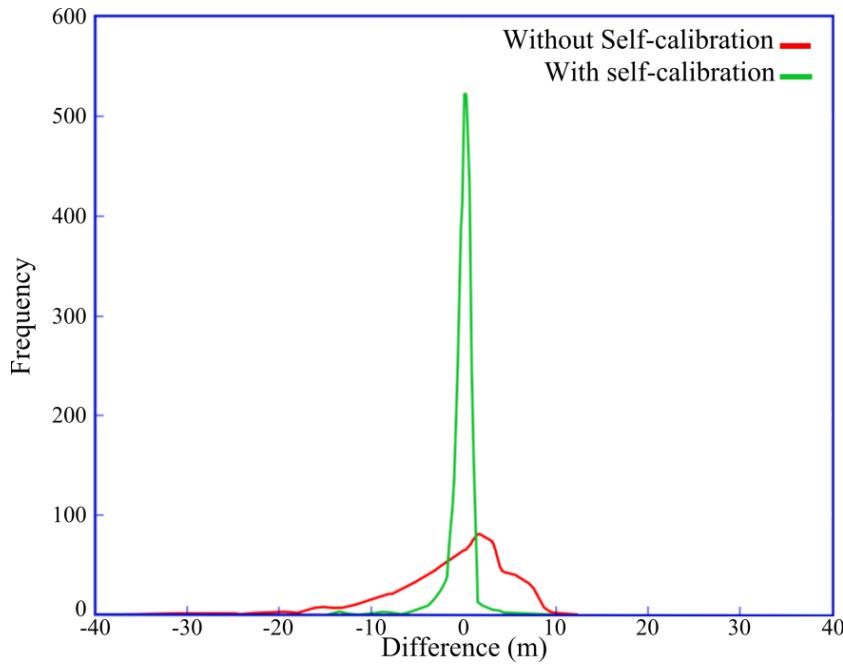


Figure 6-9 Histograms of the surface matching residuals before and after self-calibration.

The matching results after self-calibration show improvement in the planimetric accuracy of the ISO process. This is reflected in the relatively smaller values of the horizontal translation parameters  $T_x$  and  $T_y$ . A large shift in  $T_z$ , however, indicates the presence of uncompensated errors either in the camera focal length, erroneous heights of the GNSS data or change in the scale. However, the GNSS data represent accurate coordinates of the perspective centres of the camera positions at the time of image acquisition. Also, the matching results showed no significant change in scale between the photogrammetric point cloud data and the LiDAR reference DTM surface. This leads to the conclusion that the camera focal length used in the adjustment does not match the true value of the focal length. Refinement of the camera focal length, however, may be achieved using LiDAR derived control points.

## 6.7 LiDAR-derived Control Point Selection

The extraction of the reference LCPs is performed using the software developed in Matlab which controls the data flow between the BLUH bundle adjustment software and the least squares surface matching algorithm. The software also includes additional procedures for the automatic extraction of reliable LiDAR-derived control points. Despite the remaining minor errors in the second surface matching attempt, matching was regarded as successful and LCP extraction was performed based on these results using the same selection methodology described in Section 4.9 where the transformed



photogrammetric point cloud file was read and re-indexed using the reference point list file. This was followed by a series of assessments aiming to select the most reliable points based on the predefined criteria. Figure 6-10 and Figure 6-11 show examples of the point distribution of nine LCPs selected based on predefined point location and also the 50 LCPs which are based on random selection from the list of all selected control points. Figure 6-12 then shows samples of the selected point features located on different ground surfaces.

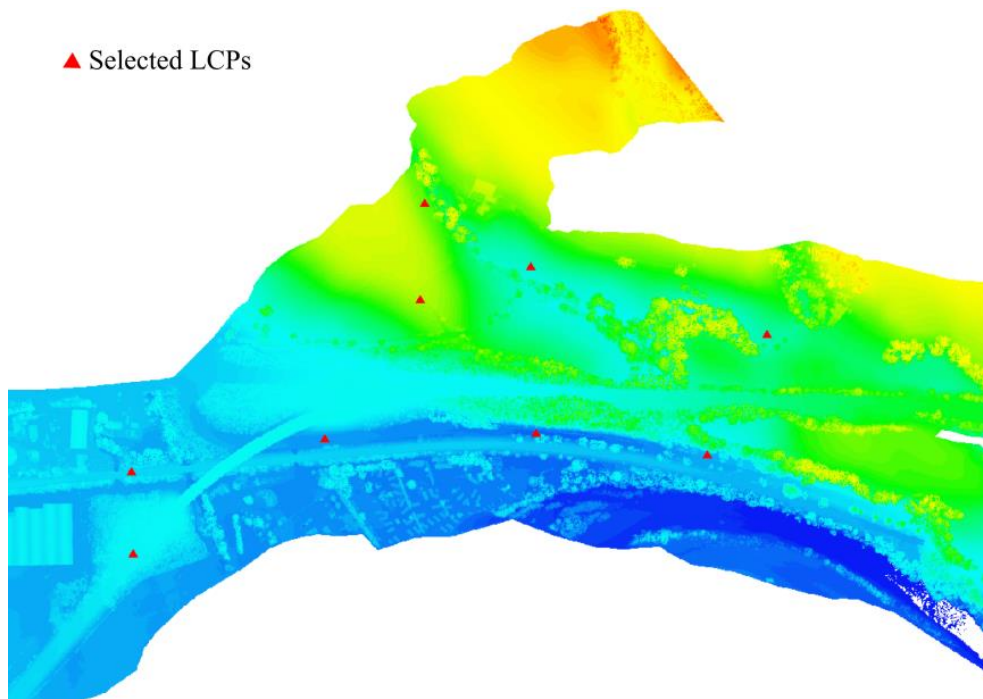


Figure 6-10 Example of nine selected LCPs.

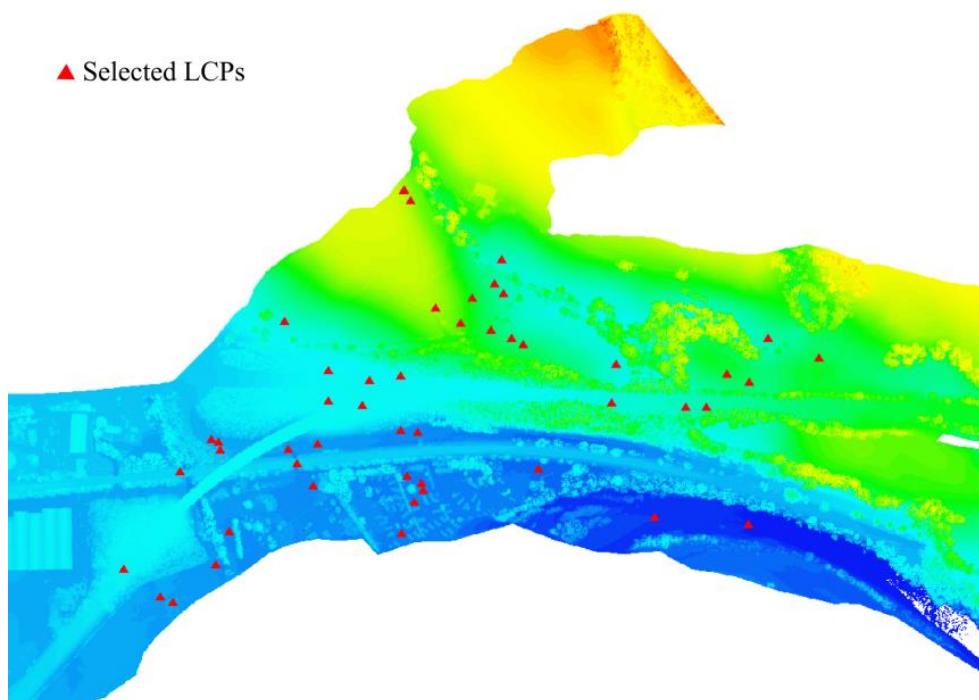


Figure 6-11 Example of 50 selected LCPs.



Figure 6-12 Samples of the selected LCPs from the DSS322 dataset.

## 6.8 Results of Aerial Triangulation Using LCPs

A testing approach similar to that used for the UltraCamX, described in Section 5.8, was used again with the DSS322 camera dataset. Here, during the triangulation procedure,



similar sensitivity tests were performed by assigning different weight values to the input LCPs ranging from 2 cm to 10 cm in the X, Y and Z components. Also, the accuracy of aerial triangulation was assessed using 50 LCPs which were randomly selected from across the block. These selected points were omitted from use in the adjustment and instead used as check points (CPs). Figure 6-13 to Figure 6-15 show the results of aerial triangulation using different sets of LCPs and different point weights without self-calibration in the bundle adjustment.

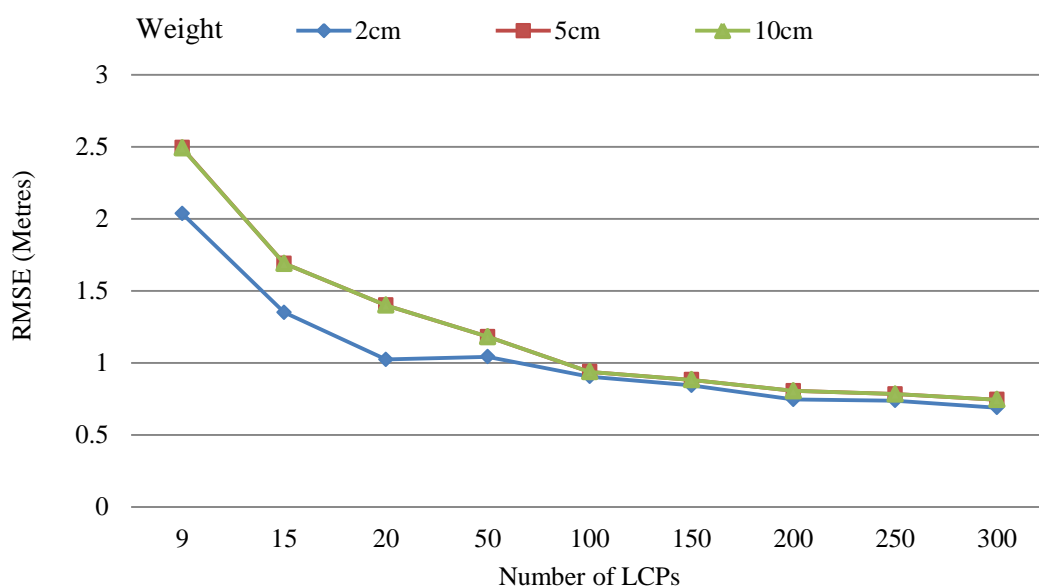


Figure 6-13 Easting RMSE at 50 check-points without self-calibration.

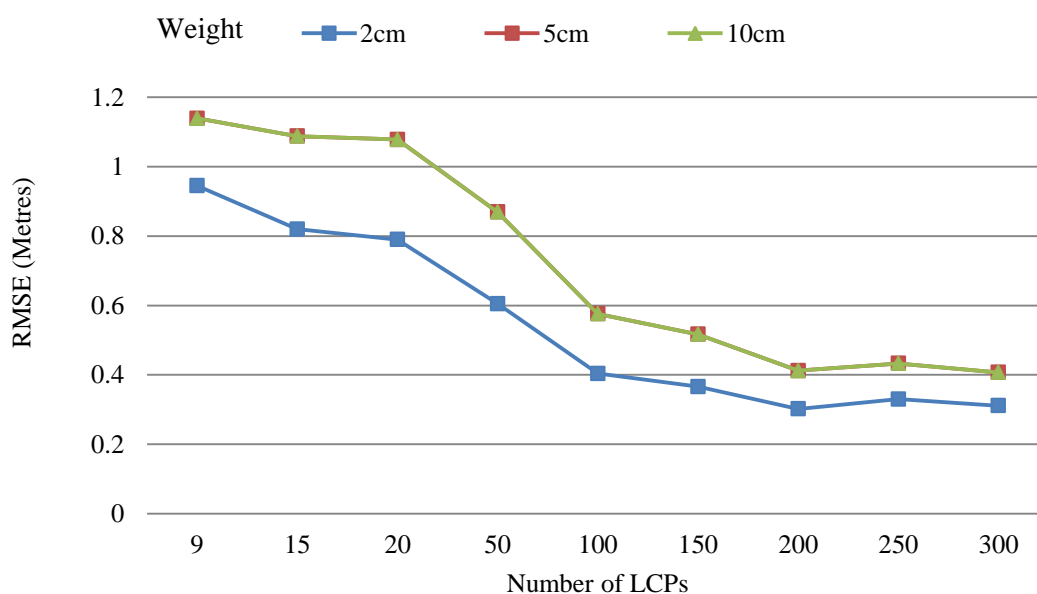


Figure 6-14 Northing RMSE at 50 check-points without self-calibration.

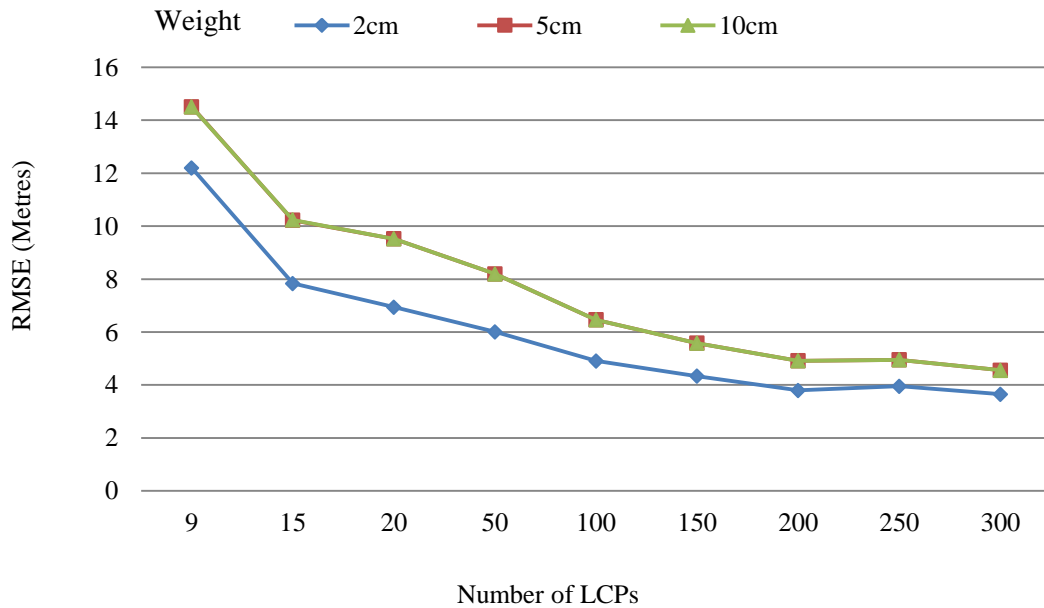


Figure 6-15 Height RMSE at 50 check-points without self-calibration.

The triangulation results without introducing the self-calibration parameters showed poor accuracy even though block accuracy improved as the number of LCPs increased. The weight of the input LCPs seems to have less influence when the number of LCPs exceeds 100. Despite this improvement, however, the level of accuracy was still far below that expected given the image resolution (5 cm). When 300 LCPs were used, the planimetric accuracy was in the range of one-half metre to four metres in height accuracy. Therefore the BLUH 12 additional parameters were introduced in the second test. Figure 6-16 to Figure 6-18 show the RMSE values at the CPs for the three Cartesian components (easting, northing and height) after introducing the BLUH 12 additional parameters. As expected, the DSS322 medium format camera imagery displayed relatively large image distortions. These distortions were eliminated through introducing the general distortion parameters in the bundle adjustment. Therefore, the accuracy of the resulting aerial triangulation was improved from the order of a metre to a decimetre after introducing the general distortion additional parameters. Further analysis of the aerial triangulation results with self-calibration show that accuracy was low when a small number of LCPs were used with 5 cm and 10 cm point weighting. The block accuracy improved when the input weighting was tightened up or when the number of LCPs was increased. It can be seen that the different weightings nearly converge at approximately 100 LCPs, with the RMSE of aerial triangulation stabilising at approximately from 8 to 10 cm in plan components. There was no improvement

beyond this number (100), regardless of weighting. The height component also converged at approximately 100 LCPs, and the RMSE in the height component stabilized at approximately 21 cm.

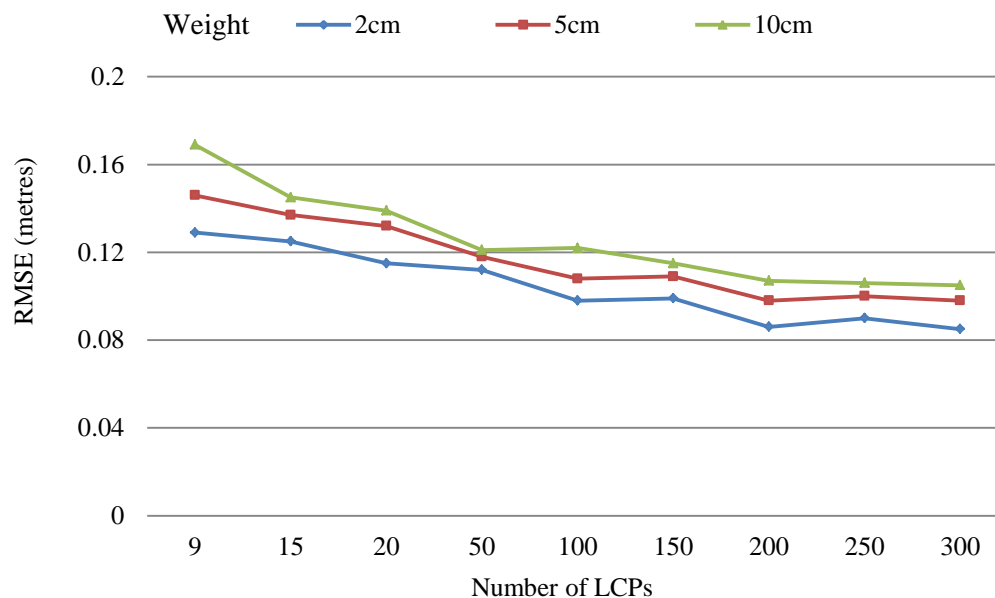


Figure 6-16 Easting RMSE at 50 check-points with 12AP self-calibration.

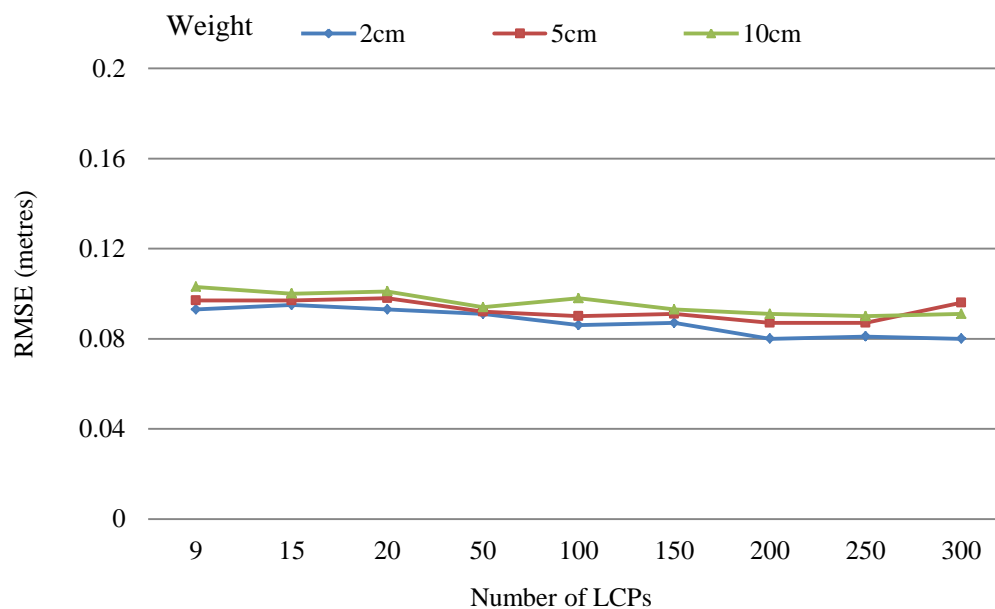


Figure 6-17 Northing RMSE at 50 check-points with 12AP self-calibration.

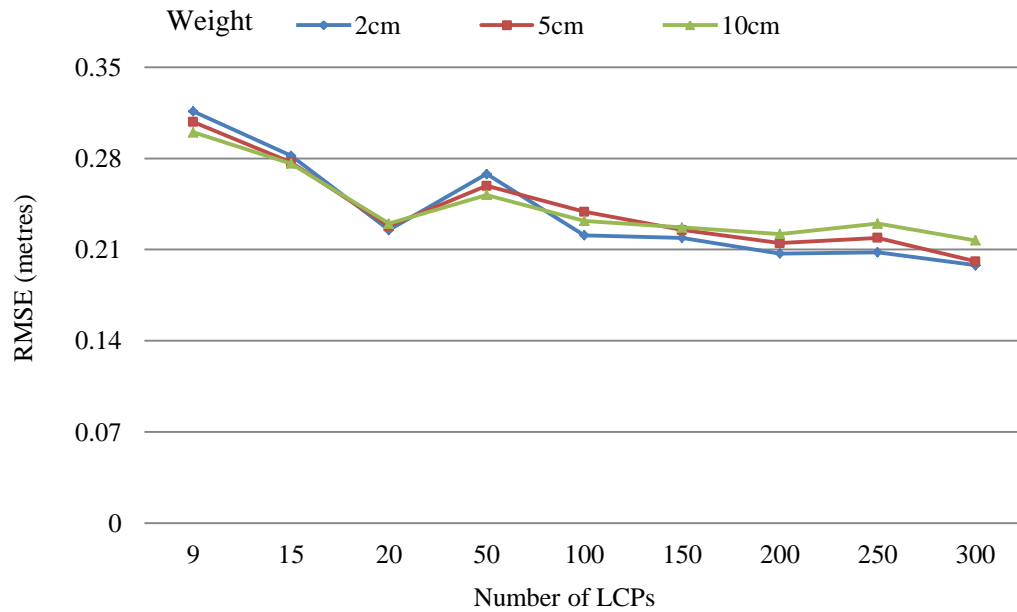


Figure 6-18 Height RMSE at 50 check-points with 12 AP self-calibration.

Based on these results, it can be seen that the DSS322 dataset showed great dependency on the use of the general distortion BLUH 12 additional parameters in order to improve the tie point quality and in turn the matching results between the reference LiDAR surface and the photogrammetric point clouds. This dependency, in addition to the radial distortion, maybe partially related to factors mainly relating to camera design. Firstly, the camera does not have panchromatic imaging and the red, green and blue images are based on Bayer CCD. The consequences of the use of this technique as discussed by Souchon *et al.* (2006) can be summarised as follows. Firstly, the red, green and red pixels are interleaved in the same CCD array. Also, due to the lack of a panchromatic channel, artifacts appear in the camera images when interpolating each individual channel, especially at the edges of linear features. This also causes what is known as chromatic aberration, where images appear to be look unfocused. Secondly, due to the absence of forward motion compensation, other types of distortions are introduced due to the motion of the aircraft. These effects were clearly visible in the aerial images, as shown in Figure 6-19. Finally, as the DSS322 camera design is based on exchangeable lenses, camera recalibration is required each time the lenses are remounted on the camera body, due to the change in interior orientation and mainly the camera's focal length (Grenzdörffer, 2008). These factors provide likely explanations for the observed difference in the camera focal length between the nominal and calibrated focal length values.



Figure 6-19 Poor image quality due to camera vibration.

## 6.9 Results of Camera Calibration Using LCPs

Even though the test area block was not originally designed for camera calibration purposes, the extracted LCPs were used to refine the camera focal length error as evidenced through the vertical shift in the matching results. Since the accuracy assigned to the GNSS measurements was  $\pm 10$  cm and the vertical accuracy of LiDAR data was also  $\pm 10$  cm, accurate calibration of the camera focal length must therefore lead to the similar heights for the camera stations. Thus, due to the lack of reference control points in the test area which could otherwise be used to conduct the reference camera calibration process, the GNSS camera station positions were used as reference benchmark measurements. These measurements were used to validate the refined camera parameters obtained using the LCPs.

Figure 6-20 shows the results of aerial triangulation using the camera's certified focal length using 300 LCPs with 12 general distortion additional parameters. The results showed a vertical difference of 6.8 meters in the camera station heights. However, introducing the focal length and principal point parameters (additional parameters no. 13 to 15) in the bundle adjustment resulted in the refinement of camera focal length and also corrections to the principal point positions. Table 6-2 shows results for refined camera parameters which were deemed to be significant in the bundle adjustment. The RMSE at the input LCPs was 0.93 m in X, 0.10 m in Y and 0.17 m in Z. Although the height variation in the test area was 75 meters which corresponds to 19% of the flying height (400 m), the layout of the block was not purely designed for camera calibration

and distortions found in some images (Figure 6-19) resulted in a higher  $\sigma_0$  (22  $\mu\text{m}$ ) and lower accuracy of the refined camera parameters, as shown in Table 6-2. These corrections in the camera parameters resulted in correction in the computed camera station heights and minimized the mean vertical difference in the exterior orientation between the triangulation results and reference GNSS measurement to -0.20 m, as shown in Table 6-3 and Figure 6-20.

	$f$ (mm)	$\sigma$ (mm)	Corrections to principal point coordinates			
			$x_0$ (-0.010 mm*)	$\sigma$ (mm)	$y_0$ (-0.096 mm*)	$\sigma$ (mm)
Nominal camera parameters	40.923	0.009	0.000	0.0036	0.000	0.0036
300 LCPs						
Without GNSS data	41.916	0.046	0.018	0.0090	0.020	0.0080

Table 6-2 Focal length refinement effect on exterior orientation accuracy.

	Mean difference (m)	Min difference (m)	Max difference (m)
Before Calibration	6.797	6.004	7.652
After Calibration	-0.200	-0.422	0.110

Table 6-3 Effect of focal length refinement on camera station height relative to GNSS height.

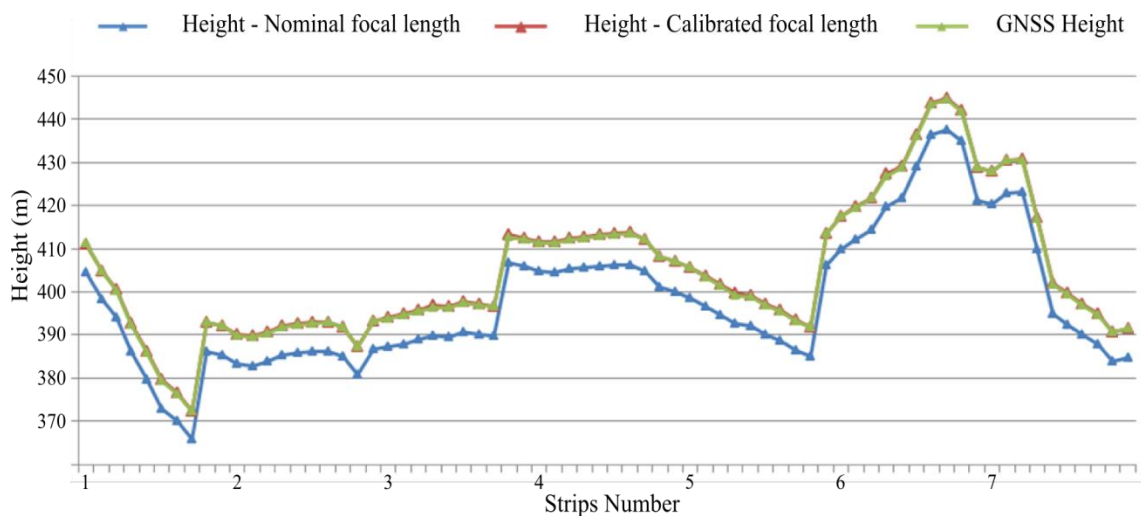


Figure 6-20 Camera station heights determined before and after focal length refinement.

## 6.10 Summary

With the evaluation of the research methodology having been demonstrated in Chapter Five, this chapter presented the results of the investigation into the transferability of the methodology to other types of aerial camera systems such as low-cost medium format digital aerial cameras. The investigation was based on aerial images acquired using the Applanix DSS322 medium format digital aerial camera system. The selected sub-block consists of 70 images arranged in 7 strips with irregular structure and overlap. The reference LiDAR DTM was generated using a LiDAR dataset captured simultaneously to the imagery using an Optech ALTM 2050 laser scanner flown at 400 metres and producing a point density of 15 points/m<sup>2</sup>.

The geographic coordinates of this data were obtained using the ISO process with and without self-calibration with additional parameters. The registration of these points to the reference LiDAR dataset was then performed using the least-squares surface matching method. The medium format camera images, however, showed large image distortions, and a successful registration was only achieved after introducing the self-calibration additional parameters.

After the successful registration and extraction of different sets and configurations of LCPs, aerial triangulation was performed to refine the camera parameters. The aerial triangulation approach using the derived LCPs was designed to allow sensitivity tests to be performed by assigning different weight values to the different numbers of input LCPs. The accuracy of aerial triangulation was assessed using 50 LCPs which were randomly selected from across the block. It has been demonstrated that using increasing numbers of LCPs is able to improve block accuracy even with low point weights. This could potentially overcome the need for conventional ground control. The effect of changes in camera parameters (in this case camera focal length) appeared in the form of a vertical shift in the transformation parameters obtained by the surface matching algorithm. Also, self-calibration using the BLUH 12 additional parameters appears to have a great influence in improving the block accuracy of the DSS322 camera system, which means that the medium format camera is largely dependent on self-calibration to achieve better results. Also, by calibrating the camera focal length using the derived LCPs it was possible to compensate for the vertical shift highlighted by the surface matching process. Validation of the calibration results was performed by comparing the

camera heights obtained using the calibrated focal length with heights computed from the reference GNSS/IMU data. The mean difference between the two heights improved from 6.8 m using the nominal focal length to -0.2 m using the calibrated focal length.



# CHAPTER

# 7

---

## 7 Conclusions and Recommendations

---

### 7.1 Revisiting the Research Aims and Objectives

The main aim of this research, as stated in Chapter One, was to investigate the use of airborne LiDAR surface for photogrammetric control through which aerial triangulation and camera system calibration can be performed using large and medium format aerial imagery. After discussion of the research outcomes, the main research objectives presented in Chapter One can now be evaluated as follows.

*Objective One:* to investigate the latest sensor technological developments in the field of airborne photogrammetry.

Chapter Two presented a comprehensive literature critique related to this objective. The rapid development in the field of CCD technology has finally enabled the production of different types of camera systems. Moreover, parallel to this development, lower cost, medium format camera models are also now produced as standard to meet the demands of different mapping applications.

*Objective Two:* to understand the characteristics of LiDAR data and to assess existing methods to integrate with photogrammetric data.

Chapter Three presented a review of the principles and main components of contemporary LiDAR systems. It also provided a detailed description of data capture, pre-processing, and also post-processing of LiDAR data. Registration methods between photogrammetric and LiDAR data were presented with relevant examples. Methods of extracting reference targets from LiDAR data for photogrammetric control were also discussed.

*Objective Three:* to build a knowledge gained from objectives 1 and 2 to develop a methodology which enables extraction of camera self-calibration parameters without the need for a conventional ground control points..

Chapter Four presented a detailed description of the developed research methodology. This methodology was based on generating dense photogrammetric point cloud data from the aerial imagery. These photogrammetric point cloud data were then registered to the reference LiDAR surface using the least-squares surface matching method. A novel procedure for automatic extraction of LiDAR-derived control points utilising the registered photogrammetric point cloud data was also implemented based on pre-defined criteria.

*Objective Four:* to validate the derived self-calibration parameters against the same parameters obtained using the conventional ground control points.

This objective was addressed in Chapter Five. The developed methodology was implemented using the UltraCamX dataset acquired over the Vaihingen/Enz test field in Germany (Cramer, 2010). Dense photogrammetric point cloud data was measured and object coordinates of these points were obtained using the ISO process. As the UltraCamX is a metric camera, the registration of this data to the LiDAR reference DTM surface was successful from the first iteration. Further improvement was made through introducing the self-calibration calibration parameters in the ISO process. The reference LCPs were extracted and used to perform aerial triangulation and refinement to the camera parameters. Comparing the calibration results with reference results obtained using GNSS surveyed reference ground control points showed good agreement between the two sets of results.

*Objective Five:* to demonstrate the flexibility of the developed research methodology using different types of airborne imagery.

The final objective was addressed in Chapter Six. It demonstrates the flexibility of the novel research methodology using two types of digital aerial camera systems. A dataset captured over Haltwistle (Northumberland, UK) using a medium format digital aerial camera (Applanix DSS322) was used in the evaluation. As expected, the camera imagery showed large dependency on self-calibration parameters to compensate for the image distortions. The use of self-calibration parameters improved the photogrammetric

point quality, surface matching and automatic extraction of reference LCPs. Finally, the camera parameters were recalibrated using the derived LCPs. Validation of the recalibrated parameters was undertaken by using the GNSS camera station data as reference measurements. This showed good agreement between the two sets of measurements.

Concluding remarks drawn from the evaluation and validation of the research methodology using different camera systems are described in the following sections.

## **7.2 Dense Photogrammetric Point Cloud Generation**

As the developed methodology was validated using two different types of digital aerial camera data, the characteristics of each camera system in terms of quality and stability had a large influence on the efficiency of this approach. In terms of the quality and density of the measured photogrammetric point cloud data, the two datasets have shown different results arising from the measurement of dense photogrammetric tie points. Although this process was performed automatically using SocetSet software (as described in Section 4.4.3), the existing pattern files used by SocetSet for tie point measurement did not provide sufficiently dense point patterns. The existing pattern files provide a minimum of 9 point and maximum of 141 point patterns. Therefore, new modified pattern files were added to the SocetSet library to provide denser photogrammetric point cloud data.

The main finding of this stage is that the results of the automated tie point measurement are dependent on the size and quality of the aerial imagery, which in turn affects the achievement of correct and accurate correlation results in the overlapping areas. The results of point measurement using the UltraCamX images resulted in measurement of a large numbers of tie points, totalling 15,707. Due to image overlaps, these points resulted in 315,232 observations in the photogrammetric adjustment. The maximum number of observations per image was 5,943 and the minimum was 1,753 for images located at the edges of the block. On the other hand, due to the smaller image footprint of the DSS322 medium format camera as well as its lower image quality, the number of measured tie points per image was less than those measured using the UltraCamX images. Therefore, the maximum number of points per image was 824 and the

minimum number of points was 172. The total number of measured tie points was 4,155 which resulted in 70,258 observations in the photogrammetric block.

The second finding here is related to the blunder detection and elimination. Due to the large number of tie points, a large number of blunders was expected. Even though the tie points were generated using the automatic point measurement method, the large image overlap introduced some erroneous measurements due to occlusion caused by trees, buildings, and rock faces in quarries. These erroneous measurements were treated before the final adjustment of the ISO process. The first treatment was made during the estimation of the image block using the data snooping method and the other treatment was performed using the robust estimators in the first iteration of the bundle adjustment.

### **7.3 Registration Approach**

As noted by Akca (2007a), “the LS3D method [surface matching] can match a 3D surface to a sparse set of 3D points provided that they have sufficiently good distribution”. A very similar least-squares surface matching procedure was used in this research to undertake the registration between the dense photogrammetric points cloud data and the reference LiDAR-derived DTM, the results of the registration being presented in Sections 5.6 and 6.6. These results showed that the quality of the registration is affected by two main factors. These factors are the quality (absolute accuracy) of the 3D photogrammetric point cloud data and also the presence of strong surface gradients in the test area to constrain the matching adjustment in the different spatial directions. Other factors such as treatment of outliers and robustness of the least-square matching solution are out of the scope of this research and are discussed elsewhere (Miller, 2007). To minimize the effects of these two factors, the quality of photogrammetric point cloud data were improved as follows: firstly, by eliminating the effect of blunders in the photogrammetric point cloud data. This was achieved using the data snooping and robust estimators methods, as described in Section 4.7.2. Secondly, improving the reference DTM height information by adding the buildings to the reference LiDAR DTM. This procedure was conducted for the DSS322 reference LiDAR dataset as the reference DTM did not provide sufficient surface gradients height information, especially in the east-west direction, as described in Section 6.4.3.

The main findings of the registration approach between the photogrammetric point cloud data and the reference LiDAR DTM applied in this research can be summarised as follows:

The use of self-calibration additional parameters is advisable in the ISO process. These parameters are used to compensate for any systematic errors in the aerial images. Therefore, it will improve the quality of the photogrammetric point cloud and, in turn, the matching results between the reference LiDAR surface and the photogrammetric point clouds. The results presented in Section 5.5.2 (Figure 5-7) showed that even the small systematic errors observed in the UltraCamX images, which are ranging up to 2  $\mu\text{m}$ , can affect photogrammetric tie point height by 5 cm, at the centre of the block, to 15 cm, at the block edges. On the other hand, the matching results from the DSS322 medium format digital aerial camera, showed great dependency on the use of self-calibration parameters.

This approach provided an automatic registration method with the ability to minimise the effects of any blunders in both datasets. Also, the point matching residuals made it possible to automatically locate points located in the 'best fit' areas within a given threshold. These points were then further assessed and used as reference LCPs in the triangulation. Moreover, the effects of changes in the camera parameters (i.e. in the case of the DSS322 camera focal length) appear in the form of vertical or horizontal shifts in the transformation parameters obtained by the surface matching algorithm.

## **7.4 Extraction of LiDAR-derived Control Points**

The automatic extraction of reference LCPs is performed by the developed Matlab algorithm. This algorithm also controls the methodology workflow. The automatic extraction process commences after achieving a successful registration between the photogrammetric point cloud data and the reference LiDAR DTM. This approach has allowed extraction of a dense network of reference LCPs, as demonstrated in Sections 5.7 and 6.7.

The LCP selection procedure, as described in Section 4.9, is designed to perform various assessments to ensure a high quality of point selection. These assessments involve a distance test to select points located in the best match areas, a planarity test to select only points located over planar surfaces, a surface gradient test to avoid points

located on steep surfaces, and a reliability test to ensure that the selected points have enough redundancy for blunder detection. Finally, the spatial distribution of the selected points across the photogrammetric block is also assessed.

The developed selection procedure, described in section 4.9, is flexible so that the threshold values assigned for the different tests (i.e. point residuals, planarity and slope angle) can be alternated to accommodate the characteristics of any other reference 3D datasets.

## 7.5 Aerial Triangulation Using LCPs

Chapters Five and Six have demonstrated the results of aerial triangulation and refinement of the camera parameters using LiDAR-derived control points. Sections 5.8 and 6.8 showed the triangulation results for the two camera systems. As the exact accuracy of the LiDAR-derived reference points is not precisely known due to the varying influence of different land cover types included in the LiDAR DTM, sensitivity tests were performed using values ranged from 2 to 15 cm which were assumed to be representative, as described in Sections 5.4.2 and 6.4.2. It was also described that the absolute vertical accuracy of the LiDAR data is in the range of 2.5 to 10 cm. Moreover, the planimetric accuracy of LiDAR data in general is assessed according to Vosselman and Maas (2010) and Lim *et al.* (2007) to be ranging from 0.1 m to 1.0 m.

The first finding drawn from the triangulation results is that by using increasing numbers of LCPs in the triangulation, it is possible to improve block accuracy even with low point weights. It also showed that, using the UltraCamX camera dataset, where the number of LCPs used exceeded 80, similar levels of accuracy were achieved regardless of the weight values of the input LCPs. A similar trend was observed with the DSS322 dataset, where the results of aerial triangulation with self-calibration parameters stabilized when the number of LCPs exceeded 100. These two results showed that in the case of low cost cameras, a large number of points must be used. Therefore, based on this finding, it is recommended that sensitivity tests be applied to each camera type and to each block configuration. This is in order to determine the optimal number of LCPs required to achieve similar block accuracies for the different point weights.

The second finding of the triangulation results is that introducing self-calibration parameters in the bundle adjustment has led to better and more accurate results.

Although this improvement varied between the two types of cameras and blocks, the UltraCamX data have shown small improvements in the planimetric and vertical accuracy when the BLUH 12 general set of additional parameters are incorporated. However, for the DSS322 medium format camera, the BLUH 12 general additional parameter set did not fully compensate for the image distortions. Therefore, it is recommended to use the new set of additional parameters designed for medium format cameras introduced in the latest versions of the BLUH software (Jacobsen, 2013). This new version was unfortunately not available for this research.

## 7.6 Camera Calibration Results

Camera test field calibration is performed to determine the camera calibration parameters in a real working environment (Honkavaara, 2003). Although these parameters have already been provided by system manufacturers through laboratory calibration, they may change under real mapping flight conditions (Kruck, 2006; Jacobsen, 2007b). For low cost cameras with less stable camera parameters, the environmental conditions between the test field and the mapping area may also differ. Establishing a new test field for every mapping area is expensive and largely impractical. Therefore, the novel methodology developed in this research enables the extraction of reference control targets from the complementary reference LiDAR dataset and provides a demonstrated alternative to perform camera calibration without the need for ground control points.

Results presented in Sections 5.10 and 6.9 showed refinement of camera IO parameters for the two camera types (UltraCamX and DSS322) using the derived reference LCPs. For validation purposes, these results, obtained using the research methodology, were compared with the reference calibration results obtained using ground control points. For the UltraCamX calibration results shown in Tables 5-8 and 5-9, it has been demonstrated that the two calibration results are in a good agreement. Also, results showed that the refined camera parameters obtained using a large number of LCPs, led to the best block accuracy in the validation test, and that this was highly similar to the results obtained using the nominal focal length. These validation results indicated that the nominal value of the focal length provided in the camera certificate is still valid. Moreover, corrections to the principal point coordinates are also similar in both calibration tests.

For the DSS322 medium format camera, due to the lack of reference GCPs in the selected test area, the GNSS data of the camera station coordinates were used as control measurements to validate the refined camera focal length. The calibration results illustrated in Table 6-2 show that the refined focal length led to camera station heights similar to the reference GNSS data and eliminated the height error shown in the matching results in Table 6-1.

Finally, as differences in the environmental conditions between the test field and mapping areas may affect the validity of the nominal camera parameters, and establishing a new test field for every mapping area is expensive and largely impractical. Therefore, this approach can be applied to perform in-situ camera calibration without the need for conventional GCPs. Also, this approach is particularly valuable in the case of medium and small format digital cameras where the traditional aerial triangulation approach would sometimes be difficult and costly, and where camera parameters may not be stable over time or regularly calibrated.

## **7.7 Research Limitations**

Although the developed research approach provides a suitable and affordable alternative to camera field calibration, some limitations of this approach can also be highlighted. The first limitation is the availability of LiDAR data for the test area. Also, if there is a reference LiDAR data already acquired, the test area must have sufficient geometric information (surface gradients) represented by the DTM. If these surface gradients are not existing then the surface marching approach may fail (Akca, 2007a). Moreover, the land cover of the test area must provide sufficient surface texture which can be detected by the point measurement software. For example, snow covered areas might not be suitable for production of dense photogrammetric point measurements.

## **7.8 Recommendations for Future Work**

The presented research has mainly focused on registration of dense photogrammetric point cloud data to reference LiDAR surfaces and automatic extraction of reference LCPs to perform aerial triangulation and camera calibration. However, further investigations and tests are recommended to be performed which could cover the following areas:



- This approach assumes that the photogrammetric block has strong connections and no systematic errors are introduced from weak block geometry. If this problem exists in any photogrammetric dataset, the suggested solution is to apply surface matching using different patches as proposed by Akca (2007a), where each part of the block will be matched individually to the corresponding part of the reference DTM. The final solution will be obtained from the combined patches.
- The self-calibration of the medium format DSS322 digital aerial camera was based on the standard BLUH 12 additional parameter set. Therefore, it is recommended to perform further investigation on the adequacy of the additional parameters for the DSS322 medium format camera. In the latest version of BLUH (unfortunately not available for this research), new additional parameters especially designed for medium format cameras were added. Therefore, these new additional parameters are expected to provide further improvement in the quality of photogrammetric point cloud data (Jacobsen, 2013).
- As the block structure plays a major role in determining the camera parameters (Honkavaara, 2003), further investigations are recommended to assess the effect of different block structures on the registration results and also the determinability of the camera parameters using different block structure configurations.
- This research focussed on using a reference DTM derived from LiDAR data. However, the approach is flexible and there is potential to use other sources of reference DTM, provided that high accuracy and consistency is provided. Moreover, investigation into the use of a DSM (rather than a DTM) as a reference surface is also recommended, as it offers the potential to provide greater surface variation (improved surface gradients).
- Further research is also recommended to investigate the utility of the developed approach in the camera GNSS/IMU boresight calibration. This investigation includes obtaining the components of the boresight angles between the camera body and IMU, and also the lever arm positional offsets between the GNSS antenna and camera perspective centre.

## References

- Aguilar, F.J., Aguera, F., Aguilar, M.A. and Carvajal, F. (2005) 'Effects of terrain morphology, sampling density, and interpolation methods on grid DEM accuracy', *Photogrammetric engineering and remote sensing*, 71(7), p. 805.
- Aguilar, F.J., Mills, J.P., Delgado, J., Aguilar, M.A., Negreiros, J.G. and Pérez, J.L. (2010) 'Modelling vertical error in lidar-derived digital elevation models', *ISPRS Journal of Photogrammetry and Remote Sensing*, 65(1), pp. 103-110.
- Akca, D. (2007a) 'Least Squares 3D surface matching', *Ph.D. thesis*, Institute of Geodesy and Photogrammetry, ETH Zurich, Zurich,(92), p. 78.
- Akca, D. (2007b) 'Matching of 3D surfaces and their intensities', *ISPRS Journal of Photogrammetry and Remote Sensing*, 62(2), pp. 112-121.
- Al-Durgham, M., Fotopoulos, G. and Glennie, C. (2010) 'On the accuracy of lidar derived digital surface models', in Mertikas, S.P. (ed.) *Gravity, Geoid and Earth Observation*. Springer Berlin Heidelberg, pp. 689-695.
- Alamús, R. and Kornus, W. (2008) 'DMC geometry analysis and virtual image characterisation', *The Photogrammetric Record*, 23(124), pp. 353-371.
- Alamús, R., Kornus, W. and Talaya, J. (2006) 'Studies on DMC Geometry', *ISPRS Journal of Photogrammetry and Remote Sensing*, 60, pp. 375 - 386.
- Armenakis, C., Gao, Y. and Sohn, G. (2012) 'Semi-automatic co-registration of photogrammetric and lidar data using buildings', *ISPRS Annals of the Photogrammetry, Remote Sensing and Spatial Information Sciences*, I-3, pp. 13-18.
- Armenakis, C., Gao, Y. and Sohn, G. (2013) 'Co-registration of aerial photogrammetric and lidar point clouds in urban environments using automatic plane correspondence', *Applied Geomatics*, 5(2), pp. 155-166.
- Axelsson, P. (2000) 'DEM generation from laser scanner data using adaptive TIN models', *International Archives of Photogrammetry and Remote Sensing*, 33(B4), pp. 111-118.
- Baarda, W. (1968) 'A testing procedure for use in geodetic networks', *Statistical Concepts in Geodesy*, Netherlands Geodetic Commission New Series, 4, Delft.
- BAE Systems (2007) 'SocetSet User's Manual', Version 5.4.1, p. 1134.

- Baltsavias, E. (2008) 'Introduction to airborne lidar and physical principles of lidar technology', *Lecture notes distributed on the international school on lidar technology, 31 March - 4 April*, Institute of Geodesy and Photogrammetry, ETH Zurich, p. 129.
- Baltsavias, E.P. (1999) 'A comparison between photogrammetry and laser scanning', *ISPRS Journal of photogrammetry and Remote Sensing*, 54(2), pp. 83-94.
- Blais, F. (2004) 'Review of 20 years of range sensor development', *Journal of Electronic Imaging*, 13(1), pp. 231-240.
- Böhm, J. (2011) 'Report of the institute for photogrammetry, University of Stuttgart', in Rönnholm, P. (ed.) *Registration quality towards integration of laser scanning and photogrammetry*. Amsterdam, The Netherlands: Official Publication - EuroSDR, (59), pp. 229-237.
- Brenner, C., Dold, C. and Ripperda, N. (2008) 'Coarse orientation of terrestrial laser scans in urban environments', *ISPRS Journal of Photogrammetry and Remote Sensing*, 63(1), pp. 4-18.
- Brown, D.C. (1966) 'Decentering distortion of lenses', *Photometric Engineering*, 32(3), pp. 444-462.
- Brown, D.C. (1971) 'Close range camera calibration', *Photogrammetric Engineering and Remote Sensing*, 37(8), pp. 855-866.
- Brown, D.C. (1976) 'The bundle adjustment—progress and prospects', *International Archives for Photogrammetry, Remote Sensing and Spatial Information Sciences*, 21(3), p. 1.1.
- Brown, D.C. (1989) 'A strategy for multi-camera on-the-job self-calibration', *International Archive of Photogrammetry and Remote Sensing*, 19(5)(5), pp. 9-21.
- Buckley, S.J. (2003) 'A geomatics data fusion technique for change monitoring', *PhD thesis*, University of Newcastle Upon Tyne, Newcastle Upon Tyne, 258p.
- Canny, J. (1986) 'A computational approach to edge detection', *IEEE Transactions on Pattern Analysis and Machine Intelligence*, 8, pp. 679-698.
- Clarke, T. and Fryer, J.G. (1998) 'The development of camera calibration methods and models', *The principal point and CCD cameras. The Photogrammetric Record*, 16 (92), pp. 293-312.
- Cramer, M. (1999) 'Direct geocoding - is aerial triangulation obsolete', *Photogrammetric week '99*.
- Cramer, M. (2002) 'Experiences on operational GPS/inertial system calibration in airborne photogrammetry', *Journal GIS - Geoinformations systeme*, 14(6), pp. 37-42.
- Cramer, M. (2003) 'Integrated GPS/inertial and digital aerial triangulation - recent test results', *Proceedings of Photogrammetric Week, Stuttgart*.

- Cramer, M. (2004a) *EuroSDR network on digital camera calibration*. Stuttgart.
- Cramer, M. (2004b) 'Performance of medium format digital aerial sensor systems', *The International Archives of the Photogrammetry, Remote Sensing and Spatial Information Sciences*, 35(B5), pp. 769-774.
- Cramer, M. (2005) '10 years ifp test site Vaihingen/Enz: An independent performance study', *Photogrammetric Week '05*, Wichmann, Heidelberg, pp. 79-92.
- Cramer, M. (2006) 'Calibration and validation of digital airborne cameras', *International Archives of Photogrammetry, Remote Sensing and Spatial Information Sciences*, 36(B1), p. unpaginated CDROM.
- Cramer, M. (2007a) *European Digital Airborne Camera Certification – EuroDAC<sup>2</sup>*. Rotterdam, The Netherlands.
- Cramer, M. (2007b) 'The EuroSDR performance test for digital aerial camera systems', *Photogrammetric Week*, 7, pp. 89-106.
- Cramer, M. (2009) 'Digital Camera Calibration', *EuroSDR Official publication*, 55, p. 257.
- Cramer, M. (2010) 'The DGPF test on digital airborne camera evaluation overview and test design', *Photogrammetrie Fernerkundung Geoinformation*, 2010(2), pp. 73-82.
- Cramer, M., Kresse, W., Skaloud, J., Haala, N., Nittel, S. and Wallgrün, J. (2012) 'Data Capture', in Kresse, W. and Danko, D.M. (eds.) *Springer Handbook of Geographic Information*. Springer Berlin Heidelberg, pp. 119-157.
- Cramer, M. and Stallmann, D. (2001) 'On the use of GPS/inertial exterior orientation parameters in airborne photogrammetry', *OEEPE- Workshop, Integrated Sensor Orientation*.
- Cramer, M., Stallmann, D. and Haala, N. (1999) 'Sensor integration and calibration of digital airborne Three-Line camera systems', *International Workshop on Mobile Mapping Technology, Bangkok, Thailand*.
- Csanyi, N. and Toth, C.K. (2007) 'Improvement of lidar data accuracy using lidar-specific ground targets', *Photogrammetric engineering and remote sensing*, 73(4), p. 385.
- Delara, R., Mitishita, E. and Habib, A. (2004) 'Bundle adjustment of images from non-metric CCD camera using LIDAR data as control points', *International Archives for Photogrammetry, Remote Sensing and Spatial Information Sciences*, 20(B3), pp. 13-18.
- Dewitt, B.A. (1996) 'Initial approximations for the three-dimensional conformal coordinate transformation', *Photogrammetric engineering and remote sensing*, 62(1), pp. 79-84.
- Dorstel, C. (2007) 'DMC - (R)evolution on Geometric Accuracy', *Photogrammetric Week 2007, Wichmann, Heidelberg*.

- Dörstel, C. (2000) 'Digital Modular Camera: System concept and data processing workflow', *International Archives of the Photogrammetry, Remote Sensing and Spatial Information Sciences*, 33(B2), pp. 164-171.
- Dörstel, C. (2009) 'RMK D - A True metric medium format digital aerial camera system practical experience and accuracy assessment', *Photogrammetric Week*, Stuttgart, Germany, pp. 91-98.
- Dörstel, C., Jacobsen, K. and Stallmann, D. (2003) 'DMC - photogrammetric accuracy - calibration aspects and generation of synthetic DMC images', *Optical 3-D Measurement techniques I(VI)*, pp. 74-88.
- Ebner, H. (1976) 'Self calibrating block adjustment', *International Archive of Photogrammetry and Remote Sensing*, 21(13), pp. 128-139.
- Filin, S. and Vosselman, G. (2004) 'Adjustment of airborne laser altimetry strips', *International Archives for Photogrammetry, Remote Sensing and Spatial Information Sciences*, 35(B3), pp. 285-289.
- Grenzdörffer, G. (2008) 'Medium format digital cameras-a EuroSDR project', *International Archives of the Photogrammetry, Remote Sensing and Spatial Information Sciences*, 37(B1), pp. 1043-1050.
- Grenzdörffer, G. (2010a) 'Medium Format Cameras', *EuroSDR Official publication* 58, pp. 233-262.
- Grenzdörffer, G. (2010b) 'Performance of medium format digital airborne cameras', *Official Publication - EuroSDR*, (58), pp. 233-265.
- Gruber, M. and Ladstädter, R. (2008) 'Calibrating the digital large format aerial camera UltraCamX', *International Calibration and Orientation Workshop, EuroCOW*, 30 January - 1 February, Castelldefels, Spain.
- Gruber, M. and Ladstätter, R. (2006) 'Geometric issues of the digital large format aerial camera UltraCamD', *International Calibration and Orientation Workshop EuroCOW*, 25-27 January, Castelldefels, Spain.
- Gruber, M., Ponticelli, M., Bernögger, S. and Leberl, F. (2008) 'Ultracamx, the Large Format Digital Aerial Camera System by Vexcel Imaging/Microsoft', *International Archives of the Photogrammetry, Remote Sensing and Spatial Information Sciences*, 37(B1), pp. 665-670.
- Gruber, M., Ponticelli, M., Ladstädter, R. and Wiechert, A. (2012) 'Ultracam Eagle , Details and insight', *International Archives for Photogrammetry, Remote Sensing and Spatial Information Sciences*, 39(B1), pp. 15-19.
- Grün, A. (1978) 'Progress in photogrammetric point determination by compensation of systematic errors and detection of gross errors', *International Society for Photogrammetry, Symposium of Comission III, Moscow, USSR*.

- Grün, A. (1982) 'The accuracy potential of the modern bundle block adjustment in aerial photogrammetry', *Photogrammetric engineering and remote sensing*, 48, pp. 45-54.
- Haala, N., Hastedt, H., Wolf, K., Ressler, C. and Baltrusch, S. (2010) 'Digital photogrammetric camera evaluation generation of digital elevation models', *Photogrammetrie Fernerkundung Geoinformation*, 2010(2), pp. 99-115.
- Habib, A., Ghanma, M. and KIM, E.M. (2005a) 'Lidar data for photogrammetric georeferencing', *FIG Working Week 2005 and GSDI-8*, April 16-21, Cairo, Egypt p. 15.
- Habib, A., Ghanma, M. and Mitishita, E. (2009) 'Co-registration of photogrammetric and lidar data: Methodology and case study', *Revista Brasileira de Cartografia*, 1(56).
- Habib, A., Ghanma, M., Morgan, M. and Al-Ruzouq, R. (2005b) 'Photogrammetric and lidar data registration using linear features', *Photogrammetric engineering and remote sensing*, 71(6), pp. 699-707.
- Habib, A., Kersting, A.P. and Kim, C.J. (2010) 'Impact of camera and system calibration on photogrammetric reconstruction using medium format digital camera', *International Archives for Photogrammetry, Remote Sensing and Spatial Information Sciences*, 38(Part A), p. 6.
- Habib, A., Kwak, E., Wang, S. and Kersting, A.P. (2011) 'Report of the University of Calgary', in Rönnholm, P. (ed.) *Registration quality towards integration of laser scanning and photogrammetry*. Amsterdam, The Netherlands: Official Publication - EuroSDR, (59), pp. 141-162.
- Habib, A., Pullivelli, A., Mitishita, E., Ghanma, M. and Kim, E.M. (2006a) 'Stability analysis of low-cost digital cameras for aerial mapping using different georeferencing techniques', *The Photogrammetric Record*, 21(113), pp. 29-43.
- Habib, A.F., Ghanma, M.S., Kima, C.J. and Mitishita, E. (2004a) 'Alternative approaches for utilizing lidar data as a source of control information for photogrammetric models', *International Archives of the Photogrammetry, Remote Sensing and Spatial Information Sciences*, 35(B1), pp. 193-198.
- Habib, A.F., Ghanma, M.S., Mitishita, E.A., Kim, E.-M. and Kim, C.J. (2005c) 'Image georeferencing using lidar data', *Geoscience and Remote Sensing Symposium, IEEE International*, 2, pp. 1158-1161.
- Habib, A.F., Ghanma, M.S., Morgan, M.F. and Mitishita, E. (2004b) 'Integration of laser and photogrammetric data for calibration purposes', *International Archives for Photogrammetry, Remote Sensing and Spatial Information Sciences*, 20(B2), pp. 170-176.
- Habib, A.F., Morgan, M. and Lee, Y.R. (2002) 'Bundle adjustment with self-calibration using straight lines', *The Photogrammetric Record*, 17(100), pp. 635-650.
- Habib, A.F., Shin, S., Kim, C. and Al-Durgham, M. (2006b) 'Integration of photogrammetric and lidar data in a multi-primitive triangulation environment', in

- Abdul-Rahman, A., Zlatanova, S. and Coors, V. (eds.) *Innovations in 3D Geo Information Systems*. Springer Berlin Heidelberg, pp. 29-45.
- Hefele, J. (2006) 'Calibration experience with the DMC', *International Calibration and Orientation Workshop EuroCOW*, 25 - 27 January, Castelldefels, Spain.
- Heipke, C., Jacobsen, K. and Wegmann, H. (2002a) 'Analysis of the results of the OEEPE test "Integrated Sensor Orientation"', *OEEPE Official Publication*, 43, pp. 31-49.
- Heipke, C., Jacobsen, K. and Wegmann, H. (2002b) 'Integrated sensor orientation—Test report and workshop proceedings', *OEEPE, Official publication*, 43.
- Hoaglin, D.C. and Welsch, R.E. (1978) 'The hat matrix in regression and ANOVA', *The American Statistician*, 32(1), pp. 17-22.
- Hobi, M.L. and Ginzler, C. (2012) 'Accuracy assessment of Digital Surface Models based on WorldView-2 and ADS80 stereo remote sensing data', *Sensors*, 12(5), pp. 6347-6368.
- Hodgson, M.E. and Bresnahan, P. (2004) 'Accuracy of airborne lidar-derived elevation: empirical assessment and error budget', *Photogrammetric Engineering and Remote Sensing*, 70(3), pp. 331-340.
- Honkavaara, E. (2003) 'Calibration Field Structures for GPS/IMU/Camera-system Calibration', *The Photogrammetric Journal of Finland*, 18(2), pp. 3-15.
- Honkavaara, E., Ilves, R. and Jaakkola, J. (2003) 'Practical results of GPS/IMU/camera system calibration', *Proceedings of International Workshop: Theory, Technology and Realities of Inertial/GPS Sensor Orientation, Spain*.
- Honkavaara, E., Jaakkola, J., Markelin, L. and Becker, S. (2006) 'Evaluation of resolving power and MTF of DMC', *International Archives of Photogrammetry, Remote Sensing and Spatial Information Sciences*, 36(1A), pp. 17-22.
- Honkavaara, E., Markelin, L., Ahokas, E., Kuittinen, R. and Peltoniemi, J. (2008) 'Calibrating digital photogrammetric airborne imaging systems in a test field', *The International Archives of the Photogrammetry, Remote Sensing and Spatial Information Sciences*, 37(B1), pp. 555-560.
- Horn, B.K.P. (1981) 'Hill shading and the reflectance map', *Proceedings of the IEEE*, 69(1), pp. 14-47.
- Hu, P., Liu, X. and Hu, H. (2009) 'Accuracy assessment of digital elevation models based on approximation theory', *Photogrammetric Engineering & Remote Sensing*, 75(1), pp. 49-56.
- Ip, A.W.L. and Mostafa, M.M.R. (2006) 'A fully integrated system for rapid response', *ASPRS annual conference, November 6 – 10, San Antonio, Texas, USA*.

- Ip, A.W.L., Mostafa, M.M.R., Hutton, J. and Barriere, J.P. (2008) 'An optimally integrated direct georeferencing and flight management system for increased productivity of airborne mapping and remote sensing', *International Archive of Photogrammetry and Remote Sensing*, 37(B1), pp. 579-584.
- Jacobsen, K. (1998a) 'Block Adjustment', *Internal report, Institute of Photogrammetry and Geo-Information*, Institute of Photogrammetry and Geo-Information, Hannover, Germany.
- Jacobsen, K. (1998b) 'Development of program system BLUH for bundle block adjustment in the University of Hannover', *Department of Surveying, University of Hannover*, (227), pp. 157-162.
- Jacobsen, K. (2000) 'Combined bundle block adjustment versus direct sensor orientation', *ASPRS annual convention, Washington , USA*.
- Jacobsen, K. (2002) 'Calibration aspects in direct georeferencing of frame imagery', *International Archives for Photogrammetry, Remote Sensing and Spatial Information Sciences*, 34(1), pp. 82-88.
- Jacobsen, K. (2004) 'Direct/integrated sensor orientation-pros and cons', *International Archives of Photogrammetry and Remote Sensing*, 35.
- Jacobsen, K. (2007a) 'Geometric handling of large size digital airborne frame camera images', *Optical 3D Measurement Techniques VIII*, pp. 164 – 171.
- Jacobsen, K. (2007b) 'Geometry of digital frame cameras', *ASPRS annual conference*, May 7-11, Tampa, Florida USA, p. 12.
- Jacobsen, K. (2008) 'BLUH bundle block adjustment', *Institute of Photogrammetry and GeoInformation, Leibniz University Hannover*, Program user manual, p. 34.
- Jacobsen, K. (2010) 'Development of Digital Aerial Cameras', *The International Archives of the Photogrammetry, Remote Sensing and Spatial Information Sciences*, 38(B1), pp. 11-13.
- Jacobsen, K. (2011a) 'Geometric property of large format digital camera DMC II 140', *Photogrammetrie-Fernerkundung-Geoinformation*, 2011(2), pp. 71-79.
- Jacobsen, K. (2011b) 'Recent developments of digital cameras and space imagery', *Proceedings of GIS symposium*, January 24-26, Ostrava, Czech Republic, p. 8.
- Jacobsen, K. (2013) 'Personal discussion during ISPRS Hannover workshop', *ISPRS Hannover Workshop 2013*, May 21-24, Hannover, Germany.
- Jacobsen, K., Cramer, M., Ladstadter, R., Ressler, C. and Spreckels, V. (2010) 'DGPF-Project: Evaluation of digital photogrammetric camera systems geometric performance', *Photogrammetrie Fernerkundung Geoinformation*, 2, pp. 83-97.



- James, T.D., Murray, T., Barrand, N.E. and Barr, S.L. (2006) 'Extracting photogrammetric ground control from lidar DEMs for change detection', *The Photogrammetric Record*, 21(116), pp. 312-328.
- Jaw, J. and Wu, Y. (2006) 'Control patches for automatic single photo orientation', *Photogrammetric Engineering and Remote Sensing*, 72(2), p. 151.
- Jaw, J.J. (1999) 'Control surface in aerial triangulation', *Ph.D. thesis, Department of Civil and Environmental Engineering and Geodetic Science*, , The Ohio State University, Columbus, Ohio, 98 p.
- Karras, G.E. and Petsa, E. (1993) 'DEM matching and detection of deformation in close-range photogrammetry without control', *Photogrammetric engineering and remote sensing*, 59(9), pp. 1419-1424.
- Kekre, H.B., Sarode, T.K. and Karani, M.R.B. (2011) '2D satellite image registration using transform based and correlation based methods', *International Journal of Advanced Computer Science and Application*, 3(5), pp. 66-72.
- Khoshelham, K. (2009) 'Role of tie points in integrated sensor orientation for photogrammetric map compilation', *Photogrammetric Engineering & Remote Sensing*, 75(3), pp. 305-311.
- Kim, C., Ghanma, M. and Habib, A. (2006) 'Integration of photogrammetric and lidar data for realistic 3D model generation', *Department of Geomatic Engineering, University of Calgary, Canada*, p. 8.
- Koechner, W. (2006) *Solid-state laser engineering*. Springer.
- Kolecka, N. (2011) 'Photo-based 3D scanning vs. laser scanning—competitive data acquisition methods for digital terrain modelling of steep mountain slopes', *International Archives of the Photogrammetry, Remote Sensing and Spatial Information Sciences*, 38(B4), pp. 203-208.
- Konecny, G. (1985) 'The International Society for Photogrammetry and Remote Sensing-75 Years Old, or 75 Years Young', *Photogrammetric Engineering and Remote Sensing*, 51(7), pp. 919-933.
- Koskinen, M., Kostamovaara, J.T. and Myllylae, R.A. (1992) 'Comparison of continuous-wave and pulsed time-of-flight laser range-finding techniques', *Optics, Illumination and image sensing for machine vision VI, SPIE*, 1614, pp. 296-305.
- Kremer, J. and Kruck, E. (2003) 'Integrated Sensor Orientation-Two Examples to show the Potential of simultaneous GPS/IMU and Image Data Processing', *ISPRS Workshop Working Group I/5 "Theory, Technology and Realities of Inertial/GPS Sensor Orientation"*, 22 - 23 September, Castelldefels, Spain.
- Kröpfl, M., Kruck, E. and Gruber, M. (2004) 'Geometric calibration of the digital large format aerial camera UltraCamD', *International Archives of Photogrammetry, Remote Sensing and Spatial Information Sciences*, 35(1), pp. 42-44.

- Kruck, E. (2006) 'Simultaneous calibration of digital aerial survey cameras', *EuroCow 2006 Proceedings*, January 25-27, Castelldefels, Spain, p. 5.
- Kunz, M., Mills, J.P., Miller, P.E., King, M.A., Fox, A.J. and Marsh, S. (2012) 'Application of surface matching for improved measurements of historic glacier volume change in the Antarctic Peninsula', *International Archives of the Photogrammetry, Remote Sensing and Spatial Information Sciences*, 39(8), pp. 579-584.
- Kwak, T.-S., Kim, Y.-I., Yu, K.-Y. and Lee, B.-K. (2006) 'Registration of aerial imagery and aerial lidar data using centroids of plane roof surfaces as control information', *KSCE Journal of Civil Engineering*, 10(5), pp. 365-370.
- Ladstädter, R. and Gruber, M. (2008) 'Geometric Aspects concerning the photogrammetric workflow of the digital aerial camera UltraCamx', *ISPRS Journal of Photogrammetry and Remote Sensing*, Commission I, WG I/4, Beijing.
- Ladstädter, R., Gruber, M. and Wiechert, A. (2010a) 'Monolithic Stitching: One sensor geometry for multiple sensor camera', *ASPRS annual conference, April 26-30, San Diego, USA*.
- Ladstädter, R., Tschemmerneegg, H. and Gruber, M. (2010b) 'Calibrating the Ultracam aerial camera systems, an update', *Proceedings: International Calibration and Orientation Workshop EuroCOW, 10 - 12 February, Castelldefels, Spain*.
- Leberl, F. and Gruber, M. (2003) 'Flying the new large format digital aerial camera Ultracam', *Photogrammetric Week*, 3, pp. 67-76.
- Leberl, F., Gruber, M., Ponticelli, M. and Wiechert, A. (2012) 'The UltraCam story', *International Archives for Photogrammetry, Remote Sensing and Spatial Information Sciences*, 39(B1), pp. 39-44.
- Leica, G. (2013a) 'Leica ADS80 Airborne Digital Sensor, Flyer', [http://www.leica-geosystems.co.uk/downloads123/zz/airborne/ads80/Flyer/ADS80\\_Flyer\\_en.pdf](http://www.leica-geosystems.co.uk/downloads123/zz/airborne/ads80/Flyer/ADS80_Flyer_en.pdf), Access date 24/04/2013.
- Leica, G. (2013b) 'Leica Geosystems News Overview', [http://www.leica-geosystems.com/en/About-us/News\\_360.htm?id=4429](http://www.leica-geosystems.com/en/About-us/News_360.htm?id=4429), Access date 25/5/2013.
- Lim, K., Treitz, P., Wulder, M., St-Onge, B. and Flood, M. (2003) 'Lidar remote sensing of forest structure', *Progress in physical geography*, 27(1), pp. 88-106.
- Lim, M., Mills, J.P., Barr, S.L., Barber, D., Glendinning, S., Parkin, G., Hall, J. and Clarke, B. (2007) 'High resolution earth imaging for transport corridor slope stability risk analysis', *International Archives for Photogrammetry, Remote Sensing and Spatial Information Sciences*, 36(A1), p. 6.
- Linder, W. (2003) *Digital photogrammetry: theory and applications*. Springer Berlin.
- Liu, X. (2008) 'Airborne LiDAR for DEM generation: some critical issues', *Progress in Physical Geography*, 32(1), pp. 31-49.

- Liu, X., Zhang, Z., Peterson, J. and Chandra, S. (2007) 'Lidar-derived high quality ground control information and DEM for image orthorectification', *GeoInformatica*, 11(1), pp. 37-53.
- Luhmann, T., Robson, S., Kyle, S. and Harley, I. (2006) *Close range photogrammetry: Principles, methods and applications*. Whittles Scotland, UK.
- Maling, D.H. (1989) 'Measurements from maps', Pergamon Press, New York, USA, p. 577.
- Mallet, C. and Bretar, F. (2009) 'Full-waveform topographic lidar: State-of-the-art', *ISPRS Journal of Photogrammetry and Remote Sensing*, 64(1), pp. 1-16.
- Markelin, L., Honkavaara, E., Peltoniemi, J., Ahokas, E., Kuittinen, R., Hyypä, J., Suomalainen, J. and Kukko, A. (2008) 'Radiometric calibration and characterization of large-format digital photogrammetric sensors in a test field', *Photogrammetric Engineering & Remote Sensing*, 74(12), pp. 1487-1500.
- Matthias, K. (2013) 'Elevation changes of mountain glaciers in the Antarctic Peninsula using ASTER-controlled archival aerial photography', *PhD thesis*, University of Newcastle Upon Tyne, Newcastle Upon Tyne, p. 232.
- McGlone, J., Mikhail, C., M., E. and S., B.J. (2004) *Manual of photogrammetry. 5th Edition*. American Society for Photogrammetry and Remote Sensing, Bethesda, Maryland, USA.
- Meier, H.K. (1978) 'The effect of environmental conditions on distortion, calibrated focal length and focus of aerial survey cameras', *International Archives of Photogrammetry*, 22(1), p. 9.
- Mikhail, E.M., Bethel, J.S. and McGlone, J.C. (2001) *Introduction to modern photogrammetry*. Wiley New York, NY.
- Miller, P. (2007) 'A robust surface matching technique for coastal zone geohazard monitoring', *PhD thesis*, University of Newcastle Upon Tyne, Newcastle Upon Tyne, p. 311.
- Miller, P., Mills, J., Edwards, S., Bryan, P., Marsh, S., Mitchell, H. and Hobbs, P. (2008) 'A robust surface matching technique for coastal geohazard assessment and management', *ISPRS Journal of Photogrammetry and Remote Sensing*, 63(5), pp. 529-542.
- Miller, P.E., Mills, J.P., Barr, S.L., Birkinshaw, S.J., Hardy, A.J., Parkin, G. and Hall, S.J. (2012) 'A remote sensing approach for landslide hazard assessment on engineered slopes', *IEEE Transactions on Geoscience and Remote Sensing*, 50(4), pp. 1048-1056.
- Mills, J.P., Buckley, S.J., Mitchell, H.L., Clarke, P.J. and Edwards, S.J. (2005) 'A geomatics data integration technique for coastal change monitoring', *Earth Surface Processes and Landforms*, 30(6), pp. 651-664.

- Mishra, R. and Zhang, Y. (2012) 'A review of optical imagery and airborne lidar data registration methods', *The Open Remote Sensing Journal*, 5, pp. 54-63.
- Mitchell, H.L. (1994) 'A comprehensive system for automated body surface measurement', *International Archives of Photogrammetry and Remote Sensing*, 30(5), pp. 265-272.
- Mitishita, E., Cortes, J. and Centeno, J. (2011) 'Indirect georeferencing of digital SLR imagery using signalised lidar control points', *The Photogrammetric Record*, 26(133), pp. 58-72.
- Mitishita, E., Debiase, P., Hainosz, F. and Centeno, J. (2012) 'Calibration of low cost digital camera using data using from simultaneous lidar and photogrammetric surveys', *International Archives of Photogrammetry, Remote Sensing and Spatial Information Sciences*, 39(B1), pp. 133-138.
- Mitishita, E., Habib, A., Centeno, J., Machado, A., Lay, J. and Wong, C. (2008) 'Photogrammetric and lidar data integration using the centroid of a rectangular roof as a control point', *The Photogrammetric Record*, 23(121), pp. 19-35.
- Mooney, K. (2011) 'Report of the Dublin Institute of Technology', in Rönnholm, P. (ed.) *Registration quality towards integration of laser scanning and photogrammetry*. Amsterdam, The Netherlands: Official Publication - EuroSDR, (59).
- Morain, A.S. and Zanoni, M.V. (2004) 'Joint Isprs/Ceos-Wgcv task force on radiometric and geometric calibration', *International Archives of Photogrammetry and Remote Sensing*, 35(B1), pp. 354-360.
- Morin, K. and El-Sheimy, N. (2002) 'Post-mission adjustment methods of airborne laser scanning data', *Proceedings XXII FIG International Congress*, April 19–26, Washington DC, USA.
- Petrie, G. (2006) 'Further advances in airborne digital imaging - Several new imagers introduced at ASPRS', *GeoInformatics*, 9(5), pp. 16-23.
- Petrie, G. and Toth, C.K. (2009) 'Introduction to laser ranging, profiling, and scanning', in Shan, J. and Toth, C. (eds.) *Topographic laser ranging and scanning: principles and processing*. CRC Press, Taylor & Francis Group, pp. 1-27.
- Petrie, G. and Walker, A.S. (2007) 'Airborne digital imaging technology: a new overview', *The Photogrammetric Record*, 22(119), pp. 203-225.
- Pilgrim, L.J. (1996) 'Surface matching and difference detection without the aid of control points', *Survey Review*, 33(259), pp. 291-304.
- Postolov, Y., Krupnik, A. and McIntosh, K. (1999) 'Registration of airborne laser data to surfaces generated by photogrammetric means', *International Archives for Photogrammetry, Remote Sensing and Spatial Information Sciences*, 32(3), pp. 95-99.

- Qtaishat, K.S., Smith, M.J. and Park, D.W.G. (2008) 'The Interior and Exterior calibration for UltraCam D', *ISPRS Journal of Photogrammetry and Remote Sensing*, Commission, WG VI/4, Bijing.
- Remondino, F. and Fraser, C.S. (2006) 'Digital camera calibration methods : considerations and comparisons', *International Archives of Photogrammetry, Remote Sensing and Spatial Information Sciences*, 36(5), pp. 266-272.
- Ressl, C. (2011) 'Report of the Vienna University of Technology', in Rönnholm, P. (ed.) *Registration quality towards integration of laser scanning and photogrammetry*. Amsterdam, The Netherlands: Official Publication - EuroSDR, (59), pp. 238-252.
- Reutebuch, S.E., Andersen, H.-E. and McGaughey, R.J. (2005) 'Light detection and ranging (LIDAR): an emerging tool for multiple resource inventory', *Journal of Forestry*, 103(6), pp. 286-292.
- Rönnholm, P. (2011a) *Registration quality - towards integration of laser scanning and photogrammetry*. Amsterdam, The Netherlands: Official Publication - EuroSDR, (59).
- Rönnholm, P. (2011b) 'Report of the Aalto University School of Engineering', in Rönnholm, P. (ed.) *Registration quality towards integration of laser scanning and photogrammetry*. Amsterdam, The Netherlands: Official Publication - EuroSDR, (59), pp. 59-65.
- Rönnholm, P., Honkavaara, E., Litkey, P., Hyypä, H. and Hyypä, J. (2007) 'Integration of laser scanning and photogrammetry', *International Archives of Photogrammetry, Remote Sensing and Spatial Information Sciences*, 36(B3), pp. 355-362.
- Rosenholm, D.A.N. and Torlegard, K. (1988) 'Three-dimensional absolute orientation of stereo models using digital elevation models', *Photogrammetric Engineering and Remote Sensing*, 54, pp. 1385-1389.
- Sampath, A. and Shan, J. (2006) 'Clustering based planar roof extraction from lidar data', *American Society For Photogrammetry And Remote Sensing Annual Conference*, May 1-5, Reno, Nevada, pp. 1-6.
- Sandau, R. (2009) 'Digital Airborne Camera: Introduction and Technology', Springer, p. 350.
- Sandau, R., Braunecker, B., Driescher, H., Eckardt, A., Hilbert, S., Hutton, J., Kirchhofer, W., Lithopoulos, E., Reulke, R. and Wicki, S. (2000) 'Design principles of the LH Systems ADS40 airborne digital sensor', *International Archives for Photogrammetry, Remote Sensing and Spatial Information Sciences*, 33(B1), pp. 258-265.
- Schenk, T. (2001) 'Modeling and analyzing systematic errors in airborne laser scanners', *Technical Notes in Photogrammetry*, 19, p. 46.

- Schmid, K., Waters, K., Dingerson, L., Hadley, B., Mataosky, R., Carter, J. and Dare, J. (2008) 'Lidar 101: An introduction to lidar technology, data, and applications', *NOAA Coastal Services Center*, p. 76.
- Shan, J. and Sampath, A. (2005) 'Urban DEM generation from raw lidar data: a labeling algorithm and its performance', *Photogrammetric Engineering & Remote Sensing*, 71(2), pp. 217-226.
- Shin, S.W., Habib, A.F., Ghanma, M., Kim, C. and Kim, E.-M. (2007) 'Algorithms for multi-sensor and multi-primitive photogrammetric triangulation', *ETRI Journal*, 29(4), pp. 411-420.
- Skaloud, J. (1999) 'Optimizing georeferencing of airborne survey systems by INS/DGPS', *PhD thesis, Department of Geomatic Engineering, University of Calgary, Alberta, Canada*, (No. 20216).
- Skaloud, J. and Schaer, P. (2003) 'Towards a more rigorous boresight calibration', *ISPRS International workshop on theory technology and realities of Inertial/GPS sensor orientation, 9-12 September, Castelldefels, Spain*.
- Smith, M.J., N. Kokas, K. S. Qtaishat (2007) 'Investigation into Self-Calibration methods for the vexcel UltraCam digital aerial camera', *ISPRS Hannover Workshop, Commission I, WG I/1*.
- Smith, M.J., Qtaishat, K.S., Park, D.W.G. and Jamieson, A. (2005) 'Initial results from the vexcel ultracamD digital aerial camera', *Proceedings of the ISPRS Workshop, Commission I, WG I/5, Hannover*.
- Soininen, A. (2004) *Terrascan user's guide*. Helsinki, Finland.
- Souchon, J.-P., Paparoditis, N., Martin, O., Meynard, C. and Thom, C. (2006) 'Is there an ideal digital aerial camera', *International Archives of Photogrammetry, Remote Sensing and Spatial Information Sciences*, 36(A1), p. 6.
- Stensaas, G. and Leeb, G. (2008) 'Driving toward a worldwide acceptance procedure for Digital Airborne Sensors', *ISPRS Journal of Photogrammetry and Remote Sensing*, WG I/4, Beijing.
- Tempelmann, U., Hinsken, L. and Recke, U. (2003) 'ADS40 calibration and verification process', *Proceedings on Optical 3-D Measurement Techniques*, 6, pp. 48-54.
- Vosselman, G. (2000) 'Slope based filtering of laser altimetry data', *International Archives for Photogrammetry, Remote Sensing and Spatial Information Sciences*, 33(3), pp. 935-942.
- Vosselman, G. (2008) 'Analysis of planimetric accuracy of airborne laser scanning surveys', *International Archives of Photogrammetry, Remote Sensing and Spatial Information Sciences*, 37(3a), pp. 99-104.
- Vosselman, G. and Maas, H.-G. (2010) *Airborne and terrestrial laser scanning*. Whittles Dunbeath, UK.

- Wager, T.D., Keller, M.C., Lacey, S.C. and Jonides, J. (2005) 'Increased sensitivity in neuroimaging analyses using robust regression', *Neuroimage*, 26(1), pp. 99-113.
- Wagner, R. (2011) 'The Leica RCD30 Medium Format Camera: Imaging Revolution', *Photogrammetric Week*, 11, pp. 89-95.
- Wagner, W., Ullrich, A., Melzer, T., Briese, C. and Kraus, K. (2004) 'From single-pulse to full-waveform airborne laser scanners: potential and practical challenges', *International Archives of Photogrammetry and Remote Sensing*, 35(3), pp. 201-206.
- Wang, M. and Tseng, Y.-H. (2011) 'Incremental segmentation of lidar point clouds with an octree-structured voxel space', *The Photogrammetric Record*, 26(133), pp. 32-57.
- Wegmann, H. (2002) 'Image orientation by combined (A) AT with GPS and IMU', *International Archives for Photogrammetry, Remote Sensing and Spatial Information Sciences*, 34(1), pp. 278-283.
- Wehr, A. and Lohr, U. (1999) 'Airborne laser scanning-an introduction and overview', *ISPRS Journal of Photogrammetry and Remote Sensing*, 54(2-3), pp. 68-82.
- Wildan, F., Aldino, R. and Aji, P.P. (2011) 'Application of LIDAR Technology for GCP Determination in Papua Topographic Mapping Scale 1:50.000', *10th Annual Asian Conference & Exhibition on Geospatial Information, Technology & Applications*. 17-19 October, Jakarta, Indonesia. p. 13.
- Wolf, P.R. and Dewitt, B.A. (2000) *Elements of Photogrammetry: with applications in GIS*. McGraw-Hill New York, NY, USA.
- Wong, A. and Orchard, J. (2008) 'Efficient FFT-accelerated approach to invariant optical-LIDAR registration', *Geoscience and Remote Sensing, IEEE Transactions on*, 46(11), pp. 3917-3925.
- Yastikli, N. and Jacobsen, K. (2005) 'Influence of system calibration on direct sensor orientation', *Photogrammetric engineering and remote sensing*, 71(5), pp. 629-633.
- Yastikli, N. and Toth, C. (2007) 'IN-Situ camera and boresight calibration with lidar data', *The 5th International Symposium on mobile mapping technology*, May 29-31, Padua, Itália, p. 6.
- Z/I-Imaging (2013a) 'Camera comparison Brochure', [http://www.ziimaging.com/media/ZI\\_Camera\\_Comparison\\_BRO\\_en.pdf](http://www.ziimaging.com/media/ZI_Camera_Comparison_BRO_en.pdf), Access date 23/04/2013.
- Z/I-Imaging (2013b) 'RMK D camera system - Product sheet', [http://www.intergraph.com/assets/plugins/sgicollaterals/downloads/RMKD-CameraSystem\\_ProductSheet.pdf](http://www.intergraph.com/assets/plugins/sgicollaterals/downloads/RMKD-CameraSystem_ProductSheet.pdf), Access date 30/5/2013.

## Appendix A

### Results of LiDAR Vertical Accuracy Test Using TerraScan Software

No.	Point ID	Easting (m)	Northing (m)	Known z (m)	Laser z (m)	$\Delta_z$ (m)
1	2193	493375.060	5421422.239	331.360	331.320	-0.040
2	2203	493342.409	5421313.947	336.524	336.494	-0.030
3	2309	493300.695	5420972.336	344.874	344.852	-0.022
4	2353	494071.008	5419323.142	286.378	286.374	-0.004
5	2363	493133.548	5419871.071	255.946	255.937	-0.009
6	2373	493347.055	5419717.365	255.083	255.044	-0.039
7	2383	494680.493	5419080.197	325.923	325.960	0.037
8	2443	495502.147	5419566.145	330.991	330.963	-0.028
9	2474	494753.205	5420817.035	346.964	346.954	-0.010
10	2563	497017.582	5421439.972	292.863	292.867	0.004
11	2593	498227.841	5421704.712	310.572	310.574	0.002
12	2723	495404.220	5420654.636	306.240	306.209	-0.031
13	2733	495454.143	5420815.460	309.065	309.085	0.020
14	2743	495397.730	5420502.820	287.433	287.399	-0.034
15	2753	495748.970	5420456.825	253.625	253.603	-0.022
16	2843	496657.506	5419634.836	251.422	251.400	-0.022
17	2863	496771.733	5419824.074	251.702	251.658	-0.044
18	2883	496885.513	5420555.971	307.825	307.785	-0.040
19	3000	495724.630	5421628.927	313.450	313.460	0.010
20	3002	495267.132	5421654.221	294.185	294.228	0.043
21	3004	497277.948	5421425.664	300.200	300.214	0.014
22	3006	497927.693	5421517.564	304.801	304.767	-0.034
23	3007	497650.529	5421199.898	313.466	313.504	0.038
24	3009	497839.856	5419982.745	329.837	329.814	-0.023
25	3010	497870.860	5419733.981	286.291	286.249	-0.042



No.	Point ID	Easting (m)	Northing (m)	Known z (m)	Laser z (m)	$\Delta_z$ (m)
26	3012	494579.662	5421138.163	346.507	346.527	0.020
27	3015	495920.129	5419991.878	284.219	284.254	0.035
28	3016	495495.378	5419767.299	324.454	324.432	-0.022
29	3020	494431.503	5420276.172	256.779	256.790	0.011
30	3004	497277.948	5421425.664	300.200	300.214	0.014
31	3021	494469.482	5421403.283	321.127	321.155	0.028
32	3022	494753.248	5421606.172	292.962	292.968	0.006
33	3023	494383.046	5419189.276	308.921	308.964	0.043
34	9001	497775.247	5420810.963	327.466	327.507	0.041
35	207029	495954.310	5419385.934	276.610	276.642	0.032
36	209019	497098.823	5419204.373	271.462	271.458	-0.004
37	209019	497098.823	5419204.373	271.462	271.458	-0.004
38	212019	499016.543	5419180.688	314.245	314.240	-0.005
39	301029	492533.946	5420537.190	289.377	289.343	-0.034
40	303019	493372.887	5420256.701	288.957	288.917	-0.040
41	303019	493372.887	5420256.701	288.957	288.917	-0.040
42	306019	495400.975	5420325.923	252.686	252.674	-0.012
43	306019	495400.975	5420325.923	252.686	252.674	-0.012
44	309019	497065.157	5420404.316	293.041	293.020	-0.021
45	309019	497065.157	5420404.316	293.041	293.020	-0.021
46	310019	497723.525	5420402.894	351.521	351.486	-0.035
47	310019	497723.525	5420402.894	351.521	351.486	-0.035
48	313029	499428.283	5420058.604	333.307	333.259	-0.048
49	313039	499508.269	5420852.813	340.759	340.726	-0.033
50	401019	492613.645	5421379.685	258.284	258.266	-0.018
51	401039	492248.200	5421137.044	259.284	259.278	-0.006
52	401049	492766.452	5421588.745	258.671	258.690	0.019
53	403019	493665.640	5421417.635	334.051	334.063	0.012
54	404019	494091.178	5421421.610	330.099	330.119	0.020
55	406019	495397.768	5421190.308	268.360	268.340	-0.020
56	408019	496650.842	5421452.116	273.623	273.644	0.021
57	410019	497945.716	5421426.463	305.163	305.160	-0.003

No.	Point ID	Easting (m)	Northing (m)	Known z (m)	Laser z (m)	$\Delta_z$ (m)
58	413029	499122.210	5421284.081	320.954	320.947	-0.007
59	2041039	494401.978	5419510.746	308.029	308.018	-0.011
60	2041059	494405.792	5419358.868	304.986	305.022	0.036
61	2051049	495255.752	5419178.765	351.101	351.144	0.043
62	3030109	493406.639	5420714.710	349.382	349.384	0.002
63	3041029	494350.318	5420660.415	255.762	255.745	-0.017
64	4031019	493440.834	5421459.538	330.310	330.333	0.023
65	4041019	494332.245	5421506.156	315.279	315.291	0.012
66	4041079	494540.101	5420972.121	357.229	357.244	0.015
67	4051029	495254.122	5421495.946	271.954	271.953	-0.001
Mean $\Delta_z$						-0.002
Min $\Delta_z$						-0.048
Max $\Delta_z$						0.043
RMSE						0.025
$\sigma$ (Standard Deviation)						0.025

## Appendix B

### Matching Results of UltraCamX Dataset – Without Self-calibration

```
=====
===                SURFACE MATCHING PROTOCOL                ===
=====

Local time & date: Tue Jul 31 17:25:04 2012

Input Data
-----
Surface 1 (Reference) : LiDAR.xyz
No. of points         : 1230811
No. of triangles      : 2461566

Surface 2 (Match)     : daxyz_noAP.xyz
No. of points         : 15031
=====

Initial Settings
-----
X      : 0.0000   Y      : 0.0000   Z      : 0.0000
Omega  : 0.0000   Phi    : 0.0000   Kappa  : 0.0000
Scale  : 1.0000

X_Offset      : 495141
Y_Offset      : 5420642
Z_Cutoff      : 295
Distance      : Euclidean
Weighting     : ON (tuning constant = 4.6849999999999996)
XYZ x_hat check : 0.010000
wpks x_hat check : 0.001000
Std. Dev. check : 0.001000
=====

Parameter  Final Transf.    Last Corr. Std. Error
-----
_X         :      -0.038610  -0.009557  0.009153
_Y         :       0.174849  -0.005713  0.006670
_Z         :      -0.196329   0.004007  0.003630
_Omega     :       0.004140   0.000001  0.000630
_Phi       :      -0.000742  -0.000000  0.000113
_Kappa     :      -0.008576  -0.000000  0.000112
_Scale     :       1.000214  -0.000010  0.000012
=====

Statistics
```

```
-----
Duration                : 1254 sec
No. of Iterations       : 6
No. of points in solution : 15031
Points of S2 outside S1  : 0.00 % (0 points)
Points of S2 over cutoff : 0.00 % (0 points)
Mean Residual           : -0.2140
RMS Residuals           : 0.5775
Reference Std. Dev.     : 0.0996
SVD Condition           : 4914.0977
Convergence criteria     : Ref. Std.Dev. change < 0.001
=====
```

Correlation Matrix (Tx, Ty, Tz, Omega, Phi, Kappa, Scale)

```
-----
1.0000  0.0545  0.0616  0.2691 -0.0522 -0.0022 -0.1238
0.0545  1.0000  0.2647  0.1754  0.0466  0.0235 -0.2565
0.0616  0.2647  1.0000  0.0083  0.1352  0.0803 -0.9632
0.2691  0.1754  0.0083  1.0000  0.0639  0.0945 -0.0057
-0.0522 0.0466  0.1352  0.0639  1.0000 -0.0357 -0.1395
-0.0022 0.0235  0.0803  0.0945 -0.0357  1.0000 -0.1010
-0.1238 -0.2565 -0.9632 -0.0057 -0.1395 -0.1010  1.0000
=====
```

```
-----
Operating System : Linux
Version          : Surfmatch 0.9 Beta
Organisation     : Newcastle University
=====
```

## Matching Results of UltraCamX Dataset – With Self-calibration

```
=====
===                SURFACE MATCHING PROTOCOL                ===
=====
```

Local time & date: Tue Jul 31 17:46:11 2012

### Input Data

```
-----
Surface 1 (Reference) : LiDAR.xyz
No. of points         : 1230811
No. of triangles      : 2461566

Surface 2 (Match)     : daxyz_12AP.xyz
No. of points         : 15031
=====
```

### Initial Settings

```
-----
X      : 0.0000   Y      : 0.0000           Z      : 0.0000
Omega  : 0.0000   Phi    : 0.0000           Kappa   : 0.0000
Scale  : 1.0000

X_Offset      : 495141
Y_Offset      : 5420642
Z_Cutoff      : 295
Distance      : Euclidean
Weighting     : ON (tuning constant = 4.6849999999999996)
XYZ x_hat check : 0.010000
wpks x_hat check : 0.001000
Std. Dev. check : 0.001000
=====
```

Parameter	Final Transf.	Last Corr.	Std. Error
_X	: 0.007907	-0.006787	0.009017
_Y	: 0.178190	-0.004399	0.006536
_Z	: -0.153002	0.003054	0.003559
_Omega	: 0.004484	0.000001	0.000619
_Phi	: -0.001032	-0.000000	0.000111
_Kappa	: -0.006367	0.000003	0.000110
_Scale	: 1.000200	-0.000008	0.000011

```
=====
```

### Statistics

```
-----
Duration                : 1245 sec
No. of Iterations       : 6
No. of points in solution : 15031
Points of S2 outside S1  : 0.00 % (0 points)
Points of S2 over cutoff : 0.00 % (0 points)
Mean Residual           : -0.2159
RMS Residuals           : 0.5797
Reference Std. Dev.     : 0.0977
SVD Condition           : 4935.4411
```

Convergence criteria : Ref. Std.Dev. change < 0.001

=====

Correlation Matrix (Tx, Ty, Tz, Omega, Phi, Kappa, Scale)

-----

1.0000	0.0530	0.0570	0.2647	-0.0571	0.0013	-0.1191
0.0530	1.0000	0.2585	0.1759	0.0465	0.0237	-0.2503
0.0570	0.2585	1.0000	0.0026	0.1347	0.0823	-0.9631
0.2647	0.1759	0.0026	1.0000	0.0637	0.0951	0.0010
-0.0571	0.0465	0.1347	0.0637	1.0000	-0.0344	-0.1383
0.0013	0.0237	0.0823	0.0951	-0.0344	1.0000	-0.1033
-0.1191	-0.2503	-0.9631	0.0010	-0.1383	-0.1033	1.0000

=====

-----

Operating System : Linux

Version : Surfmatch 0.9 Beta

Organisation : Newcastle University

=====

## Matching Results of DSS322 Dataset – Without Self-calibration

```
=====
===                SURFACE MATCHING PROTOCOL                ===
=====
```

Local time & date: Wed Nov 21 15:19:07 2012

### Input Data

```
-----
Surface 1 (Reference) : A2_dtm_building_flat.xyz
No. of points         : 1440641
No. of triangles      : 2881104
```

```
Surface 2 (Match)      : daxyz_dtm_bld.xyz
No. of points          : 4155
=====
```

### Initial Settings

```
-----
X      : 0.0000   Y      : 0.0000           Z      : 0.0000
Omega  : 0.0000   Phi    : 0.0000           Kappa   : 0.0000
Scale  : 1.0000

X_Offset      : 371885
Y_Offset      : 564001
Z_Cutoff      : 120
Distance      : Euclidean
Weighting     : ON (tuning constant = 4.6849999999999996)
XYZ x_hat check : 0.010000
wpks x_hat check : 0.001000
Std. Dev. check : 0.001000
=====
```

```
-----
Parameter  Final Transf.    Last Corr. Std. Error
-----
_X         :      -2.511299   0.044535  0.421243
_Y         :      18.332266   0.088908  0.391050
_Z         :      -1.226675   0.005126  0.082088
_Omega     :       2.433255  -0.000024  0.061658
_Phi       :      -0.304779  -0.000023  0.028094
_Kappa     :       0.731722   0.000321  0.016858
=====
```

### Statistics

```
-----
Duration                : 1795 sec
No. of Iterations        : 8
No. of points in solution : 4155
Points of S2 outside S1  : 0.00 % (0 points)
Points of S2 over cutoff : 0.00 % (0 points)
Mean Residual            : -0.9350
RMS Residuals            : 6.1230
Reference Std. Dev.      : 4.1227
SVD Condition            : 1797.2081
Convergence criteria     : Ref. Std.Dev. change < 0.001
```

```

=====
Correlation Matrix (Tx, Ty, Tz, Omega, Phi, Kappa, Scale)
-----
  1.0000 -0.0862  0.0843 -0.2096  0.0579 -0.0494  ---
-0.0862  1.0000  0.1872  0.5654  0.2686 -0.1572  ---
  0.0843  0.1872  1.0000  0.1073  0.0095 -0.4712  ---
-0.2096  0.5654  0.1073  1.0000  0.0039 -0.3210  ---
  0.0579  0.2686  0.0095  0.0039  1.0000  0.1524  ---
-0.0494 -0.1572 -0.4712 -0.3210  0.1524  1.0000  ---
=====
-----
Operating System   : Linux
Version           : Surfmach 0.9 Beta
Organisation      : Newcastle University
=====

```



## Matching Results of DSS322 Dataset – With Self-calibration

```
=====
===                SURFACE MATCHING PROTOCOL                ===
=====
```

Local time & date: Fri Nov 23 12:28:12 2012

### Input Data

```
-----
Surface 1 (Reference) : A2_dtm_building_flat.xyz
No. of points         : 1440641
No. of triangles      : 2881104
```

```
Surface 2 (Match)      : daxyz_12Ap_mask.xyz
No. of points          : 3960
=====
```

### Initial Settings

```
-----
X      : 0.0000   Y      : 0.0000           Z      : 0.0000
Omega  : 0.0000   Phi    : 0.0000           Kappa   : 0.0000
Scale  : 1.0000

X_Offset      : 371885
Y_Offset      : 564001
Z_Cutoff      : 120
Distance      : Euclidean
Weighting     : ON (tuning constant = 4.6849999999999996)
XYZ x_hat check : 0.010000
wpks x_hat check : 0.001000
Std. Dev. check : 0.001000
=====
```

Parameter	Final Transf.	Last Corr.	Std. Error
_X	: 0.381897	-0.005211	0.074769
_Y	: 0.284880	-0.007223	0.053235
_Z	: -7.144690	0.013197	0.025576
_Omega	: 0.069736	0.000002	0.008849
_Phi	: 0.010025	0.000004	0.004034
_Kappa	: 0.078303	-0.000078	0.002194
_Scale	: 1.000996	-0.000119	0.000204

```
=====
```

### Statistics

```
-----
Duration                : 1769 sec
No. of Iterations       : 8
No. of points in solution : 3960
Points of S2 outside S1  : 0.00 % (0 points)
Points of S2 over cutoff : 0.00 % (0 points)
Mean Residual           : -0.1772
RMS Residuals           : 1.3134
Reference Std. Dev.     : 0.5555
SVD Condition           : 2261.8471
```

Convergence criteria : Ref. Std.Dev. change < 0.001

=====

Correlation Matrix (Tx, Ty, Tz, Omega, Phi, Kappa, Scale)

-----

1.0000	-0.1204	-0.3787	-0.0954	-0.0355	-0.1294	0.4388
-0.1204	1.0000	0.0720	0.3358	0.2816	-0.0731	0.0551
-0.3787	0.0720	1.0000	0.0259	0.1410	-0.0720	-0.9028
-0.0954	0.3358	0.0259	1.0000	-0.0340	-0.2286	0.0177
-0.0355	0.2816	0.1410	-0.0340	1.0000	0.1215	-0.1196
-0.1294	-0.0731	-0.0720	-0.2286	0.1215	1.0000	-0.0900
0.4388	0.0551	-0.9028	0.0177	-0.1196	-0.0900	1.0000

=====

-----

Operating System : Linux

Version : Surfmatch 0.9 Beta

Organisation : Newcastle University

=====

# Appendix C

## BLUH Bundle Block Adjustment - List File

```

=====
PROGRAM  BLUH      LEIBNIZ UNIVERSITY HANNOVER      JAN 2010
      ----- BUNDLE BLOCK ADJUSTMENT -----
      INSTITUTE OF PHOTOGRAMMETRY AND GEOINFORMATION
DATE: 12.07.2012   10:38:40
=====
VERSION FOR Newcastele University  BY UNI HANNOVER
TEXT
=====

DAXYZ
daxyz.dat
DAPOR
dapor.dat
BLUINF
bluinf.dat
DABLUH
dabluh.dat
NUMBER OF PHOTOS      GPS      GPSWXY      GPSWZ      GPS ANTENNA OFFSET
      40      1      .100      .100      .000      .000      .000      2.
CALIBRATED FOCAL LENGTH 660
      100.500 100.500 100.500 100.500
MAXI  IW  GW(1)  GW(2)  GW(3)  IB  FEG REC.SCALE ABIT  IOUT APPR IFR
10   1   1.000  1.000  3.0   0   20.0   0.  .81   0   0   0
FROM PT      TO POINT  WEIGHT  AD PAR  WARNING  OUTSIDE
      0      0      1.000      2      50. 9999999999999999
      . SYSIM LIST
      0      0      Y
1  0  2  0  3  0  4  0  5  0  6  0  7  0  8  0  9  0 10  0 11  0 12  0

      REA      REB      REC      REC2      IMAR      IMA2
      .050      5.00      4.40      3.00      0      0
N
APRIORI STANDARD DEVIATIONS: CONTROL POINTS SX = SY =      1.000
                                SZ =      1.000
                                PHOTO COORDINATES Sy = Sx =      3.0
                                GPS      SX = SY =      .100
                                SZ =      .100

GPS FITTING CODE:      2.
EXCENTRICITY      :      .000      .000      .000
      IPPP      IPU      IFILT      NGPSIT      NGPSHI      IEROUT      ISTAR
      23      15734      7      1      0      1      3
PHOTO NUMBER LIST
213  2      283  4      246  3      176  1      212  2      177  1
247  3      282  4      211  2      281  4      178  1      248  3
210  2      179  1      249  3      280  4      209  2      250  3
279  4      180  1      208  2      181  1      251  3      278  4
207  2      252  3      277  4      182  1      206  2      183  1
253  3      276  4      205  2      254  3      184  1      275  4
204  2      185  1      255  3      274  4

```

```

          0          0
CONTROL POINTS
POINT      X          Y          Z    FSP    FSZ
*****
NO HORIZONTAL AND / OR VERTICAL CONTROLPOINT
***** NO CHECK FOR CONSTANT SHIFTS *****
GPS PROJECTION CENTRES
  176    495836.065    5419895.465    1501.458 385413.0000
  177    495689.344    5419896.207    1501.221 385416.0000
  178    495537.653    5419897.943    1500.994 385418.0000
  179    495386.060    5419899.507    1500.563 385420.0000
  180    495233.048    5419899.426    1499.726 385423.0000
  181    495086.318    5419897.753    1499.195 385425.0000
  182    494932.361    5419895.776    1499.222 385428.0000
  183    494787.425    5419893.928    1500.033 385430.0000
  184    494635.810    5419891.885    1501.152 385432.0000
  185    494483.567    5419890.110    1501.912 385435.0000
  204    494484.034    5420296.873    1499.489 385657.0000
  205    494630.965    5420296.687    1499.401 385659.0000
  206    494784.734    5420294.855    1500.120 385662.0000
  207    494932.204    5420293.762    1500.745 385664.0000
  208    495085.473    5420293.656    1500.694 385666.0000
  209    495240.082    5420293.894    1500.509 385669.0000
  210    495385.503    5420293.488    1500.197 385671.0000
  211    495536.904    5420292.638    1500.441 385674.0000
  212    495687.277    5420292.424    1500.511 385676.0000
  213    495840.740    5420293.285    1500.439 385678.0000
  246    495836.757    5420687.702    1502.395 385912.0000
  247    495690.366    5420688.079    1502.935 385914.0000
  248    495537.065    5420689.006    1502.454 385917.0000
  249    495385.189    5420688.654    1501.035 385919.0000
  250    495239.608    5420688.517    1499.520 385921.0000
  251    495085.462    5420690.023    1497.904 385924.0000
  252    494935.798    5420692.293    1496.707 385926.0000
  253    494787.005    5420694.912    1496.211 385928.0000
  254    494638.355    5420696.747    1496.121 385931.0000
  255    494482.046    5420697.293    1496.823 385933.0000
  274    494480.115    5421094.948    1498.199 386174.0000
  275    494630.560    5421096.175    1499.659 386176.0000
  276    494782.530    5421097.930    1500.519 386179.0000
  277    494934.214    5421098.811    1500.725 386181.0000
  278    495085.705    5421097.626    1500.748 386183.0000
  279    495238.175    5421095.917    1500.123 386186.0000
  280    495386.169    5421095.421    1498.782 386188.0000
  281    495540.561    5421095.781    1497.760 386191.0000
  282    495686.004    5421097.039    1497.529 386193.0000
  283    495838.237    5421099.080    1497.922 386195.0000

```

```

  10 GPS-DATA FOR UNIT 1
  10 GPS-DATA FOR UNIT 2
  10 GPS-DATA FOR UNIT 3
  10 GPS-DATA FOR UNIT 4

```

```

MODE UNIT INFORMATION COORDINATE SYSTEM
0 1.000000 500000.000 .000 1.0000000 90.000000
.0000 .0000

```

```

RANGE OF PHOTO COORDINATES

```

```

X MINIMUM = -33.661 X MAXIMUM = 34.012
Y MINIMUM = -51.884 Y MAXIMUM = 51.896
R MAXIMUM = 62.048 FACTOR = 2.62053

```

```

UP TO 6064 POINTS / PHOTO

```

```

NO.ITER MS CORR X MS CORR Y MS CORR Z SIGMA 0
(ITER) TIME

```

[ground unit]

[microns]

```

=====
0  .744301E-01  .768810E-01  .262426E+00  7.1  10:38:41
1  .286972E-01  .173532E-01  .257758E+00  7.1  10:38:43
      MEAN HEIGHT
CAMERA PROJECTION CENTER TERRAIN PHOTO SCALE
1  1501. 281. 12138. FOR [ft]: 3700. 308. inch/ft
2  1500. 289. 12052. FOR [ft]: 3673. 306. inch/ft
3  1499. 293. 12001. FOR [ft]: 3658. 305. inch/ft
4  1499. 307. 11866. FOR [ft]: 3617. 301. inch/ft

MAIN KAPPA FOR DATA SET 1 : 201.334 10 10
MAIN KAPPA FOR DATA SET 2 : 2.055 10 10
MAIN KAPPA FOR DATA SET 3 : 199.273 10 10
MAIN KAPPA FOR DATA SET 4 : -.185 10 10
2  .000000E+00 .000000E+00 .000000E+00 7.1 10:38:44
3  .219208E-02 .409422E-02 .117926E-01 7.1 10:38:45

FILTERING OF GPS-VALUES BASED ON 7 NEIGHBORED POINTS

FITTING DATA SET 1 10 GPS-VALUES T**2 +/- .036 .033 .007
FITTING DATA SET 2 10 GPS-VALUES T**2 +/- .010 .032 .010
FITTING DATA SET 3 10 GPS-VALUES T**2 +/- .025 .034 .004
FITTING DATA SET 4 10 GPS-VALUES T**2 +/- .035 .030 .011
RMS AT GPS-POINTS FITTED BY LINEAR SYSTEMATICS .024 .026 .009
RMS AT GPS-POINTS FITTED BY SYSTEMATICS T*T .019 .022 .008
4  .229761E-02 .425115E-02 .120658E-01 7.1 10:38:47
5  .465452E-01 .187517E-01 .204469E-01 7.1 10:38:50

NUMBER AND VALUES OF ADDITIONAL PARAMETERS
1000 -.24364E-04 2000 -.53432E-05 3000 .45932E-05 4000 .10684E-05
5000 .67484E-05 6000 -.17345E-04 7000 .13767E-04 8000 .14618E-04
9000 .52889E-05 10000 .30013E-05 11000 -.20009E-05 12000 -.14488E-05

TOTAL CORRELATION
.21 .20 .19 .21 .41 .67 .67 .40 .18 .09 .09 .12

ADDITIONAL PARAMETERS
1000 2000 3000 4000 5000 6000 7000 8000 9000 10000 11000 12000

STUDENT TEST
1 8.76 1.58 7.93 1.85 9.69 16.83 17.36 2.98 .89 6.53 5.75 4.20
+++ +++ +++ +++ ++ +++ +++ +++

CORRELATION BETWEEN ADDITIONAL PARAMETERS
1000 1.00 .01 .00 .35 -.10 .00 -.01 -.01 .06 .02 .02 -.17
+++D +++ +++ +++ +++ +++ ++ +++ +++ +++
2000 .01 1.00 .29 .01 -.03 .10 .03 .03 -.19 .00 .02 .01
+++ D +++ +++ +++ +++ +++ +++ +++ +++
3000 .00 .29 1.00 -.01 .00 .00 -.01 .04 .18-.04 -.23 .00
+++ +++D +++ + +++ +++ +++ +++ +++
4000 .35 .01 -.01 1.00 -.01 .00 .00 -.05 .02 .00 .00 .22
+++ +++ +++ D ++ +++ +++ +++ +++
5000 -.10 -.03 .00 -.01 1.00 -.01 -.01 .62 -.03 -.01 .01 -.04
+++ +++ + ++ +++D ++ +++ +++ +++ +++
6000 .00 .10 .00 .00 -.01 1.00 -.81 .00 .04 -.05 -.02 .00
+++ +++ ++ +++D +++ + +++ +++ +++ +
7000 -.01 .03 -.01 .00 -.01 -.81 1.00 -.01 -.10 .03 .02 .00
+++ +++ +++ +++ +++ +++D +++ +++ +++
8000 -.01 .03 .04 -.05 .62 .00 -.01 1.00 .00 -.01 .01 -.07
++ +++ +++ +++ +++ + +++ ++D + +++ ++ +++
9000 .06 -.19 .18 .02 -.03 .04 -.10 .00 1.00 -.25 -.13 .00
+++ +++ +++ +++ +++ +++ +++ + D +++ +++
10000 .02 .00 -.04 .00 -.01 -.05 .03 -.01 -.25 1.00 -.12 -.02

```

# Appendix C

	+++		+++		+++	+++	+++	+++	+++	+++D	+++	+++
11000	.02	.02	-.23	.00	.01	-.02	.02	.01	-.13	-.12	1.00	-.02
	+++	+++	+++		+++	+++	+++	++	+++	+++	+++D	+++
12000	-.17	.01	.00	.22	-.04	.00	.00	-.07	.00	-.02	-.02	1.00
	+++	+++	+++	+++	+			+++		+++	+++	+++D

+ = SIGNIFICANCE 95% ++ = SIGNIFICANCE 99% +++ = SIGNIFICANCE 99.9%

SHIFT OF PRINCIPAL POINT X: .000  
SHIFT OF PRINCIPAL POINT Y: .000

FOLLOWING ADDITIONAL PARAMETERS SHALL BE REMOVED:

9000  
6 .564335E-03 .571393E-03 .111354E-02 7.1 10:38:52

NUMBER AND VALUES OF ADDITIONAL PARAMETERS

1000	-.24417E-04	2000	-.57425E-05	3000	.45602E-05	4000	.10652E-05
5000	.67516E-05	6000	-.17339E-04	7000	.13752E-04	8000	.14588E-04
10000	.29969E-05	11000	-.19993E-05	12000	-.14477E-05		

TOTAL CORRELATION

.20	.17	.17	.21	.41	.67	.66	.40	.03	.08	.12
-----	-----	-----	-----	-----	-----	-----	-----	-----	-----	-----

ADDITIONAL PARAMETERS

1000	2000	3000	4000	5000	6000	7000	8000	10000	11000	12000
------	------	------	------	------	------	------	------	-------	-------	-------

STUDENT TEST

1	8.79	1.73	8.00	1.84	9.70	16.84	17.43	2.98	6.73	5.79	4.19
	+++		+++		+++	+++	+++	++	+++	+++	+++

CORRELATION BETWEEN ADDITIONAL PARAMETERS

1000	1.00	.02	-.01	.35	-.10	.00	-.01	.00	.04	.02	-.17
	+++D	+++	+++	+++	+++		+++	+	+++	+++	+++
2000	.02	1.00	.34	.01	-.04	.11	.01	.03	-.05	.00	.01
	+++	D	+++	+++	+++	+++	+++	+++	+++		+++
3000	-.01	.34	1.00	-.01	.00	-.01	.01	.04	.00	-.21	.00
	+++	+++	+++D	+++		+++	++	+++		+++	
4000	.35	.01	-.01	1.00	.00	.00	.00	-.05	.01	.01	.22
	+++	+++	+++	D	+	+		+++	+++	++	+++
5000	-.10	-.04	.00	.00	1.00	.00	-.01	.62	-.02	.00	-.04
	+++	+++		+	+++D		+++	+++	+++		+++
6000	.00	.11	-.01	.00	.00	1.00	-.81	.00	-.04	-.02	.00
		+++	+++	+		+++D	+++	+	+++	+++	+
7000	-.01	.01	.01	.00	-.01	-.81	1.00	-.01	.00	.01	.00
	+++	+++	++		+++	+++	+++D	+++	+	+++	
8000	.00	.03	.04	-.05	.62	.00	-.01	1.00	-.01	.00	-.07
	+	+++	+++	+++	+++	+	+++	++D	+++	+	+++
10000	.04	-.05	.00	.01	-.02	-.04	.00	-.01	1.00	-.16	-.02
	+++	+++		+++	+++	+++	+	+++	+++D	+++	+++
11000	.02	.00	-.21	.01	.00	-.02	.01	.00	-.16	1.00	-.02
	+++		+++	++		+++	+++	+	+++	+++D	+++
12000	-.17	.01	.00	.22	-.04	.00	.00	-.07	-.02	-.02	1.00
	+++	+++		+++	+++	+		+++	+++	+++	+++D

+ = SIGNIFICANCE 95% ++ = SIGNIFICANCE 99% +++ = SIGNIFICANCE 99.9%

SHIFT OF PRINCIPAL POINT X: .000  
SHIFT OF PRINCIPAL POINT Y: .000

NO ADDITIONAL PARAMETER SHALL BE REMOVED

RANGE OF PHOTO COORDINATES

X MINIMUM = -33.661 X MAXIMUM = 34.012

Y MINIMUM = -51.884 Y MAXIMUM = 51.896

R MAXIMUM = 62.048 FACTOR = 2.62053

UP TO 6064 POINTS / PHOTO

# Appendix C

NO.ITER (ITER)	MS CORR X TIME	MS CORR Y [ground unit]	MS CORR Z [microns]	SIGMA 0
0	.123013E-01	.114236E-01	.287191E-01	2.2 10:38:56
1	.788683E-02	.238352E-01	.251545E-01	2.1 10:39:01
MEAN HEIGHT				
CAMERA PROJECTION CENTER TERRAIN PHOTO SCALE				
1	1501.	280.	12147.	FOR [ft]: 3702. 309. inch/ft
2	1500.	289.	12055.	FOR [ft]: 3674. 306. inch/ft
3	1499.	293.	12004.	FOR [ft]: 3659. 305. inch/ft
4	1499.	306.	11872.	FOR [ft]: 3619. 302. inch/ft
MAIN KAPPA FOR DATA SET 1 : 201.336 10 10				
MAIN KAPPA FOR DATA SET 2 : 2.056 10 10				
MAIN KAPPA FOR DATA SET 3 : 199.274 10 10				
MAIN KAPPA FOR DATA SET 4 : -.184 10 10				
2	.364878E-01	.404663E-01	.614567E-01	2.2 10:39:06
NUMBER AND VALUES OF ADDITIONAL PARAMETERS				
1000	-.51569E-04	2000	-.12283E-04	3000 .90076E-05 4000 .26177E-05
5000	.22789E-04	6000	-.33183E-04	7000 .27381E-04 8000 .29414E-04
10000	.62716E-05	11000	-.40274E-05	12000 -.26761E-05
TOTAL CORRELATION				
.02	.01	.05	.12	.07 .47 .47 .07 .10 .12 .06
ADDITIONAL PARAMETERS				
1000	2000	3000	4000	5000 6000 7000 8000 10000 11000 12000
STUDENT TEST				
1	63.40	14.61	16.45	4.78 32.49 37.35 50.00 11.67 11.45 7.35 4.89
	+++	+++	+++	+++ +++ +++ +++ +++ +++ +++
CORRELATION BETWEEN ADDITIONAL PARAMETERS				
1000	1.00	.00	.01	-.08 -.03 -.03 .01 .01 .00 .00 .00
	+++D	+++	+++	+++ +++ +++ +++ +++
2000	.00	1.00	-.03	-.01 -.04 .02 -.02 -.02 .00 .00 .00
	+++	+++D	+++	+++ +++ +++ +++ +++
3000	.01	-.03	1.00	.00 -.02 -.03 -.01 .00 .02 -.03 .00
	+++	+++	+++D	+++ +++ +++ +++ +++
4000	-.08	-.01	.00	1.00 .07 .00 .01 -.07 .00 .00 .04
	+++	+++	+++D	+++ +++ +++ +++ +++
5000	-.03	-.04	-.02	.07 1.00 .03 .02 .20 .01 .00 .00
	+++	+++	+++	+++ +++D +++ +++ +++
6000	-.03	.02	-.03	.00 .03 1.00 -.48 .00 .00 .00 .00
	+++	+++	+++	+++ +++D +++ +++ +
7000	.01	-.02	-.01	.01 .02 -.48 1.00 -.01 .00 .00 .00
	+++	+++	+++	+++ +++ +++D +++ +
8000	.01	-.02	.00	-.07 .20 .00 -.01 1.00 .00 .00 -.01
	+++	+++	+++	+++ +++ +++ +++D +++
10000	.00	.00	.02	.00 .01 .00 .00 .00 1.00 -.03 .00
		+++	+++	+++ + + +++D +++
11000	.00	.00	-.03	.00 .00 .00 .00 .00 -.03 1.00 .00
		+++	+++	+++ +++ +++D +++
12000	.00	.00	.04	.00 .00 .00 .00 -.01 .00 .00 1.00
		++	+++	++ +++ +++D +++
+ = SIGNIFICANCE 95% ++ = SIGNIFICANCE 99% +++ = SIGNIFICANCE 99.9%				
NO ADDITIONAL PARAMETER SHALL BE REMOVED				
PHOTO ORIENTATION [GRADS] SEQUENCE OF ROTATION: PHI, OMEGA, KAPPA				
=====				
PHOTO	PHI	OMEGA	KAPPA	EASTING NORTHING HEIGHT
213	.1713	-1.0162	2.5711	495840.835 5420293.348 1500.430

# Appendix C

283	-.3013	.1658	.2982	495838.298	5421099.015	1497.927
246	-.3914	1.0717	-199.8281	495836.591	5420687.726	1502.336
176	-.3767	-.2666	-199.7300	495836.067	5419895.453	1501.418
212	.0855	-.7444	1.9943	495687.352	5420292.455	1500.499
177	-.4191	-.5086	-199.9687	495689.409	5419896.129	1501.200
247	-.4151	.8457	199.7541	495690.289	5420688.020	1502.894
282	-.2984	.2820	.0876	495686.051	5421097.070	1497.524
211	.0224	-.3280	1.6746	495536.997	5420292.611	1500.449
281	-.3254	.5644	-.1448	495540.649	5421095.778	1497.754
178	-.4017	-.5563	199.7913	495537.770	5419897.936	1500.958
248	-.5109	.7934	199.6245	495536.956	5420688.976	1502.426
210	-.0578	-.4526	2.0455	495385.558	5420293.564	1500.207
179	-.3762	-.2387	-199.5594	495386.036	5419899.547	1500.546
249	-.5237	1.0967	199.5586	495385.141	5420688.676	1501.011
280	-.3268	.8734	-.2854	495386.255	5421095.359	1498.744
209	-.0435	-.5407	2.2953	495240.167	5420293.891	1500.494
250	-.5469	1.0335	199.0800	495239.511	5420688.536	1499.504
279	-.3559	1.0330	-.7881	495238.248	5421095.883	1500.123
180	-.4033	-.0443	-198.8404	495233.044	5419899.462	1499.715
208	-.3318	-.5893	2.0068	495085.539	5420293.726	1500.688
181	-.3959	.2189	-198.3413	495086.241	5419897.698	1499.199
251	-.6141	.6691	198.6087	495085.336	5420690.005	1497.894
278	-.4492	1.0833	-.8154	495085.744	5421097.601	1500.741
207	-.6157	-.4612	1.9258	494932.280	5420293.786	1500.756
252	-.6322	.4105	198.3611	494935.733	5420692.347	1496.686
277	-.5829	.7809	-.4142	494934.383	5421098.756	1500.733
182	-.3308	.2089	-198.5599	494932.261	5419895.688	1499.211
206	-.7450	-.3087	1.7164	494784.769	5420294.902	1500.137
183	-.0110	.1249	-198.8469	494787.346	5419893.866	1500.011
253	-.5233	.2480	198.5712	494786.979	5420694.869	1496.188
276	-.5395	.6562	.0980	494782.606	5421097.945	1500.547
205	-.7566	-.5212	2.0568	494630.995	5420296.761	1499.402
254	-.5008	.4493	198.9650	494638.357	5420696.754	1496.109
184	.3754	.0799	-198.5830	494635.710	5419891.804	1501.111
275	-.5149	.7973	-.1192	494630.645	5421096.215	1499.657
204	-.7225	-.5789	2.2759	494484.050	5420296.923	1499.480
185	.3929	-.2217	-198.9348	494483.552	5419889.986	1501.838
255	-.4219	.7147	199.4996	494482.079	5420697.254	1496.825
274	-.4785	.6064	.2432	494480.251	5421094.962	1498.197

PHOTO ORIENTATIONS IN ROTATION SEQUENCE OMEGA, PHI, KAPPA [GRADS]

STORED IN DAPORO.DAT

PHOTO ORIENTATIONS IN PAT-B-FORMAT STORED IN DAPORP.DAT

BLUH ORIENTATIONS WITH ROTATION SEQUENCE PHI OMEGA KAPPA [GRADS]

STORED IN dapor.dat

=====

ADJUSTED COORDINATES ERROR LIMIT FOR LISTING RESIDUALS 20.00 MICRONS

=====

POINT NAME	EASTING	NORTHING	HEIGHT	PHOTOS/POINT
D.I.:	IMAGE	Dx [microns]	Dy	P ROB.E.
Dx EAST	Dy NORTH			
DATASNO	MAX			

DCP: DIFFERENCE AT OBJECT COORDS. OF CONTROL POINTS SWEIGHT

-----

1768	496224.331	5420332.330	253.559	3
1778	496000.223	5420343.969	253.469	6
1818	495443.958	5420401.613	266.912	18
2093	495497.105	5420755.590	304.561	16
2098	495559.279	5419839.331	326.717	10
2099	495525.091	5419861.725	324.676	10
2102	495592.484	5420799.500	298.431	15
2103	495676.287	5420761.434	290.203	12
2104	495662.982	5420419.775	252.870	12



# Appendix C

2106	495666.920	5419861.951	324.166	8	
2107	495637.366	5419897.048	324.554	9	
2108	495625.375	5419838.788	326.144	10	
2115	495798.021	5420760.558	280.680	9	
2119	495869.276	5419899.015	286.325	6	
2121	495907.441	5420851.806	274.038	9	
2123	495986.649	5420336.635	253.450	6	
2125	495707.381	5419747.207	322.384	8	
2126	496026.591	5419837.330	276.284	4	
2127	496009.847	5419764.260	276.478	4	
2128	495981.600	5419817.799	279.946	4	
2131	495528.662	5420743.853	300.855	15	
2132	496047.413	5420812.428	258.270	6	
2135	495521.495	5419756.050	325.869	10	
2136	495506.848	5419783.809	324.543	10	
2137	496128.640	5419908.690	273.738	2	BASE 397.93
2138	496159.133	5419809.401	272.151	2	BASE 397.93
2139	496131.486	5419834.722	273.572	2	BASE 397.93
2463	496212.064	5420246.321	253.236	3	
2471	496049.220	5420201.215	253.639	6	
2483	495910.018	5420212.425	257.275	9	
2491	495758.231	5420260.885	252.648	12	
2503	495567.687	5420305.497	251.586	15	
2799	495505.909	5420747.149	303.321	15	
2819	495577.837	5420687.425	290.890	15	
17626	496242.108	5419692.130	266.389	2	BASE 397.93
17633	496242.627	5419925.255	267.930	2	BASE 397.93
17638	496219.438	5419943.504	267.976	2	BASE 397.93
17639	496244.591	5419942.935	267.240	2	BASE 397.93
17678	496192.317	5419692.282	269.351	2	BASE 397.93

-----  
 -----  
 List of adjusted coordinates of 15734 tie points  
 Reduced By A. Gneeniss  
 -----  
 -----

274296	494211.167	5421243.288	346.411	2	BASE 397.71
274306	494190.323	5421012.801	366.851	2	BASE 397.71
274307	494239.792	5420942.074	363.359	2	BASE 397.71
274308	494238.087	5420896.380	357.489	2	BASE 397.71
274343	494256.050	5421268.440	342.091	2	BASE 397.71
274347	494256.305	5421243.824	345.223	2	BASE 397.71
274349	494233.769	5421172.547	354.232	2	BASE 397.71
274350	494329.541	5421082.176	359.498	2	BASE 397.71
274357	494213.284	5421033.491	365.548	2	BASE 397.71
274360	494236.491	5420917.854	358.587	2	BASE 397.71
274404	494258.818	5421055.835	363.475	2	BASE 397.71
274414	494256.470	5420872.079	351.019	2	BASE 397.71
2551180	494303.394	5420853.623	345.025	2	BASE 397.71
2551184	494214.119	5420968.196	363.729	2	BASE 397.71
2551185	494215.399	5421011.143	365.806	2	BASE 397.71
2551187	494260.635	5421011.267	364.636	2	BASE 397.71
2551238	494215.659	5421036.438	365.346	2	BASE 397.71
2551239	494236.473	5421013.262	365.035	2	BASE 397.71
2551244	494251.107	5421252.055	344.417	2	BASE 397.71
2551246	494259.597	5421227.899	347.025	2	BASE 397.71
2551280	494237.877	5420898.009	356.753	2	BASE 397.71
2551281	494189.916	5420875.387	351.127	2	BASE 397.71
2551283	494119.546	5420935.352	362.354	2	BASE 397.71
2551289	494161.874	5421178.949	355.983	2	BASE 397.71
2551291	494235.135	5421265.853	342.954	2	BASE 397.71
2551292	494229.537	5421294.841	339.402	2	BASE 397.71
2551325	494191.122	5420921.095	361.332	2	BASE 397.71

# Appendix C

2551337	494129.769	5421178.430	357.421	2	BASE	397.71
2551368	494212.494	5420876.007	351.953	2	BASE	397.71
2551373	494193.054	5420965.491	366.104	2	BASE	397.71
2551382	494163.241	5421203.794	352.862	2	BASE	397.71
2551417	494189.893	5420897.973	356.021	2	BASE	397.71
2551419	494166.854	5420922.268	359.921	2	BASE	397.71
2551429	494134.096	5421114.277	363.337	2	BASE	397.71
2551465	494139.217	5420855.837	344.564	2	BASE	397.71
2551470	494146.652	5420966.377	367.067	2	BASE	397.71
2551471	494167.402	5421013.530	367.076	2	BASE	397.71
2551475	494167.514	5421059.964	365.814	2	BASE	397.71
2551476	494190.981	5421035.677	366.490	2	BASE	397.71

```

=====
ROOT MEAN SQUARE OF DIFFERENCES AT CONTROL POINTS      FOR UNIT WEIGHT
  0 HORIZONTAL CONTROL POINTS      RMSE X = +/-   .000      +/-   .000
                                   RMSE Y = +/-   .000      +/-   .000
  0 VERTICAL CONTROL POINTS      RMSE Z = +/-   .000      +/-   .000
                                   [ground units]
MEAN DIFFERENCE AT CONTROL POINTS:
  X:   .000      Y:   .000      Z:   .000 [ground units]

ROOT MEAN SQUARE OF RELATIVE DIFFERENCES AT GPS POINTS
  40 POSITIONS      RMSE X = +/-   .019
                   RMSE Y = +/-   .022
                   RMSE Z = +/-   .008
AVERAGE BASE FOR 2-RAY-POINTS:      256.70
MEAN SQUARE ERRORS      [microns]
POINT CODE      NO IN GROUP      NO PHOT PTS      INT MSE X      INT MSE Y
  CPZ      1      15734      157708      6.64      6.43
  CPXY      2      15734      157708      3.06      2.96

MEAN SQUARE CORRECTIONS OF LAST ITERATION
X:   .0138      Y:   .0132      Z:   .0323 [ground units]

```

OBSERVATIONS	UNKNOWN	REDUNDANCE	SIGMA 0
315416	47453	267963	.67 10:39:15
			[microns]

```

NUMBER AND VALUE OF ADDITIONAL PARAMETERS
1000 -.26E-04 2000 -.61E-05 3000 .44E-05 4000 .15E-05 5000 .16E-04
6000 -.15E-04 7000 .13E-04 8000 .15E-04 10000 .33E-05 11000 -.20E-05
12000 -.12E-05

```

```

TOTAL CORRELATION
.02 .01 .05 .12 .07 .47 .47 .07 .10 .12 .06

```

```

ADDITIONAL PARAMETERS
1000 2000 3000 4000 5000 6000 7000 8000 10000 11000 12000

```

```

STUDENT TEST
1
825.05188.31432.41135.22575.70432.46887.11149.02421.79314.40182.73
+++ +++ +++ +++ +++ +++ +++ +++ +++ +++ +++

```

```

CORRELATION BETWEEN ADDITIONAL PARAMETERS
1000 2000 3000 4000 5000 6000 7000 8000 10000 11000 12000
1000 1.00 .00 .01 -.15 -.03 -.03 .02 .01 .00 .00 .00
      DIAG +++ +++ +++ +++ +++ +++ +++ +++ ++ +
2000 .00 1.00 -.06 -.01 -.04 .02 -.02 -.02 -.01 .01 .01

```

# Appendix C

	+++	DIAG	+++	+++	+++	+++	+++	+++	+++	+++	+++	+++
3000	.01	-.06	1.00	.00	-.04	-.06	-.02	.00	.09	-.18	.00	
	+++	+++	DIAG		+++	+++	+++		+++	+++		
4000	-.15	-.01	.00	1.00	.12	-.01	.02	-.14	.00	.00	.24	
	+++	+++		DIAG	+++	+++	+++	+++	+	+++	+++	
5000	-.03	-.04	-.04	.12	1.00	.02	.03	.20	.01	.01	.01	
	+++	+++	+++	+++	DIAG	+++	+++	+++	+++	+++	+++	
6000	-.03	.02	-.06	-.01	.02	1.00	-.68	-.01	.01	.00	.00	
	+++	+++	+++	+++	+++	DIAG	+++	+++	+++	+++	+++	
7000	.02	-.02	-.02	.02	.03	-.68	1.00	-.01	-.01	.00	.00	
	+++	+++	+++	+++	+++	+++	DIAG	+++	+++	+++	+++	
8000	.01	-.02	.00	-.14	.20	-.01	-.01	1.00	.00	.00	-.03	
	+++	+++		+++	+++	+++	+++	DIAG		+	+++	
10000	.00	-.01	.09	.00	.01	.01	-.01	.00	1.00	-.31	.00	
	++	+++	+++	+	+++	+++	+++		DIAG	+++	++	
11000	.00	.01	-.18	.00	.01	.00	.00	.00	-.31	1.00	-.01	
	+	+++	+++	+++	+++	+++	+++	+	+++	DIAG	+++	
12000	.00	.01	.00	.24	.01	.00	.00	-.03	.00	-.01	1.00	
	++	+++		+++	+++		+++	+++	++	+++	DIAG	

+ = SIGNIFICANCE 95%      ++ = SIGNIFICANCE 99%      +++ = SIGNIFICANCE 99.9%

## MEAN VALUES OF RESIDUALS AND MSE IN RADIAL COMPONENTS

1ST LINE	RADIUS		[CM]											
2ND LINE	MEAN RADIAL		[MICRONS]											
3RD LINE	MSE RADIAL		[MICRONS]											
4TH LINE	MSE TANGENTIAL		[MICRONS]											
5TH LINE	NUMBER OF POINTS		IN GROUP											
DATA SET	1													
.0	.4	.8	1.1	1.5	1.9	2.3	2.7	3.1	3.4	3.8	4.2	4.6	5.0	5.3
-.2	-.1	-.1	.0	.1	.2	.0	-.1	.0	-.1	-.1	-.2	-.1	.0	.4
1.0	1.0	1.4	2.1	2.7	3.5	4.2	3.2	3.9	5.2	4.9	6.5	6.5	9.6	11.1
.9	1.3	1.9	4.2	4.3	5.2	3.7	3.3	5.8	6.3	4.5	7.2	5.5	6.3	6.6
54	630	1350	2982	4839	5844	6291	7218	8256	7920	6534	6570	7299	6960	4233
MSE (RADIAL) = +/- 5.9    MSE (TANGENTIAL) = +/- 5.5    78927 PHOTO POINTS														

DATA SET	2													
	.0	.4	.8	1.1	1.5	1.9	2.3	2.7	3.1	3.4	3.8	4.2	4.6	5.0
	-.4	-.5	.1	.1	.1	.1	.1	.3	.1	.0	-.1	-.1	.0	.0
	4.2	7.8	6.6	5.6	5.9	9.1	6.9	8.4	9.2	8.2	6.4	4.2	3.8	4.5
	3.3	5.4	5.7	4.7	4.6	6.3	6.8	7.6	7.2	7.9	6.0	7.5	5.2	9.5
	216	2040	4152	6123	8553	9360	9957	11187	12567	10899	9237	9795	12477	12447
	7125													

MSE (RADIAL) = +/- 6.7    MSE (TANGENTIAL) = +/- 6.7    129090 PHOTO POINTS

DATA SET	3													
	.0	.4	.8	1.1	1.5	1.9	2.3	2.7	3.1	3.4	3.8	4.2	4.6	5.0
	.0	-.1	-.1	-.1	-.2	-.1	-.2	-.2	-.2	.1	.0	.1	.2	.1
	2.0	3.6	4.7	4.8	5.8	7.1	7.4	6.6	8.5	8.8	6.2	4.3	5.0	6.6
	2.1	2.6	3.5	4.5	4.7	4.3	5.4	5.3	10.2	9.0	10.3	10.8	10.2	15.8
	333	2385	4791	7800	9738	11124	13197	14823	15666	14052	12153	10914	11310	10143
	5469													

MSE (RADIAL) = +/- 6.8    MSE (TANGENTIAL) = +/- 9.2    146337 PHOTO POINTS

DATA SET	4													
	.0	.4	.8	1.1	1.5	1.9	2.3	2.7	3.1	3.4	3.8	4.2	4.6	5.0
	-.1	-.2	-.2	.0	.0	.0	-.1	.0	.0	.1	.0	.0	.1	.2
	1.1	1.3	2.4	6.1	2.2	2.9	2.6	2.9	2.7	5.3	3.3	4.9	7.2	13.1
	1.2	2.1	1.7	6.8	3.0	2.5	6.2	2.6	2.6	4.9	3.1	5.8	5.7	7.8
	12.6													

# Appendix C

216 1458 2778 4947 6840 7791 994212189126871243510755 9951 9330 8244  
4434

MSE (RADIAL) = +/- 7.0                      MSE (TANGENTIAL) = +/- 5.6    115734  
PHOTO POINTS

MEAN SQUARE NADIR ANGLE :                      .8

MEAN PHOTO SCALE = 1:            12027.3            40 PHOTOS  
FOR [ft]: 1:            3666.            =            305. in/ft

ADJUSTED COORDINATES            COMPUTED : DATE: 12.07.2012            10:39:15

=====

1765	495583.061	5419394.637	334.725	5	Tie
1768	496224.331	5420332.330	253.559	3	Pass
1771	496100.836	5419382.555	264.618	2	Tie
1776	496027.929	5420291.094	253.056	3	Pass
1778	496000.223	5420343.969	253.469	6	Pass
1781	495922.042	5419392.510	278.319	3	Tie
1789	495250.082	5420360.837	272.519	15	Pass
1791	495707.434	5419347.133	323.857	4	Tie
1801	495603.266	5419409.351	333.234	5	Tie
1808	494912.913	5420361.254	284.064	15	Pass
1809	495628.480	5419340.057	333.984	5	Tie
1818	495443.958	5420401.613	266.912	18	Pass
1819	495353.632	5420385.937	269.431	15	Pass
1821	495327.415	5419414.650	337.313	6	Tie
1827	495240.947	5420337.448	265.078	15	Pass
1828	494974.996	5420417.858	287.422	15	Pass
1829	494650.987	5420275.420	252.668	12	Pass
1831	495123.139	5419433.325	335.040	5	Tie
1851	494865.186	5419420.011	328.532	6	Tie
2041	494168.166	5420738.920	274.093	3	Pass
2042	494164.092	5420780.508	297.006	3	Pass
2043	494718.077	5420796.421	314.891	10	Pass
2044	494745.349	5420775.256	313.767	14	Pass
2045	494146.239	5419853.680	290.551	2	Pass
2046	494173.325	5419805.961	290.913	2	Pass
2047	494247.671	5419787.067	294.314	3	Pass
2051	494323.208	5420815.825	334.930	6	Pass
2052	494372.199	5420814.726	337.885	6	Pass
2053	494926.199	5420832.251	338.740	15	Pass
2054	494977.439	5420831.815	336.378	15	Pass
2055	494321.198	5420324.667	256.651	6	Pass
2058	494291.790	5419785.374	296.933	4	Pass
2061	494756.489	5420788.269	310.245	15	Pass
2062	495045.190	5420814.646	331.803	15	Pass
2063	495020.812	5420836.826	334.188	17	Pass
2064	495065.432	5420394.788	284.272	15	Pass
2065	494479.779	5419774.606	315.567	6	Pass
2067	495080.828	5419818.157	323.464	10	Pass
2071	494647.923	5420772.069	328.684	12	Pass
2072	494958.737	5420825.966	336.664	15	Pass
2073	495212.382	5420815.831	323.228	15	Pass
2074	495188.542	5420824.310	324.591	15	Pass
2077	495272.642	5419885.029	318.374	10	Pass
2078	495223.568	5419789.600	325.879	10	Pass
2079	495201.333	5419812.858	324.819	11	Pass

-----  
-----  
List of adjusted coordinates of 15734 tie points  
Reduced By A. Gneeniss

2081	494764.887	5420752.330	305.346	15	Pass
2082	494778.776	5420681.908	290.391	15	Pass
2083	495099.770	5420736.663	322.563	15	Pass
2084	495365.456	5420768.802	313.353	15	Pass
2085	495339.686	5420792.476	315.555	16	Pass
2086	495367.612	5420341.074	256.147	11	Pass
2087	495060.074	5419776.198	324.764	10	Pass
2088	495369.166	5419881.930	319.004	10	Pass
2091	494909.618	5420760.526	290.290	15	Pass
2092	494880.896	5420779.960	293.019	14	Pass
2093	495497.105	5420755.590	304.561	16	Pass
2098	495559.279	5419839.331	326.717	10	Pass
2099	495525.091	5419861.725	324.676	10	Pass
2101	495063.256	5420818.270	331.007	15	Pass
2102	495592.484	5420799.500	298.431	15	Pass
2103	495676.287	5420761.434	290.203	12	Pass
2104	495662.982	5420419.775	252.870	12	Pass
2831114	496061.119	5421467.834	297.828	2	Tie
2831127	496065.385	5421151.437	284.887	4	Pass
2831129	496017.132	5421124.991	281.421	4	Pass
2831138	496046.832	5420850.305	259.201	6	Pass
2831144	496052.550	5420710.854	289.727	4	Pass
2831145	496064.531	5420662.503	292.893	6	Pass
2831150	496076.686	5420610.396	289.785	6	Pass
2831151	496071.610	5420637.842	293.075	6	Pass
2831153	496037.889	5420619.238	290.600	6	Pass
2831154	496122.011	5420533.025	277.651	3	Pass
2831169	496089.230	5421322.670	288.675	2	Pass
2831171	496113.675	5421298.237	289.744	2	Pass
2831173	496089.374	5421297.693	283.808	4	Pass
2831174	496089.657	5421247.592	288.137	4	Pass
2831175	496062.375	5421259.208	282.545	4	Pass
2831176	496090.392	5421225.855	288.427	4	Pass
2831177	496091.531	5421175.200	288.197	3	Pass
2831183	496095.979	5420977.080	262.124	4	Pass
2831185	496094.434	5421000.494	263.467	4	Pass
2831186	496088.277	5420885.609	258.253	5	Pass
2831188	496098.246	5420875.533	259.325	5	Pass
2831189	496103.643	5420850.396	259.059	5	Pass
2831198	496091.071	5420636.621	292.205	5	Pass
2831204	496145.287	5420532.784	278.331	3	Pass
2831224	496112.631	5421322.696	289.700	2	Pass
2831225	496087.989	5421274.533	287.413	4	Pass
2831227	496140.428	5421224.297	289.149	2	Pass
2831233	496095.782	5420990.172	262.642	3	Pass
2831237	496060.840	5420886.504	258.938	6	Pass
2831250	496189.531	5420638.514	292.649	3	Pass
2831270	496189.435	5421297.234	287.733	2	Pass
2831271	496189.836	5421275.536	288.183	2	Pass
2831272	496162.503	5421299.433	288.276	2	Pass
2831274	496161.815	5421248.894	289.671	2	Pass
2831275	496136.844	5421226.260	289.741	2	Pass
2831280	496135.918	5421128.385	264.700	2	Pass
2831290	496086.498	5420806.255	259.078	5	Pass
2831292	496177.301	5420766.113	290.675	3	Pass
2831304	496216.683	5420512.836	276.620	3	Pass
2831322	496212.509	5421298.155	287.104	2	Pass
2831337	496239.772	5420884.548	287.029	2	Pass
2831387	496211.112	5420810.679	292.366	2	Pass
2831391	496196.129	5420733.501	292.124	3	Pass
2831400	496190.956	5420588.621	289.953	3	Pass

# Appendix C

2831401	496195.112	5420533.861	278.516	3	Pass
2831403	496164.440	5420526.228	277.098	3	Pass
2831420	496211.407	5421275.561	287.587	2	Pass
2831434	496221.671	5420931.152	283.608	2	Pass
2831437	496217.164	5420879.220	285.364	2	Pass
2831438	496213.569	5420831.599	292.470	2	Pass
2831439	496190.272	5420808.310	289.074	3	Pass
2831440	496216.002	5420857.975	291.254	2	Pass
2831441	496213.345	5420808.077	292.372	2	Pass
2831442	496191.689	5420760.627	290.981	3	Pass
2831443	496212.285	5420782.017	288.538	3	Pass
9205019	494825.991	5419532.030	325.870	5	Tie
9306019	495401.045	5420325.999	252.837	15	Pass
9307019	496114.050	5420265.587	251.119	5	Pass
9405109	495241.222	5420919.209	319.321	10	Pass
9406019	495397.798	5421190.263	268.404	10	Pass
92041029	494294.169	5419912.763	294.942	4	Pass
92041059	494406.100	5419359.153	305.009	3	Tie
93041029	494350.549	5420660.487	255.803	6	Pass
94041019	494332.435	5421506.122	315.336	2	Tie
94041079	494540.275	5420972.179	357.245	6	Pass
94051029	495254.131	5421495.907	271.941	5	Tie

POINT COORDINATES STORED IN daxyz.dat

DATA FOR TRANSFER TO BLAN STORED IN bluinf.dat

NUMBER AND VALUES OF ADDITIONAL PARAMETERS

1000 -.260215E-04 2000 -.614115E-05 3000 .440268E-05 4000 .151159E-05  
5000 .156596E-04 6000 -.148950E-04 7000 .133088E-04 8000 .145661E-04  
10000 .325709E-05 11000-.201564E-05 12000-.121790E-05

EFFECT OF ADDITIONAL PARAMETERS TO PHOTO COORDINATES WITHOUT F, XP, YP

DATA SET 1 MEAN SQUARE X: 2.8 Y: 3.5 MICRONS

X - COORDINATE [0.1 MICRONS]													
-60.0 .0													
60.0													
+	-18	-20	-27	-32	-34	-36	-37	-36	-32	-27	-23	-23	-16
-9	-19	-22	-22	-24	-28	-31	-32	-30	-24	-15	-11	-12	
-7	-13	-10	-12	-16	-21	-25	-27	-24	-20	-14	-3	0	
-4	-2	-1	-4	-6	-13	-19	-22	-20	-14	-9	0	9	
3	7	4	4	0	-7	-13	-14	-13	-9	-1	3	15	
13	15	12	11	3	-1	-6	-5	-1	-1	5	10	20	
+	23	22	19	16	7	4	0	4	9	7	13	18	26
	31	31	26	23	13	8	6	10	15	14	20	23	31
	38	39	32	29	22	15	14	15	15	18	24	27	36
	47	45	40	33	29	24	21	19	19	23	26	31	38
	62	50	47	42	36	32	28	26	26	27	29	36	34
	80	63	53	49	45	40	36	33	31	32	35	35	27
+	91	81	67	57	52	48	44	41	39	38	35	28	27
Y - COORDINATE [0.1 MICRONS]													
-60.0 .0													
60.0													
+	-20	-20	-12	-9	-11	-14	-16	-17	-18	-24	-37	-56	-70
	-14	-5	-3	-9	-13	-16	-17	-18	-21	-25	-31	-45	-68
	-3	1	-2	-6	-9	-13	-15	-16	-18	-25	-33	-42	-61
	3	3	2	0	-7	-11	-13	-15	-18	-23	-33	-45	-59
	6	6	7	3	0	-2	-5	-7	-15	-24	-34	-48	-62
	7	9	10	8	7	2	-2	-4	-12	-25	-36	-51	-67
+	8	11	12	12	9	5	0	-7	-17	-28	-41	-56	-73

## Appendix C

7	11	12	13	8	2	-4	-15	-25	-34	-48	-63	-81
4	10	11	11	7	-1	-10	-19	-28	-41	-56	-71	-90
1	6	7	6	3	-1	-9	-19	-32	-48	-62	-79	-98
0	0	2	1	-3	-8	-15	-26	-39	-52	-68	-88	-102
2	-3	-6	-6	-8	-14	-21	-30	-42	-59	-77	-91	-101
+	-1	0	-7	-15	-19	-23	-30	-40	-53	-67	-77	-87
												-105

EFFECT OF ADDITIONAL PARAMETERS TO PHOTO COORDINATES STORED IN  
sysim1.dat

RADIAL SYMMETRIC COMPONENT OF EFFECT OF ADDITIONAL PARAMETERS

RADIUS	4.62	9.24	13.85	18.47	23.09	27.71	32.32	36.94	MM
DISTORTION	.0	.0	.1	.2	.1	-.2	-.4	-.3	MICRONS

RADIUS	41.56	46.18	50.79	55.41	60.03	64.65	69.26	73.88	MM
DISTORTION	-.1	.0	.0	.1	.4	.8	.6	-.1	MICRONS

RADIUS	78.50	83.12	87.73	92.35	96.97	101.59	106.20	110.82	MM
DISTORTION	-.8	-.9	-.5	.0	.0	.0	.3	1.1	MICRONS

RADIUS	115.44	120.06	124.68	129.29	133.91	138.53	143.15	147.76	MM
DISTORTION	1.3	.6	-.7	-1.5	-1.2	-.4	.1	.0	MICRONS

MAXIMAL VALUE OF SYSTEMATIC IMAGE ERRORS = 9. MICRONS

### OUTPUT FILES

-----

OBJECT COORDINATES	:	daxyz.dat
ORIENTATIONS PHI OMEGA KAPPA:	:	dapor.dat
ORIENTATIONS OMEGA PHI KAPPA:	:	daporo.dat
ORIENTATIONS PAT-B-FORMAT	:	daporp.dat
RESIDUALS AT IMAGE POSITIONS:	:	resi.dat
SYSTEMATIC IMAGE ERRORS	:	sysim1.dat
SYSTEMATIC IMAGE ERRORS	:	pcgrid1.dat
SYSTEMATIC IMAGE ERRORS	:	sysim2.dat
SYSTEMATIC IMAGE ERRORS	:	pcgrid2.dat
SYSTEMATIC IMAGE ERRORS	:	sysim3.dat
SYSTEMATIC IMAGE ERRORS	:	pcgrid3.dat
SYSTEMATIC IMAGE ERRORS	:	sysim4.dat
SYSTEMATIC IMAGE ERRORS	:	pcgrid4.dat
DATA FOR TRANSFER TO BLAN	:	bluinf.dat

END OF BLUH    DATE: 12.07.2012    10:39:25  
LARGEST BLUNDER WITH \*\*\*\*

## Appendix D

**Sample of the Generated 9 LCPs Control Points File in BLUH Format for the UltraCamX dataset.**

<i>Point ID</i>	<i>Easting</i>	<i>Northing</i>	<i>Height</i>	<i>Type of control point</i> <i>1 =vertical, 2 =Horizontal</i> <i>and 3 = Full</i>
27418	494490.235	5420755.003	340.941	3
185594	494520.449	5420113.452	259.721	3
207683	495177.987	5420086.304	252.172	3
212586	495866.264	5420059.849	283.017	3
275607	494592.919	5421421.820	316.817	3
278507	495147.363	5421364.514	288.048	3
282944	495851.470	5421324.596	253.909	3
2771015	495199.714	5420749.446	320.423	3
2811406	495916.660	5420742.825	255.268	3



**Sample of the Generated 20 LCPs Control Points File in BLUH Format for the DSS322 dataset.**

<i>Point ID</i>	<i>Easting</i>	<i>Northing</i>	<i>Height</i>	<i>Type of control point</i> <i>1 =vertical, 2 =Horizontal</i> <i>and 3 = Full</i>
417	372006.776	563991.054	127.143	3
15975	371524.771	564011.196	114.199	3
18343	372239.256	564041.635	136.381	3
55624	372148.300	563827.236	100.498	3
109224	371874.876	563939.987	104.290	3
110576	371700.037	564019.437	119.530	3
111688	371351.637	563889.488	112.145	3
111688	371351.637	563889.488	112.145	3
279971	372206.069	563921.395	136.879	3
314765	371934.878	564048.284	130.476	3
315231	372173.989	564067.337	130.644	3
371639	371353.955	563784.249	116.877	3
540254	371601.712	563932.517	107.056	3
543225	371726.567	563880.910	105.356	3
556160	372096.852	563912.201	108.613	3
1116150	371476.007	563830.475	106.211	3
1589100	371868.130	564155.579	128.383	3
1594136	371730.849	564236.411	143.147	3
1602174	371724.623	564112.266	147.088	3
1610103	371557.588	564095.598	128.765	3